

Submitted by
Andreas Gebhard

Submitted at
Institute of
Signal Processing

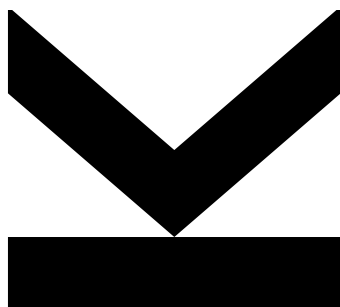
Supervisor and
First Examiner
Univ.-Prof. Dr.
Mario Huemer

Second Examiner
Prof. Dr.-Ing.
Bin Yang

Co-Supervisors
-

April 2019

Self-Interference Cancellation and Rejection in FDD RF-Transceivers



Doctoral Thesis
to obtain the academic degree of
Doktor der technischen Wissenschaften
in the Doctoral Program
Technische Wissenschaften

Abstract

Modern mobile communication devices offer a variety of data intensive services like video telephony or multimedia streaming. To support the high data rates needed for these services, the 3rd Generation Partnership Project (3GPP) introduced Long Term Evolution-Advanced (LTE-A) which includes the carrier aggregation (CA) feature. With CA, multiple parts of the spectrum which are scattered across the frequency bands may be aggregated to increase the data throughput. LTE-A supports the frequency division duplex (FDD) operation for simultaneous transmission and reception in over 40 frequency bands. For each operating band a separate band-pass filter (duplexer) is needed to provide isolation between the transmitters and the receivers which is a driving cost factor within the analog front-end of the transceiver. Consequently, in cost effective front-ends duplexers with reduced isolation are used. The resulting transmitter leakage signal into the CA receivers in combination with front-end non-idealities leads to a receiver desensitization.

In this dissertation three major contributions are provided. As a first step, the transmitter leakage (TxL) signal caused receiver interferences are modeled in the radio frequency (RF) domain and the resulting baseband (BB) equivalent receiver interferences are determined. This includes the modeling of the modulated spur-, and the second-order intermodulation distortion (IMD2) interference. The down-conversion of the TxL signal by spurs creates the modulated spur interference which may consist of a main and an image component. The second-order nonlinearity of the mixer creates an IMD2 interference which always falls around the zero-frequency. In case of direct-conversion receiver architectures, this leads to a BB interference which disturbs the wanted receive signal. Furthermore, the 25% duty-cycle current driven passive mixer which is preferably used in direct-conversion receivers is modeled. Due to the square-wave control signals, harmonics are produced within the mixer which may lead to the down-conversion of unwanted spectral components into the receiver BB. This down-conversion by the harmonic response of the mixer may degrade the receiver performance.

In a second step, the BB equivalent interference models are used to derive dedicated adaptive filters to cancel the TxL signal caused self-interferences in the digital BB of the transceiver. This dissertation provides solutions to cancel the modulated spur-, and the IMD2 interference by adaptive filtering. Simulation results show that a widely-linear adaptive filter structure is able to cancel the main-, and image modulated spur interference. A major part of this thesis investigates solutions for the digital cancellation of the IMD2 interference. Nonlinear Wiener model least-mean-squares (LMS)-, and recursive-least-squares (RLS) based adaptive filters are developed which outperform the traditional Volterra kernel based adaptive filters in terms of performance and complexity. The functionality of the proposed nonlinear adaptive filters is demonstrated using simulated and measured IMD2 data.

The third contribution is the development of a harmonic rejection mixer concept for the 25% duty-cycle current driven passive mixer. With this approach, the down-conversion of blocker signals by the harmonic response of the mixer can be suppressed. Circuit simulations using a 28 nm technology package show a superior suppression of the mixer harmonic response.

Kurzfassung

Moderne mobile Kommunikationssysteme ermöglichen eine Vielzahl datenintensiver Anwendungen wie etwa die Videotelefonie oder das Streamen von Multimedia-Inhalten. Um die für diese Anwendungen erforderlichen Datenraten bereitzustellen wurde vom Standardisierungsgremium 3GPP der LTE-A Standard eingeführt welcher u.a. das sogenannte Carrier Aggregation (CA) ermöglicht. Mit Hilfe von CA können mehrere verteilte Anteile des Kommunikationsspektrums vereint werden um eine höhere Datenrate zu erreichen. LTE-A unterstützt das Frequenzmultiplexverfahren welches das simultane Senden und Empfangen von Daten in über 40 Frequenzbändern ermöglicht. Für jedes Frequenzband wird ein separates Bandpassfilter zur Isolation zwischen den Sendern und den Empfängern benötigt was ein treibender Kostenfaktor für das analoge Front-End ist. Somit werden in kosteneffizienten Front-Ends Bandpassfilter mit reduzierter Dämpfung eingesetzt um die Kosten zu senken. Daraus resultierend ergibt sich ein Lecksignal vom Sender in jeden einzelnen CA Empfänger welches in Kombination mit Nichtidealitäten des Front-Ends zu einer Desensibilisierung der Empfänger führt.

Diese Dissertation liefert drei wesentliche Beiträge. Der erste Beitrag besteht aus der Modellierung der Störungen im Empfänger welche durch das Lecksignal und die Front-End Nichtidealitäten erzeugt werden. Dabei wird ausgehend von den Nichtidealitäten im Hochfrequenzbereich ein Basisband-äquivalentes Modell der Störungen hergeleitet. Zu den modellierten Störungen zählen u.a. die Modulated Spur Interferenz und Intermodulationsprodukte zweiter Ordnung. Die Modulated Spur Interferenz wird erzeugt indem das Lecksignal des Senders durch sogenannte Spurs in das Empfänger Basisband heruntergemischt wird. Hierbei kommt es aufgrund der IQ Imbalance der Spurs neben der Haupt-Interferenz auch zu einer zusätzlichen Bild-Interferenz. Die Nichtlinearität zweiter Ordnung des Mischers erzeugt ein Intermodulationsprodukt welches immer um die Null-Frequenz fällt. Bei Verwendung eines Homodynempfängers führt dies zu einer Störung des gewünschten Empfangssignals. Auch der in der Stromdomäne betriebene Mischer, der mit Rechtecksignalen und dem Tastverhältnis von 25% arbeitet und vorzugsweise in Homodynempfängern zum Einsatz kommt, wird modelliert. Durch die verwendeten Rechtecksignale, die zur Ansteuerung des Mischers verwendet werden, entstehen Harmonische welche unerwünschte Signalkomponenten ins Basisband mischen und somit die Empfängerempfindlichkeit reduzieren.

Im zweiten Beitrag werden die Basisband-äquivalenten Modelle der Störungen zur Herleitung dedizierter adaptiver Filter verwendet mit deren Hilfe die Störungen vom Empfangssignal herausgerechnet werden können. In dieser Dissertation werden adaptive Filter zur Unterdrückung der Modulated Spur Interferenz und von Intermodulationsprodukten zweiter Ordnung entwickelt. In Simulationen wird gezeigt, dass durch eine Erweiterung des adaptiven Filters beide Störkomponenten der Modulated Spur Interferenz unterdrückt werden können. Ein großer Teil der Arbeit behandelt Methoden zur Unterdrückung von Intermodulationsprodukten zweiter Ordnung durch adaptive Filterung im Basisband des Transceivers. Hierfür wurden zwei nichtlineare Algorithmen entwickelt die auf dem LMS-, und dem RLS Algorithmus basieren. Diese Algorithmen verwenden das nichtlineare Wiener Modell, und sind in der Lage traditionelle Algorithmen, die auf dem Volterra Modell basieren in Bezug auf Konvergenzgeschwindigkeit

und geringerer Komplexität zu übertreffen. Die Funktion der entwickelten nichtlinearen adaptiven Algorithmen wurde mit Hilfe von Simulations-, und Messdaten evaluiert.

Im dritten Beitrag wird ein Konzept zur Unterdrückung von Harmonischen in Mischern, welche nach dem 25% Tastverhältnis arbeiten, präsentiert. Damit kann das Heruntermischen von unerwünschten Störsignalen durch die Harmonischen des Mischer unterdrückt werden. Das Konzept wird durch Schaltungssimulationen die ein 28 nm Technologiepaket einbinden verifiziert, wobei eine sehr gute Unterdrückung der Harmonischen nachgewiesen werden kann.

Statutory Declaration

I hereby declare that the thesis submitted is my own unaided work, that I have not used other than the sources indicated, and that all direct and indirect sources are acknowledged as references. This printed thesis is identical with the electronic version submitted.

Acknowledgements

First, I would like to express my sincere gratitude to my supervisor Univ.-Prof. Dr. Mario Huemer for giving me the opportunity to write my PhD thesis at the Institute of Signal Processing at the Johannes Kepler University Linz. I would like to thank him for the fruitful technical discussions which increased the quality of our publications, my thesis and finally our research.

I wish to thank Thomas Buchegger who supported my wish of starting a PhD thesis while I was working in his team at the Linz Center of Mechatronics (LCM). My deep gratitude goes to my colleagues at the Institute of Signal Processing for their great team spirit and the numerous technical discussions which we had.

I thank the self-interference cancellation (SIC) team of our Christian-Doppler Laboratory (CD-Lab) for the great collaboration, and particularly I would like to express my gratitude to Christian Motz for reviewing my draft version of the thesis. Furthermore, I would like to thank all members of the CD-Lab for their collaboration and the inspiring working environment. A big thank you goes out to Matthias Wagner who established the RF measurement station at the institute. I also want to thank Alexander Gruber for his support in doing measurements at the RF transceiver chip of the industrial partner.

I want to thank Michael Lunglmayr for becoming a good friend and for his support in even non-technical (mostly LaTeX related) issues. I also would like to express my sincere gratitude to Ram Sunil Kanumalli and Silvester Sadjina for the great collaboration during our PhD period and for becoming great friends.

I would like to thank my family and especially my father for supporting me in all my projects. Finally, I want to thank my wife Nadine for her support during my PhD period and for being a great mother for our son Noah.

I wish to acknowledge DMCE GmbH & Co KG as part of Intel for supporting this work carried out at the Christian Doppler Laboratory for Digitally Assisted RF Transceivers for Future Mobile Communications. The financial support by the Austrian Federal Ministry for Digital and Economic Affairs and the National Foundation for Research, Technology and Development is gratefully acknowledged.

*Engineers should be able to act nonlinearly and are expected to have good memory.
This is just the opposite from what an engineer wants from a system.
- Myself*

Contents

1	Introduction	1
1.1	Mobile Communication Devices	1
1.2	Functionality of an FDD CA Transceiver	2
1.3	Transmitter Leakage Induced Self-Interferences	4
1.4	State of the Art	6
1.5	Scope of this Work	8
2	Interferences in FDD RF Transceivers	13
2.1	Interference Overview	13
2.1.1	Non-Carrier Aggregation Related Interferences	14
2.1.2	Rx Carrier Aggregation Related Interference Problems	15
2.1.3	Tx Carrier Aggregation Related Interference Problems	19
2.2	Operation of the 25% Duty-Cycle Current-Driven Passive Mixer	20
2.3	Self-Interference Modelling	26
2.3.1	Nonlinearity in the Transmitter	27
2.3.2	Nonlinearity in the Receiver	32
2.3.3	Spur IQ-Imbalance	35
2.3.4	Modulated Spur Interference with Spur IQ-Imbalance	35
2.3.5	Mixer Terminal Coupling Induced IMD2	37
2.3.6	Higher Even-Order Intermodulation Interferences	40
2.4	Quantification of the IMD2 Interference	41
2.4.1	Two-Tone IIP2 Derivation	41
2.4.2	Modulated IMD2 Distortion	43
2.4.3	IIP2 Characterization	46
2.4.4	Severity of the IMD2 Interference	46
2.5	Modulated Spurs in Split-LNA Configuration	47
2.5.1	Phase-Noise Model of the 25% Duty-Cycle Mixer	49
2.5.2	Spur Modeling	49
2.5.3	Modulated Spur with IQ-Imbalance and Tx/Rx PN	50
3	Interference Rejection	53
3.1	Introduction	53
3.2	State of the Art	54
3.3	Proposed Harmonic Rejection Control Signals	55
3.3.1	Proposed Waveform A	56
3.3.2	Proposed Waveform B	58
3.4	Circuit Simulation Results	60
4	Adaptive Interference Cancellation	63
4.1	Introduction	63
4.2	Basic Adaptive Filter Structure	63
4.3	Complex Derivatives	65
4.3.1	The Cauchy-Riemann Equations	65
4.3.2	Adaptive Learning Algorithms	65

4.3.3	Wirtinger Derivatives	66
4.3.4	Iterative Minimization of a Real Valued Cost Function	67
4.4	The Least-Mean-Squares Algorithm	68
4.5	The Recursive Least-Squares Algorithm	71
4.6	Modulated Spur Cancellation	73
4.6.1	Widely-Linear Modulated Spur Cancellation	75
4.6.2	Simulation Results	77
4.6.3	Conclusion	79
5	Adaptive IMD2 Cancellation	81
5.1	Introduction	81
5.2	State of the Art	82
5.3	Polynomial Filters	82
5.3.1	Hammerstein Model	83
5.3.2	Truncated Volterra Model	86
5.4	Wiener Model Based Cancellation	89
5.4.1	Interference Replica Model	89
5.4.2	The IMD2 Problem from an Optimization Point of View	91
5.4.3	Multiple Solutions	94
5.4.4	Wiener-Model LMS Based IMD2 Cancellation (IM2LMS)	95
5.4.5	Reduced Complexity IM2LMS Algorithm	98
5.4.6	Simplified Derivation of the IM2LMS Algorithm	101
5.4.7	Wiener-Model RLS Based IMD2 Cancellation (IM2RLS)	103
5.4.8	Incorporating the Estimation of the Q-Path IMD2 Interference	111
5.4.9	Complexity Comparison	111
5.5	Simulation Results	114
5.5.1	LMS Based IMD2 Cancellation	114
5.5.2	RLS Based IMD2 Cancellation	117
5.6	Verification with Measured Data	121
5.6.1	Measurements from the Transceiver Chip	121
5.6.2	Measurement Setup with Discrete RF Components	124
5.7	Conclusion	127
6	Conclusion and Outlook	129
A	Appendix	131
A.1	Power Spectral Density Plots	131
A.2	Spur Generation in 25% Duty-Cycle Mixers with the Split-LNA Configuration	131
A.3	Receiver Noise Floor	134
A.4	Scaling of Complex Baseband Signals for a Desired Power Level, SNR and SINR	135
A.4.1	Complex White Gaussian Noise	135
A.4.2	Generation of an Rx Signal with Desired Power Level	135
A.4.3	Generation of an Rx Signal with Desired SNR	136
A.4.4	Generation of an Rx Signal with Desired SINR	136
A.5	Derivative of a Channel-Select Filtered Signal	137

List of Abbreviations	141
Bibliography	143
Curriculum Vitae	151

1

Introduction

1.1 Mobile Communication Devices

Modern mobile communication devices such as smartphones are enabling multiple services for the consumer. Starting from global positioning for navigation purposes, video streaming, internet browsing, fitness tracking and social networks, the smartphone becomes a device which is indispensable. However, the use of smartphones for traditional voice calls and text messages is faded into the background. This variety of services, especially the data intensive ones as multimedia streaming and video-telephony led to an enormous increase of data traffic. To satisfy this need for higher data rates Long Term Evolution-Advanced (LTE-A) was introduced in the 3rd Generation Partnership Project (3GPP) Release 10 [1], which offers the carrier aggregation (CA) feature. This enables the aggregation of multiple parts of the spectrum (component carriers (CC)) to increase the effective data rate. These CCs may be scattered across the spectrum due to the fact that the available bandwidth was distributed by auctions between the mobile operators. Therefore, to offer the CA feature to the customers the mobile device has to be prepared to receive/transmit data from a scattered spectral environment. LTE-A supports the frequency division duplex (FDD) operation for simultaneous transmission and reception of data at different frequencies. To increase the data rate the FDD operation is combined with the CA feature. Also the time-division duplex (TDD) mode is supported where data is transmitted or received alternately at the same frequency.

Today's mobile devices such as smartphones or tablets consist of several subsystems like the application processor, an audio subsystem (speaker, microphone), the video subsystem (LCD display, touchscreen), the power management subsystem to generate the different operating voltages of the subsystems from one battery source, and the connectivity subsystem (Fig. 1.1). The connectivity subsystem provides wireless communication including WiFi, Bluetooth, cellular networks and near field communication (NFC), and the included Global Positioning System (GPS) receiver serves for positioning applications. The cellular subsystem is used for the mobile communication including the LTE-A, the Global System for Mobile Communications (GSM) and the Universal Mobile Telecommunication System (UMTS) standards. It consists of the antenna(s), duplexer(s), power amplifiers (PAs), the radio frequency (RF) transceiver chip, and the digital baseband (BB). The digital front-end (DFE) as part of the RF transceiver chip connects the analog front-end with the digital BB where user data is exchanged between the end-application and the transceiver device.

Mobile devices for LTE-A should support the TDD and FDD mode including CA, and

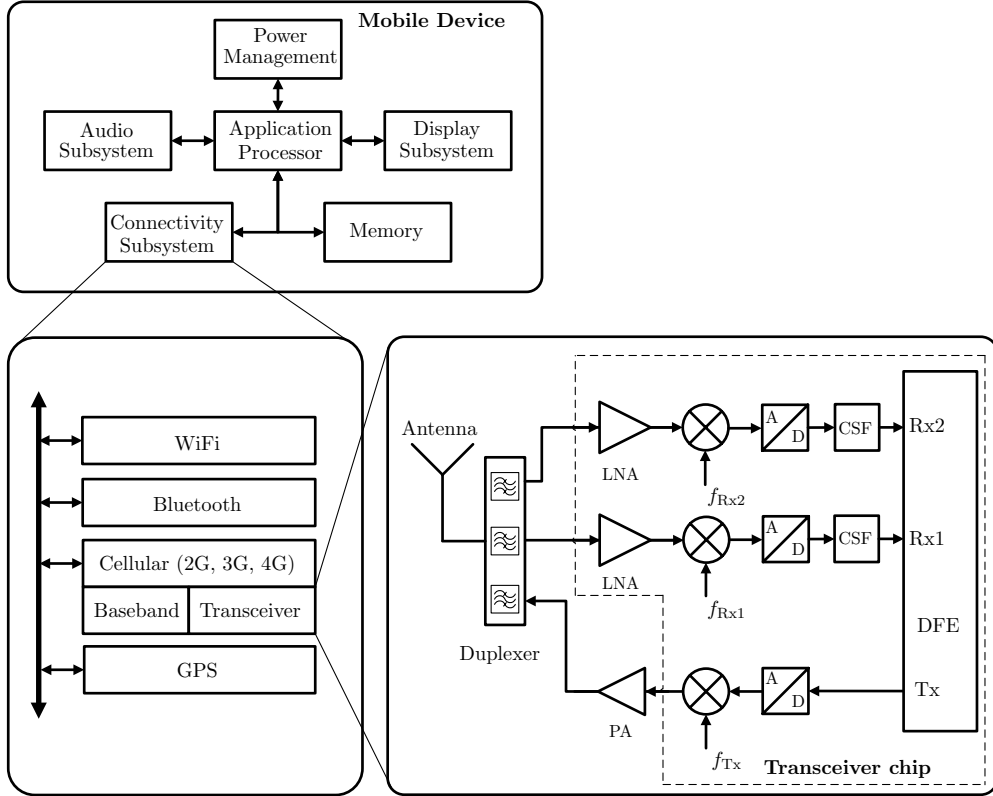


Figure 1.1: Block diagram of a typical mobile device.

the operation in multiple frequency bands to access the scattered spectrum. But restrictions like power consumption and costs are driving design parameters for the transceiver chip architecture. The transceiver contains the transmitter(s) and the receiver(s), and therefore enables the exchange of data between the base-stations and the mobile device. The direct-conversion receiver architecture (also known as zero-intermediate frequency (IF)-, or homodyne receiver) [2] is mainly used in modern transceivers due to the lower power consumption and the lower hardware complexity compared to e.g. low-IF receivers. In this architecture, the wanted receive (Rx) signal is directly down-converted from the RF to the BB (zero-frequency). In this way the required sampling frequency to digitize the signal is kept at the minimum which saves power. Also for the transmitters direct conversion architectures are frequently used.

1.2 Functionality of an FDD CA Transceiver

The FDD operation mode which is used in Long Term Evolution (LTE) has the advantage that data can be simultaneously transmitted and received at different frequencies over one common antenna. This is enabled by the frequency-selectivity of the analog front-end (duplexers). In Fig. 1.1 an RF transceiver with two CA receivers and one transmitter is depicted. The operating frequency f_{Rx1} of receiver Rx1 (primary receiver) is related to the transmitter operating frequency f_{Tx} via the duplexing distance.

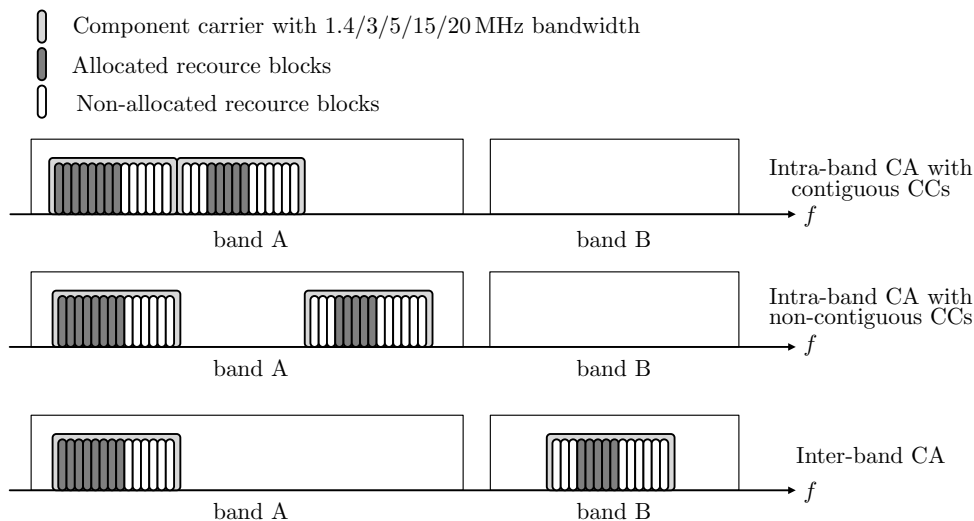


Figure 1.2: Different types of CA.

As an example, if LTE band 5 is used with $f_{Tx} = 831$ MHz, then $f_{Rx1} = 876$ MHz which corresponds to the duplexing distance of 45 MHz. Usually in mobile user equipments (UEs) the transmit (Tx) frequency is lower than the Rx frequency because the generation of a transmit signal at a lower frequency consumes less power. The operating frequency of the secondary receiver Rx2 (in LTE-A up to five secondary receivers may be aggregated using CA) is not coupled to the primary transmit frequency and may be located at any different frequency depending on the intra/inter-band CA combination [3]. In LTE-A three types of CA are defined which are visualized in Fig. 1.2. In the first CA scenario, the *intra-band contiguous CA*, the aggregated CCs are next to each other and within the same LTE band. Both aggregated CCs may be received by one receiver if the receive center-frequency is set between the CCs and the sampling frequency is increased according to the overall bandwidth. The second CA scenario is the *intra-band non-contiguous CA* where the aggregated CCs are within the same LTE band but separated by a frequency gap. In this scenario, usually a split-low noise amplifier (LNA) configuration is used where each receiver is configured to receive one CC. As we will see later, this configuration using a split-LNA is prone to transmitter leakage self-interference (modulated-spur interference in split-LNA configuration) due to the limited Tx-to-Rx (duplexer) isolation. In the third CA scenario, the *inter-band CA*, the CCs are in different LTE bands. In this case each receiver uses its own LNA (no split-LNA is used) to amplify the received signal as depicted in Fig. 1.1. Also in this configuration the mentioned modulated-spur interference may occur. However, it is caused by a different mechanism as will be described in the next sections.

Using Fig. 1.3, the functionality of an LTE-A transceiver operating in the FDD mode and using the CA feature will be explained. The complex valued discrete-time transmit signal $x_{BB}[n]$ is converted into the analog domain using a digital-to-analog converter (DAC). Subsequently, the signal is up-converted to the frequency f_{Tx} and amplified by the PA. The duplexer connects the transmitter and the CA receivers to the common antenna. The duplexer is a device composed of band-pass filters which provide isolation between

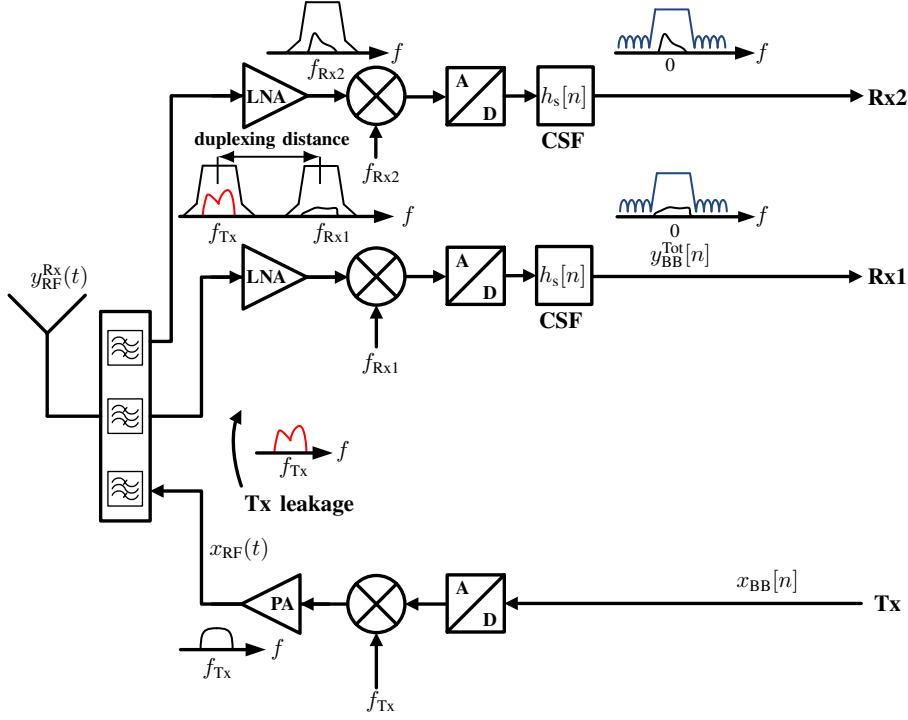


Figure 1.3: The transmitter leakage signal into the own receivers.

the Tx and Rx paths. Thereby, the duplexer passes the transmit signal to the antenna where it is radiated to the base-station. At the same time signals at the frequencies f_{Rx1} and f_{Rx2} are received by the antenna and fed by the duplexer to the corresponding receivers. RF switches are used to select the appropriate duplexer depending on the frequency band. The received signals are amplified by the LNAs, and assuming direct-conversion receivers, the wanted receive signals are down-converted to the BB. This BB signals are then digitized by the analog-to-digital converters (ADCs), and filtered by the channel-select filters (CSFs). As indicated in Fig. 1.1, the DFE provides the connection to the digital BB where the received data streams are demodulated, and the Tx data is modulated for the transmission, respectively.

1.3 Transmitter Leakage Induced Self-Interferences

Due to the limited duplexer isolation between the transmitter and the receivers which is in the range of 50 dB to 55 dB [4, 5], a transmitter leakage (TxL) signal occurs in the receivers which may be stronger than the actual receive signal. Assuming a transmitter power of 23 dBm at the antenna¹, and an average Tx-to-Rx duplexer isolation of 50 dB around the transmit frequency, the TxL signal power at the input of the receiver is $P_{RF}^{TxL} = 23 \text{ dBm} - 50 \text{ dB} = -27 \text{ dBm}$. On the other hand, in so called reference sensitivity cases (where the mobile equipment is far away from the base-station), the wanted signal power at the antenna can be as low as -97 dBm [3], which is 70 dB below the TxL signal power. In an ideal transceiver this would not be an issue due to the fact that

¹At the PA output the Tx power may be even higher due to the switch-, and duplexer insertion losses.

the signals are located at different frequencies. However, because of non-idealities in the analog front-end this TxL signal can create a BB interference which disturbs the wanted receive signal significantly.

The TxL signal is the root cause of several receiver interferences which degrade the receiver performance. The actual type of receiver interference depends on the transceiver operating conditions, e.g., enabled Rx/Tx CA. The following section gives an overview about the different types of interferences. A detailed explanation of each interference follows in Section 2.1.

Non-CA related Interferences:

- **Second-Order Intermodulation Distortion (IMD2) Interference**

The leaking transmitter signal may cause a second-order intermodulation distortion (IMD2) interference in direct-conversion receivers [6], [7]. This second-order nonlinear distortion always falls around zero-frequency and is caused by e.g. a coupling between the RF- and local oscillator (LO)-ports in the in-phase (I)-, and quadrature-phase (Q)-path of the Rx IQ-mixer [8].

- **Tx Noise in Rx Band**

The TxL signal may have a spectral emission (skirt) due to the nonlinearity of the PA which may reach up to the Rx frequency range. As a consequence, this Tx noise spectral content may overlay the wanted receive signal leading to a receive signal degradation.

- **Reciprocal Mixing**

Reciprocal mixing means that a blocker² signal (e.g. the TxL signal) is down-converted into the BB due to the LO phase noise (PN) where it degrades the wanted signal quality.

Receiver CA related interferences:

- **Continuous-Wave Spur**

Continuous-Wave Spurs may be generated by device nonlinearities and coupling between the receive mixer harmonics of the square-wave mixers. Such a continuous wave (CW)-spur (cosine-like signal) may be down-converted by the Rx mixer and may occur as spectral peak in the receive spectrum.

- **Modulated Spur Interference in Inter-Band CA**

Due to multiple clock sources, which are needed to cover the different CA scenarios and band combinations, cross-talk between the LO lines of the receivers on the chip together with device nonlinearities may create spurs in the receiver front-end. If the frequency of such a spur falls near the actual Tx frequency, the TxL signal may be down-converted into the Rx BB. This so called modulated spur interference can disturb the wanted receive signal significantly [9, 10].

²A blocker signal is an unwanted signal at the input of the receiver which is either received by the antenna or created by the own transmitter leakage.

- **Modulated Spur Interference in Intra-Band CA with Split-LNA**

In intra-band CA where a split-LNA is used, the TxL signal may be mixed by the harmonics of the mixer in the first CA receiver. This mixed TxL signal is reflected back to the input of the split-LNA where it reaches the input of the secondary receiver. The harmonics of the mixer in the secondary receiver may down-convert the reflected signal to the BB where it disturbs the wanted signal.

- **Tx Harmonics in Downlink**

The potentially leaking transmitter harmonic distortions caused by the nonlinear PA may overlap the wanted receive signal of the secondary CA receiver which is not coupled to the primary transmit frequency [11].

- **Tx Harmonics in Downlink Harmonic Response**

Due to the square-wave mixer implementation in the receiver, leaking transmitter harmonic distortions caused by the nonlinearity in the transmitter may be down-converted to the BB by the harmonics of the mixer.

Transmitter CA related Interferences:

- **Multiple Modulated Spurs**

Each transmitter causes its own TxL signal which may cause multiple modulated spurs.

- **Multiple Tx Harmonics in Downlink/Downlink Harmonic Response**

The harmonics of each transmitter may fall on top of the wanted Rx signal or may be down-converted into the BB by the mixer harmonics.

- **Intermodulation Distortions**

When several transmitters are operated in parallel, each transmitter may create an IMD2 interference in the receiver(s). If the transmit signal is either created in an *intra-band non-contiguous CA*, or an *inter-band CA* scenario, nonlinearities in the analog front-end may create a third-order intermodulation distortion (IMD3) which interferes with the wanted receive signal.

The severity of the TxL signal caused interferences could be reduced by increasing the duplexer isolation. However, besides the increasing costs, improving the Tx-to-Rx isolation of the duplexer would lead to a higher insertion loss of the wanted receive signal and thereby to a reduction of the Rx signal quality. Therefore, instead of using improved duplexers, efficient ways to cancel the transmitter induced self-interferences are of special interest.

1.4 State of the Art

In the existing literature several approaches are discussed to mitigate the TxL signal and PA spurious emission caused receiver desensitization. A natural approach would be to cancel the transmitter leakage signal in the RF domain before it enters the input of the LNA or mixer. This would significantly reduce the generation of nonlinear distortions due to receiver RF front-end nonlinearities. The authors in [12] propose an RF cancellation architecture using an auxiliary transmitter to generate a Tx leakage

signal replica (including nonlinear PA distortions) in the RF domain which is subtracted from the received signal before it enters the LNA. The replica signal is generated by an nonlinear adaptive decorrelation-based learning algorithm which uses the known Tx samples and the received signal in the digital BB. With this approach, the authors are able to increase the effective Tx-to-Rx isolation by 54 dB.

A different way to suppress the leakage signal may be achieved by using N-path filters which act as a notch filter at the transmit frequency. In [5, 13] and [14], such N-path filters are placed in front of the mixer input to reject the TxL signal.

To limit the computational complexity of a pure digital modulated spur interference cancellation, the authors in [15] use an auxiliary receiver to sense the TxL signal at the receiver input which is subsequently used as a reference signal for a digital cancellation algorithm. With this mixed-signal approach, the auxiliary receiver senses the Tx signal including nearby out-of-band (OOB) emissions after it passed the duplexer Tx-to-Rx stop-band. This means, the duplexer stop-band frequency response including the Tx OOB emissions are already included in the sensed TxL signal and do not need to be estimated by the digital algorithm. This heavily reduces the complexity of the digital part of the cancellation approach. The same auxiliary receiver could also be used to sense spurious emissions of the transmitter which desensitize the receiver. However, nonlinearities of the receiver are not covered and need to be estimated by the digital cancellation algorithm. Using an auxiliary receiver with a serial-mixing concept to cancel the modulated spur interference [9], [10] including the PN of the involved transmitter and receiver LOs is presented in [16].

An IMD2 interference in the receiver may also be generated by external blocker signals received by the antenna. The author in [17, 18], extracts the blocker signal after the Rx mixer by a high-pass filter. The squared envelope of this signal is then used as a reference for the subsequent adaptive filter which cancels the generated IMD2 interference.

Although, analog and mixed signal cancellation techniques offer good cancellation results as stated in [12], [15], [16], their additional hardware effort is not negligible. Especially in CA, where multiple receiver chains are operated in parallel, each receiver (possibly including the diversity receivers) requires its own auxiliary transmitter (RF cancellation)/receiver (mixed signal cancellation) because of the different duplexer stop-band responses seen from the Tx to each receiver. A big challenge in designing analog or mixed-signal cancellation circuits is to limit the degradation of the wanted receive signal by connecting the auxiliary receiver [15], or transmitter [12] to the main receiver. Beside this, pure digital approaches offer technology independence and scalability and do not need any changes of the analog front-end circuit. However, the computational burden in the digital BB is increased.

Several fully digital techniques to cancel Tx-induced self-interferences can be found in the existing literature. The authors in [19] present the modeling and digital mitigation of transmitter self-interference in the presence of transmitter and receiver nonlinearities. In [20], the digital suppression of the nonlinear PA OOB emission (Tx noise in Rx band)

1 Introduction

which reaches up to the Rx band in case of low duplexing distances is presented. The nonlinearity of the PA induces also spurious distortions (Tx harmonics) which may degrade one of the CA receivers. The digital cancellation of such distortions in the presence of transmitter IQ-imbalance is suggested in [11].

There is also existing literature for the pure digital cancellation of the transmitter induced IMD2 interference in direct-conversion receivers. In [21] a frequency flat duplexer stop-band in the region of the leaked Tx signal is assumed. The IMD2 interference is estimated adaptively by a least-mean-squares (LMS) filter where only the coefficient with largest magnitude is used for the cancellation. Similar assumptions are made in [22]. However, the assumption of a frequency-flat duplexer response is not valid for LTE-A signals due to the wider bandwidth. In [23] a Volterra kernel based least-squares (LS) approach for frequency-selective duplexers is introduced. The CSF in the receiver is equalized to obtain the unfiltered IMD2 interference with twice the Tx signal bandwidth for the IMD2 LS estimation. Finally the authors in [6] present a compensation of the IMD2 interference in the presence of a static 3rd-order PA nonlinearity and Tx mixer IQ-imbalance. The estimation process consists of a two-step LS approach which has a high computational complexity. Further, [21] and [22] are assuming equal IMD2 interferences in the I- and Q-branch of the Rx mixer, whereas in [23] they are assumed to be different.

1.5 Scope of this Work

Although, the existing literature provides solutions for pure digital cancellation of TxL signal caused receiver interferences, the computational complexity of most solutions is far too high to be implemented in a real mobile transceiver. Additionally, no literature regarding the pure digital cancellation of the modulated spur interference was available at the time when this PhD work has started. The goal of this thesis is the development of specialized low-complexity adaptive filter algorithms which could be implemented in today's transceivers. Motivated by this, and by using the detailed interference models which are derived in this thesis, low-complexity adaptive algorithms for a pure digital cancellation of the modulated spur-, and the IMD2 interference are proposed.

This thesis resulted in the following achievements:

- The derivation of a detailed baseband equivalent model of the modulated-spur-, Tx-harmonics-, IMD2-, and third-order nonlinear interferences.
- The development of a normalized widely-linear variable step-size LMS adaptive filter to cancel the main and image modulated spur interference in the digital BB of the CA transceiver.
- The development of a low-complexity nonlinear LMS-type adaptive filter to cancel the IMD2 interference generated by a Tx signal which traveled through a highly frequency-selective Tx-to-Rx leakage path.
- The development of a robust nonlinear recursive-least-squares (RLS)-type adaptive filter for the IMD2 cancellation which is suitable for highly frequency-selective duplexer stop-band responses and clustered-transmit signals.

- The development of a harmonic rejection (HR) mixer concept to suppress specific harmonics in 25% duty-cycle mixers. With this approach, the down-conversion of blocker signals by the harmonics of the mixer can be suppressed.

During the work on this thesis the following scientific contributions have been published in peer reviewed conference proceedings and journals or have been filed as patents. Some ideas and figures presented in this thesis previously appeared in these publications and patents:

Journal Publications

- A. Gebhard, O. Lang, M. Lunglmayr, C. Motz, R. S. Kanumalli, C. Auer, T. Paireder, M. Wagner, H. Pretl and M. Huemer, "A Robust Nonlinear RLS Type Adaptive Filter for Second-Order-Intermodulation Distortion Cancellation in FDD LTE and 5G Direct Conversion Transceivers," In *IEEE Transactions on Microwave Theory and Techniques*, 16 pages, Early Access, January 2019.
- S. Sadjina, R. S. Kanumalli, A. Gebhard, K. Dufrene, M. Huemer and H. Pretl, "A Mixed-Signal Circuit Technique for Cancellation of Interferers Modulated by LO Phase-Noise in 4G/5G CA Transceivers," In *IEEE Transactions on Circuits and Systems – I Regular Papers*, Vol. 65, No. 11, pp. 3745-3755, Nov 2018.
- R. S. Kanumalli, T. Buckel, C. Preissl, P. Preyler, A. Gebhard, C. Motz, J. Markovic, D. Hamidovic, E. Hager, H. Pretl, A. Springer and M. Huemer, "Digitally-intensive Transceivers for Future Mobile Communications - Emerging Trends and Challenges," In *e&Ei Elektrotechnik und Informationstechnik*, Vol. 135, No. 1, pp. 30-39, January 2018.

Conference Publications

- A. Gebhard and C. Motz and R. S. Kanumalli and H. Pretl and M. Huemer, "Non-linear Least-Mean-Squares Type Algorithm for Second-Order Interference Cancellation in LTE-A RF Transceivers," In *Proceedings of the 51st IEEE Asilomar Conference on Signals, Systems, and Computers*, Oct 2017, pp. 802-807.
- A. Gebhard, M. Lunglmayr and M. Huemer, "Investigations on Sparse System Identification with l_0 -LMS, Zero-Attracting LMS and Linearized Bregman Iterations," In *Proceedings of the 16th International Conference on Computer Aided System Theory - EUROCAST*, February 2018.
- A. Gebhard and R. S. Kanumalli and B. Neurauder and M. Huemer, "Adaptive Self-Interference Cancellation in LTE-A Carrier Aggregation FDD Direct-Conversion Transceivers," In *Proceedings of the IEEE Sensor Array and Multichannel Signal Processing Workshop (SAM 2016)*, July 2016, 5 pages.
- R. S. Kanumalli, A. Gebhard, A. Elmaghraby, A. Mayer, D. Schwartz and M. Huemer, "Active Digital Cancellation of Transmitter Induced Modulated Spur Interference in 4G LTE Carrier Aggregation Transceivers," In *Proceedings of the 83rd IEEE Vehicular Technology Conference (VTC Spring)*, May 2016, 5 pages.

Scientific Talks

- A. Gebhard, "All Digital Interference Cancellation Architectures for RF Transceivers," *Evaluation of the Christian Doppler Laboratory for Digitally Assisted RF Transceivers for Future Mobile Communications*, Johannes Kepler University, Linz, Austria, November 2018.
- A. Gebhard, "Investigations on Sparse System Identification with l_0 -LMS, Zero-Attracting LMS and Linearized Bregman Iterations", *International Conference on Computer Aided Systems Theory (EUROCAST 2017)*, Las Palmas, Gran Canaria, February 2017.
- A. Gebhard, "Adaptive Self-Interference Cancellation in LTE-A Carrier Aggregation FDD Direct-Conversion Transceivers", *62. Fachgruppentreffen der ITG Fachgruppe "Algorithmen für die Signalverarbeitung"*, Johannes Kepler University, Linz, Austria, October 2016.
- A. Gebhard, "Adaptive Self-Interference Cancellation in LTE-A Carrier Aggregation FDD Direct-Conversion Transceivers", *IEEE Sensor Array and Multichannel Signal Processing Workshop (SAM 2016)*, Rio de Janeiro, Brazil, July 2016.
- A. Gebhard, "Self-Interference Cancellation in LTE Carrier Aggregation Transceivers" *PhD-Day at DMCE/Intel Austria*, Linz, Austria, May 2016.

Poster Presentations

- A. Gebhard, "Nonlinear Least-Mean-Squares Type Algorithm for Second-Order Interference Cancellation in LTE-A RF Transceivers", *ASILOMAR Conference on Signals, Systems, and Computers*, Pacific Grove, USA, October 2017.
- A. Gebhard, "Modulated Spurs in LTE-A Carrier Aggregation Transceivers", *Microelectronic Systems Symposium (MESS16)*, Vienna, Austria, April 2016.

Patents / Patent Applications

- A. Gebhard, S. Sadjina, K. Dufrene and S. Tertinek, "Harmonic Suppressing Local Oscillator Signal Generation," U.S. Patent US 9,935,722 B2, filed June 2016, granted April 2018.
- S. Tertinek, A. Gebhard, S. Sadjina and K. Dufrene, "Pulse Generation Using Digital-to-Time Converter," U.S. Patent US 9,755,872 B1, filed August 2016, granted September 2017.
- K. Dufrene, Ram S. Kanumalli, S. Sadjina and A. Gebhard, "Multiple Modulated Spur Cancellation Apparatus," U.S. Patent Application US 2017/0359136 A1, filed June 2016, published December 2017.
- A. Gebhard, "Second Order Intermodulation Cancellation for RF Transceivers," U.S. Patent US 10,172,143 B2, filed June 2017, granted January 2019.
- K. Dufrene, S. Sadjina, A. Gebhard and Ram S. Kanumalli, "Interference Detection Device, Interference Detection Apparatus, Interference Detection Method, Computer Program, Receiver, Mobile Terminal and Base Station," U.S. Patent US 10,097,220 B2, filed May 2017, granted October 2018.

The outline of the work presented in this thesis is:

Chapter 2 gives a detailed explanation of the most important TxL signal caused receiver self-interferences. Here, two mechanisms are explained which lead to the modulated spur interference. The first mechanism is caused by LO-to-LO crosstalk in inter-band CA scenarios, and the second mechanism occurs in intra-band CA where a split-LNA is used. Furthermore, baseband equivalent models for the modulated spur-, Tx harmonics-, IMD2-, and the third-order nonlinear interferences are derived considering nonlinearities in the transmitter- and in the receiver path. Finally, BB equivalent models for higher even-order intermodulation distortions which are caused by a combination of the LNA-, and the mixer nonlinearity are deduced.

In Chapter 3, the HR mixer concept is explained and a novel HR concept for 25% duty-cycle current-driven passive mixers is proposed. The rejection of a specific harmonic content of the Rx square-wave mixers is used to suppress specific receiver interferences like the modulated spur-, or the Tx harmonics interference.

In Chapter 4, linear adaptive filters like the complex-valued LMS-, and RLS algorithm are recapitulated using the Wirtinger Calculus [24]. These algorithms are subsequently used to demonstrate the digital cancellation of the modulated spur interference. The results and key findings of this chapter have been published in [9, 16].

Chapter 5 starts with an introduction of nonlinear adaptive filtering in the context of the pure digital IMD2 interference cancellation. Polynomial filters [25, 26] like the Volterra kernel based filter are investigated for the IMD2 cancellation. Subsequently, a novel Wiener-model based nonlinear LMS-type algorithm (IM2LMS), and a novel nonlinear RLS-type algorithm (IM2RLS) are proposed to cancel the IMD2 interference in the digital BB. The suggested IMD2 cancellation algorithms are evaluated using simulated and measured IMD2 data. The measured IMD2 data is obtained from two different measurement setups. The first setup includes a transceiver chip provided by the industrial partner, whereas the second setup uses discrete RF components. The derivation and the performance results of the IM2LMS-, and IM2RLS algorithms have been presented in [7] and [27], respectively.

Finally, Chapter 6 concludes the work and gives an outlook on potential future research topics in this field.

2

Interferences in FDD RF Transceivers

2.1 Interference Overview

One of the main reasons of receiver desensitization in FDD transceivers is the limited duplexer isolation between the transmitter(s) and the receiver(s) which is around 50 dB to 55 dB [4, 5]. The resulting TxL signal into the receivers in combination with front-end non-idealities may generate BB interferences which degrade the receiver performance. The Tx-to-Rx stop-band isolation versus frequency obtained by a 4-pole S-parameter measurement of a commercial band 5 duplexer [28] is depicted in Fig. 2.1. The dashed lines indicate the change of the Tx-to-Rx isolation caused by a variation of the antenna impedance mismatch corresponding to a maximally allowed voltage-standing-wave-ratio (VSWR) of 2 [28]¹. It can be observed, that the resulting TxL signal into the receiver experiences a frequency-selective behavior of the duplexer in the stop-band. This TxL signal can be identified as the root cause of several receiver BB interferences.

In this chapter the TxL signal caused receiver interferences are modeled in the RF domain, and the resulting BB equivalent receiver interferences are determined. This includes the modeling of the modulated spur-, Tx harmonics-, IMD2-, and higher even-order intermodulation interferences. The down-conversion of the TxL signal by spurs creates the modulated spur interference which may consist of a main and an image component. This spurs may be generated through cross-talk between the LO lines of the receivers on the chip together with device nonlinearities. The modulated spur interference may also be generated by the use of split-LNAs in intra-band CA scenarios. The second-order nonlinearity of the mixer creates an IMD2 interference which always falls around the zero-frequency. In case of direct-conversion receiver architectures, this leads to a BB interference which disturbs the wanted receive signal. Furthermore, the 25% duty-cycle current driven passive mixer [29] which is preferably used in direct-conversion receivers is modeled. Due to the square-wave control signals, harmonics are produced within the mixer which may lead to the down-conversion of unwanted spectral components into the receiver BB. This down-conversion by the harmonic response of the mixer may degrade the receiver performance.

The receiver interferences can be split into interferences which occur in a single Tx/Rx FDD transceiver, and in Tx/Rx CA related interferences. The next sections will explain the different TxL signal caused receiver interferences, and for each interference methods for the prevention are discussed briefly.

¹A VSWR of 2 corresponds to a reflection coefficient with magnitude 0.333. To obtain the dashed lines in Fig. 2.1 the angle of the complex valued reflection coefficient is varied between 0° and 360° and the min./max. value is plotted.

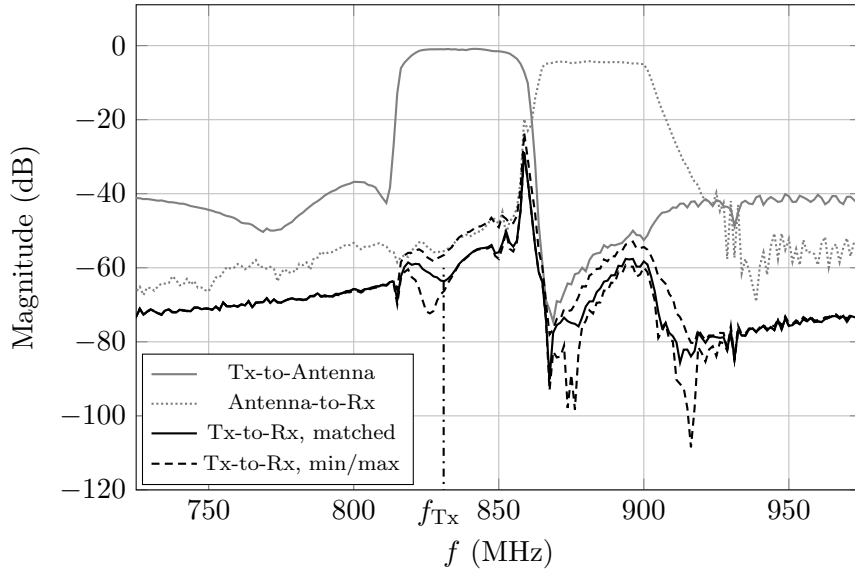


Figure 2.1: Magnitude response of the TDK band 5 duplexer. The dashed lines indicate the change of the stop-band response due to an antenna impedance mismatch.

In this work, the used mathematical operators $(\cdot)^*$, $(\cdot)^T$, $(\cdot)^H$, and $*$ denote the complex conjugate, transpose, Hermitian transpose, and convolution, respectively. Lower-case bold face variables (\mathbf{w} , \mathbf{x} , ...) indicate column vectors, and upper-case bold face variables (\mathbf{A} , \mathbf{B} , ...) indicate matrices. For the derivative $\frac{\partial J}{\partial \mathbf{w}}$ of the scalar function J a row-vector is used.

2.1.1 Non-Carrier Aggregation Related Interferences

Non-CA related receiver interferences occur when only one transmitter and one receiver are active in FDD mode of the transceiver. The TxL signal may generate a BB interference by the nonlinearity within the receiver chain or by other effects like described below.

Second-Order Intermodulation Distortion

The TxL signal in combination with the second-order nonlinearity of the receiver may create a baseband IMD2 interference. This second-order nonlinear distortion is caused by e.g. a coupling between the RF- and LO-port of the Rx mixer [8]. An interesting fact of this nonlinear interference is, that one part of the generated second-order intermodulation products always falls around zero-frequency independently of the Tx-to-Rx frequency offset (duplexing distance). In case of direct-conversion receiver architectures, this leads to a disturbance of the wanted receive signal. In this thesis, the mathematical modeling of the IMD2 interference is provided in Section 2.3.5, and a nonlinear LMS type algorithm (IM2LMS) to cancel the IMD2 interference in the digital BB is developed in Section 5.4.4. In Section 5.4.7, a nonlinear RLS type algorithm (IM2RLS) to cancel the IMD2 interference is derived which shows an improved convergence speed and steady-state cancellation performance compared to the IM2LMS algorithm.

Prevention/mitigation methods:

The IMD2 interference may be minimized by using duplexers with higher Tx-to-Rx isolation to attenuate the TxL signal. However, this leads to higher costs for the duplexers and increased insertion losses. In this thesis, the IMD2 cancellation by adaptive signal processing techniques is suggested. The IM2LMS, and the IM2RLS algorithm are proposed for this purpose.

Tx Noise in the Rx Band

The overall nonlinearity of the transmitter (including the nonlinear PA) which may include a memory effect generates a spectral skirt around the Tx signal bandwidth which reaches up to the Rx frequency range. The residual skirt content after passing through the duplexer Tx-to-Rx stop-band together with the wanted receive signal is down-converted by the receiver LO. This may lead to a receiver desensitization when the transceiver is operating in LTE bands with small duplexing distance. E.g. as described in [20, 30], for Tx intra-band CA scenarios, the duplexing distance can be as small as 15 MHz.

Prevention/mitigation methods:

The nonlinearity of the transmitter can be reduced by using a pre-distortion of the transmit signal. Another possibility to limit the OOB emission at the Rx band would be the use of duplexers with higher isolation which generates additional costs.

Reciprocal Mixing

The Rx mixer is down-converting the wanted Rx signal to the BB. Similarly, also the TxL signal is down-converted by the mixer resulting in a strong blocker signal at the duplexing distance. Due to the LO PN, the spectral content of the down-converted TxL blocker signal may reach the wanted signal frequency range. This effect is called reciprocal mixing, where the spectral skirt caused by the down-conversion of the blocker due to the LO PN disturbs the wanted signal. The cancellation of the reciprocal mixing interference using an auxiliary receiver is presented in [31]. As the PN of the LO is random, a pure digital cancellation is not feasible.

Prevention/mitigation methods:

The reciprocal down-conversion of the TxL signal may be mitigated by using duplexers with higher Tx-to-Rx isolation or employing LOs with high spectral purity.

2.1.2 Rx Carrier Aggregation Related Interference Problems

Continuous-Wave Spurs

Due to the square-wave mixer implementation, harmonics of the different LO frequencies are generated which may couple over the LO lines on the chip. If additional device nonlinearities are present, new spur frequencies may occur through the nonlinear mixing process. The resulting CW spurs may either overly the wanted Rx signal, or directly fall into the BB. Also other clock sources on the RF-transceiver chip like the ADC or the digitally controlled oscillator (DCO) may lead to spurs. If such a CW spur is present in

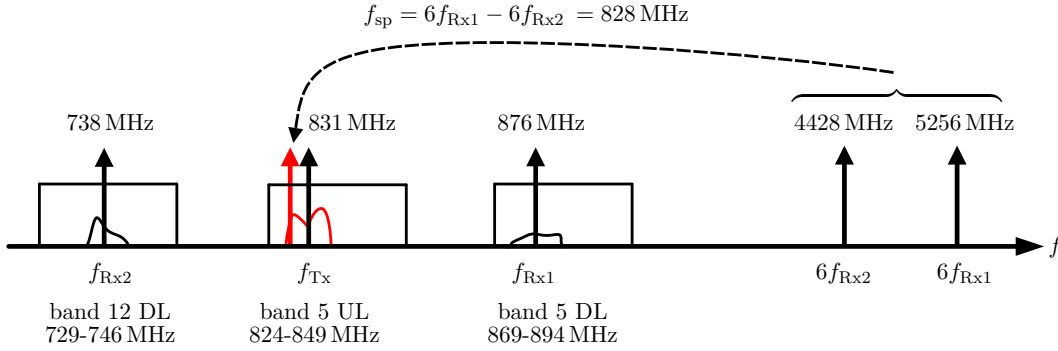


Figure 2.2: Device nonlinearities and the mixer harmonics on the transceiver chip lead to a spur which is 3 MHz below the transmit frequency f_{Tx} .

the Rx baseband it occurs there as spectral peak which disturbs the wanted signal.

Prevention/mitigation methods:

In the transceiver layout, oscillators are placed on the chip die with largest possible distance between them. This minimizes coupling effects. Decoupling of the supplies with large shunt capacitors may reduce the supply-crosstalk related spurs. From a signal processing point of view, a CW spur falling into the Rx BB may be mitigated by using digital interference cancellation in the BB e.g. by using a single tap LMS algorithm.

Modulated Spurs

In FDD transceivers the transmitter and the receiver are connected to the same antenna operating simultaneously at different frequencies. The limited Tx-to-Rx duplexer isolation leads to a TxL signal located at the duplexing distance frequency offset at the receiver input. The modulated spur interference may arise because of two different mechanisms: First, if a CW spur with the frequency f_{sp} close to the actual transmit frequency f_{Tx} is present in the receiver chain, then the CW spur may down-convert the TxL signal to the Rx BB. The following receiver CA scenario illustrates the generation of such a CW spur which falls near the actual transmit frequency.

Spur Generation Example:

Assume a downlink (DL) inter-band CA case with LTE band 5 and band 12 with the receiver frequencies at $f_{Rx1} = 876$ MHz, $f_{Rx2} = 738$ MHz, and the transmitter uplink (UL) frequency at $f_{Tx} = 831$ MHz. Device nonlinearities in combination with the harmonics of the square-wave LO signals may generate a spur at $f_{sp} = 6f_{Rx1} - 6f_{Rx2} = 828$ MHz which is 3 MHz below the transmit frequency. This spur generation scenario is illustrated in Fig. 2.2. A detailed modeling of this interference is presented in Section 2.3.1 where the modulated spur interference is a sub-class of other interferences.

The second mechanism that can generate modulated spurs occurs in intra-band non-contiguous CA scenarios where a split-LNA is used. In Fig. 2.3 the block diagram of an intra-band CA receiver using a split-LNA is depicted. It can be observed, that both LNA inputs are directly connected without any filter in between. The transmit signal leaks through the duplexer into the receiver. This TxL signal/energy is mixed by the

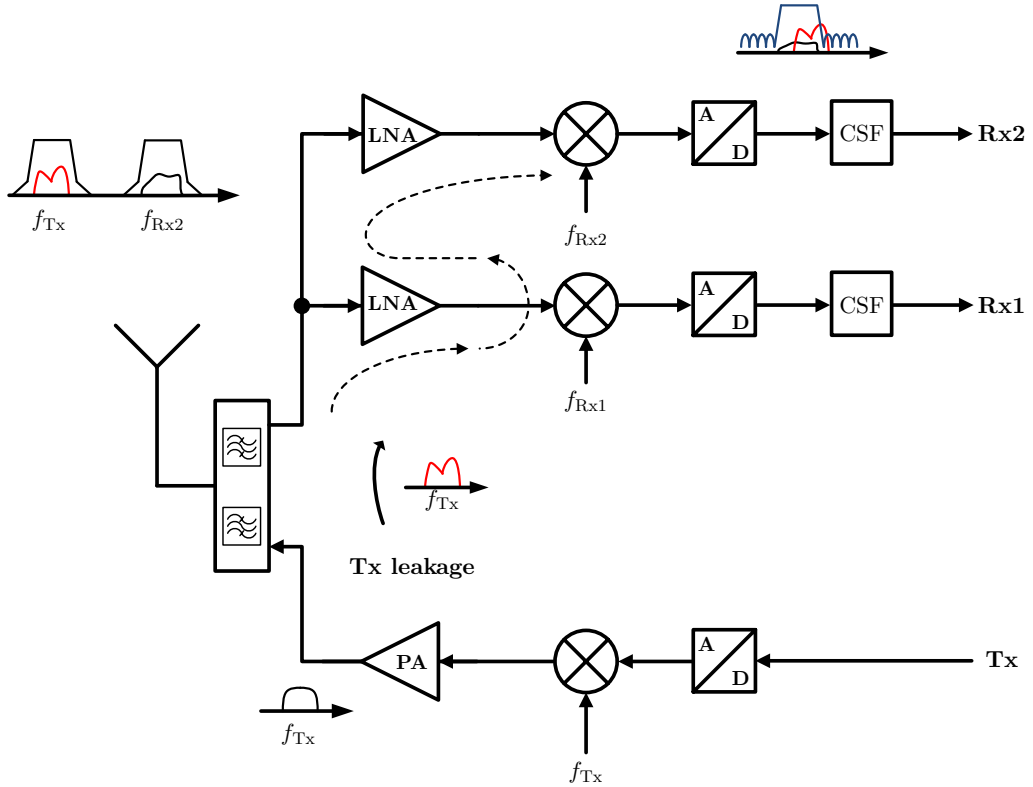


Figure 2.3: Modulated spur interference occurring in intra-band non-contiguous CA scenarios using a split-LNA.

harmonics of the mixer Rx1 and reflected back to the split-LNA input. This reflected energy/signal reaches the input of the secondary LNA because of the lack of reverse isolation of the LNAs. The Rx2 mixer is down-converting this reflected energy by another mixer harmonic down to the BB.

A detailed modeling of the modulated spur interference in split-LNA configuration is presented in Section 2.5. Interestingly, both mechanisms are leading to the same BB modulated spur interference which disturbs the wanted Rx signal. In [10, 9] the author of this thesis gives a detailed description of the modulated spur cancellation in FDD RF transceivers by adaptive filtering.

Prevention/mitigation methods:

As the generation of CW spurs cannot be prevented only by layout techniques, a high duplexer isolation is needed to suppress the TxL signal. This increases the costs of the duplexers and has the undesirable side effect of increased insertion loss, too. Split-LNA related modulated spurs may be prevented by increasing the reverse isolation of the LNA. Consequently, no signal energy is reflected to the other split-LNA. Another possibility is the use of HR mixers to suppress the harmful harmonics of the square-wave mixers. The contributions [9, 10, 16] published by the author of this thesis provide a mathematical model and the digital cancellation of the modulated-spur interference.

Tx Harmonics in Downlink

In DL CA, the primary Rx (Rx1) LO frequency is always coupled via the duplexing distance to the primary Tx (Tx1) frequency. But the secondary Rx (Rx2) LO frequency is not coupled to the primary Tx frequency and may be located at any different frequency depending on the intra/inter-band CA combination. When one of the harmonics of Tx1 (e.g. 2nd, 3rd or 5th) which are produced by the nonlinearity of the transmitter (including Tx switches) is close to the Rx2 LO frequency, then the Tx harmonic is directly down-converted to the BB. Example: $f_{Tx} = 700$ MHz (low band) and $f_{Rx2} \approx 3f_{Tx} = 2100$ MHz (high band).

Prevention/mitigation:

The linearization of the PA using pre-distortion of the transmit signal may reduce the generation of Tx harmonics. A high duplexer isolation suppresses the leaking Tx harmonics but leads to higher costs and insertion losses. The mathematical model which is provided in Section 2.3.1 indicates, that the Tx harmonics interference may be efficiently canceled by adaptive signal processing techniques.

Tx Harmonics in the Downlink Harmonic Response

The nonlinearity of the transmitter (including the PA and the switches) produces harmonics of the Tx signal which may fall into the harmonic response of the 25% duty-cycle square-wave mixer as will be described in Section 2.2. In this scenario the Tx harmonics located at the frequencies $2f_{Tx}, 3f_{Tx}, \dots$ are down-converted by a mixer harmonic response (located at the frequencies $3f_{LO2}, 5f_{LO2}, \dots$) to the Rx BB.

Example:

Assuming an LTE inter-band CA scenario with the uplink primary component carrier (PCC) in band 2 at $f_{Tx} = 1875$ MHz, and the downlink secondary component carrier (SCC) in band 13 at $f_{LO2} = 750$ MHz, the 2nd order Tx harmonic signal will be present around 3750 MHz. At the same time, the 5th harmonic of the SCC Rx LO occurs at 3750 MHz which down-converts the unwanted 2nd order Tx harmonic signal to the Rx BB. The described example scenario is depicted in the power spectral density (PSD) plot in Fig. 2.4.

Prevention/mitigation:

In the above example, the rejection of the 5th order harmonic response of the mixer would suppress the down-conversion of the Tx harmonic signal. This may be achieved by using a harmonic rejection mixer technique as described in Chapter 3. Other prevention strategies are the linearization of the PA or the use of a duplexer with higher isolation.

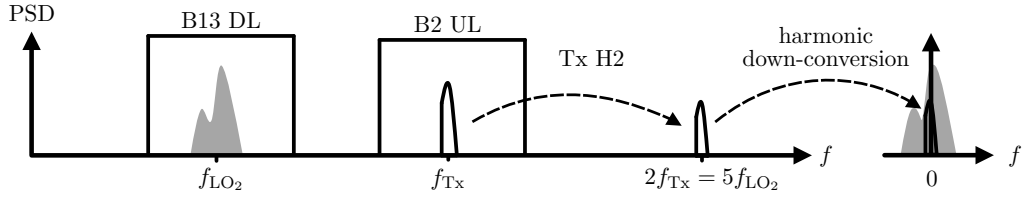


Figure 2.4: Down-conversion of the 2nd Tx harmonic by the harmonic response of the secondary CA mixer.

2.1.3 Tx Carrier Aggregation Related Interference Problems

Multiple Modulated Spurs

If Tx CA is used, each of the transmitters may cause a modulated spur interference if spurs around the corresponding Tx frequencies occur.

Prevention/mitigation:

The same prevention strategies as for the single modulated spur case apply.

Tx Harmonics in Downlink/Downlink Harmonic Response

When multiple transmitters are used, each transmitter generates harmonics due to the transmitter nonlinearity (PA, switches). Each harmonic content may be down-converted by the fundamental or the harmonic response of the secondary mixer, thereby resulting in a disturbance of the wanted receive signal.

Prevention/mitigation:

The same prevention strategies as for the single Tx case apply.

Intermodulation Distortions

In UL inter-band-, or intra-band non-contiguous CA, nonlinearities in the analog front-end can produce intermodulation distortions. E.g. the third-order intermodulation product (IM3) is generated at the frequencies $f_{IM3_1} = 2f_{Tx_1} - f_{Tx_2}$ and $f_{IM3_2} = 2f_{Tx_2} - f_{Tx_1}$ which may fall on top of the wanted receive signal or around the harmonic response of the mixer. In both cases, the IM3 product is down-converted into the BB where it disturbs the wanted signal. Intermodulation products may also be generated by blocker signals received by the antenna. In this thesis Tx CA related interferences are not further investigated.

Prevention/mitigation:

By using duplexers with high isolation the transmitter leakage signal may be reduced. Consequently, the power of the generated intermodulation products will be lowered. Intermodulation distortions may also be reduced by linearizing the Tx chain using circuit techniques. A digital cancellation technique of Tx CA induced intermodulation interferences is presented in [32].

2.2 Operation of the 25% Duty-Cycle Current-Driven Passive Mixer

Mixers are used to shift the desired RF signal to the baseband or an intermediate-frequency where the wanted signal is digitized for further digital signal processing. Frequency translation may be realized by a nonlinear operation, or, as in modern RF transceivers with linear time-variant systems. In order to cover the high frequency range used by modern communication standards as e.g in LTE, a wide-band frequency synthesizer is needed. Realizing a pure sine-wave in the giga-hertz range for the mixing process is not affordable in terms of hardware effort. Alternatively, switched square-wave systems are used with a design related duty-cycle. In modern mobile transceivers, the 25% duty-cycle complex IQ mixer architecture is preferably used in the receiver. It consists of the four mixer switches (transistors) I_+ , I_- , Q_+ and Q_- which are switched ON and OFF by a 25% duty-cycle scheme where at any moment only one switch is turned ON. The switch control signals $p_{I_+}(\varphi)$, $p_{Q_+}(\varphi)$, $p_{I_-}(\varphi)$ and $p_{Q_-}(\varphi)$ and the analog circuit of the 25 % duty-cycle mixer are visualized in Fig. 2.5 and Fig. 2.6, respectively. The switching period of the control signals corresponds to 2π and $z_{BB}(t)$ is a low-pass filter impulse response in the unit of an impedance. Each switch is turned ON for 25 % of the LO period thereby rejecting the flow of image-currents through simultaneously switched ON switches. This has the advantage, that the RF current at the output of the LNA is not split between the branches which leads to a 3 dB higher conversion gain and a lower receiver noise figure compared to a 50% duty-cycle mixer. Furthermore, no IQ-crosstalk occurs because no image current can circulate from the I-, to the Q-branch [33, 29].

One drawback of switched square-wave mixers is that the square-wave control signals introduce harmonics (harmonic response of the mixer) which lead to the down-conversion of interference signals which are located at the harmonics of the fundamental LO frequency. To be able to provide a mathematical description of the interferences caused by the harmonic response, a detailed understanding of the used square-wave mixers is necessary.

The IQ mixer is directly connected to the current output of the LNA, and the switches of the four mixer branches are switched ON and OFF by the 25% duty-cycle signals

$$\begin{aligned} \tilde{p}_{I_+}(t) &= \begin{cases} 1, & kT_{LO} \leq t \leq (k + \frac{1}{4}) T_{LO} \\ 0, & (k + \frac{1}{4}) T_{LO} < t < (k + 1) T_{LO} \end{cases} & \tilde{p}_{I_-}(t) &= \tilde{p}_{I_+} \left(t - \frac{T_{LO}}{2} \right) \\ \tilde{p}_{Q_+}(t) &= \tilde{p}_{I_+} \left(t - \frac{T_{LO}}{4} \right) & \tilde{p}_{Q_-}(t) &= \tilde{p}_{I_+} \left(t - \frac{3T_{LO}}{4} \right) \end{aligned} \quad (2.1)$$

which are depicted in Fig. 2.5 using the variable substitution $p_{I_+}(\varphi) = \tilde{p}_{I_+}(\varphi T_{LO}/(2\pi))$. Here k is any integer number and T_{LO} corresponds to the LO period. The RF current $i_{RF}(t)$ is split to the branches according to the switching functions (2.1). The resulting currents in each branch are

$$\begin{aligned} i_{RF,I_+}(t) &= \tilde{p}_{I_+}(t) i_{RF}(t) & i_{RF,I_-}(t) &= \tilde{p}_{I_-}(t) i_{RF}(t) \\ i_{RF,Q_+}(t) &= \tilde{p}_{Q_+}(t) i_{RF}(t) & i_{RF,Q_-}(t) &= \tilde{p}_{Q_-}(t) i_{RF}(t). \end{aligned} \quad (2.2)$$

By expressing the control signal $\tilde{p}_{I_+}(t)$ by its complex Fourier series with the coefficients

2.2 Operation of the 25% Duty-Cycle Current-Driven Passive Mixer

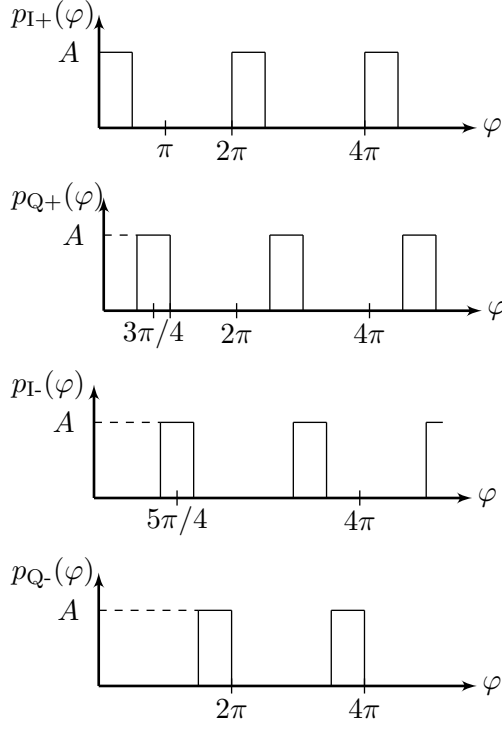


Figure 2.5: Control signals of the 25% duty-cycle mixer.

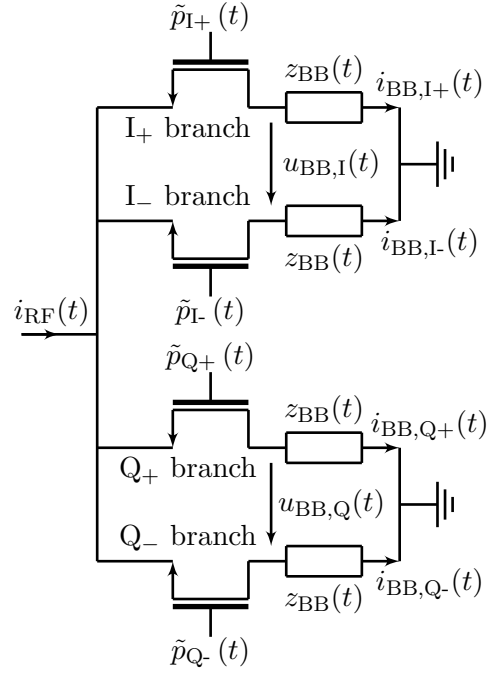


Figure 2.6: Analog circuit of the 25% duty-cycle mixer.

$$\begin{aligned}
 c_k &= \frac{1}{T_{LO}} \int_0^{T_{LO}} \tilde{p}_{I+}(t) e^{-jk2\pi f_{LO}t} dt \\
 &= \frac{1}{2\pi} \int_0^{2\pi} p_{I+}(\varphi) e^{-jk\varphi} d\varphi \\
 &= \frac{1}{2\pi} \left[\frac{A}{-jk} e^{-jk\varphi} \right]_0^{\pi/2} \\
 &= \frac{-A}{2\pi k j} \left(e^{-jk\frac{\pi}{2}} - 1 \right) \\
 &= \frac{A}{\pi k} e^{-jk\frac{\pi}{4}} \frac{e^{jk\frac{\pi}{4}} - e^{-jk\frac{\pi}{4}}}{2j} \\
 &= \frac{A}{\pi k} e^{-jk\frac{\pi}{4}} \sin\left(k\frac{\pi}{4}\right) \\
 &= \frac{A}{4} e^{-jk\frac{\pi}{4}} \text{sinc}\left(k\frac{\pi}{4}\right),
 \end{aligned} \tag{2.3}$$

2 Interferences in FDD RF Transceivers

the control signals may be rewritten as [29]

$$\begin{aligned}
\tilde{p}_{I+}(t) &= \sum_{k=-\infty}^{\infty} c_k e^{jk2\pi f_{LO}t} \\
\tilde{p}_{I-}(t) &= \sum_{k=-\infty}^{\infty} (-1)^k c_k e^{jk2\pi f_{LO}t} \\
\tilde{p}_{Q+}(t) &= \sum_{k=-\infty}^{\infty} e^{-jk\frac{\pi}{2}} c_k e^{jk2\pi f_{LO}t} \\
\tilde{p}_{Q-}(t) &= \sum_{k=-\infty}^{\infty} e^{jk\frac{\pi}{2}} c_k e^{jk2\pi f_{LO}t}.
\end{aligned} \tag{2.4}$$

The Fourier series of each control signal contains even and odd harmonics. The Fourier coefficient may be rewritten as $c_k = c'_k e^{-jk\frac{\pi}{4}}$ using $c'_k = \frac{A}{4} \text{sinc}\left(k\frac{\pi}{4}\right)$. The I+ and I- current flows into the differential amplifier connected to the output of the mixer which results in the differential current in the I-branch

$$\begin{aligned}
i_{\text{RF},I}(t) &= i_{\text{RF},I+}(t) - i_{\text{RF},I-}(t) \\
&= i_{\text{RF}}(t) \tilde{p}_{I+}(t) - i_{\text{RF}}(t) \tilde{p}_{I-}(t) \\
&= i_{\text{RF}}(t) \left(\sum_{k=-\infty}^{\infty} c_k e^{jk2\pi f_{LO}t} - \sum_{k=-\infty}^{\infty} (-1)^k c_k e^{jk2\pi f_{LO}t} \right) \\
&= 2 i_{\text{RF}}(t) \sum_{k=-\infty, k \text{ odd}}^{\infty} c'_k e^{j(k2\pi f_{LO}t - k\frac{\pi}{4})} \\
&= 4 i_{\text{RF}}(t) \sum_{k=1, k \text{ odd}}^{\infty} c'_k \cos\left(k2\pi f_{LO}t - k\frac{\pi}{4}\right)
\end{aligned} \tag{2.5}$$

and similarly in the Q-branch

$$\begin{aligned}
i_{\text{RF},Q}(t) &= i_{\text{RF},Q+}(t) - i_{\text{RF},Q-}(t) \\
&= i_{\text{RF}}(t) \tilde{p}_{Q+}(t) - i_{\text{RF}}(t) \tilde{p}_{Q-}(t) \\
&= i_{\text{RF}}(t) \left(\sum_{k=-\infty}^{\infty} e^{-jk\frac{\pi}{2}} c_k e^{jk2\pi f_{LO}t} - \sum_{k=-\infty}^{\infty} e^{jk\frac{\pi}{2}} c_k e^{jk2\pi f_{LO}t} \right) \\
&= 2 i_{\text{RF}}(t) \sum_{k=-\infty, k \text{ odd}}^{\infty} e^{-jk\frac{\pi}{2}} c_k e^{jk2\pi f_{LO}t} \\
&= 2 i_{\text{RF}}(t) \sum_{k=-\infty, k \text{ odd}}^{\infty} e^{-jk\frac{\pi}{2}} c'_k e^{j(k2\pi f_{LO}t - k\frac{\pi}{4})} \\
&= 4 i_{\text{RF}}(t) \sum_{k=1, k \text{ odd}}^{\infty} \sigma_k c'_k \sin\left(k2\pi f_{LO}t - k\frac{\pi}{4}\right)
\end{aligned} \tag{2.6}$$

where $\sigma_k = 1$ for $k = 1, 5, 9, 13, \dots$ and $\sigma_k = -1$ otherwise. It can be observed that due to the differential implementation the even harmonics cancel out each other, whereas

2.2 Operation of the 25% Duty-Cycle Current-Driven Passive Mixer

the odd harmonics add up constructively. E.g. evaluating the terms for $k = \pm 2$ in the third line of (2.5) results in

$$i_{\text{RF,I}}(t)|_{k=\pm 2} = i_{\text{RF}}(t) \cdot \left[\left(c_2^* e^{-j4\pi f_{\text{LO}} t} + c_2 e^{j4\pi f_{\text{LO}} t} \right) - \left((-1)^{-2} c_2^* e^{-j4\pi f_{\text{LO}} t} + (-1)^2 c_2 e^{j4\pi f_{\text{LO}} t} \right) \right] = 0. \quad (2.7)$$

All even harmonics cancel each other out which is an advantage of the implementation using differential amplifiers. The equivalent complex valued BB voltage after filtering the RF currents with the low-pass filter $z_{\text{BB}}(t)$ becomes

$$\begin{aligned} u_{\text{BB}}(t) &= u_{\text{BB,I}}(t) + j u_{\text{BB,Q}}(t) \\ &= [i_{\text{RF,I}}(t) + j i_{\text{RF,Q}}(t)] * z_{\text{BB}}(t) \\ &= \left[4 i_{\text{RF}}(t) \sum_{k=1, k \text{ odd}}^{\infty} c'_k e^{\sigma_k j (k2\pi f_{\text{LO}} t - k\frac{\pi}{4})} \right] * z_{\text{BB}}(t). \end{aligned} \quad (2.8)$$

Assuming that $i_{\text{RF}}(t)$ contains the wanted signal at the frequency f_{Rx} and a blocker signal around the frequency $f_{\text{BL}} \approx 3f_{\text{Rx}}$, the BB voltage becomes

$$\begin{aligned} u_{\text{BB}}(t) &= \left[4 \left(\Re \left\{ i_{\text{BB}}^{\text{Rx}}(t) e^{j2\pi f_{\text{Rx}} t} \right\} + \Re \left\{ i_{\text{BB}}^{\text{BL}}(t) e^{j2\pi f_{\text{BL}} t} \right\} \right) \right. \\ &\quad \cdot \left. \sum_{k=1, k \text{ odd}}^{\infty} c'_k e^{\sigma_k j (k2\pi f_{\text{LO}} t - k\frac{\pi}{4})} \right] * z_{\text{BB}}(t) \\ &= \left[2 \left(i_{\text{BB}}^{\text{Rx}}(t) e^{j2\pi f_{\text{Rx}} t} + i_{\text{BB}}^{\text{Rx}*}(t) e^{-j2\pi f_{\text{Rx}} t} + i_{\text{BB}}^{\text{BL}}(t) e^{j2\pi f_{\text{BL}} t} + i_{\text{BB}}^{\text{BL}*}(t) e^{-j2\pi f_{\text{BL}} t} \right) \right. \\ &\quad \cdot \left. \sum_{k=1, k \text{ odd}}^{\infty} c'_k e^{\sigma_k j (k2\pi f_{\text{LO}} t - k\frac{\pi}{4})} \right] * z_{\text{BB}}(t) \end{aligned} \quad (2.9)$$

In case of a direct-conversion receiver with $f_{\text{LO}} = f_{\text{Rx}}$, the BB voltage after low-pass filtering with the low-pass filter $z_{\text{BB}}(t)$ becomes

$$\begin{aligned} u_{\text{BB}}(t) &= 2c'_1 i_{\text{BB}}^{\text{Rx}*}(t) e^{-j\frac{\pi}{4}} Z_{\text{BB}} + \underbrace{2c'_3 i_{\text{BB}}^{\text{BL}}(t) e^{+j\frac{3\pi}{4}} Z_{\text{BB}}}_{\text{down-converted blocker}} \\ &= 2c_1 i_{\text{BB}}^{\text{Rx}*}(t) Z_{\text{BB}} + \text{BB disturbance}, \end{aligned} \quad (2.10)$$

where $Z_{\text{BB}} = 50 \Omega$ is the low-frequency BB impedance. The Rx signal is down-converted by the fundamental Fourier coefficient c_1 (see (2.3)). The blocker signal is down-converted by the mixer's 3rd order harmonic response (Fourier coefficient c'_3) which leads to a disturbance of the wanted signal. Similar disturbances may occur if $i_{\text{RF}}(t)$ contains blocker signals at other odd harmonics of the mixer LO frequency. Interestingly, (2.10) shows that the control of the mixer switches as described in Fig. 2.5 and (2.1) leads to the down-conversion of the complex conjugate Rx spectral component into the baseband. This leads to an inverted Q-component of the received signal. The odd harmonics ($k = 3, 5, 7, \dots$) of the control signal lead to the down-conversion of all spectral RF components located around the frequencies $k f_{\text{LO}}$ to the BB.

The sign of the Q-component can be corrected by the following options:

- Interchanging the Q+ and Q- mixer control signals
- Interchanging the I+ with the Q+ and the I- with the Q- control signal
- Sign-change of the Q-component in the digital BB

The first two options are discussed in the following section.

Interchanging the Q₊ and Q₋ control signals

By changing the control signal of the Q₊-branch to $\tilde{p}_{Q-}(t)$ and the control signal of the Q₋-branch to $\tilde{p}_{Q+}(t)$, the differential current in the Q-branch changes to

$$\begin{aligned} i_{\text{RF},Q}(t) &= -(i_{\text{RF},Q+}(t) - i_{\text{RF},Q-}(t)) \\ &= -4 i_{\text{RF}}(t) \sum_{k=1, k \text{ odd}}^{\infty} \sigma_k c'_k \sin\left(k2\pi f_{\text{LO}}t - k\frac{\pi}{4}\right). \end{aligned} \quad (2.11)$$

The equivalent complex valued BB voltage (without any unwanted blockers) becomes

$$\begin{aligned} u_{\text{BB}}(t) &= [i_{\text{RF},I}(t) + j i_{\text{RF},Q}(t)] * z_{\text{BB}}(t) \\ &= \left[4 i_{\text{RF}}(t) \sum_{k=1, k \text{ odd}}^{\infty} c'_k e^{-\sigma_k j(k2\pi f_{\text{LO}}t - k\frac{\pi}{4})} \right] * z_{\text{BB}}(t) \\ &= \left[4\Re \left\{ i_{\text{BB}}^{\text{Rx}}(t) e^{j2\pi f_{\text{Rx}}t} \right\} \sum_{k=1, k \text{ odd}}^{\infty} c'_k e^{-\sigma_k j(k2\pi f_{\text{LO}}t - k\frac{\pi}{4})} \right] * z_{\text{BB}}(t) \\ &= \left[2 \left[i_{\text{BB}}^{\text{Rx}}(t) e^{j2\pi f_{\text{Rx}}t} + i_{\text{BB}}^{\text{Rx}*}(t) e^{-j2\pi f_{\text{Rx}}t} \right] \cdot \sum_{k=1, k \text{ odd}}^{\infty} c'_k e^{-\sigma_k j(k2\pi f_{\text{LO}}t - k\frac{\pi}{4})} \right] * z_{\text{BB}}(t) \end{aligned} \quad (2.12)$$

and after low-pass filtering, the down-converted signal

$$\begin{aligned} u_{\text{BB}}(t) &= 2c'_1 i_{\text{BB}}^{\text{Rx}}(t) e^{+j\frac{\pi}{4}} Z_{\text{BB}} \\ &= 2c_1^* i_{\text{BB}}^{\text{Rx}}(t) Z_{\text{BB}} \end{aligned} \quad (2.13)$$

contains the wanted Rx signal.

Interchanging the I+ with the Q+ and the I- with the Q- control signal

When this option is chosen to swap the sign of the Q-component of the received signal, then

$$\begin{aligned} i_{\text{RF},I}(t) &= i_{\text{RF},Q+}(t) - i_{\text{RF},Q-}(t) \\ &= 4 i_{\text{RF}}(t) \sum_{k=1, k \text{ odd}}^{\infty} \sigma_k c'_k \sin\left(k2\pi f_{\text{LO}}t - k\frac{\pi}{4}\right) \end{aligned} \quad (2.14)$$

2.2 Operation of the 25% Duty-Cycle Current-Driven Passive Mixer

and

$$\begin{aligned} i_{\text{RF,Q}}(t) &= i_{\text{RF,I+}}(t) - i_{\text{RF,I-}}(t) \\ &= 4 i_{\text{RF}}(t) \sum_{k=1, k \text{ odd}}^{\infty} c'_k \cos\left(k2\pi f_{\text{LO}}t - k\frac{\pi}{4}\right) \end{aligned} \quad (2.15)$$

which leads for $k = 1, 5, 9, 13, \dots$ ($\sigma_k = 1$) to

$$\begin{aligned} u_{\text{BB}}(t) &= [i_{\text{RF,I}}(t) + j i_{\text{RF,Q}}(t)] * z_{\text{BB}}(t) \\ &= \left[4 i_{\text{RF}}(t) \left\{ \sum_{k=1, k \text{ odd}}^{\infty} \sigma_k c'_k \sin\left(k2\pi f_{\text{LO}}t - k\frac{\pi}{4}\right) \right. \right. \\ &\quad \left. \left. + j \sum_{k=1, k \text{ odd}}^{\infty} c'_k \cos\left(k2\pi f_{\text{LO}}t - k\frac{\pi}{4}\right) \right\} \right] * z_{\text{BB}}(t) \\ &= \left[4 i_{\text{RF}}(t) \left\{ \frac{1}{2j} \left(\sum_{k=1, k \text{ odd}}^{\infty} \sigma_k c'_k e^{j(k2\pi f_{\text{LO}}t - k\frac{\pi}{4})} - \sum_{k=1, k \text{ odd}}^{\infty} \sigma_k c'_k e^{-j(k2\pi f_{\text{LO}}t - k\frac{\pi}{4})} \right) \right. \right. \\ &\quad \left. \left. + \frac{j}{2} \left(\sum_{k=1, k \text{ odd}}^{\infty} c'_k e^{j(k2\pi f_{\text{LO}}t - k\frac{\pi}{4})} + \sum_{k=1, k \text{ odd}}^{\infty} c'_k e^{-j(k2\pi f_{\text{LO}}t - k\frac{\pi}{4})} \right) \right\} \right] * z_{\text{BB}}(t) \\ &= \left[4 i_{\text{RF}}(t) j \sum_{k=1, 5, 9, 13, \dots} c'_k e^{-j(k2\pi f_{\text{LO}}t - k\frac{\pi}{4})} \right] * z_{\text{BB}}(t) \\ &= \left[2 \left[i_{\text{BB}}^{\text{Rx}}(t) e^{j2\pi f_{\text{Rx}}t} + i_{\text{BB}}^{\text{Rx}*}(t) e^{-j2\pi f_{\text{Rx}}t} \right] j \sum_{k=1, 5, 9, 13, \dots} c'_k e^{-j(k2\pi f_{\text{LO}}t - k\frac{\pi}{4})} \right] * z_{\text{BB}}(t). \end{aligned} \quad (2.16)$$

It can be observed, that the fundamental and all harmonics are shifted by $\pi/2$. After low-pass filtering the mixer output signal, by assuming a direct-conversion receiver with $f_{\text{LO}} = f_{\text{Rx}}$, the resulting Rx BB voltage becomes

$$u_{\text{BB}}(t) = 2j c_1^* i_{\text{BB}}^{\text{Rx}}(t) Z_{\text{BB}}. \quad (2.17)$$

In this configuration, the main Rx signal $i_{\text{BB}}^{\text{Rx}}(t)$ is down-converted to the BB. However, due to the multiplication with j an IQ-swap occurs.

The detailed mathematical model of the 25% duty-cycle current driven passive mixer describes how the wanted Rx signal is down-converted by square-wave signals. Furthermore, the harmonic response of the mixer due to the square-wave implementation, which leads to the down-conversion of unwanted spectral components, is explained. In Chapter 3 a harmonic rejection concept is presented to suppress specific harmonics in the control signals of the 25% duty-cycle mixer. This prevents the down-conversion of spectral content located at the harmonic response of the mixer. In Section 2.5, the mathematical model of the 25% duty-cycle current driven passive mixer is extended by a jitter in the pulse duration of the control signals and a fundamental LO phase variation. This leads to a mathematical model of the mixer which includes an amplitude, and a PN component.

2.3 Self-Interference Modelling

In this section, the generated self-interferences due to the TxL signal and the nonlinearities in the transmitter or the receiver are investigated. The derivation is carried out by using static nonlinearities without memory. The use of static nonlinearities is sufficient to derive an analytical model which indicates at which frequency location each interference component occurs. Apart from the nonlinearity of the PA, also the RF switches which are used to switch between the different band-pass filters (duplexers) introduce nonlinear distortions. Fig. 2.1 showed that the duplexer Tx-to-Rx frequency response might be heavily frequency selective. Consequently, the duplexer stop-band response introduces a memory-effect to the overall Tx-to-Rx leakage path. As a result of that, a nonlinearity in the Tx path will result in an interference model which corresponds to the nonlinear Hammerstein model. On the other side, a nonlinearity in the receiver path will lead to a nonlinear Wiener or Volterra model [25]. Depending on that, different interference cancellation algorithms need to be derived.

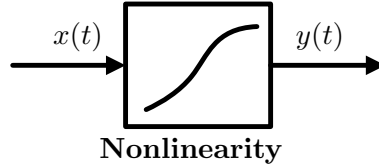


Figure 2.7: Memoryless nonlinear system.

Fig. 2.7 shows a block indicating a nonlinearity. Let's assume, that the output signal of the nonlinear system is described by the third-order nonlinear relationship

$$y(t) = \alpha_1 x(t) + \alpha_2 [x(t)]^2 + \alpha_3 [x(t)]^3 \quad (2.18)$$

where α_1, α_2 and α_3 are the polynomial coefficients. A nonlinearity in the signal path creates new undesired frequency content which may interfere with the desired signal. This may be the case if the created distortion falls directly in the receive signal frequency range where it is down-converted to the BB together with the wanted receive signal. Furthermore, in CA receivers spurs may down-convert the nonlinear distortion to the BB. In both cases, the wanted signal will be disturbed.

The difficulty in nonlinear interference cancellation is the generation of the reference signal for the digital cancellation algorithm (e.g. adaptive filter). The reference signal generation is dependent on where the nonlinearity occurs. Therefore, the cancellation of nonlinear distortions in the RF transceiver may be divided into two cases:

1. The case where the nonlinearity occurs in the transmitter path
2. Nonlinearity in the receiver

In the first case, the Tx signal passes through the nonlinearity and is subsequently convoluted with the duplexer Tx-to-Rx stop-band impulse response. This corresponds to a Hammerstein model [25] where the reference signal can be generated using a static

nonlinearity. In the second case, the transmit signal leaks through the duplexer with memory and subsequently the TxL signal experiences the nonlinearity. The second case is the more challenging task for the reference signal generation of the adaptive filter and results usually in the use of Volterra kernel filters [25]. In the next sections interference models for both cases will be derived.

2.3.1 Nonlinearity in the Transmitter

A third-order nonlinearity in the transmit path may e.g. be introduced by the duplexer switches or the PA itself. The nonlinearity creates new frequency content which leads to e.g. the 2nd and 3rd Tx-harmonic distortions located at the frequencies $2f_{\text{Tx}}$ and $3f_{\text{Tx}}$, respectively. Fig. 2.8 shows that in a CA receiver this Tx-harmonics may interfere with the desired Rx signal. The 2nd Tx-harmonic is in the same frequency range as the desired Rx signal of receiver Rx2 which leads to a disturbance of the desired receive signal. In the following derivation, the transmitter nonlinearity (including the nonlinearity of the PA and the duplexer switches) is modeled as a static third-order polynomial nonlinearity at the output of the PA. With the linear amplification A_{PA} of the PA, the RF signal at the output of the PA becomes

$$x_{\text{RF}}(t) = A_{\text{PA}} \Re \left\{ x_{\text{BB}}(t) e^{j2\pi f_{\text{Tx}} t} \right\}, \quad (2.19)$$

where $x_{\text{BB}}(t)$ is the complex valued BB transmit signal and f_{Tx} is the transmit carrier frequency. By using the identity

$$\Re \{ \xi \} = \frac{1}{2} (\xi + \xi^*), \quad (2.20)$$

the signal $\tilde{x}_{\text{RF}}(t)$ at the output of the nonlinearity becomes

$$\begin{aligned} \tilde{x}_{\text{RF}}(t) &= \alpha_1 x_{\text{RF}}(t) + \alpha_2 [x_{\text{RF}}(t)]^2 + \alpha_3 [x_{\text{RF}}(t)]^3 \\ &= \alpha_2 \frac{A_{\text{PA}}^2}{2} |x_{\text{BB}}(t)|^2 + \alpha_1 \frac{A_{\text{PA}}}{2} \left(x_{\text{BB}}(t) e^{j2\pi f_{\text{Tx}} t} + x_{\text{BB}}(t)^* e^{-j2\pi f_{\text{Tx}} t} \right) \\ &\quad + \alpha_3 \frac{3A_{\text{PA}}^3}{8} \left(x_{\text{BB}}(t) |x_{\text{BB}}(t)|^2 e^{j2\pi f_{\text{Tx}} t} + x_{\text{BB}}(t)^* |x_{\text{BB}}(t)|^2 e^{-j2\pi f_{\text{Tx}} t} \right) \\ &\quad + \alpha_2 \frac{A_{\text{PA}}^2}{4} \left(x_{\text{BB}}(t)^2 e^{j4\pi f_{\text{Tx}} t} + [x_{\text{BB}}(t)^*]^2 e^{-j4\pi f_{\text{Tx}} t} \right) \\ &\quad + \alpha_3 \frac{A_{\text{PA}}^3}{8} \left(x_{\text{BB}}(t)^3 e^{j6\pi f_{\text{Tx}} t} + [x_{\text{BB}}(t)^*]^3 e^{-j6\pi f_{\text{Tx}} t} \right) \\ &= \alpha_2 \frac{A_{\text{PA}}^2}{2} |x_{\text{BB}}(t)|^2 + \alpha_1 A_{\text{PA}} \Re \left\{ x_{\text{BB}}(t) e^{j2\pi f_{\text{Tx}} t} \right\} \\ &\quad + \alpha_3 \frac{3A_{\text{PA}}^3}{4} \Re \left\{ x_{\text{BB}}(t) |x_{\text{BB}}(t)|^2 e^{j2\pi f_{\text{Tx}} t} \right\} \\ &\quad + \alpha_2 \frac{A_{\text{PA}}^2}{2} \Re \left\{ x_{\text{BB}}(t)^2 e^{j4\pi f_{\text{Tx}} t} \right\} \\ &\quad + \alpha_3 \frac{A_{\text{PA}}^3}{4} \Re \left\{ x_{\text{BB}}(t)^3 e^{j6\pi f_{\text{Tx}} t} \right\}. \end{aligned} \quad (2.21)$$

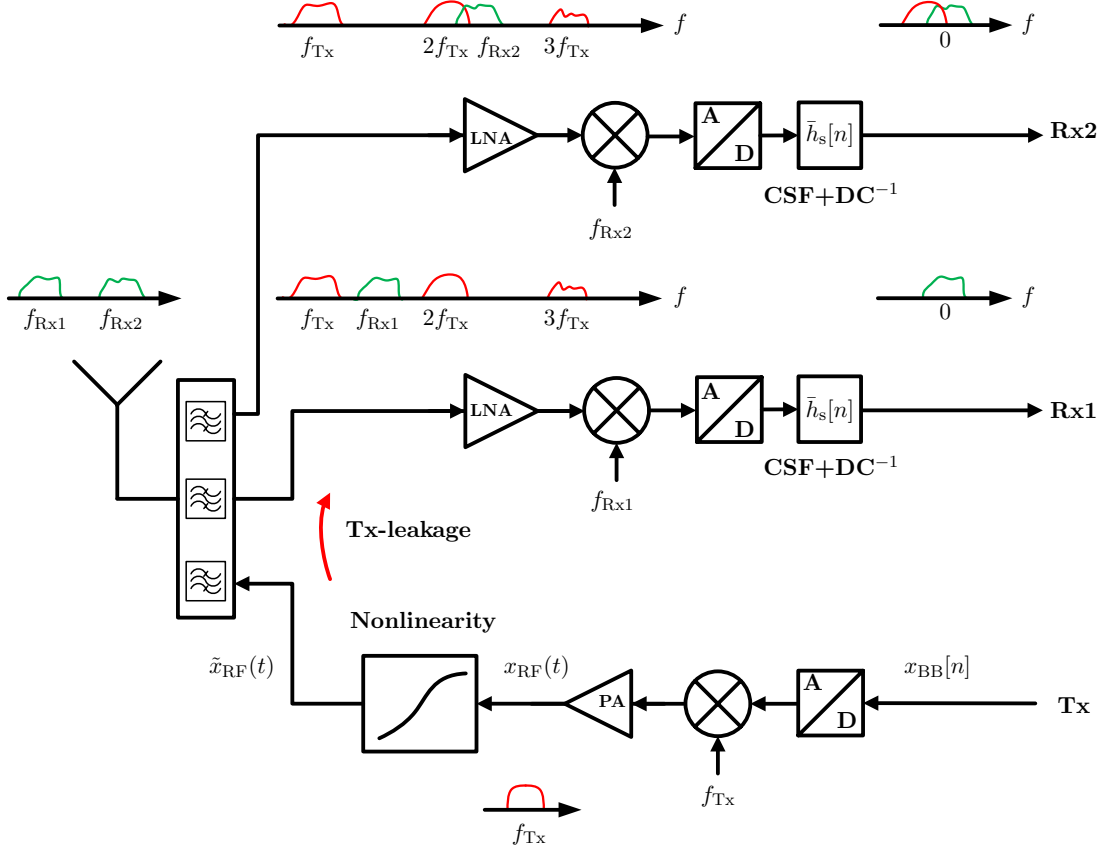


Figure 2.8: LTE-A FDD CA transceiver with a static third-order nonlinearity in the transmitter path. Receiver Rx2 is affected by the second-order Tx-harmonic distortion.

It contains new undesired frequency content at the harmonics of the transmit frequency. The signal components at the output of the nonlinearity are leaking at different frequencies through the duplexer into the receiver. For each signal component (fundamental at the frequency f_{Tx} , 2nd harmonic or H2 at the frequency $2f_{Tx}$, 3rd harmonic or H3 at the frequency $3f_{Tx}$), a different BB equivalent stop-band impulse response of the duplexer as described in (2.22) can be identified. Here, $h_{RF}^{TxL}(t)$ is the RF duplexer Tx-to-Rx stop-band impulse response at the frequency f_{Tx} and $h_{BB}^{TxL}(t)$ the corresponding complex valued BB equivalent impulse response. The pre-factor 2 in (2.22) is used to compensate for the factor $\frac{1}{2}$ in the identity (2.20).

$$\begin{aligned}
 h_{RF}^{TxL}(t) &= 2\Re \left\{ h_{BB}^{TxL}(t) e^{j2\pi f_{Tx}t} \right\} \\
 h_{RF}^{H2}(t) &= 2\Re \left\{ h_{BB}^{H2}(t) e^{j4\pi f_{Tx}t} \right\} \\
 h_{RF}^{H3}(t) &= 2\Re \left\{ h_{BB}^{H3}(t) e^{j6\pi f_{Tx}t} \right\}
 \end{aligned} \tag{2.22}$$

The duplexer is assumed to be a band-pass filter and therefore the signal component around direct-current (DC) in (2.21) is attenuated. Consequently, the Tx-path nonlinearity does not create a relevant interference around DC in the receiver. Fig. 2.9 shows a

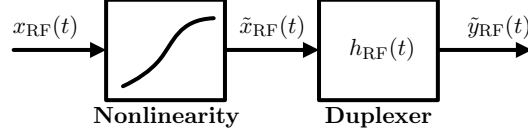


Figure 2.9: Nonlinear system and duplexer.

simplified block diagram of the signals and the duplexer impulse response. The received interference signal after the duplexer is

$$\begin{aligned}
 \tilde{y}_{\text{RF}}(t) &= \tilde{x}_{\text{RF}}(t) * h_{\text{RF}}(t) \\
 &= \alpha_1 A_{\text{PA}} \Re \left\{ [x_{\text{BB}}(t) * h_{\text{BB}}^{\text{TxL}}(t)] e^{j2\pi f_{\text{Tx}} t} \right\} \\
 &+ \alpha_3 \frac{3A_{\text{PA}}^3}{4} \Re \left\{ [x_{\text{BB}}(t) |x_{\text{BB}}(t)|^2 * h_{\text{BB}}^{\text{TxL}}(t)] e^{j2\pi f_{\text{Tx}} t} \right\} \\
 &+ \alpha_2 \frac{A_{\text{PA}}^2}{2} \Re \left\{ [x_{\text{BB}}(t)^2 * h_{\text{BB}}^{\text{H2}}(t)] e^{j4\pi f_{\text{Tx}} t} \right\} \\
 &+ \alpha_3 \frac{A_{\text{PA}}^3}{4} \Re \left\{ [x_{\text{BB}}(t)^3 * h_{\text{BB}}^{\text{H3}}(t)] e^{j6\pi f_{\text{Tx}} t} \right\},
 \end{aligned} \tag{2.23}$$

which is amplified by the LNA with gain A_{LNA} . The resulting LNA output signal becomes

$$\tilde{y}_{\text{RF,LNA}}(t) = A_{\text{LNA}} \tilde{y}_{\text{RF}}(t). \tag{2.24}$$

For modeling purposes it is assuming that each interference component at frequency $\psi \cdot f_{\text{Tx}}$ for $\psi = 1,2,3$ is down-converted with an appropriate spur with amplitude $A_{\text{sp},\psi}$ and frequency $f_{\text{sp},\psi}$ to the receiver BB². The down-converted interference signals appear in the BB with the frequency shifts

$$f_{\Delta_\psi} = \psi \cdot f_{\text{Tx}} - f_{\text{sp},\psi}. \tag{2.25}$$

Consequently, each signal component is amplified with the combined LNA and spur gain $G_\psi = A_{\text{LNA}} A_{\text{sp},\psi}$. The received signal after the down-conversion of each interference

²In practice, usually not for all interference components a corresponding spur occurs at the same time.

2 Interferences in FDD RF Transceivers

component $\tilde{y}_{\text{RF,LNA},\psi}(t)$ with a corresponding spur becomes

$$\begin{aligned}
y_{\text{RF}}(t) &= \sum_{\psi=1}^3 \tilde{y}_{\text{RF,LNA},\psi}(t) \cdot A_{\text{sp},\psi} e^{-j2\pi f_{\text{sp},\psi} t} \\
&= \alpha_1 \frac{A_{\text{PA}} G_1}{2} \left\{ [x_{\text{BB}}(t) * h_{\text{BB}}^{\text{TxL}}(t)] e^{j2\pi(f_{\text{Tx}} - f_{\text{sp},1})t} \right. \\
&\quad \left. + [x_{\text{BB}}(t) * h_{\text{BB}}^{\text{TxL}}(t)]^* e^{-j2\pi(f_{\text{Tx}} + f_{\text{sp},1})t} \right\} \\
&\quad + \alpha_3 \frac{3A_{\text{PA}}^3 G_1}{8} \left\{ [x_{\text{BB}}(t) |x_{\text{BB}}(t)|^2 * h_{\text{BB}}^{\text{TxL}}(t)] e^{j2\pi(f_{\text{Tx}} - f_{\text{sp},1})t} \right. \\
&\quad \left. + [x_{\text{BB}}(t) |x_{\text{BB}}(t)|^2 * h_{\text{BB}}^{\text{TxL}}(t)]^* e^{-j2\pi(f_{\text{Tx}} + f_{\text{sp},1})t} \right\} \\
&\quad + \alpha_2 \frac{A_{\text{PA}}^2 G_2}{4} \left\{ [x_{\text{BB}}(t)^2 * h_{\text{BB}}^{\text{H2}}(t)] e^{j2\pi(2f_{\text{Tx}} - f_{\text{sp},2})t} \right. \\
&\quad \left. + [x_{\text{BB}}(t)^2 * h_{\text{BB}}^{\text{H2}}(t)]^* e^{-j2\pi(2f_{\text{Tx}} + f_{\text{sp},2})t} \right\} \\
&\quad + \alpha_3 \frac{A_{\text{PA}}^3 G_3}{8} \left\{ [x_{\text{BB}}(t)^3 * h_{\text{BB}}^{\text{H3}}(t)] e^{j2\pi(3f_{\text{Tx}} - f_{\text{sp},3})t} \right. \\
&\quad \left. + [x_{\text{BB}}(t)^3 * h_{\text{BB}}^{\text{H3}}(t)]^* e^{-j2\pi(3f_{\text{Tx}} + f_{\text{sp},3})t} \right\}, \tag{2.26}
\end{aligned}$$

where the ideally assumed anti-aliasing filter in front of the ADC attenuates the signal components which are far away from the BB. The resulting received interference signal in discrete time at the output of the ADC is approximated by

$$\begin{aligned}
y_{\text{BB,ADC}}[n] &= \alpha_1 \frac{A_{\text{PA}} G_1}{2} [x_{\text{BB}}[n] * h_{\text{BB}}^{\text{TxL}}[n]] e^{j2\pi \frac{f_{\Delta 1}}{f_s} n} \\
&\quad + \alpha_3 \frac{3A_{\text{PA}}^3 G_1}{8} [x_{\text{BB}}[n] |x_{\text{BB}}[n]|^2 * h_{\text{BB}}^{\text{TxL}}[n]] e^{j2\pi \frac{f_{\Delta 1}}{f_s} n} \\
&\quad + \alpha_2 \frac{A_{\text{PA}}^2 G_2}{4} [x_{\text{BB}}[n]^2 * h_{\text{BB}}^{\text{H2}}[n]] e^{j2\pi \frac{f_{\Delta 2}}{f_s} n} \\
&\quad + \alpha_3 \frac{A_{\text{PA}}^3 G_3}{8} [x_{\text{BB}}[n]^3 * h_{\text{BB}}^{\text{H3}}[n]] e^{j2\pi \frac{f_{\Delta 3}}{f_s} n}. \tag{2.27}
\end{aligned}$$

Here, f_s is the sampling frequency and the baseband equivalent discrete-time duplexer impulse response

$$h_{\text{BB}}^{\text{TxL}}[n] = T_s h_{\text{BB}}^{\text{TxL}}(t) \Big|_{t=nT_s} \tag{2.28}$$

is a scaled and sampled (impulse invariant) version of the continuous-time BB impulse response $h_{\text{BB}}^{\text{TxL}}(t)$ [34, 35]. The DC in the received signal is time-variant and has many sources like e.g. LO-LO self mixing [8]. Therefore, to prevent the ADC from saturation, the receiver contains a mixed-signal DC cancellation. This DC cancellation in combination with the channel-select filtering is modeled by the combined impulse response

$\bar{h}_s[n] = h_{\text{DC}}[n] * h_s[n]$. The resulting BB interference model becomes

$$\begin{aligned}
 y_{\text{BB}}[n] &= y_{\text{BB,ADC}}[n] * \bar{h}_s[n] \\
 &= \left\{ \alpha_1 \frac{A_{\text{PA}} G_1}{2} h_{\text{BB}}^{\text{TxL}}[n] e^{j2\pi \frac{f_{\Delta_1}}{f_s} n} \right\} * \left[x_{\text{BB}}[n] e^{j2\pi \frac{f_{\Delta_1}}{f_s} n} \right] * \bar{h}_s[n] \\
 &+ \left\{ \alpha_3 \frac{3A_{\text{PA}}^3 G_1}{8} h_{\text{BB}}^{\text{TxL}}[n] e^{j2\pi \frac{f_{\Delta_1}}{f_s} n} \right\} * \left[x_{\text{BB}}[n] |x_{\text{BB}}[n]|^2 e^{j2\pi \frac{f_{\Delta_1}}{f_s} n} \right] * \bar{h}_s[n] \quad (2.29) \\
 &+ \left\{ \alpha_2 \frac{A_{\text{PA}}^2 G_2}{4} h_{\text{BB}}^{\text{H2}}[n] e^{j2\pi \frac{f_{\Delta_2}}{f_s} n} \right\} * \left[x_{\text{BB}}[n]^2 e^{j2\pi \frac{f_{\Delta_2}}{f_s} n} \right] * \bar{h}_s[n] \\
 &+ \left\{ \alpha_3 \frac{A_{\text{PA}}^3 G_3}{8} h_{\text{BB}}^{\text{H3}}[n] e^{j2\pi \frac{f_{\Delta_3}}{f_s} n} \right\} * \left[x_{\text{BB}}[n]^3 e^{j2\pi \frac{f_{\Delta_3}}{f_s} n} \right] * \bar{h}_s[n].
 \end{aligned}$$

In (2.29), four interference components can be identified. The first part at frequency f_{Tx} is the modulated spur interference as it occurs in intra/inter-band CA scenarios. The second part at frequency f_{Tx} is caused by the cubic nonlinearity. The third and fourth part are the 2nd and 3rd Tx-harmonics, respectively. Usually not all interferences are present in the BB simultaneously because not all spurs which down-convert the individual interference components occur at the same time. However, this combined interference model shows how each interference component hits the receiver BB if a corresponding spur occurs. The derived signal model is used to extract the Tx-signal kernels which are needed for the digital cancellation (e.g. by an adaptive algorithm) to cancel each interference in the receiver BB. Table 2.1 summarizes the derived reference signals. Each reference signal may be used as an input signal for a dedicated adaptive filter to

Interference	Reference signal for the digital cancellation
Modulated spur	$x_{\text{BB}}[n] e^{j2\pi \frac{f_{\Delta_1}}{f_s} n} * \bar{h}_s[n]$
3 rd order nonlinearity	$x_{\text{BB}}[n] x_{\text{BB}}[n] ^2 e^{j2\pi \frac{f_{\Delta_1}}{f_s} n} * \bar{h}_s[n]$
2 nd Tx-harmonic	$x_{\text{BB}}[n]^2 e^{j2\pi \frac{f_{\Delta_2}}{f_s} n} * \bar{h}_s[n]$
3 rd Tx-harmonic	$x_{\text{BB}}[n]^3 e^{j2\pi \frac{f_{\Delta_3}}{f_s} n} * \bar{h}_s[n]$

Table 2.1: Required reference signals for the adaptive filter to cancel the transmitter nonlinearity induced receiver interference.

cancel each individual interference. The spur frequency $f_{\text{sp},\psi}$ depends on the receiver configuration and the involved CA scenario. However, for a specific CA scenario, the spur frequencies may be predicted by the knowledge of the LO frequencies, the frequency location of their harmonics, and the knowledge of other clock frequencies (e.g. ADC) on the transceiver chip. When the harmful spur frequency $f_{\text{sp},\psi}$ is identified, its frequency is used to derive the frequency shift f_{Δ_ψ} which is needed in the reference signal generation.

2.3.2 Nonlinearity in the Receiver

Nonlinear distortions in the receiver chain are generated by the duplexer switches, the LNA, and the mixer. To simplify the derivation of the interference terms a combined memoryless third-order nonlinearity is used to model the nonlinearity of the duplexer switch and the LNA. The coupling between the mixer input and LO terminal causes an IMD2 interference which will be described in Section 2.3.5. The cascading of the switch/LNA third-order nonlinearity and the mixer second-order nonlinearity will be described in Section 2.3.6. As will be derived below, an IMD2 interference may also be caused by the second-order nonlinearity of the duplexer switches or the LNA. However, because the second-order nonlinearity of the switch/LNA, and the mixer DC feed-through coupling term are small, this IMD2 interference is much weaker than the IMD2 interference which is caused by the mixer terminal coupling. In the following section, a BB equivalent interference model based on the memoryless third-order nonlinearity in the receiver input is derived (see Fig. 2.10). The transmitter leakage signal $y_{\text{RF}}^{\text{TxL}}(t)$ is mathematically described by the convolution of the RF transmit signal

$$x_{\text{RF}}(t) = A_{\text{PA}} \Re \left\{ x_{\text{BB}}(t) e^{j2\pi f_{\text{Tx}} t} \right\} \quad (2.30)$$

with the duplexer impulse response

$$h_{\text{RF}}^{\text{TxL}}(t) = 2\Re \left\{ h_{\text{BB}}^{\text{TxL}}(t) e^{j2\pi f_{\text{Tx}} t} \right\}, \quad (2.31)$$

which results in the leakage signal

$$\begin{aligned} y_{\text{RF}}^{\text{TxL}}(t) &= x_{\text{RF}}(t) * h_{\text{RF}}^{\text{TxL}}(t) \\ &= A_{\text{PA}} \Re \left\{ [x_{\text{BB}}(t) * h_{\text{BB}}^{\text{TxL}}(t)] e^{j2\pi f_{\text{Tx}} t} \right\} \\ &= \frac{A_{\text{PA}}}{2} \left([x_{\text{BB}}(t) * h_{\text{BB}}^{\text{TxL}}(t)] e^{j2\pi f_{\text{Tx}} t} + [x_{\text{BB}}(t) * h_{\text{BB}}^{\text{TxL}}(t)]^* e^{-j2\pi f_{\text{Tx}} t} \right). \end{aligned} \quad (2.32)$$

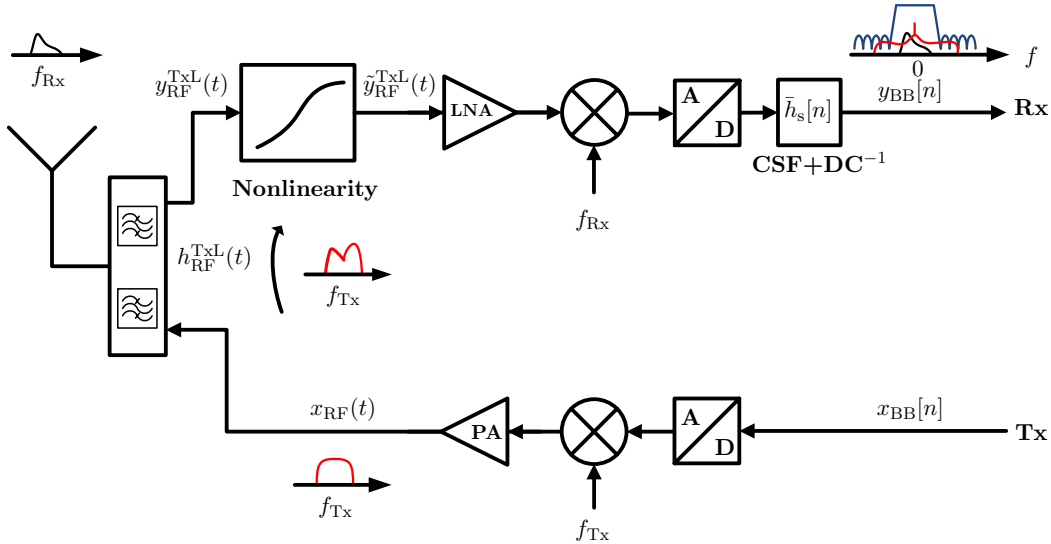


Figure 2.10: Direct conversion RF transceiver depicting a switch/LNA caused memoryless third-order nonlinearity in the receiver input.

Using (2.32), the signal at the output of the third-order nonlinearity becomes

$$\begin{aligned}
 \tilde{y}_{\text{RF}}(t) &= \alpha_1 y_{\text{RF}}^{\text{TxL}}(t) + \alpha_2 [y_{\text{RF}}^{\text{TxL}}(t)]^2 + \alpha_3 [y_{\text{RF}}^{\text{TxL}}(t)]^3 \\
 &= \alpha_2 \frac{A_{\text{PA}}^2}{2} |x_{\text{BB}}(t) * h_{\text{BB}}^{\text{TxL}}(t)|^2 \\
 &\quad + \alpha_1 \frac{A_{\text{PA}}}{2} \left([x_{\text{BB}}(t) * h_{\text{BB}}^{\text{TxL}}(t)] e^{j2\pi f_{\text{Tx}} t} + [x_{\text{BB}}(t) * h_{\text{BB}}^{\text{TxL}}(t)]^* e^{-j2\pi f_{\text{Tx}} t} \right) \\
 &\quad + \alpha_3 \frac{3A_{\text{PA}}^3}{8} \left([x_{\text{BB}}(t) * h_{\text{BB}}^{\text{TxL}}(t)] |x_{\text{BB}}(t) * h_{\text{BB}}^{\text{TxL}}(t)|^2 e^{j2\pi f_{\text{Tx}} t} \right. \\
 &\quad \left. + [x_{\text{BB}}(t) * h_{\text{BB}}^{\text{TxL}}(t)]^* |x_{\text{BB}}(t) * h_{\text{BB}}^{\text{TxL}}(t)|^2 e^{-j2\pi f_{\text{Tx}} t} \right) \\
 &\quad + \alpha_2 \frac{A_{\text{PA}}^2}{4} \left([x_{\text{BB}}(t) * h_{\text{BB}}^{\text{TxL}}(t)]^2 e^{j4\pi f_{\text{Tx}} t} + [x_{\text{BB}}(t) * h_{\text{BB}}^{\text{TxL}}(t)]^{*2} e^{-j4\pi f_{\text{Tx}} t} \right) \\
 &\quad + \alpha_3 \frac{A_{\text{PA}}^3}{8} \left([x_{\text{BB}}(t) * h_{\text{BB}}^{\text{TxL}}(t)]^3 e^{j6\pi f_{\text{Tx}} t} + [x_{\text{BB}}(t) * h_{\text{BB}}^{\text{TxL}}(t)]^{*3} e^{-j6\pi f_{\text{Tx}} t} \right).
 \end{aligned} \tag{2.33}$$

The signal $\tilde{y}_{\text{RF}}(t)$ is amplified by the LNA with gain A_{LNA} which leads to the LNA output signal

$$\tilde{y}_{\text{RF,LNA}}(t) = A_{\text{LNA}} \tilde{y}_{\text{RF}}(t). \tag{2.34}$$

The first interference term in (2.34) falls directly around DC and produces therefore a receiver BB interference. The other terms are located at the frequencies $\psi \cdot f_{\text{Tx}}$ with $\psi = 1, 2, 3$. However, spurs which occur in the analog front-end may down-convert these terms into the BB. In this interference derivation, it is assumed that each interference term is down-converted by a corresponding spur (with frequency $f_{\text{sp},\psi}$) into the Rx baseband where it appears with the frequency offset $f_{\Delta_\psi} = \psi \cdot f_{\text{Tx}} - f_{\text{sp},\psi}$. The signal term around DC in (2.34) may leak to the mixer output by the DC feed-through term $\alpha_{\text{DC}}^{\text{Mix}}$, therefore creating an IMD2 interference in the receiver BB. Recalling that G_ψ is the combined LNA and spur gain, the resulting interference model becomes

$$\begin{aligned}
 y_{\text{RF}}(t) &= \alpha_2 \frac{A_{\text{PA}}^2 \alpha_{\text{DC}}^{\text{Mix}}}{2} |x_{\text{BB}}(t) * h_{\text{BB}}^{\text{TxL}}(t)|^2 + \sum_{\psi=1}^3 \tilde{y}_{\text{RF,LNA},\psi}(t) \cdot A_{\text{sp},\psi} e^{-j2\pi f_{\text{sp},\psi} t} \\
 &= \alpha_2 \frac{A_{\text{PA}}^2 \alpha_{\text{DC}}^{\text{Mix}}}{2} |x_{\text{BB}}(t) * h_{\text{BB}}^{\text{TxL}}(t)|^2 \\
 &\quad + \alpha_1 \frac{A_{\text{PA}} G_1}{2} \left([x_{\text{BB}}(t) * h_{\text{BB}}^{\text{TxL}}(t)] e^{j2\pi(f_{\text{Tx}} - f_{\text{sp},1})t} \right. \\
 &\quad \left. + [x_{\text{BB}}(t) * h_{\text{BB}}^{\text{TxL}}(t)]^* e^{-j2\pi(f_{\text{Tx}} + f_{\text{sp},1})t} \right) \\
 &\quad + \alpha_3 \frac{3A_{\text{PA}}^3 G_1}{8} \left([x_{\text{BB}}(t) * h_{\text{BB}}^{\text{TxL}}(t)] |x_{\text{BB}}(t) * h_{\text{BB}}^{\text{TxL}}(t)|^2 e^{j2\pi(f_{\text{Tx}} - f_{\text{sp},1})t} \right. \\
 &\quad \left. + [x_{\text{BB}}(t) * h_{\text{BB}}^{\text{TxL}}(t)]^* |x_{\text{BB}}(t) * h_{\text{BB}}^{\text{TxL}}(t)|^2 e^{-j2\pi(f_{\text{Tx}} + f_{\text{sp},1})t} \right) \\
 &\quad + \alpha_2 \frac{A_{\text{PA}}^2 G_2}{4} \left([x_{\text{BB}}(t) * h_{\text{BB}}^{\text{TxL}}(t)]^2 e^{j2\pi(2f_{\text{Tx}} - f_{\text{sp},2})t} \right. \\
 &\quad \left. + [x_{\text{BB}}(t) * h_{\text{BB}}^{\text{TxL}}(t)]^{*2} e^{-j2\pi(2f_{\text{Tx}} + f_{\text{sp},2})t} \right) \\
 &\quad + \alpha_3 \frac{A_{\text{PA}}^3 G_3}{8} \left([x_{\text{BB}}(t) * h_{\text{BB}}^{\text{TxL}}(t)]^3 e^{j2\pi(3f_{\text{Tx}} - f_{\text{sp},3})t} \right. \\
 &\quad \left. + [x_{\text{BB}}(t) * h_{\text{BB}}^{\text{TxL}}(t)]^{*3} e^{-j2\pi(3f_{\text{Tx}} + f_{\text{sp},3})t} \right).
 \end{aligned} \tag{2.35}$$

2 Interferences in FDD RF Transceivers

The anti-aliasing filter attenuates the frequency content which is far away from the BB. By using the impulse invariant discrete-time impulse response $h_{\text{BB}}^{\text{TxL}}[n] = T_s h_{\text{BB}}^{\text{TxL}}(t)|_{t=nT_s}$, the resulting discrete-time BB interference model may be expressed as

$$\begin{aligned}
y_{\text{BB,ADC}}[n] &= \alpha_2 \frac{A_{\text{PA}}^2 \alpha_{\text{DC}}^{\text{Mix}}}{2} |x_{\text{BB}}[n] * h_{\text{BB}}^{\text{TxL}}[n]|^2 \\
&+ \alpha_1 \frac{A_{\text{PA}} G_1}{2} [x_{\text{BB}}[n] * h_{\text{BB}}^{\text{TxL}}[n]] e^{j2\pi \frac{f_{\Delta,1}}{f_s} n} \\
&+ \alpha_3 \frac{3A_{\text{PA}}^3 G_1}{8} [x_{\text{BB}}[n] * h_{\text{BB}}^{\text{TxL}}[n]] |x_{\text{BB}}[n] * h_{\text{BB}}^{\text{TxL}}[n]|^2 e^{j2\pi \frac{f_{\Delta,1}}{f_s} n} \\
&+ \alpha_2 \frac{A_{\text{PA}}^2 G_2}{4} [x_{\text{BB}}[n] * h_{\text{BB}}^{\text{TxL}}[n]]^2 e^{j2\pi \frac{f_{\Delta,2}}{f_s} n} \\
&+ \alpha_3 \frac{A_{\text{PA}}^3 G_3}{8} [x_{\text{BB}}[n] * h_{\text{BB}}^{\text{TxL}}[n]]^3 e^{j2\pi \frac{f_{\Delta,3}}{f_s} n}.
\end{aligned} \tag{2.36}$$

After channel-select filtering and the DC cancellation the BB equivalent interference becomes

$$\begin{aligned}
y_{\text{BB}}[n] &= \tilde{y}_{\text{BB,ADC}}[n] * \bar{h}_s[n] \\
&= \alpha_2 \frac{A_{\text{PA}}^2 \alpha_{\text{DC}}^{\text{Mix}}}{2} \left\{ |x_{\text{BB}}[n] * h_{\text{BB}}^{\text{TxL}}[n]|^2 \right\} * \bar{h}_s[n] \\
&+ \left\{ \alpha_1 \frac{A_{\text{PA}} G_1}{2} h_{\text{BB}}^{\text{TxL}}[n] e^{j2\pi \frac{f_{\Delta,1}}{f_s} n} \right\} * \left[x_{\text{BB}}[n] e^{j2\pi \frac{f_{\Delta,1}}{f_s} n} \right] * \bar{h}_s[n] \\
&+ \alpha_3 \frac{3A_{\text{PA}}^3 G_1}{8} \left\{ [x_{\text{BB}}[n] * h_{\text{BB}}^{\text{TxL}}[n]] |x_{\text{BB}}[n] * h_{\text{BB}}^{\text{TxL}}[n]|^2 e^{j2\pi \frac{f_{\Delta,1}}{f_s} n} \right\} * \bar{h}_s[n] \\
&+ \alpha_2 \frac{A_{\text{PA}}^2 G_2}{4} \left\{ [x_{\text{BB}}[n] * h_{\text{BB}}^{\text{TxL}}[n]]^2 e^{j2\pi \frac{f_{\Delta,2}}{f_s} n} \right\} * \bar{h}_s[n] \\
&+ \alpha_3 \frac{A_{\text{PA}}^3 G_3}{8} \left\{ [x_{\text{BB}}[n] * h_{\text{BB}}^{\text{TxL}}[n]]^3 e^{j2\pi \frac{f_{\Delta,3}}{f_s} n} \right\} * \bar{h}_s[n].
\end{aligned} \tag{2.37}$$

In (2.37) several interferences can be identified: An IMD2 interference which is fed through the mixer by its DC feed-through gain $\alpha_{\text{DC}}^{\text{Mix}}$, the linear modulated spur interference, interference caused by the cubic nonlinearity, a quadratic interference at $2f_{\text{Tx}}$ similar to the 2nd Tx-harmonic and a cubic interference at $3f_{\text{Tx}}$ similar to the 3rd Tx-harmonic. Unfortunately, the extraction of the reference signal for a digital cancellation algorithm is not as straight forward as in the case where the nonlinearity occurs in the Tx path. The strength of the individual interference terms depends heavily on the magnitude of the nonlinearity coefficients. However, the second and third interference term in (2.37) may occur simultaneously when a spur at $f_{\text{sp},1} \approx f_{\text{Tx}}$ is present. If the PA-, and the LNA gain are both high³, the third term may be even stronger than the second. As will be discussed later in Chapter 5, the nonlinear interferences terms as they occur in (2.37) may be canceled by the use of Volterra-, or Wiener model based filters [25].

³For high LNA gains the factor α_3 may increase and for high PA gains the term A_{LNA}^3 may dominate.

2.3.3 Spur IQ-Imbalance

Till now it was assumed that the spur which is down-converting the RF interference to the BB may be modeled as an equivalent complex valued spur of the form

$$\begin{aligned} p_{\text{sp}}(t) &= A_{\text{sp}} e^{-j2\pi f_{\text{sp}} t} \\ &= A_{\text{sp}} (\cos(2\pi f_{\text{sp}} t) - j \sin(2\pi f_{\text{sp}} t)) \end{aligned} \quad (2.38)$$

with amplitude A_{sp} and frequency f_{sp} . However, measurements at the real transceiver chip showed that the observed BB interference not only contains the down-converted RF interference but also its spectral image. This means that the spur model needs to be extended to be able to describe the true BB interference. This may be done by incorporating the IQ-imbalance model [36, 37]. By including a gain imbalance g , and phase imbalance ϕ , the spur model becomes

$$p_{\text{sp}}(t) = A_{\text{sp}} (\cos(2\pi f_{\text{sp}} t) - j g \sin(2\pi f_{\text{sp}} t + \phi)). \quad (2.39)$$

By using the identities $\cos(\psi) = \frac{1}{2}(e^{j\psi} + e^{-j\psi})$ and $\sin(\psi) = \frac{1}{2j}(e^{j\psi} - e^{-j\psi})$ the spur may be expressed as

$$\begin{aligned} p_{\text{sp}}(t) &= A_{\text{sp}} \left[\frac{1}{2} (e^{j2\pi f_{\text{sp}} t} + e^{-j2\pi f_{\text{sp}} t}) - \frac{g}{2} (e^{j(2\pi f_{\text{sp}} t + \phi)} - e^{-j(2\pi f_{\text{sp}} t + \phi)}) \right] \\ &= A_{\text{sp}} [K_1 e^{-j2\pi f_{\text{sp}} t} + K_2 e^{j2\pi f_{\text{sp}} t}] \end{aligned} \quad (2.40)$$

where

$$K_1 = \frac{1 + g e^{-j\phi}}{2}, \quad \text{and} \quad K_2 = \frac{1 - g e^{j\phi}}{2}. \quad (2.41)$$

When (2.40) is used to replace the spur terms in (2.26) or (2.35), the resulting main and image interference component appear in the BB. In Section 2.3.4, the modulated spur interference including an IQ-imbalance in the spur will be derived in detail.

2.3.4 Modulated Spur Interference with Spur IQ-Imbalance

In this section, the modulated spur interference which was derived in Section 2.3.1 is extended by a spur IQ-imbalance. In the introduction of this thesis it was already mentioned that the modulated spur interference may be generated by LO-LO cross-talk spurs, or by the use of a split-LNA. In the following derivation it is assumed that the modulated spur interference is generated by an LO-LO cross-talk spur. Also the wanted Rx signal and the noise are added in the interference model. Using the same modeling as introduced in Section 2.3.1, the RF transmitter leakage signal into the receiver becomes

$$y_{\text{RF}}^{\text{TxL}}(t) = A_{\text{PA}} \Re \left\{ [x_{\text{BB}}(t) * h_{\text{BB}}^{\text{TxL}}(t)] e^{j2\pi f_{T_x} t} \right\}. \quad (2.42)$$

The LNA output signal

$$y_{\text{RF,LNA}}^{\text{Tot}}(t) = A_{\text{LNA}} [y_{\text{RF}}^{\text{TxL}}(t) + y_{\text{RF}}^{\text{Rx}}(t) + v_{\text{RF}}(t)] \quad (2.43)$$

contains the amplified TxL signal $y_{\text{RF}}^{\text{TxL}}(t)$, the wanted Rx signal $y_{\text{RF}}^{\text{Rx}}(t)$ and the noise $v_{\text{RF}}(t)$. In the next step, the signal after the down-conversion mixer (2.44) is derived.

2 Interferences in FDD RF Transceivers

The wanted Rx and the noise signal are down-converted by the Rx mixer local oscillator, whereas the TxL signal is down-converted by the spur with IQ-imbalance (2.40) which appears at the Rx mixer⁴. The TxL signal is amplified by $G_{\text{sp}} = A_{\text{LNA}} A_{\text{sp}}$, where A_{sp} is the spur gain. By neglecting the mixing products of the Rx and noise signal with the spur, the total received signal at the output of the mixer becomes

$$\begin{aligned} y_{\text{RF,mixer}}^{\text{Tot}}(t) &= y_{\text{RF}}^{\text{TxL}}(t) G_{\text{sp}} \left[K_1 e^{-j2\pi f_{\text{sp}} t} + K_2 e^{+j2\pi f_{\text{sp}} t} \right] \\ &\quad + A_{\text{LNA}} \left[y_{\text{RF}}^{\text{Rx}}(t) + v_{\text{RF}}(t) \right] e^{-j2\pi f_{\text{Rx}} t}. \end{aligned} \quad (2.44)$$

Using the identity $\Re\{\xi\} = \frac{1}{2}(\xi + \xi^*)$, (2.44) results in

$$\begin{aligned} y_{\text{RF,mixer}}^{\text{Tot}}(t) &= \frac{A_{\text{PA}} G_{\text{sp}}}{2} \left\{ K_1 \left[x_{\text{BB}}(t) * h_{\text{BB}}^{\text{TxL}}(t) \right] e^{j2\pi(f_{\text{Tx}} - f_{\text{sp}})t} \right. \\ &\quad + K_2 \left[x_{\text{BB}}(t) * h_{\text{BB}}^{\text{TxL}}(t) \right] e^{j2\pi(f_{\text{Tx}} + f_{\text{sp}})t} \\ &\quad + K_1 \left[x_{\text{BB}}(t) * h_{\text{BB}}^{\text{TxL}}(t) \right]^* e^{-j2\pi(f_{\text{Tx}} + f_{\text{sp}})t} \\ &\quad \left. + K_2 \left[x_{\text{BB}}(t) * h_{\text{BB}}^{\text{TxL}}(t) \right]^* e^{-j2\pi(f_{\text{Tx}} - f_{\text{sp}})t} \right\} \\ &\quad + A_{\text{LNA}} \left[\frac{1}{2} y_{\text{BB}}^{\text{Rx}}(t) + \frac{1}{2} y_{\text{BB}}^{\text{Rx}}(t)^* e^{-j4\pi f_{\text{Rx}} t} \right] \\ &\quad + A_{\text{LNA}} \left[\frac{1}{2} v_{\text{BB}}(t) + \frac{1}{2} v_{\text{BB}}(t)^* e^{-j4\pi f_{\text{Rx}} t} \right]. \end{aligned} \quad (2.45)$$

The ideally assumed anti-aliasing filter in front of the ADC attenuates the mixing products in $y_{\text{RF,mixer}}^{\text{Tot}}(t)$ which are far away from the BB. The resulting received discrete-time signal using (2.22) and (2.28) is approximated by

$$\begin{aligned} y_{\text{BB,ADC}}^{\text{Tot}}[n] &= \frac{A_{\text{PA}} G_{\text{sp}}}{2} \left\{ K_1 \left[x_{\text{BB}}[n] * h_{\text{BB}}^{\text{TxL}}[n] \right] e^{j2\pi \frac{f_{\Delta}}{f_s} n} \right. \\ &\quad \left. + K_2 \left[x_{\text{BB}}[n] * h_{\text{BB}}^{\text{TxL}}[n] \right]^* e^{-j2\pi \frac{f_{\Delta}}{f_s} n} \right\} \\ &\quad + \frac{A_{\text{LNA}}}{2} y_{\text{BB}}^{\text{Rx}}[n] + \frac{A_{\text{LNA}}}{2} v_{\text{BB}}[n], \end{aligned} \quad (2.46)$$

where $f_{\Delta} = f_{\text{Tx}} - f_{\text{sp}}$. Thus, the main modulated spur interference component appears in the receiver BB with the frequency offset f_{Δ} , and the image with the offset $-f_{\Delta}$. Considering the combined channel-select filtering and DC-cancellation with the impulse response $\bar{h}_s[n]$, (2.46) leads to the BB equivalent received signal

$$\begin{aligned} y_{\text{BB}}^{\text{Tot}}[n] &= y_{\text{BB,ADC}}^{\text{Tot}}[n] * \bar{h}_s[n] \\ &= \underbrace{x_{\text{BB}}^{\text{s}}[n] * h_{\text{BB},1}^{\text{Tot}}[n] + x_{\text{BB}}^{\text{s}*}[n] * h_{\text{BB},2}^{\text{Tot}}[n]}_{y_{\text{BB}}^{\text{MS}}} \\ &\quad + \frac{A_{\text{LNA}}}{2} y_{\text{BB}}^{\text{Rx}}[n] * \bar{h}_s[n] + \frac{A_{\text{LNA}}}{2} v_{\text{BB}}[n] * \bar{h}_s[n]. \end{aligned} \quad (2.47)$$

⁴In the real mixing process the overall signal which appears at the mixer input (including the Rx, the noise and the TxL signal) is mixed with the LO frequency and the spur. However, some of the mixing products fall outside the relevant frequency range and may be neglected.

In this final result $y_{\text{BB}}^{\text{MS}}$ is the BB equivalent modulated spur interference which contains a main and an image interference component. In

$$x_{\text{BB}}^{\text{s}}[n] = \left[x_{\text{BB}}[n] e^{j2\pi \frac{f_{\Delta}}{f_s} n} \right] * \bar{h}_{\text{s}}[n], \quad (2.48)$$

the Tx signal is shifted by f_{Δ} and subsequently filtered by the CSF and

$$h_{\text{BB},1}^{\text{Tot}}[n] = \frac{A_{\text{PA}} G_{\text{sp}} K_1}{2} h_{\text{BB}}^{\text{TxL}}[n] e^{j2\pi \frac{f_{\Delta}}{f_s} n}, \quad (2.49)$$

$$h_{\text{BB},2}^{\text{Tot}}[n] = \frac{A_{\text{PA}} G_{\text{sp}} K_2}{2} h_{\text{BB}}^{\text{TxL}}[n] e^{-j2\pi \frac{f_{\Delta}}{f_s} n} \quad (2.50)$$

are the main and image impulse responses of the Tx-to-Rx leakage channel. The digital cancellation of this modulated spur interference by adaptive filtering is presented in Section 4.6.

2.3.5 Mixer Terminal Coupling Induced IMD2

The second-order nonlinearity of the switch/LNA creates an IMD2 interference which may leak through the mixer DC feed-through to the BB. However, the larger contribution of IMD2 interference is created by a coupling between the RF and LO port of the IQ-mixer [8]. Based on the block diagram in Fig. 2.11 depicting an RF transceiver operating in FDD mode, a detailed IMD2 interference model is derived. The transmitted complex valued BB signal $x_{\text{BB}}(t) = x_{\text{I}}(t) + jx_{\text{Q}}(t)$ is up-converted to the passband and amplified by the PA gain A_{PA} which is for simplicity assumed to be linear (neglecting the transmitter nonlinearity). The resulting RF transmit signal

$$x_{\text{RF}}(t) = A_{\text{PA}} \Re \left\{ x_{\text{BB}}(t) e^{j2\pi f_{\text{Tx}} t} \right\} \quad (2.51)$$

is radiated by the antenna, but a small portion of the signal is leaking through the duplexer stop-band which is modeled by the RF impulse response

$$h_{\text{RF}}^{\text{TxL}}(t) = 2\Re \left\{ h_{\text{BB}}^{\text{TxL}}(t) e^{j2\pi f_{\text{Tx}} t} \right\}, \quad (2.52)$$

where $h_{\text{BB}}^{\text{TxL}}(t)$ is the BB equivalent duplexer impulse response. The resulting transmitter leakage signal in the receiver can be expressed as

$$\begin{aligned} y_{\text{RF}}^{\text{TxL}}(t) &= x_{\text{RF}}(t) * h_{\text{RF}}^{\text{TxL}}(t) \\ &= A_{\text{PA}} \Re \left\{ [x_{\text{BB}}(t) * h_{\text{BB}}^{\text{TxL}}(t)] e^{j2\pi f_{\text{Tx}} t} \right\}. \end{aligned} \quad (2.53)$$

The total received signal at the output of the LNA

$$y_{\text{RF,LNA}}^{\text{Tot}}(t) = A_{\text{LNA}} [y_{\text{RF}}^{\text{TxL}}(t) + y_{\text{RF}}^{\text{Rx}}(t) + v_{\text{RF}}(t)], \quad (2.54)$$

with the gain A_{LNA} contains the amplified Tx leakage signal, the wanted Rx signal $y_{\text{RF}}^{\text{Rx}}(t)$ and the noise $v_{\text{RF}}(t)$. The output signal of the I-, and Q-path mixer is combined into the complex valued signal $y_{\text{RF,mixer}}^{\text{Tot}}(t)$ (2.55). It contains the wanted signal which is down-converted with the linear gain $\alpha_1 = \alpha_1^{\text{I}} = \alpha_1^{\text{Q}}$, and the second order interference

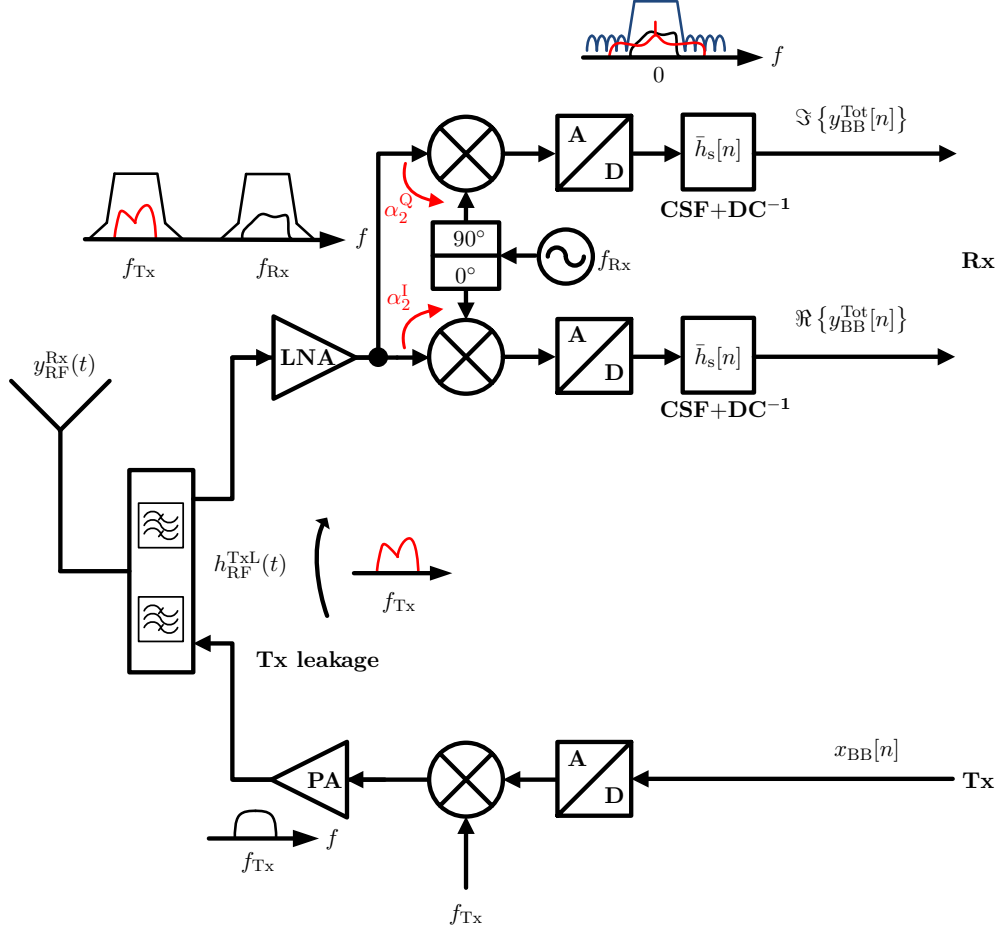


Figure 2.11: Block diagram depicting an RF transceiver operating in FDD mode which experiences a second-order intermodulation distortion in the I-, and Q-path of the receiver due to the transmitter leakage signal and the Rx mixer RF-to-LO terminal coupling.

with the mixer RF-to-LO terminal coupling coefficient $\alpha_2 = \alpha_2^I + j\alpha_2^Q$. With $\alpha_2^I \neq \alpha_2^Q$ a different scaling of the I-, and Q-path IMD2 interference is assumed [23, 6].

$$\begin{aligned}
 y_{RF,mixer}^{Tot}(t) &= y_{RF,LNA}^{Tot}(t)\alpha_1^I \cos(2\pi f_{Rx}t) \\
 &+ y_{RF,LNA}^{Tot}(t) [\alpha_2^I y_{RF,LNA}^{Tot}(t)] \\
 &- jy_{RF,LNA}^{Tot}(t)\alpha_1^Q \sin(2\pi f_{Rx}t) \\
 &+ jy_{RF,LNA}^{Tot}(t) [\alpha_2^Q y_{RF,LNA}^{Tot}(t)] \\
 &= y_{RF,LNA}^{Tot}(t)\alpha_1 e^{-j2\pi f_{Rx}t} + \alpha_2 y_{RF,LNA}^{Tot}(t)^2
 \end{aligned} \tag{2.55}$$

Assuming a direct conversion receiver, and using the identity

$$\Re\{\eta e^{j\kappa}\} = \frac{1}{2}(\eta e^{j\kappa} + \eta^* e^{-j\kappa}), \tag{2.56}$$

the total mixer output signal by neglecting the signal content which falls outside the BB bandwidth becomes

$$\begin{aligned}
 y_{\text{RF,mixer}}^{\text{Tot}}(t) &= \alpha_1 \frac{A_{\text{LNA}}}{2} y_{\text{BB}}^{\text{Rx}}(t) + \alpha_1 \frac{A_{\text{LNA}}}{2} v_{\text{BB}}(t) \\
 &+ \frac{\alpha_2 A_{\text{LNA}}^2}{2} \left[|A_{\text{PA}} (x_{\text{BB}}(t) * h_{\text{BB}}^{\text{TxL}}(t))|^2 + |y_{\text{BB}}^{\text{Rx}}(t)|^2 \right. \\
 &\left. + |v_{\text{BB}}(t)|^2 + 2\Re \{ y_{\text{BB}}^{\text{Rx}}(t) v_{\text{BB}}^*(t) \} \right]. \tag{2.57}
 \end{aligned}$$

The third term in (2.57) contains the squared envelope of the TxL signal denoted as the IMD2 interference. As in critical, e.g., cell edge scenarios the Rx and noise signal are much weaker than the TxL signal, the last three terms in (2.57) may be neglected [6, 7]. The resulting total received discrete time BB signal

$$\begin{aligned}
 y_{\text{BB}}^{\text{Tot}}[n] &= \alpha_1 \frac{A_{\text{LNA}}}{2} y_{\text{BB}}^{\text{Rx}}[n] * \bar{h}_s[n] + \alpha_1 \frac{A_{\text{LNA}}}{2} v_{\text{BB}}[n] * \bar{h}_s[n] \\
 &+ \underbrace{\frac{\alpha_2}{2} |A_{\text{LNA}} A_{\text{PA}} (x_{\text{BB}}[n] * h_{\text{BB}}^{\text{TxL}}[n])|^2}_{y_{\text{BB}}^{\text{IMD2}}[n]} * \bar{h}_s[n], \tag{2.58}
 \end{aligned}$$

contains the BB IMD2 interference $y_{\text{BB}}^{\text{IMD2}}[n]$ and includes the DC cancellation and channel-select filtering using the combined impulse response $\bar{h}_s[n]$. In (2.58) it can be observed, that the IMD2 interference is generated by the squared envelope of the BB equivalent TxL signal. This squared envelope contains a DC and has twice the Tx signal bandwidth (BW). The DC is eliminated in the receiver by its mixed-signal DC cancellation and the BW is reduced to the LTE signal BW by the CSF.

2.3.6 Higher Even-Order Intermodulation Interferences

Cascading the third-order nonlinearity of the switch/LNA (Section 2.3.2), with the second-order nonlinearity of the mixer (Section 2.3.5), additional nonlinear interference terms occur. The output signal of the LNA including a third-order polynomial nonlinearity and by neglecting the intermodulation products of the Rx and noise signal becomes

$$\begin{aligned}
 y_{\text{RF,LNA}}^{\text{Tot}}(t) &= A_{\text{LNA}} y_{\text{RF}}^{\text{TxL}}(t) + \alpha_2^{\text{LNA}} [y_{\text{RF}}^{\text{TxL}}(t)]^2 + \alpha_3^{\text{LNA}} [y_{\text{RF}}^{\text{TxL}}(t)]^3 \\
 &\quad + A_{\text{LNA}} [y_{\text{RF}}^{\text{Rx}}(t) + v_{\text{RF}}(t)] \\
 &= \alpha_2^{\text{LNA}} \frac{A_{\text{PA}}^2}{2} |x_{\text{BB}}(t) * h_{\text{BB}}^{\text{TxL}}(t)|^2 \\
 &\quad + A_{\text{LNA}} \frac{A_{\text{PA}}}{2} \left([x_{\text{BB}}(t) * h_{\text{BB}}^{\text{TxL}}(t)] e^{j2\pi f_{\text{Tx}}t} + [x_{\text{BB}}(t) * h_{\text{BB}}^{\text{TxL}}(t)]^* e^{-j2\pi f_{\text{Tx}}t} \right) \\
 &\quad + \alpha_3^{\text{LNA}} \frac{3A_{\text{PA}}^3}{8} \left([x_{\text{BB}}(t) * h_{\text{BB}}^{\text{TxL}}(t)] |x_{\text{BB}}(t) * h_{\text{BB}}^{\text{TxL}}(t)|^2 e^{j2\pi f_{\text{Tx}}t} \right. \\
 &\quad \left. + [x_{\text{BB}}(t) * h_{\text{BB}}^{\text{TxL}}(t)]^* |x_{\text{BB}}(t) * h_{\text{BB}}^{\text{TxL}}(t)|^2 e^{-j2\pi f_{\text{Tx}}t} \right) \\
 &\quad + \alpha_2^{\text{LNA}} \frac{A_{\text{PA}}^2}{4} \left([x_{\text{BB}}(t) * h_{\text{BB}}^{\text{TxL}}(t)]^2 e^{j4\pi f_{\text{Tx}}t} + [x_{\text{BB}}(t) * h_{\text{BB}}^{\text{TxL}}(t)]^{*2} e^{-j4\pi f_{\text{Tx}}t} \right) \\
 &\quad + \alpha_3^{\text{LNA}} \frac{A_{\text{PA}}^3}{8} \left([x_{\text{BB}}(t) * h_{\text{BB}}^{\text{TxL}}(t)]^3 e^{j6\pi f_{\text{Tx}}t} + [x_{\text{BB}}(t) * h_{\text{BB}}^{\text{TxL}}(t)]^{*3} e^{-j6\pi f_{\text{Tx}}t} \right) \\
 &\quad + A_{\text{LNA}} [y_{\text{RF}}^{\text{Rx}}(t) + v_{\text{RF}}(t)].
 \end{aligned} \tag{2.59}$$

With the mixer RF-to-LO terminal coupling coefficient $\alpha_2^{\text{Mix}} = \alpha_2^I + j\alpha_2^Q$ for the I- and Q-branch of the IQ mixer, the down-conversion gain α_1^{Mix} ⁵, and the DC feed-through gain $\alpha_{\text{DC}}^{\text{Mix}} = \alpha_{\text{DC}}^I + j\alpha_{\text{DC}}^Q$, the output signal of the mixer becomes

$$y_{\text{RF,mixer}}^{\text{Tot}}(t) = \alpha_{\text{DC}}^{\text{Mix}} y_{\text{RF,LNA}}^{\text{Tot}}(t) + y_{\text{RF,LNA}}^{\text{Tot}}(t) \alpha_1^{\text{Mix}} e^{-j2\pi f_{\text{Rx}}t} + \alpha_2^{\text{Mix}} y_{\text{RF,LNA}}^{\text{Tot}}(t)^2. \tag{2.60}$$

Neglecting the signal components which are outside the CSF bandwidth, the total received BB signal may be described by

$$\begin{aligned}
 y_{\text{RF,mixer}}^{\text{Tot}}(t) &= \frac{A_{\text{PA}}^2}{2} (\alpha_2^{\text{Mix}} A_{\text{LNA}}^2 + \alpha_2^{\text{LNA}} \alpha_{\text{DC}}^{\text{Mix}}) |x_{\text{BB}}(t) * h_{\text{BB}}^{\text{TxL}}(t)|^2 \\
 &\quad + \alpha_2^{\text{Mix}} \frac{A_{\text{PA}}^4}{8} \left[3(\alpha_2^{\text{LNA}})^2 + 6\alpha_3^{\text{LNA}} A_{\text{LNA}} \right] |x_{\text{BB}}(t) * h_{\text{BB}}^{\text{TxL}}(t)|^4 \\
 &\quad + \alpha_2^{\text{Mix}} (\alpha_3^{\text{LNA}})^2 \frac{10A_{\text{PA}}^6}{32} |x_{\text{BB}}(t) * h_{\text{BB}}^{\text{TxL}}(t)|^6 \\
 &\quad + \alpha_1^{\text{Mix}} \frac{A_{\text{LNA}}}{2} y_{\text{BB}}^{\text{Rx}}(t) + \alpha_1^{\text{Mix}} \frac{A_{\text{LNA}}}{2} v_{\text{BB}}(t).
 \end{aligned} \tag{2.61}$$

⁵An identical down-conversion gain for the I-, and Q-branch is assumed.

The resulting total received discrete time BB signal after the combined channel-select-, and DC-filtering using $\bar{h}_s[n] = h_s[n] * h_{DC}[n]$ is approximated by

$$\begin{aligned}
 y_{BB}^{\text{Tot}}[n] = & \left[\frac{A_{PA}^2}{2} (\alpha_2^{\text{Mix}} A_{LNA}^2 + \alpha_2^{\text{LNA}} \alpha_{DC}^{\text{Mix}}) |x_{BB}[n] * h_{BB}^{\text{TxL}}[n]|^2 \right] * \bar{h}_s[n] \\
 & + \left[\alpha_2^{\text{Mix}} \frac{A_{PA}^4}{8} \left[3 (\alpha_2^{\text{LNA}})^2 + 6 \alpha_3^{\text{LNA}} A_{LNA} \right] |x_{BB}[n] * h_{BB}^{\text{TxL}}[n]|^4 \right] * \bar{h}_s[n] \\
 & + \left[\alpha_2^{\text{Mix}} (\alpha_3^{\text{LNA}})^2 \frac{10 A_{PA}^6}{32} |x_{BB}[n] * h_{BB}^{\text{TxL}}[n]|^6 \right] * \bar{h}_s[n] \\
 & + \left[\alpha_1^{\text{Mix}} \frac{A_{LNA}}{2} y_{BB}^{\text{Rx}}[n] + \alpha_1^{\text{Mix}} \frac{A_{LNA}}{2} v_{BB}[n] \right] * \bar{h}_s[n].
 \end{aligned} \tag{2.62}$$

The first term in (2.62) corresponds to the IMD2 interference. It is generated by the second-order nonlinearity of the mixer and the combination of the second-order nonlinearity of the LNA and the DC feed-through of the mixer. The second term is the fourth-order intermodulation distortion (IMD4) interference which is a combination of the second-order-, and third-order nonlinearity of the LNA and the second-order nonlinearity of the mixer. The third term is the sixth-order intermodulation distortion (IMD6) interference which is generated by the third-order nonlinearity of the LNA in combination with the second-order nonlinearity of the mixer.

2.4 Quantification of the IMD2 Interference

2.4.1 Two-Tone IIP2 Derivation

The second-order intermodulation product (IM2) is created by the quadratic nonlinearity of the mixer [38]. At the output of the mixer, undesired frequency content is generated but only the signal part which falls into the BB interferes with the desired Rx signal. The second-order receiver nonlinearity is typically specified by the two-tone second-order input intercept point (IIP2) value [39]. This value determines at which input power level the total input power $P_{in} = A^2/Z_0$ of the two-tone (2t) RF input signal

$$x(t) = A \cos(2\pi f_1 t) + A \cos(2\pi f_2 t) \tag{2.63}$$

equals the total mixer input-referred⁶ IM2 power. It also allows the calculation of the mixer input-referred two-tone IM2 signal power by the well known formula [39]

$$P_{\text{IM2,dBm}}^{\text{Tot,2t}} = 2P_{\text{in,dBm}} - \text{IIP2}_{\text{dBm}} \tag{2.64}$$

⁶The IMD2 signal power which occurs at the output of the nonlinear mixer may be related to an equivalent power at the input of the mixer which (when amplified with the linear power gain α_1^2 of the mixer) generates the same IMD2 output power. This so-called input-referred IMD2 power is obtained by dividing the mixer IMD2 output power $P_{\text{IM2}}^{\text{Tot,2t,OR}}$ by α_1^2 .

derived in the following. The mixer output signal

$$\begin{aligned}
 y(t) &= x(t)\alpha_1 e^{-j2\pi f_{Rx}t} + \alpha_2 x(t)^2 \\
 &= \underbrace{x(t)\alpha_1 e^{-j2\pi f_{Rx}t}}_{y_{\text{lin}}(t)} + \underbrace{\frac{\alpha_2}{2} A^2 \{\cos(4\pi f_1 t) + \cos(4\pi f_2 t)\}}_{2^{\text{nd}} \text{ harmonics}} \\
 &\quad + \underbrace{\alpha_2 A^2 \{1 + \cos(2\pi [f_1 + f_2] t) + \cos(2\pi [f_2 - f_1] t)\}}_{y_{\text{IM2}}^{\text{Tot,2t}}(t)}
 \end{aligned} \tag{2.65}$$

consists of the linearly down-converted input signal $y_{\text{lin}}(t)$, the 2nd order harmonics, and the two-tone IM2 signal. The resulting mixer output-referred (OR) IM2 signal power becomes

$$P_{\text{IM2}}^{\text{Tot,2t,OR}} = \frac{E \{ y_{\text{IM2}}^{\text{Tot,2t}}(t)^2 \}}{Z_0} = \frac{2\alpha_2^2 A^4}{Z_0}. \tag{2.66}$$

At the IIP2 input power it holds that the input power P_{in} equals the input-referred IM2 power:

$$P_{\text{in}} \stackrel{!}{=} \frac{1}{\alpha_1^2} P_{\text{IM2}}^{\text{Tot,2t,OR}} = \frac{2\alpha_2^2 A^4}{\alpha_1^2 Z_0} \tag{2.67}$$

Inserting the input signal amplitude $A_{\text{IIP2}}^2 = P_{\text{in,IIP2}} Z_0$ and solving for α_2 results in

$$\alpha_2 = \sqrt{\frac{\alpha_1^2}{2 P_{\text{in,IIP2}} Z_0}} = \sqrt{\frac{\alpha_1^2}{2 \text{IIP2}_W Z_0}} = 0.0316 \frac{1}{\text{V}}, \tag{2.68}$$

for a down-conversion gain of 0 dBm ($\alpha_1 = 1$), a typical mixer IIP2 of +40dBm [40, 6], and the network impedance $Z_0 = 50\Omega$. By rearranging (2.68), the corresponding IIP2 in watts becomes

$$\text{IIP2}_W = \frac{\alpha_1^2}{2\alpha_2^2 Z_0}. \tag{2.69}$$

The mixer input-referred total IM2 power may be expressed by the input power P_{in} and the IIP2_W value:

$$P_{\text{IM2}}^{\text{Tot,2t}} = \frac{1}{\alpha_1^2} P_{\text{IM2}}^{\text{Tot,2t,OR}} = \frac{2\alpha_2^2 A^4}{\alpha_1^2 Z_0} = \frac{P_{\text{in}}^2}{\text{IIP2}_W} \tag{2.70}$$

Finally, (2.70) leads to the input-referred IM2 power in dBm

$$P_{\text{IM2,dBm}}^{\text{Tot,2t}} = 2P_{\text{in,dBm}} - \text{IIP2}_{\text{dBm}}. \tag{2.71}$$

The derivation of α_2 from a given two-tone IIP2 value is required for the simulations in Chapter 5 where a BB equivalent IMD2 interference in the time domain is generated.

2.4.2 Modulated IMD2 Distortion

In this section, the TxL signal induced IMD2 signal power is derived to be able to bring it in relation with the two-tone IM2 power $P_{\text{IM2}}^{\text{Tot},2t}$ (2.71). As a first step we need to understand the relationship between the RF TxL signal power $P_{\text{RF}}^{\text{TxL}}$ and the corresponding BB equivalent TxL signal power $P_{\text{BB}}^{\text{TxL}}$ at the mixer input (LNA output). The RF TxL signal at the LNA output is

$$y_{\text{RF,LNA}}^{\text{TxL}}(t) = A_{\text{LNA}} A_{\text{PA}} \Re \left\{ [x_{\text{BB}}(t) * h_{\text{BB}}^{\text{TxL}}(t)] e^{j2\pi f_{\text{Tx}} t} \right\}, \quad (2.72)$$

which has the power

$$\begin{aligned} P_{\text{in}} = P_{\text{RF,LNA}}^{\text{TxL}} &= \frac{1}{Z_0} E \left\{ y_{\text{RF,LNA}}^{\text{TxL}}(t)^2 \right\} \\ &= \frac{1}{Z_0} E \left\{ \left(A_{\text{LNA}} A_{\text{PA}} \Re \left\{ [x_{\text{BB}}(t) * h_{\text{BB}}^{\text{TxL}}(t)] e^{j2\pi f_{\text{Tx}} t} \right\} \right)^2 \right\} \\ &= \frac{1}{2} \frac{1}{Z_0} E \left\{ \underbrace{A_{\text{LNA}} A_{\text{PA}} |x_{\text{BB}}(t) * h_{\text{BB}}^{\text{TxL}}(t)|^2}_{=P_{\text{BB,LNA}}^{\text{TxL}}} \right\}. \end{aligned} \quad (2.73)$$

It can be observed, that the RF TxL signal power is half of the corresponding complex valued BB equivalent TxL signal power⁷. The total IMD2 interference signal at the output of the mixer according to (2.58) (with twice the Tx signal BW and including the DC) is

$$y_{\text{BB}}^{\text{IMD2}}(t) = \frac{\alpha_2}{2} |A_{\text{LNA}} A_{\text{PA}} x_{\text{BB}}(t) * h_{\text{BB}}^{\text{TxL}}(t)|^2. \quad (2.74)$$

The resulting mixer OR IMD2 interference power becomes

$$\begin{aligned} P_{\text{IMD2}}^{\text{Tot,mod,OR}} &= \frac{1}{Z_0} E \left\{ \left(\frac{\alpha_2}{2} |A_{\text{LNA}} A_{\text{PA}} x_{\text{BB}}(t) * h_{\text{BB}}^{\text{TxL}}(t)|^2 \right)^2 \right\} \\ &= \frac{1}{Z_0} \frac{\alpha_2^2}{4} E \left\{ |A_{\text{LNA}} A_{\text{PA}} x_{\text{BB}}(t) * h_{\text{BB}}^{\text{TxL}}(t)|^4 \right\}. \end{aligned} \quad (2.75)$$

By using the identity

$$E \{ X^4 \} = 2E \{ X^2 \}^2 \quad (2.76)$$

which holds for a scalar complex valued and zero-mean Gaussian distributed random variable X [41, 42, 43], the OR IMD2 power becomes

$$P_{\text{IMD2}}^{\text{Tot,mod,OR}} = \frac{1}{Z_0} \frac{\alpha_2^2}{2} E \left\{ |A_{\text{LNA}} A_{\text{PA}} x_{\text{BB}}(t) * h_{\text{BB}}^{\text{TxL}}(t)|^2 \right\}^2. \quad (2.77)$$

⁷Assuming an RF TxL signal power of -7 dBm, the corresponding power of the complex BB equivalent TxL signal is -4 dBm.

2 Interferences in FDD RF Transceivers

At the input power $P_{\text{in,IIP2}}$ (2.73), which has the value of the IIP2_W, the input power equals the input-referred IMD2 interference power:

$$\begin{aligned}
 P_{\text{in,IIP2}} &\stackrel{!}{=} \frac{1}{\alpha_1^2} P_{\text{IMD2}}^{\text{Tot,mod,OR}} \\
 \frac{1}{2} \frac{1}{Z_0} E \left\{ |A_{\text{LNA}} A_{\text{PA}} x_{\text{BB}}(t) * h_{\text{BB}}^{\text{TxL}}(t)|^2 \right\} &= \frac{\alpha_2^2}{2\alpha_1^2 Z_0} E \left\{ |A_{\text{LNA}} A_{\text{PA}} x_{\text{BB}}(t) * h_{\text{BB}}^{\text{TxL}}(t)|^2 \right\}^2 \\
 \frac{1}{Z_0} &= \frac{\alpha_2^2}{\alpha_1^2} \frac{1}{Z_0} E \left\{ |A_{\text{LNA}} A_{\text{PA}} x_{\text{BB}}(t) * h_{\text{BB}}^{\text{TxL}}(t)|^2 \right\} \\
 &\qquad\qquad\qquad = 2P_{\text{in,IIP2}} = 2\text{IIP2}_W
 \end{aligned} \tag{2.78}$$

Rearranging (2.78) leads to the IIP2 value

$$\text{IIP2}_W = \frac{\alpha_1^2}{2\alpha_2^2 Z_0}, \tag{2.79}$$

which is exactly the same as in the two-tone signal case. The resulting mixer input-referred IMD2 interference power (with twice the Tx signal BW and including the DC) which is generated by the modulated RF TxL signal becomes

$$P_{\text{IMD2,dBm}}^{\text{Tot,mod}} = 2P_{\text{RF,LNA}}^{\text{TxL}} - \text{IIP2}_{\text{dBm}}. \tag{2.80}$$

However, care has to be taken in simulations where the BB equivalent signals are used instead of the RF signals. It is quite common [44]⁸ to set the power of the BB equivalent TxL signals to the power of the RF TxL signal (not scaled to twice of the corresponding RF TxL signal power as stated in (2.73)). Then, the IMD2 signal power obtained in the BB equivalent simulation corresponds to

$$\begin{aligned}
 P_{\text{IMD2,dBm}}^{\text{Tot,mod}} &= 2(P_{\text{RF,LNA}}^{\text{TxL}} - 3 \text{ dB}) - \text{IIP2}_{\text{dBm}} \\
 &= 2P_{\text{RF,LNA}}^{\text{TxL}} - \text{IIP2}_{\text{dBm}} - 6 \text{ dB}.
 \end{aligned} \tag{2.81}$$

Because the TxL signal is typically non-Gaussian distributed, the correction factor CF_{dist} is introduced which accounts for the violation of (2.76). The resulting IMD2 signal power becomes

$$P_{\text{IMD2,dBm}}^{\text{Tot,mod}} = 2P_{\text{RF,LNA}}^{\text{TxL}} - \text{IIP2}_{\text{dBm}} - 6 \text{ dB} - \text{CF}_{\text{dist}}. \tag{2.82}$$

The reduction of the total IMD2 power in case of non-Gaussian distributed Tx signals (e.g. orthogonal frequency-division multiplexing (OFDM) or single-carrier frequency-division multiple access (SC-FDMA) modulated) is summarized in Table 2.2. After DC-, and channel-select filtering, the modulated IMD2 interference power is further reduced by 6 dB if the total IMD2 signal spectrum with twice the Tx BW is assumed flat and has half of the power at DC. If the spectrum is non-flat, which typically is the case, the IMD2 power needs to be corrected by the factor CF_{flat} which leads to the final estimate

$$P_{\text{IMD2,dBm}}^{\text{Tot,mod,CSF}} = 2P_{\text{RF,LNA}}^{\text{TxL}} - \text{IIP2}_{\text{dBm}} - 12 \text{ dB} - \text{CF}_{\text{dist}} - \text{CF}_{\text{flat}} \tag{2.83}$$

⁸In this publication, the Tx signal induced IMD2 signal power is compared between a two-tone-, and a modulated Tx signal. The modulated RF Tx signal power is set to half of the two-tone RF signal power. This implies that the modulated complex BB equivalent Tx signal has the same power as the two-tone RF signal (see Fig. 2 in [44]).

Table 2.2: Reduction of IMD2 power due to non-Gaussian distributed TxL signal: Full allocated 10 MHz Tx signal

Tx distribution	Gaussian	OFDM	SC-FDMA		
			QPSK	16QAM	64QAM
CF _{dist} (dB)	0	0	0.72	0.51	0.48

of the DC-, and channel-select filtered IMD2 interference power. In [39, 45], the equation

$$P_{\text{IMD2,dBm}}^{\text{Tot,mod,CSF}} = 2P_{\text{RF,LNA}}^{\text{TxL}} - \text{IIP2}_{\text{dBm}} - \text{CF}, \quad (2.84)$$

is used to estimate the DC-, and channel-select filtered IMD2 power, where the correction factor CF is obtained by simulations and verified by measurements, but not derived in detail as in (2.83). The estimated CF for W-CDMA Tx signals is 13.7 dB and 15.7 dB in [39] and [45], respectively. The authors in [44] derived the IIP2 requirements for 4G handset receivers by using a combined correction factor of 11 dB and 13.7 dB for 10 MHz SC-FDMA (LTE) and WCDMA modulated Tx signals, respectively. It has to be mentioned, that in [44] the ideal Tx signals are used⁹ to obtain the correction factors. With (2.83) it is possible to estimate the IMD2 power and thereby the resulting Rx signal-to-interference-plus-noise ratio (SINR)

$$\begin{aligned} \text{SINR}_{\text{dB}} &= 10 \log_{10} \left(\frac{P_{\text{Rx}}}{P_{\text{IMD2}}^{\text{Tot,mod,CSF}} + P_n} \right) \\ &= P_{\text{Rx,dBm}} - 10 \log_{10} \left(\frac{P_{\text{IMD2}}^{\text{Tot,mod,CSF}} + P_n}{1\text{mW}} \right) \end{aligned} \quad (2.85)$$

when the Tx power increases. Assuming an Rx signal with -90 dBm with a signal-to-noise ratio (SNR) of 10 dB, an SC-FDMA LTE Tx signal with QPSK modulation (CF_{dist} = 0.72 dBm), LNA gain of 20 dB, an average duplexer isolation of 50 dB, mixer IIP2 of +40 dBm and using CF_{flat} = 0.67 dBm (duplexer dependent), the resulting Rx SINR with increasing Tx power may be estimated as summarized in Table 2.3. The combined correction factor is obtained by CF = 12 dB + CF_{dist} + CF_{flat} = 13.4 dB.

Table 2.3: Drop of the Rx SINR due to the Tx induced IMD2 interference which is generated by a fully allocated 10 MHz LTE Tx signal

$P_{\text{BB}}^{\text{Tx}}$ (dBm)	0	6	12	18	23
$P_{\text{IMD2}}^{\text{Tot,mod,CSF}}$ (dBm)	-113.4	-101.4	-89.4	-77.4	-67.4
SINR (dB)	9.99	9.96	9.52	5.5	-2.84

⁹No frequency-selective duplexer Tx-to-Rx stop-band response is used to generate a TxL signal.

2.4.3 IIP2 Characterization

The receiver IIP2 is characterized by using two cosine signals at the input of the nonlinear mixer with the frequencies f_1 and f_2 of equal amplitude A and the combined power $P_{\text{in},2\text{t}}$. The resulting total IMD2 power in dBm generated at DC, $f_1 + f_2$ and $f_2 - f_1$ at the output of the mixer can be calculated by $P_{\text{IM2}}^{\text{Tot},2\text{t}} = 2P_{\text{in},2\text{t}} - \text{IIP2}$ [45]. Here, half of the total IMD2 power falls to DC, and one quarter each to $f_1 + f_2$ and $f_2 - f_1$. To characterize the IIP2 in a zero-IF receiver, the frequencies f_1 and f_2 are chosen such that $f_2 - f_1$ falls within the CSF bandwidth. Thereby the power $P_{\text{IM2}}^{f_2-f_1}$ at the frequency $f_2 - f_1$ is measured and the IIP2 is determined by $\text{IIP2} = 2P_{\text{in},2\text{t}} - P_{\text{IM2}}^{f_2-f_1} - 6$ dB.

2.4.4 Severity of the IMD2 Interference

For modulated TxL signals, the BB IMD2 signal power is modulation dependent and further reduced by the DC cancellation and channel-select filtering. Also the shape of the duplexer stop-band frequency response has an influence of the resulting BB IMD2 signal power. All this factors may be considered in a combined correction factor as shown in Section 2.4.2 [39, 44]. Although the DC-, and channel-select filtering in the receiver reduces the IMD2 BB interference power by 6 dB in the two-tone signal case [45], and by about 13.4 dB [7, 39, 44] in the case of modulated Tx signals, the left-over IMD2 interference may lead to a severe SNR degradation of the wanted Rx signal in reference sensitivity cases [3]. Assuming a transmitter power of 23 dBm at the antenna, and an average Tx-to-Rx duplexer isolation at the transmit frequency of 50 dB, the TxL signal power at the input of the receiver is $P_{\text{RF}}^{\text{TxL}} = 23 \text{ dBm} - 50 \text{ dB} = -27 \text{ dBm}$. After amplification with the LNA gain which is assumed as 20 dB, the RF TxL signal power increases to $P_{\text{RF}}^{\text{TxL}} = -7 \text{ dBm}$ at the input of the nonlinear mixer. The IIP2 value of typical RF mixers is between 50 dBm and 70 dBm [46, 47]. Assuming an IIP2 of 60 dBm, the resulting BB IMD2 power with a fully allocated LTE10 QPSK modulated transmission and the determined correction factor of $\text{CF} = 13.4 \text{ dB}$ is $P_{\text{IM2}}^{\text{CSF,LTE}} = 2P_{\text{RF}}^{\text{TxL}} - \text{IIP2} - \text{CF} = -87.4 \text{ dBm}$ [7]. In an LTE10 reference sensitivity case, the wanted signal power at the antenna can be as low as -97 dBm [3]. The thermal noise power within 10 MHz bandwidth is -104.5 dBm and the assumed receiver noise figure (NF) is 4.5 dB which results in a receiver noise floor at -100 dBm. After amplification with 20 dB LNA gain, the wanted signal power is -77 dBm and the noise floor at -80 dBm corresponding to an Rx SNR of 3 dB. The SNR drops from 3 dB to an SINR of 2.27 dB due to the IMD2 interference assuming an IIP2 of +60 dBm. This may be examined using (2.85). In case of a reduced IIP2 of 55 dBm / 50 dBm, the SINR drops even further to 1 dB / -1.4 dB, respectively. Table 2.3 summarizes the SINR drop with respect to increasing Tx power levels for an IIP2 of 40 dBm, the Rx power level of -90 dBm and the Rx SNR of 10 dB. Fig. 2.12 depicts the spectrum of the frequency selective BB equivalent TxL signal $y_{\text{BB}}^{\text{TxL}}$ which generates the complex valued IMD2 interference $y_{\text{BB}}^{\text{IMD2}}$ by a coupling between the RF-to-LO terminals of the I-, and Q-path mixer. The total received signal $y_{\text{BB}}^{\text{Tot}}$ contains the wanted Rx signal $y_{\text{BB}}^{\text{Rx}}$ which is degraded by the IMD2 interference and the noise. Appendix A.1 provides a description of the y-axis scaling (dBm/15 kHz) which is used in Fig. 2.12.

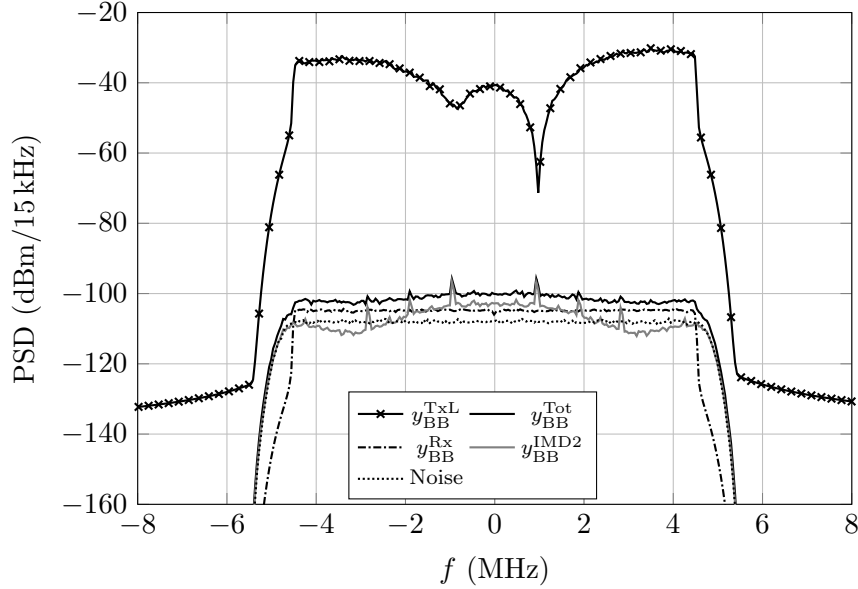


Figure 2.12: Equivalent BB spectrum of the frequency-selective Tx leakage signal $y_{\text{BB}}^{\text{TxL}}$ (the corresponding passband signal is located at f_{Tx}) and the total received signal $y_{\text{BB}}^{\text{Tot}}$ after amplification with 20 dB LNA gain. The wanted Rx signal with SNR = 3 dB, and the receiver noise floor after amplification with 20 dB LNA gain are at -77 dBm and -80 dBm $\hat{=}$ -108.2 dBm/15 kHz respectively. The total received signal contains the DC-, and channel-select filtered IMD2 interference for $P_{\text{Tx}} = 23$ dBm and an assumed IIP2 of 50 dBm.

2.5 Modulated Spurs in Split-LNA Configuration

As already described in Section 2.1.2, the modulated spur interference may be generated by two mechanisms. The first mechanism occurs in inter-band CA scenarios where the LO-LO cross-talk may create spurs which down-convert the TxL signal into the BB. This section presents a BB equivalent model of the modulated spur interference which is generated in an intra-band CA scenario where a split-LNA is used. Additionally, the Tx/Rx phase-noise in combination with 25% duty-cycle current driven passive mixers in the receivers is included. The derived model is published in the journal [16] where the pure digital and the mixed-signal modulated spur cancellation are compared. In this publication it is shown that the mixed-signal approach using a serial-mixing approach is able to cancel the modulated spur interference including the PN of the transmitter and the Rx LOs. The latter is important because the combined PN of both involved Rx LOs is included in the spur which down-converts the TxL signal. Fig. 2.13 depicts a simplified transceiver block diagram including the duplexer which connects the transmitter and the two receive chains with split-LNA to the common antenna. Both receivers are connected to the same duplexer port and are therefore receiving data in the same LTE band. To simplify the block diagram, only the 25% duty-cycle mixers without ADCs and CSFs is depicted. In the following explanation it is assumed that receiver Rx1 is the aggressor and Rx2 is the victim. This means that the modeling describes the modulated spur interference in receiver Rx2.

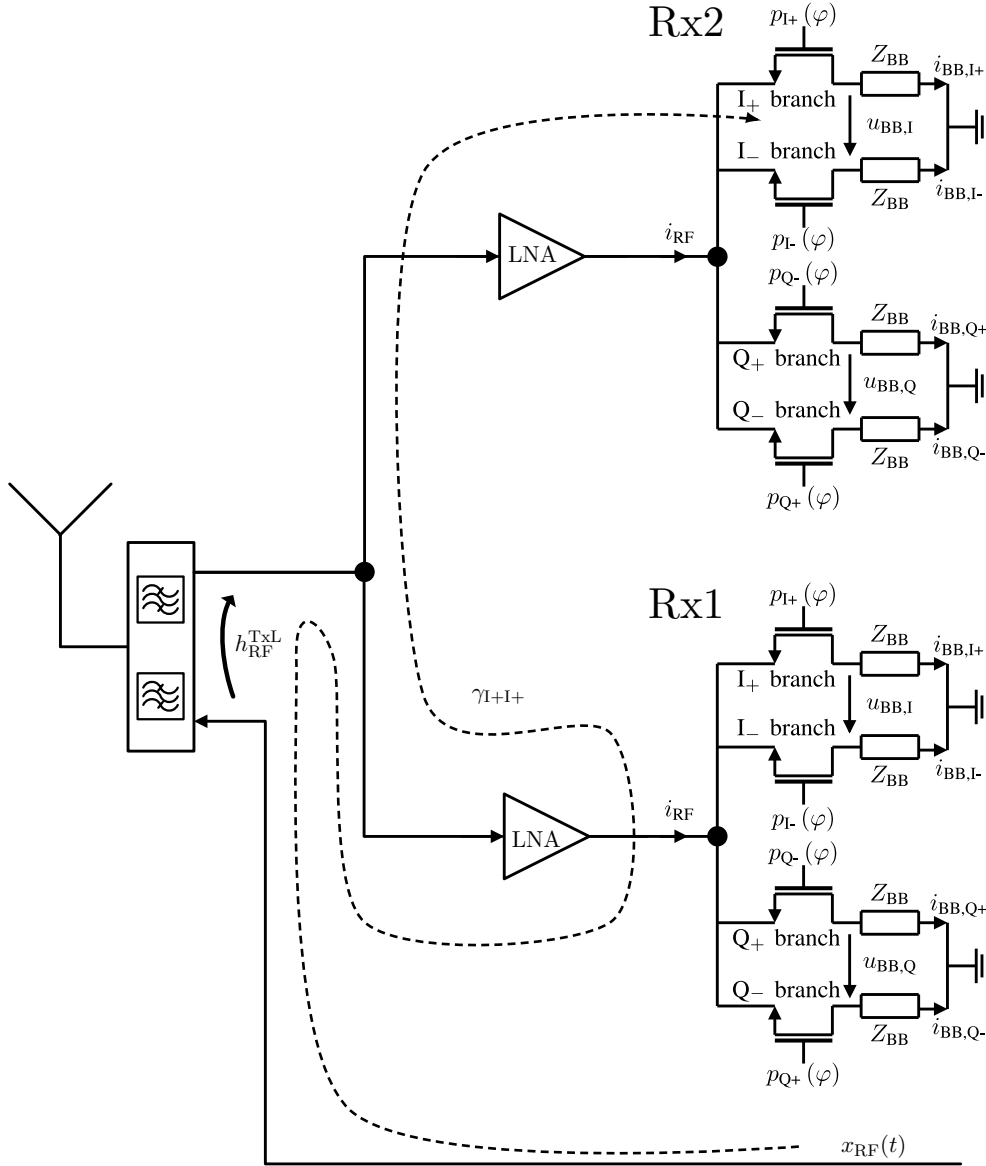


Figure 2.13: Modulated spur interference caused by the lack of LNA reverse isolation and the harmonics of the 25% duty-cycle mixers in split-LNA configuration. The dashed line indicates the coupling path of the Rx1 mixer (aggressor) branches to the I_+ branch of the Rx2 mixer (victim).

The TxL signal is amplified by the Rx1 LNA and mixed by the four individual branches of the 25% duty-cycle Rx1 mixer. Each mixer branch contains harmonics which are up-/down-converting the TxL signal. This up-/down-converted TxL signal is reflected back to the input of the LNA because only the signal content which is mixed to the BB (the Rx signal) experiences the impedance matching with the impedance Z_{BB} . The reflected signal leaks into receiver Rx2 where it is amplified by the Rx2 LNA and mixed into the BB by an appropriate harmonic of LO_2 . Consequently, the TxL signal is down-converted into the BB of Rx2 where it degrades the receiver performance. The presented modeling

is carried out for 25% duty-cycle mixers [29], although the derivation may be easily adapted for 50% duty-cycle mixers. The derived model shows, that the equivalent complex valued spur, which down-converts the TxL signal to the BB, has a gain-imbalance due to the different coupling factors between each of the 8 mixer phases of the two 25% duty-cycle CA mixers. Consequently, the modulated spur interference consists of a main and an image interference in the digital baseband.

2.5.1 Phase-Noise Model of the 25% Duty-Cycle Mixer

To be able to derive a mathematical model of the modulated spur, a detailed spur model including the jitter in the pulse duration and variations in the LO period is needed. The Fourier coefficients c_k of the 25% duty-cycle mixer phase waveform $p_{I+}(t)$ (introduced in Section 2.2, Fig. 2.5) with amplitude A including the jitter 2δ in the pulse duration and the LO phase variation φ_{LO} are

$$\begin{aligned} c_k &= \frac{1}{T_{LO}} \int_0^{T_{LO}} \tilde{p}_{I+}(t) e^{-jk(2\pi f_{LO}t + \varphi_{LO})} dt \\ &= \frac{1}{T_{LO}} \int_{-\delta}^{T_{LO}/4 + \delta} A e^{-jk(2\pi f_{LO}t + \varphi_{LO})} dt \\ &= A \left[\frac{1}{4} + 2 \frac{\delta}{T_{LO}} \right] e^{-jk\frac{\pi}{4}} \text{sinc} \left(k \frac{\pi}{4} + k 2\pi \frac{\delta}{T_{LO}} \right) e^{-jk\varphi_{LO}}. \end{aligned} \quad (2.86)$$

A detailed derivation of the Fourier coefficients c_k including the PN may be found in Appendix A.2. Allowing slow variations of δ and φ_{LO} , the Fourier coefficients including amplitude- and phase-noise may be expressed as

$$c_k(t) = A \left[\frac{1}{4} + 2 \frac{\delta(t)}{T_{LO}} \right] e^{-jk\frac{\pi}{4}} \text{sinc} \left(k \frac{\pi}{4} + k 2\pi \frac{\delta(t)}{T_{LO}} \right) e^{-jk\varphi_{LO}(t)}. \quad (2.87)$$

The resulting model of the I+ phase in the 25% duty-cycle mixer including amplitude-, and phase-noise is

$$\tilde{p}_{I+}(t) = \sum_{k=-\infty}^{\infty} c_k(t) e^{jk 2\pi f_{LO} t}. \quad (2.88)$$

The model for the I-,Q+ and Q- mixer phases of LO₁ and LO₂ are presented in Appendix A.2.

2.5.2 Spur Modeling

In a CA receiver including two receivers in split-LNA configuration, the coupling and mixing between the I+ branch mixer waveform of aggressor LO₁

$$p_{LO_1, I+}(t) = \sum_{m_1=-\infty}^{\infty} a_{m_1}(t) e^{jm_1 2\pi f_{LO_1} t} \quad (2.89)$$

with the I+ branch mixer waveform of LO₂ (victim)

$$p_{LO_2, I+}(t) = \sum_{m_2=-\infty}^{\infty} b_{m_2}(t) e^{jm_2 2\pi f_{LO_2} t} \quad (2.90)$$

2 Interferences in FDD RF Transceivers

corresponds to the equivalent spur $p_{\text{sp},\text{I}+}(t) = \gamma_{\text{I}+\text{I}+} \cdot p_{\text{LO}_1,\text{I}+}(t) \cdot p_{\text{LO}_2,\text{I}+}(t)$ including amplitude- and phase-noise in the I+ phase of LO₂. Here $\gamma_{\text{I}+\text{I}+}$ is the coupling factor between the I+ phases of LO₁ and LO₂. As a particular example, the local oscillator fundamental frequencies $f_{\text{LO}_1} = 1940$ MHz and $f_{\text{LO}_2} = 1980$ MHz are chosen. Through the coupling between the harmonics $m_1 = \pm 2$ of LO₁ and $m_2 = \pm 1$ of LO₂, the real valued spur

$$\begin{aligned} p_{\text{sp},\text{I}+}(t) &= \gamma_{\text{I}+\text{I}+} \left[a_2(t)b_1^*(t)e^{j2\pi f_{\text{sp}}t} + a_2^*(t)b_1(t)e^{-j2\pi f_{\text{sp}}t} \right] \\ &= 2\gamma_{\text{I}+\text{I}+} a_2'(t)b_1'(t) \cdot \cos \left(2\pi f_{\text{sp}}t - 2\varphi_{\text{LO}_1}(t) + \varphi_{\text{LO}_2}(t) - \frac{\pi}{4} \right) \end{aligned} \quad (2.91)$$

with $f_{\text{sp}} = 2f_{\text{LO}_1} - f_{\text{LO}_2} = 1900$ MHz is generated in the I+ phase of LO₂. Here, the spur terms at the frequencies $\pm(2f_{\text{LO}_1} + f_{\text{LO}_2})$ are neglected. Similar spurs are generated through the coupling between all other mixer phases (I,Q+,Q-) of the two involved IQ-mixers (in Appendix A.2 all coupling paths are derived). Combining all spurs which are generated in the 16 coupling paths, an equivalent complex valued RF spur of the form

$$\begin{aligned} p_{\text{sp}}(t) &= a_2^*(t)b_1(t)K_1e^{-j2\pi f_{\text{sp}}t} \\ &\quad + a_2(t)b_1^*(t)K_2e^{j2\pi f_{\text{sp}}t} \end{aligned} \quad (2.92)$$

is generated with $K_1 = (\gamma_{\text{I}} + \gamma_{\text{Q}}) / 2$ and $K_2 = (\gamma_{\text{I}} - \gamma_{\text{Q}}) / 2$ which down-converts any blocker signal located near f_{sp} into the Rx2 BB. Here γ_{I} and γ_{Q} are the resulting coupling factors from LO₁ to the I-, and Q-path of LO₂, respectively. The modeling in Appendix A.2 shows that the spur can have a gain imbalance if γ_{I} and γ_{Q} are not identical. In the literature, this is known as IQ-imbalance [15, 36, 37]. If the transmit frequency f_{Tx} is close to the spur frequency f_{sp} , the TxL signal is down-converted to the receiver baseband resulting in a main and image interference which leads to a degradation of the desired receive signal.

2.5.3 Modulated Spur with IQ-Imbalance and Tx/Rx PN

The transmitter signal including phase-noise

$$x_{\text{RF}}(t) = A_{\text{PA}} \Re \left\{ x_{\text{BB}}(t) e^{j(2\pi f_{\text{Tx}}t + \varphi_{\text{Tx}}(t))} \right\} \quad (2.93)$$

leaks through the frequency-selective duplexer stop-band, which is modeled by the impulse response $h_{\text{RF}}^{\text{TxL}}(t)$, into the receiver. Here A_{PA} is the power amplifier gain, the signal $x_{\text{BB}}(t) = x_{\text{I}}(t) + jx_{\text{Q}}(t)$ is the baseband transmit signal and $\varphi_{\text{Tx}}(t)$ the phase noise. The resulting transmitter leakage signal is

$$\begin{aligned} y_{\text{RF}}^{\text{TxL}}(t) &= x_{\text{RF}}(t) * h_{\text{RF}}^{\text{TxL}}(t) \\ &= A_{\text{PA}} \Re \left\{ [x_{\text{BB}}(t) * h_{\text{BB}}^{\text{TxL}}(t)] e^{j(2\pi f_{\text{Tx}}t + \varphi_{\text{Tx}}(t))} \right\}, \end{aligned} \quad (2.94)$$

and the total received signal at the output of the LNA with gain A_{LNA} becomes

$$y_{\text{RF,LNA}}^{\text{Tot}}(t) = A_{\text{LNA}} [y_{\text{RF}}^{\text{TxL}}(t) + y_{\text{RF}}^{\text{Rx}}(t) + v_{\text{RF}}(t)], \quad (2.95)$$

including the desired receive signal $y_{\text{RF}}^{\text{Rx}}(t)$ and the noise $v_{\text{RF}}(t)$. The signal after the mixer

$$\begin{aligned} y_{\text{RF,mixer}}^{\text{Tot}}(t) &= A_{\text{LNA}} y_{\text{RF}}^{\text{TxL}}(t) p_{\text{sp}}(t) \\ &\quad + A_{\text{LNA}} [y_{\text{RF}}^{\text{Rx}}(t) + v_{\text{RF}}(t)] e^{-j2\pi f_{\text{LO}_1}t} \end{aligned} \quad (2.96)$$

includes the desired receive signal, the noise, and the leakage signal which is down-converted by the noisy spur with IQ-imbalance. Here, the cross-modulation terms e.g. between the Rx signal and the spur, and the amplitude- and phase-noise in the down-conversion of the desired signal are neglected. By using the identity

$$\Re \{ \eta e^{j\kappa} \} = \frac{1}{2} (\eta e^{j\kappa} + \eta^* e^{-j\kappa}) \quad (2.97)$$

and assuming an anti-aliasing filter in front of the ADC which attenuates the mixer products in (2.96) which are outside the desired BB bandwidth, the total received discrete-time baseband signal becomes¹⁰

$$\begin{aligned} y_{\text{BB}}^{\text{Tot}}[n] = & \underbrace{\left[\sum_{l=-\infty}^n x_{\text{BB}}^s[l] h_{\text{BB}}^{\text{Tot}}[l, n-l] + \frac{K_2}{K_1^*} \sum_{l=-\infty}^n x_{\text{BB}}^{s*}[l] h_{\text{BB}}^{\text{Tot}*}[l, n-l] \right]}_{=y_{\text{BB}}^{\text{MS}}[n] \dots \text{modulated spur interference (main + image)}} * \bar{h}_s[n] \\ & + \frac{A_{\text{LNA}}}{2} [y_{\text{BB}}^{\text{Rx}}[n] + v_{\text{BB}}[n]] * \bar{h}_s[n]. \end{aligned} \quad (2.98)$$

Here,

$$h_{\text{BB}}^{\text{Tot}}[l, n] = \frac{A_{\text{LNA}} A_{\text{PA}} K_1}{2} \left[e^{j(\varphi_{\text{Tx}}[l] + 2\varphi_{\text{LO}_1}[l] - \varphi_{\text{LO}_2}[l] + \frac{\pi}{4})} \cdot a_2'[l] b_1'[l] h_{\text{BB}}^{\text{TxL}}[n] e^{j2\pi \frac{f_{\Delta}}{f_s} n} \right] \quad (2.99)$$

is the time-variant BB equivalent Tx-to-Rx impulse response including the PN terms and

$$x_{\text{BB}}^s[n] = \left[x_{\text{BB}}[n] e^{j2\pi \frac{f_{\Delta}}{f_s} n} \right] * \bar{h}_s[n], \quad (2.100)$$

is a frequency shifted version of the transmit baseband signal with $f_{\Delta} = f_{\text{Tx}} - f_{\text{sp}}$. The frequency f_s denotes the sampling frequency and $\bar{h}_s[n]$ is the impulse response of the combined DC-cancellation and channel-select filter. The derived model shows, that the modulated spur interference consists of a main and an image component reasoned by the gain imbalance of the spur. Furthermore, it can be observed in (2.99), that the jitter 2δ in the pulse duration of the 25% duty-cycle waveform leads to an amplitude noise in $h_{\text{BB}}^{\text{Tot}}[n, l]$. Whereas the PN of both LOs contribute to an equivalent PN of $h_{\text{BB}}^{\text{Tot}}[n, l]$. Both individual effects are finally leading to a time-variant impulse response $h_{\text{BB}}^{\text{Tot}}[n, l]$ which degrades the estimation of the impulse response by an adaptive filter and thereby the cancellation of the modulated spur interference.

The author of this thesis contributed this section to the journal [16]. There it is shown by the derived modulated spur model and also verified by using Matlab post-cancellation using measured data that the pure digital modulated spur cancellation approach is not able to cancel the PN. However, in this journal a mixed-signal modulated spur cancellation concept is proposed. This approach mimics the spur generation mechanism by using a serial-mixing approach where the real LO signals including their PN are used. The proposed solution is able to cancel the modulated spur interference including the Tx and LO₁/LO₂ PN and therefore outperforms the pure digital approach.

¹⁰Due to the time-variant Tx-to-Rx impulse response $h_{\text{BB}}^{\text{Tot}}[n, l]$, the convolution in (2.47) changes to that in (2.98).

3

Interference Rejection

3.1 Introduction

As described in Section 2.2, the 25% duty-cycle current driven passive mixer is widely used in modern RF receivers. It is preferably used in direct-conversion receivers and low-voltage applications [29]. The RF output current i_{RF} of the LNA flows into the four switching branches of the passive mixer and creates a differential I and Q BB voltage. Depending on the switching functions at the four transistor gates of the mixer, the passive mixer has different properties. Traditional designs using 50% duty-cycle gate control signals suffer by an IQ cross-talk problem due to the overlapping ON-states of the switches in the I-, and Q-branch. The conversion gain is also reduced because the RF input current is divided into two branches [48]. To overcome this drawbacks, the 25% duty-cycle control scheme was introduced which offers a 3 dB higher conversion gain and a reduced noise figure compared to the 50% duty-cycle concept [29, 33].

A well known issue in square-wave mixers is the generation of harmonics in the mixer branches [49, 50, 51] which lead to the down-conversion of unwanted spectral components contained in the RF input current i_{RF} . This down-conversion by the so-called harmonic response of the mixer may lead to a degradation of the wanted signal.

This chapter presents a novel HR strategy for 25% duty-cycle current-driven passive mixers. With this approach, the down-conversion of unwanted spectral content by the mixer's harmonic response may be significantly reduced.

Problem statement

Due to the design of wide-band analog front-ends in order to cover the high frequency range used in LTE, blocker signals may reach the mixer input. These blocker signals may be down-converted to the Rx BB through the harmonic response of the mixer thereby degrading the wanted signal. Such a harmonic down-conversion for an LTE CA scenario with two receivers and one transmitter is depicted in Fig. 3.1 (a). The carrier frequency f_{LO_1} of the PCC downlink receiver is coupled to the primary Tx frequency f_{Tx} by the duplexing distance. However, the carrier frequency f_{LO_2} of the SCC receiver may be located at any different frequency depending on intra/inter-band CA [3]. This may lead to the harmonic down-conversion of transmitter harmonics which leak through the duplexer into the receiver. Assuming an LTE inter-band CA mode with the uplink PCC in band 11 at $f_{\text{Tx}} = 1433$ MHz, and the downlink SCC in band 8 at $f_{\text{LO}_2} = 955$ MHz, the 2nd order Tx harmonic signal will be present at 2866 MHz. At the same time, the

3 Interference Rejection

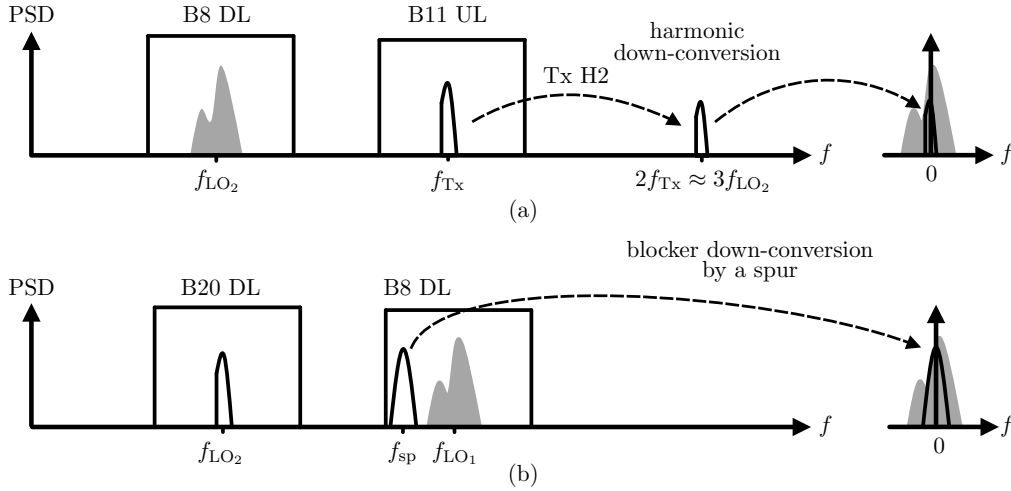


Figure 3.1: Down-conversion of the 2nd Tx harmonic by the harmonic response of the mixer (a), and down-conversion of an in-band blocker signal by a spur which is generated through a coupling of the two CA LO harmonics (b).

3rd harmonic of the SCC Rx LO occurs at 2865 MHz which down-converts the unwanted 2nd order Tx harmonic signal to the Rx BB. Rejecting the 3rd harmonic content of the Rx mixer LO signal would suppress the down-conversion of the Tx harmonic signal. In Fig. 3.1 (b), the down-conversion of in-band blockers through spurs is depicted. Spurs at the frequency locations $f_{sp} = \pm n f_{LO_1} \pm k f_{LO_2}$ for $n, k \in \mathbb{N}$ may be generated by device nonlinearities and the harmonics of the CA LOs [10]. An in-band blocker signal which is located at the frequency $f_{BL} \approx f_{sp}$ is down-converted into the Rx BB where it degrades the wanted signal SNR. E.g. consider an inter-band CA scenario with $f_{LO_1} = 942.5$ MHz in LTE band 8 (925 MHz to 960 MHz) and $f_{LO_2} = 806$ MHz (band 20) which is defined in 3GPP release 11. A spur which is created by the building law $f_{sp} = -5f_{LO_1} + 7f_{LO_2} = 929.5$ MHz falls within band 8 and down-converts the blocker signal. If the 5th harmonic of LO₁ or the 7th harmonic of LO₂ is rejected, then the down-conversion of the in-band blocker would be suppressed. Similarly, if the spur frequency f_{sp} falls near the actual Tx frequency, the Tx signal which leaks through the duplexer in the receiver is down-converted to the receiver BB. The digital cancellation of this so called modulated spur interference is presented in [9, 10] and later in Chapter 4 of this thesis. However, with an HR approach which suppresses specific harmonics of the LO signal the generation of such modulated spur interferences may be significantly suppressed.

3.2 State of the Art

To avoid the harmonic down-conversion of unwanted spectral components several approaches can be found in the existing literature. In [52], a 33% duty-cycle mixer for the rejection of the 3rd harmonic is proposed. The HR mixers proposed in [50, 51] use an LO signal with suppressed harmonics by approximating the ideal sine wave by a 3-bit amplitude-quantized signal as depicted in Fig. 3.2. The waveform is composed of three

45° shifted square-wave signals which are weighted and added. While this LO signal rejects the 3rd and 5th harmonic simultaneously, amplitude-, and phase mismatches result in a lowered suppression. In [49], this HR concept is used in IQ-transmitters, and in [53, 54] for receivers. Higher order harmonics may be rejected by using more than three mixer phases. E.g. by increasing the hardware effort to 5 mixer phases with 30° phase shift between the square-waves suppresses simultaneously the 3rd, 5th, 7th and 9th harmonic [51]. The authors in [55] demonstrate a voltage driven HR mixer with 8 branches

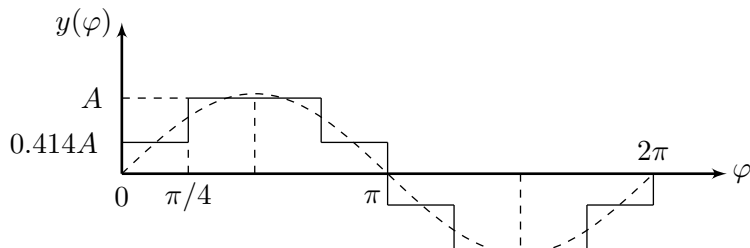


Figure 3.2: Harmonic rejection strategy proposed in [49] by approximating the sine-wave with an 3-bit amplitude-quantized signal. A simultaneous suppression of the 3rd and 5th harmonic can be achieved.

using 12.5 % duty-cycle and resistors to perform the amplitude scaling. This contribution describes an HR strategy, which modifies the waveform of an 25 % duty-cycle mixer to suppress specific harmonics by maintaining its advantages. By inserting gaps and adding pulses at specific positions within the 25 % duty-cycle waveform harmonics are suppressed. At the same time the beneficial property of no overlapping ON states of the switches is maintained which minimizes IQ cross-talk. A big advantage of this approach is that no weighting and summation of RF signals as needed in [51, 56] is required to realize the rejection of harmonics. Furthermore, only one transistor is needed in each of the mixer phases I_+ , I_- , Q_+ and Q_- .

3.3 Proposed Harmonic Rejection Control Signals

The harmonics in the mixer switch control signals cause the down-conversion of unwanted interferences into the BB. The proposed harmonic rejection strategy suppresses specific harmonics by inserting gaps and pulses into the control signal by maintaining the constraint that at each time only one of the four branch switches is turned ON. Thereby no IQ crosstalk occurs. Due to the absence of any reverse isolation in passive mixers, the low-Q BB impedance is transformed into a high-Q RF band-pass filter seen from the RF input side [33]. Because of this reason, at any time at least one switch should be turned ON in order to provide a constant impedance seen from the RF input. By maintaining these constraints, the two proposed switch control waveforms A and B are developed.

3.3.1 Proposed Waveform A

In Section 2.2 the Fourier coefficients of the 25% duty-cycle control signal of the I+ phase was derived as (see (2.3))

$$\begin{aligned}
 c_k &= \frac{1}{T_{LO}} \int_0^{T_{LO}} \tilde{p}_{I+}(t) e^{-jk2\pi f_{LO}t} dt \\
 &= \frac{1}{2\pi} \int_0^{2\pi} p_{I+}(\varphi) e^{-jk\varphi} d\varphi \\
 &= \frac{A}{4} e^{-jk\frac{\pi}{4}} \text{sinc}\left(k\frac{\pi}{4}\right).
 \end{aligned} \tag{3.1}$$

It may be observed that the Fourier coefficients c_k are unequal zero for even and odd harmonics k . However, due to the differential implementation of the IQ mixer the even harmonics cancel each other out. But the odd harmonics are still present and lead to the down-conversion of unwanted spectral components. In the proposed waveform A (Fig. 3.3), a gap in the middle of the 25% duty-cycle pulse, and a pulse at the offset of π with the same width δ is inserted. With careful selection of the width δ , a specific odd harmonic in the control signal may be rejected. The Fourier coefficients of waveform A

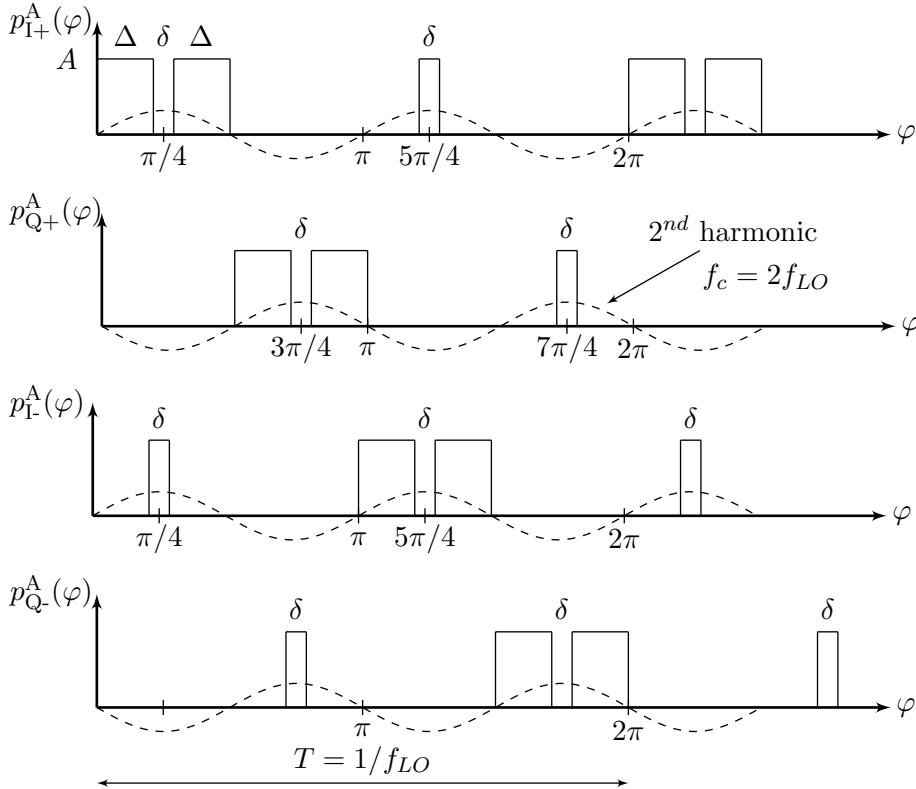


Figure 3.3: Mixer control signals using the proposed waveform A in a 25% duty-cycle mixer to reject specific harmonics.

3.3 Proposed Harmonic Rejection Control Signals

can be composed by using the Fourier coefficients

$$\begin{aligned} c_k^p(\varphi_c, \Delta) &= \frac{1}{2\pi} \int_{\varphi_c - \frac{\Delta}{2}}^{\varphi_c + \frac{\Delta}{2}} A e^{-jk\varphi} d\varphi \\ &= \frac{A\Delta}{2\pi} e^{-jk\varphi_c} \text{sinc}\left(k \frac{\Delta}{2}\right) \end{aligned} \quad (3.2)$$

of a single periodic prototype pulse centered around the angle φ_c with the width Δ and the constant amplitude A . Thereby, the Fourier coefficients of the I+ control signal using waveform A with $\Delta = \frac{\pi}{4} - \frac{\delta}{2}$, $\varphi_{c,1} = \frac{\Delta}{2}$, $\varphi_{c,2} = \frac{\pi}{2} - \frac{\Delta}{2}$ and $\varphi_{c,3} = \frac{5\pi}{4}$ are

$$\begin{aligned} c_k^A(\delta) &= \frac{1}{2\pi} \int_0^{2\pi} p_{I+}^A(\varphi) e^{-jk\varphi} d\varphi \\ &= c_k^p(\varphi_{c,1}, \Delta) + c_k^p(\varphi_{c,2}, \Delta) + c_k^p(\varphi_{c,3}, \delta) \\ &= \frac{A}{2\pi} e^{-jk\frac{\pi}{4}} \left[2\Delta \cos\left(k \left(\frac{\pi}{4} - \frac{\Delta}{2}\right)\right) \text{sinc}\left(k \frac{\Delta}{2}\right) + \delta (-1)^k \text{sinc}\left(k \frac{\delta}{2}\right) \right]. \end{aligned} \quad (3.3)$$

To reject a specific harmonic r in waveform A, the nonlinear equation

$$|c_r^A(\delta)| = 0 \quad (3.4)$$

needs to be solved which leads to

$$2\cos\left(r \left(\frac{\pi}{4} - \frac{\Delta}{2}\right)\right) \sin\left(r \frac{\Delta}{2}\right) + (-1)^r \sin\left(r \frac{\delta}{2}\right) = 0. \quad (3.5)$$

The required gap/pulse width δ can be derived by using the trigonometric identity

$$\cos(\alpha) \sin(\beta) = \frac{1}{2} [\sin(\alpha + \beta) - \sin(\alpha - \beta)] \quad (3.6)$$

in (3.5) which leads to the nonlinear relationship

$$\sin\left(r \frac{\delta}{2}\right) = \frac{\sin\left(r \frac{\pi}{4}\right)}{1 - (-1)^r}. \quad (3.7)$$

The differential implementation of the mixers requires only the suppression of odd harmonics which leads to $1 - (-1)^r = 2$. Due to the periodicity of the sine function, the solutions of (3.7) have the form

$$\delta_r^A = \frac{2}{r} \left[(-1)^m \sin^{-1}\left(\frac{1}{2} \sin\left(r \frac{\pi}{4}\right)\right) + m\pi \right] \quad (3.8)$$

for $m \in \mathbb{Z}$, where only the solutions with $0 < \delta < 25\%$ are of interest. The gap/pulse width δ_r^A to reject the odd harmonics using waveform A in each of the four mixer control signals is summarized in Table 3.1. The down-conversion of the wanted Rx signal occurs with the fundamental $c_1^A(\delta_r^A)$ which may be reduced by using the proposed HR strategy. The relative reduction of the fundamental Fourier coefficient compared to the ordinary 25% duty-cycle scheme is included in Table. 3.1. The resulting complex valued BB

3 Interference Rejection

Table 3.1: Harmonic rejection with waveform A

Rejected r^{th} harmonic	δ_r^A in % of duty-cycle	$\left \frac{c_1^A(\delta_r^A)}{c_1} \right _{\text{dB}}$
3 rd	3,83 %	-3,61 dB
5 th	22,30 %	-1,68 dB
7 th	15,93 %	-8.94 dB
9 th	9,83 %, 23.5 %	-17 dB, -0.88 dB
13 th	14.5 %	-12.24 dB
15 th	20.76 %	-2.88 dB

voltage (see (2.8))

$$\begin{aligned}
 u_{\text{BB}}(t) &= u_{\text{BB,I}}(t) + ju_{\text{BB,Q}}(t) \\
 &= \left[4 i_{\text{RF}}(t) \sum_{\substack{k=1 \\ k \text{ odd} \\ k \neq r}}^{\infty} c'_k e^{-\sigma_k j(k2\pi f_{\text{LO}}t - k\frac{\pi}{4})} \right] * z_{\text{BB}}(t)
 \end{aligned} \tag{3.9}$$

using the HR strategy with waveform A does not contain the r^{th} harmonic response anymore. As a consequence of that, the r^{th} harmonic response of the mixer is removed and the down-conversion of unwanted spectral components within $i_{\text{RF}}(t)$ at the frequency $r \cdot f_{\text{LO}}$ is suppressed.

3.3.2 Proposed Waveform B

To avoid narrow pulses and gaps which may be limited by the rise-, and fall-time of the control signal edges, waveform B depicted in Fig. 3.4 is proposed. During the period where non of the switches is turned ON, a fifth switch is needed in the IQ mixer which terminates the LNA output current to the BB impedance. This is needed to maintain a constant mixer input impedance seen from the LNA output current. The Fourier coefficients of waveform B are

$$\begin{aligned}
 c_k^{\text{B}}(\delta) &= \frac{1}{2\pi} \int_0^{2\pi} p_{\text{I}+}^{\text{B}}(\varphi) e^{-jk\varphi} d\varphi \\
 &= c_k^p(\varphi_{c,1}, \Delta) + c_k^p(\varphi_{c,2}, \Delta) \\
 &= \frac{A\Delta}{\pi} e^{-jk\frac{\pi}{4}} \cos\left(k\left(\frac{\pi}{4} - \frac{\Delta}{2}\right)\right) \text{sinc}\left(k\frac{\Delta}{2}\right),
 \end{aligned} \tag{3.10}$$

and by setting

$$|c_r^{\text{B}}(\delta)| = 0 \tag{3.11}$$

for a specific harmonic r the nonlinear equation

$$\sin\left(r\frac{\delta}{2}\right) = \sin\left(r\frac{\pi}{4}\right) \tag{3.12}$$

3.3 Proposed Harmonic Rejection Control Signals

is obtained. Solving (3.12) leads to the multiple solutions

$$\delta_r^B = \frac{2}{r} \left[(-1)^m r \frac{\pi}{4} + m\pi \right] \quad (3.13)$$

for $m \in \mathbb{Z}$, where only the solutions with $0 < \delta < 25\%$ are of interest. The required gap widths to reject specific harmonics using waveform B are summarized in Table 3.2. With the duty-cycle of 8.33%, the 3rd, 9th and 15th harmonic are suppressed simultaneously.

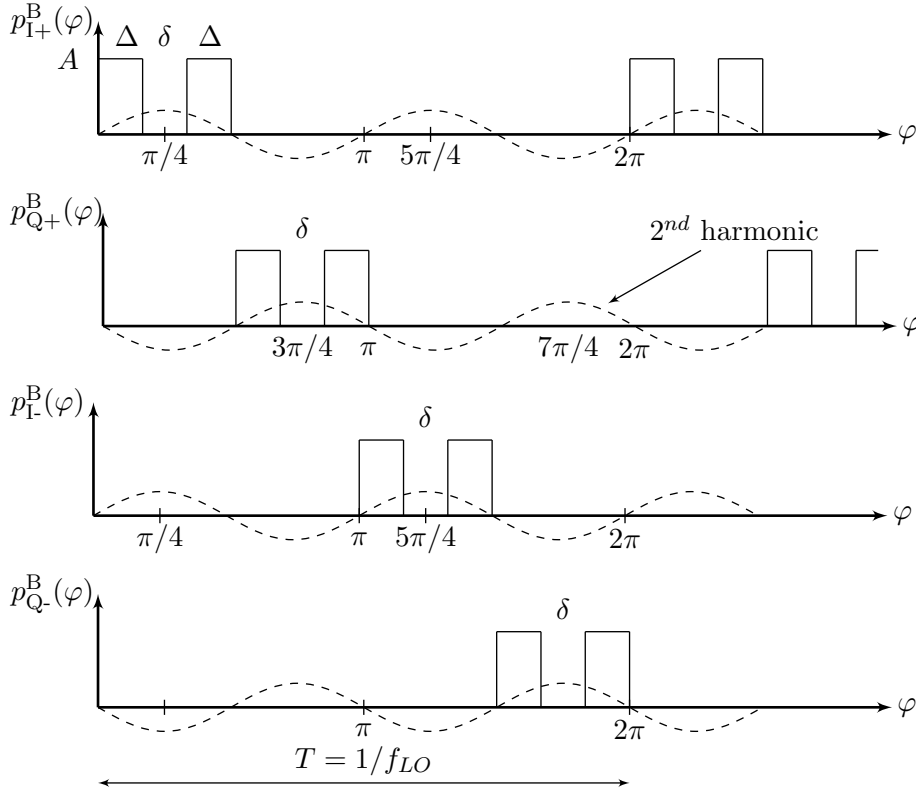


Figure 3.4: Mixer control signals using the proposed waveform B in a 25% duty-cycle mixer to reject specific harmonics.

Table 3.2: Harmonic rejection with waveform B

Rejected r^{th} harmonic	δ in % of duty-cycle	$\left \frac{c_1^B(\delta_r^B)}{c_1} \right _{\text{dB}}$
3 rd	8,33 %	-3.96 dB
5 th	n.a.	n.a.
7 th	17,86 %	-12,12 dB
9 th	2.77 %, 8,33 %	-1.14 dB, -3.96 dB
13 th	9,62 %	-4,74 dB
15 th	8,33 %	-3.96 dB

3.4 Circuit Simulation Results

The proposed HR strategy using waveform A and B is evaluated using a circuit simulation using the Virtuoso platform from Cadence which involved a 28nm technology package. The simulation architecture is visualized in Fig. 3.5, where the LNA is implemented as a transconductance amplifier (TCA) (voltage-to-current converter) which drives the succeeding 25% duty-cycle current driven passive mixer. The RF signal is down-converted by the mixer, filtered by the anti-aliasing-filter (AAF) and digitized by the ADC. For the simulation, the receiver was configured for the reception of 10 MHz LTE signals in band 8 at $f_{LO} = 955$ MHz. For Fig. 3.6, waveform A and B are con-

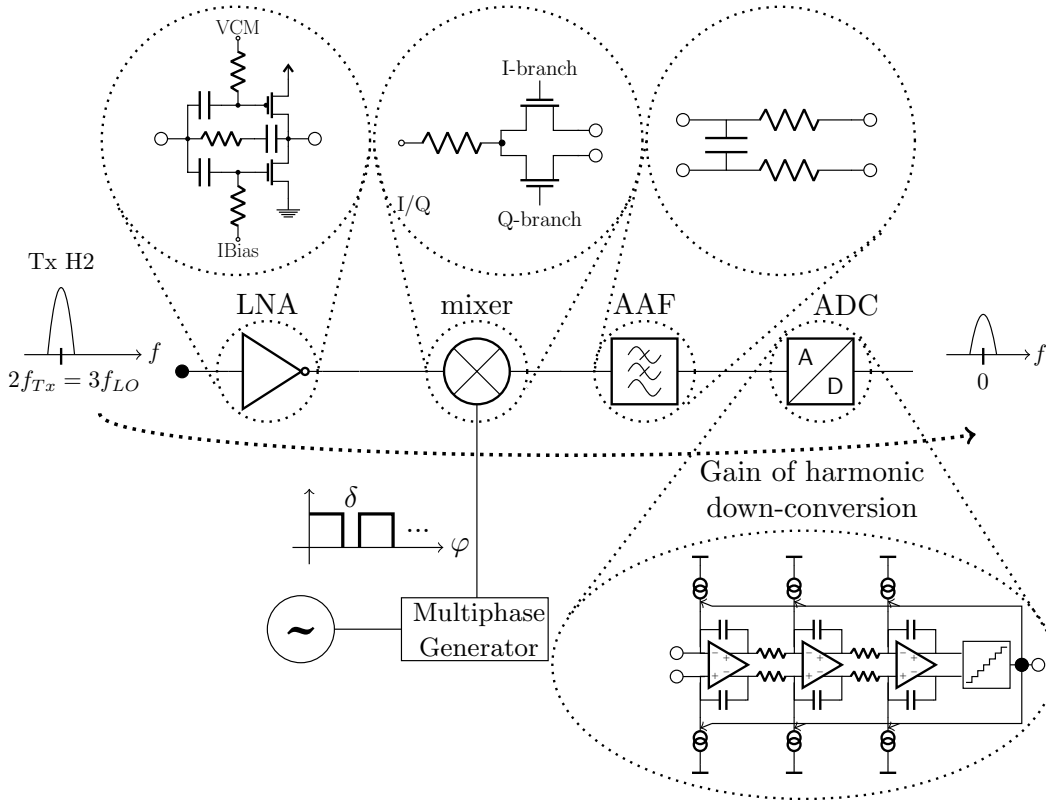


Figure 3.5: Circuit simulation setup.

figured to reject the 3rd harmonic in a 25% duty-cycle current driven passive IQ mixer. At the LNA input a 10 MHz blocker signal is inserted at the frequencies $k \cdot f_{LO}$ and the resulting BB signal power with and without using the HR was evaluated. The BB power $P_k^{A/B}$ using waveform A and B, which is a result of the harmonic down-conversion with the k^{th} harmonic is normalized to the BB power $P_1^{25\%}$ (down-conversion with the fundamental of the ordinary 25% duty-cycle mixer). It can be observed that the fundamental amplitude ($k = 1$) is reduced by about 4 dB when HR is activated. However, the down-converted power at the third harmonic response ($k = 3$) is reduced by 30.5 dB when the HR feature is used. With waveform B, simultaneously the 9th harmonic is reduced by 12.8 dB. In Fig. 3.7, waveform A and B are still configured to reject the 3rd harmonic response of the mixer which is at 2865 MHz. At the input of the LNA a

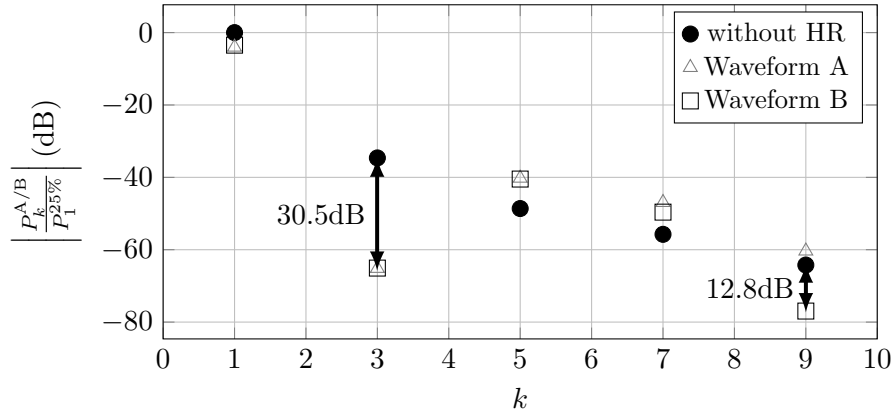


Figure 3.6: Rejection of the 3rd harmonic with waveform A and B. The gain of each harmonic down-conversion is normalized to the gain of the original 25% duty-cycle waveform (without HR).

Tx related blocker signal at 2866 MHz was inserted which corresponds to the 2nd Tx harmonic. The transmitter therefore operates in band 11 at $f_{Tx} = 1433$ MHz. This scenario is visualized in Fig. 3.1 (a). The pulse/gap width δ is varied and the influence on the blocker suppression is evaluated. An increased relative suppression of 30.5 dB and 30.4 dB is achieved compared to the ordinary 25% duty-cycle mixer for the optimal values of δ . Due to the finite rise and fall times of the control signals in the circuit simulation, the optimal value of δ differs slightly from the value presented in Table 3.1 and 3.2, respectively. Deviations of the optimal value lead to an increased harmonic response of the mixer and therefore to less suppression of the blocker. It can be observed that waveform B is less sensitive to small variations in δ .

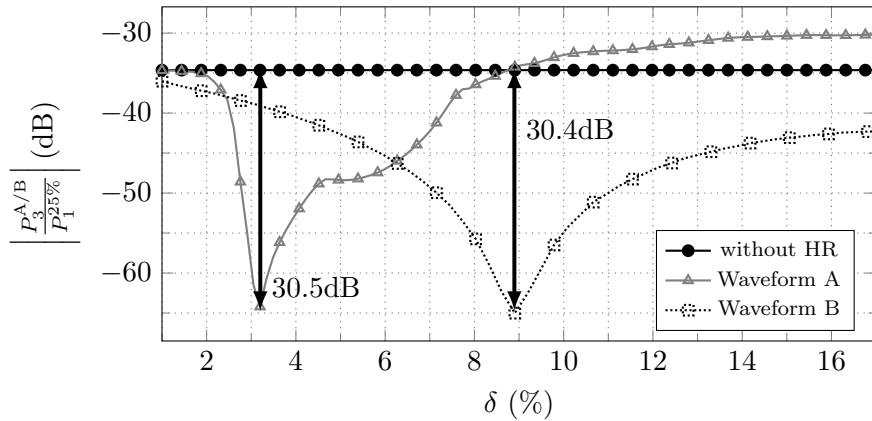


Figure 3.7: Normalized third-order harmonic rejection of waveform A and B, respectively, with variations in δ .

The same 2nd Tx harmonic scenario is used in Fig. 3.8 which shows the NF of the receiver depending on the blocker power at the LNA input. With enabled harmonic rejection the NF can be significantly improved compared to the ordinary 25% duty-cycle mixer without HR.

3 Interference Rejection

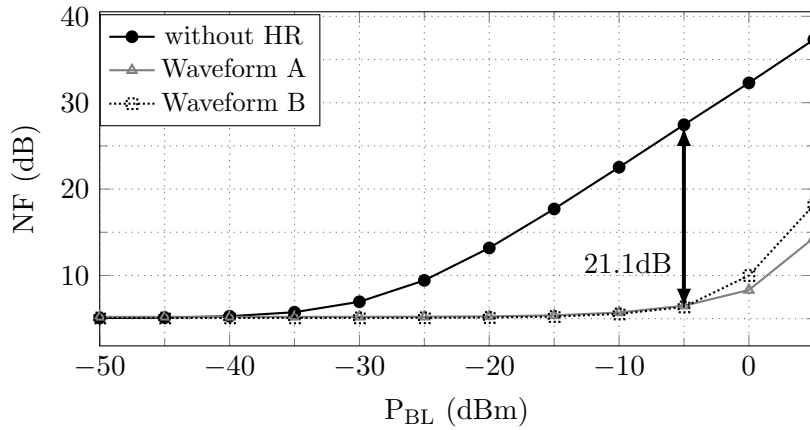


Figure 3.8: Blocker power dependent NF of the receiver.

At the blocker power of -5 dB, the NF can be improved by about 21 dB with both proposed waveforms.

The presented HR strategy with inserting gaps and pulses into the ordinary 25% duty-cycle waveform has been patented by the industrial partner and resulted in the U.S. Patent [57] which was granted in March 2018.

4

Adaptive Interference Cancellation

4.1 Introduction

This chapter deals with the digital cancellation of the modulated spur interference by adaptive filtering. As a starting point, adaptive filtering in the context of interference cancellation using BB equivalent complex valued signals and systems is introduced in Section 4.2. Motivated by that, the Wirtinger derivatives [24, 58] will be recapitulated in Section 4.3 which are used in the derivation of the complex valued LMS,- and RLS algorithms in Section 4.4 and Section 4.5, respectively. As derived in Chapter 2, the modulated spur interference may be generated by LO-to-LO crosstalk in inter-band CA scenarios, or by the use of a split-LNA in intra-band CA scenarios. The main novelty of this chapter is the derivation of a widely-linear [58] adaptive filter structure in Section 4.6 which is applicable for both cases. An additional contribution of this chapter is the performance evaluation of four adaptive filter algorithms for modulated spur cancellation with respect to their convergence¹ time and steady-state performance. At the time when this PhD work has started no literature regarding the pure digital cancellation of the modulated spur interference was available. The modeling of the modulated spur interference, and the performance evaluation of the algorithms have been presented in [9] and [10].

4.2 Basic Adaptive Filter Structure

An adaptive filter is a self-adjusting filter, with a dedicated algorithm to update the filter coefficients, to be able to react to changes of the unknown environment. The impulse response of an unknown system may change due to environmental influences. In the context of adaptive interference cancellation in RF transceivers, the unknown system is the Tx-to-Rx transmitter leakage channel which may change over time due to temperature drifts and/or a time varying antenna impedance mismatch. This leakage channel is mainly determined by the duplexer Tx-to-Rx stop-band frequency response which may be heavily frequency-selective. In contrast to system identification applications where the impulse response of the unknown system is estimated, interference cancellation applications focus on the estimation (or more precisely reconstruction) of the output signal of the unknown system. In the RF transceiver context, the estimated/reconstructed signal is the BB receiver interference caused by the TxL signal. This means that the receiver

¹Gradient-based adaptive filters converge only in the mean because the noise influences the gradient. Consequently, when the filter reaches its steady state, the coefficients fluctuate around their optimal values [58].

4 Adaptive Interference Cancellation

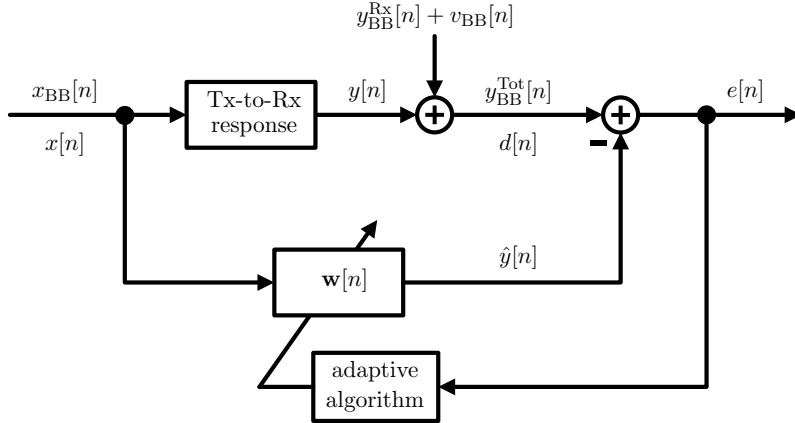


Figure 4.1: Adaptive interference cancellation in the digital BB of the transceiver.

is desensitized by self-interference of the transceiver's own transmit signal which implies that the interference signal is a function of the known transmit BB samples. The update of the adaptive filter coefficients is based on the underlying performance criterion which is usually a convex cost function. This performance criterion is a function of the error signal $e[n]$ which is the difference between the estimated filter output and the desired signal. The cost function is minimized by adjusting the coefficient vector $\mathbf{w}[n]$ [59].

Fig. 4.1 shows the basic adaptive filter structure for the self-interference cancellation in the digital BB. The Tx-to-Rx response represents the BB equivalent response of the involved RF impulse response experienced by the TxL signal. Therefore, the adaptive filter estimates the BB equivalent Tx-to-Rx response by updating the vector $\mathbf{w}[n]$. According to that, all involved signals in Fig. 4.1 are BB signals. In this work the notations $y_{\text{BB}}^{\text{Tot}}[n]$ or $d[n]$ are used for the desired signal which is the total received signal of the receiver including the wanted Rx signal, the noise, and the self-interference. The BB self-interference signal $y[n]$ adds to the wanted Rx signal $y_{\text{BB}}^{\text{Rx}}[n]$ which is received by the antenna and the noise $v_{\text{BB}}[n]$. The estimated self-interference signal $\hat{y}[n]$ is subtracted from the total received signal $y_{\text{BB}}^{\text{Tot}}[n]$ to form the error signal $e[n]$ which contains the wanted Rx signal and the noise and should be interference free in the ideal case. The error signal and the known BB transmit samples $x_{\text{BB}}[n]$ ($x[n]$) are used in the adaptive algorithm to update the filter coefficient vector $\mathbf{w}[n]$. The adaptive signal processing in the digital BB of the transceiver implies that complex valued signals and systems are involved. Due to the nature of SC-FDMA BB transmit signals [60], the BB transmit samples $x_{\text{BB}}[n] = x_{\text{I}}[n] + jx_{\text{Q}}[n]$ are complex valued. Furthermore, the reception of RF signals using an IQ-mixer as e.g. the 25% duty-cycle passive mixer which was introduced in Section 2.2 creates an in-phase and quadrature-phase signal which are combined to the complex receive signal $y_{\text{BB}}^{\text{Tot}}[n]$.

The adaptive algorithm minimizes a real valued cost function J with respect to the coefficient vector \mathbf{w} . In LMS-based algorithms, this is usually achieved by updating the complex valued filter coefficients $\mathbf{w}[n]$ iteratively using the derivative of the cost function [58]. Therefore a complex derivative of a non-holomorphic (non-analytic) cost function

is needed. For this special case, the Cauchy-Riemann equations are not fulfilled and consequently the traditional complex differentiation is not applicable. Because of this reason, the Wirtinger Calculus [58] is discussed in Section 4.3 which introduces generalized complex derivatives of non-holomorphic cost functions, which exist whenever the cost function is real-differentiable.

4.3 Complex Derivatives

4.3.1 The Cauchy-Riemann Equations

The standard approach for complex differentiation is based on the Cauchy-Riemann equations. Let

$$f(\mathbf{w}) = f_r + jf_i \quad (4.1)$$

be a complex valued function $f : \mathbb{C}^M \rightarrow \mathbb{C}$. The function f can be interpreted as a function $\mathbf{g} : \mathbb{R}^{2M} \rightarrow \mathbb{R}^2$ where the first coordinate represents the real part and the second the imaginary part of f :

$$f = f_r + jf_i \rightarrow \mathbf{g} = \begin{bmatrix} f_r \\ f_i \end{bmatrix} \quad (4.2)$$

The function f is complex differentiable in the standard sense if and only if \mathbf{g} is totally real differentiable and the Cauchy-Riemann equations

$$\begin{aligned} \frac{\partial f_r(\mathbf{w}_r, \mathbf{w}_i)}{\partial \mathbf{w}_r} &= \frac{\partial f_i(\mathbf{w}_r, \mathbf{w}_i)}{\partial \mathbf{w}_i} \\ \frac{\partial f_i(\mathbf{w}_r, \mathbf{w}_i)}{\partial \mathbf{w}_r} &= -\frac{\partial f_r(\mathbf{w}_r, \mathbf{w}_i)}{\partial \mathbf{w}_i} \end{aligned} \quad (4.3)$$

hold [58]. If a function f on an open domain is complex-differentiable for every \mathbf{w} in the domain it is called holomorphic (analytic).

4.3.2 Adaptive Learning Algorithms

In statistical signal processing, a suitable objective (cost) function $J(\mathbf{w})$ which is a function of the coefficient vector \mathbf{w} is either numerically or analytically minimized. For real valued adaptive filters, this optimization problem is easily understood. The minimization may be done by updating the length M coefficient vector $\mathbf{w}[n]$ by e.g. the stochastic gradient algorithm [61]

$$\mathbf{w}[n] = \mathbf{w}[n-1] - \mu \nabla_{\mathbf{w}} J[n], \quad (4.4)$$

where

$$J(\mathbf{w})[n] = e^2[n] \quad (4.5)$$

is the real valued cost function $J : \mathbb{R}^M \mapsto \mathbb{R}$, and $\nabla_{\mathbf{w}} J[n]$ the gradient with real valued elements. However, as discussed in Section 4.2, adaptive filtering in the equivalent BB requires the minimization of a cost function $J : \mathbb{C}^M \mapsto \mathbb{R}$ because the BB equivalent signals and systems are in general complex valued. This type of cost function is not

4 Adaptive Interference Cancellation

complex differentiable in the standard sense because the partial derivatives

$$\begin{aligned}\frac{\partial J_i(\mathbf{w}_r, \mathbf{w}_i)}{\partial \mathbf{w}_i} &= \mathbf{0} \\ \frac{\partial J_i(\mathbf{w}_r, \mathbf{w}_i)}{\partial \mathbf{w}_r} &= \mathbf{0}\end{aligned}$$

both vanish and therefore the Cauchy-Riemann equations (4.3) do not apply. Consequently, to be able to derive adaptive learning algorithms which operate in the equivalent BB, a different way to derive an update equation as in (4.4) has to be found.

4.3.3 Wirtinger Derivatives

We will now discuss the differential change of \mathbf{g} and f , respectively which gives motivations for the definition of the gradient of f as well as for the so-called Wirtinger derivatives. The Jacobian matrix of \mathbf{g} becomes

$$\nabla_{\mathbf{w}} \mathbf{g} = \begin{bmatrix} \frac{\partial f_r}{\partial \mathbf{w}_r} & \frac{\partial f_r}{\partial \mathbf{w}_i} \\ \frac{\partial f_i}{\partial \mathbf{w}_r} & \frac{\partial f_i}{\partial \mathbf{w}_i} \end{bmatrix}, \quad (4.6)$$

and the differential change of the function due to a change of the coefficients becomes

$$d\mathbf{g} = \begin{bmatrix} df_r \\ df_i \end{bmatrix} = \begin{bmatrix} \frac{\partial f_r}{\partial \mathbf{w}_r} & \frac{\partial f_r}{\partial \mathbf{w}_i} \\ \frac{\partial f_i}{\partial \mathbf{w}_r} & \frac{\partial f_i}{\partial \mathbf{w}_i} \end{bmatrix} \begin{bmatrix} d\mathbf{w}_r \\ d\mathbf{w}_i \end{bmatrix}. \quad (4.7)$$

Switching back to the complex valued function, this leads to

$$df = df_r + jdf_i = \frac{\partial f_r}{\partial \mathbf{w}_r} d\mathbf{w}_r + \frac{\partial f_r}{\partial \mathbf{w}_i} d\mathbf{w}_i + j \frac{\partial f_i}{\partial \mathbf{w}_r} d\mathbf{w}_r + j \frac{\partial f_i}{\partial \mathbf{w}_i} d\mathbf{w}_i, \quad (4.8)$$

and with the variable swap

$$\begin{aligned}d\mathbf{w}_r &= \frac{1}{2} [d\mathbf{w} + d\mathbf{w}^*] \\ d\mathbf{w}_i &= \frac{1}{2j} [d\mathbf{w} - d\mathbf{w}^*]\end{aligned} \quad (4.9)$$

we obtain

$$\begin{aligned}df(\mathbf{w}_r, \mathbf{w}_i) &= \frac{\partial f_r}{\partial \mathbf{w}_r} \frac{1}{2} [d\mathbf{w} + d\mathbf{w}^*] + \frac{\partial f_r}{\partial \mathbf{w}_i} \frac{1}{2j} [d\mathbf{w} - d\mathbf{w}^*] + j \frac{\partial f_i}{\partial \mathbf{w}_r} \frac{1}{2} [d\mathbf{w} + d\mathbf{w}^*] \\ &\quad + j \frac{\partial f_i}{\partial \mathbf{w}_i} \frac{1}{2j} [d\mathbf{w} - d\mathbf{w}^*] \\ &= \frac{1}{2} \left[\frac{\partial f_r}{\partial \mathbf{w}_r} + j \frac{\partial f_i}{\partial \mathbf{w}_r} - j \left(\frac{\partial f_r}{\partial \mathbf{w}_i} + j \frac{\partial f_i}{\partial \mathbf{w}_i} \right) \right] d\mathbf{w} \\ &\quad + \frac{1}{2} \left[\frac{\partial f_r}{\partial \mathbf{w}_r} + j \frac{\partial f_i}{\partial \mathbf{w}_r} + j \left(\frac{\partial f_r}{\partial \mathbf{w}_i} + j \frac{\partial f_i}{\partial \mathbf{w}_i} \right) \right] d\mathbf{w}^* \\ &= \frac{1}{2} \left[\frac{\partial f}{\partial \mathbf{w}_r} - j \frac{\partial f}{\partial \mathbf{w}_i} \right] d\mathbf{w} + \frac{1}{2} \left[\frac{\partial f}{\partial \mathbf{w}_r} + j \frac{\partial f}{\partial \mathbf{w}_i} \right] d\mathbf{w}^*.\end{aligned} \quad (4.10)$$

Motivated by (4.10), the Wirtinger derivatives (4.11) (\mathbb{R} – derivative) and (4.12) (\mathbb{R}^* – derivative) may be defined as

$$\frac{\partial f(\mathbf{w}, \mathbf{w}^*)}{\partial \mathbf{w}} = \frac{1}{2} \left[\frac{\partial f}{\partial \mathbf{w}_r} - j \frac{\partial f}{\partial \mathbf{w}_i} \right] \quad (4.11)$$

and

$$\frac{\partial f(\mathbf{w}, \mathbf{w}^*)}{\partial \mathbf{w}^*} = \frac{1}{2} \left[\frac{\partial f}{\partial \mathbf{w}_r} + j \frac{\partial f}{\partial \mathbf{w}_i} \right] \quad (4.12)$$

which results in the form [62]

$$df(\mathbf{w}, \mathbf{w}^*) = \underbrace{\left[\frac{\partial f(\mathbf{w}, \mathbf{w}^*)}{\partial \mathbf{w}} \quad \frac{\partial f(\mathbf{w}, \mathbf{w}^*)}{\partial \mathbf{w}^*} \right]}_{\nabla_{\mathbf{w}} f} \begin{bmatrix} d\mathbf{w} \\ d\mathbf{w}^* \end{bmatrix} \quad (4.13)$$

where $\nabla_{\mathbf{w}} f$ is the gradient. When f is holomorphic (analytic), then the \mathbb{R}^* – derivative vanishes. Furthermore, the \mathbb{R} – derivative is equivalent to the standard complex derivative in that case. As a consequence, all functions f which are real differentiable and independent of \mathbf{w}^* are analytic [58].

When we search for local extrema of a real valued function f , we search for points with $\nabla_{\mathbf{w}} f = \mathbf{0}$. However, for real valued cost functions² $J : \mathbb{C}^M \mapsto \mathbb{R}$, the imaginary part of the cost function $J_i = 0$. Consequently, the Wirtinger derivatives (4.11) and (4.12) become

$$\begin{aligned} \frac{\partial J(\mathbf{w}, \mathbf{w}^*)}{\partial \mathbf{w}} &= \frac{1}{2} \left[\frac{\partial J}{\partial \mathbf{w}_r} - j \frac{\partial J}{\partial \mathbf{w}_i} \right] \\ &= \frac{1}{2} \left[\frac{\partial J_r}{\partial \mathbf{w}_r} - j \frac{\partial J_r}{\partial \mathbf{w}_i} \right] \end{aligned} \quad (4.14)$$

and

$$\frac{\partial J(\mathbf{w}, \mathbf{w}^*)}{\partial \mathbf{w}^*} = \frac{1}{2} \left[\frac{\partial J_r}{\partial \mathbf{w}_r} + j \frac{\partial J_r}{\partial \mathbf{w}_i} \right] \quad (4.15)$$

which results in the identity

$$\frac{\partial J(\mathbf{w}, \mathbf{w}^*)}{\partial \mathbf{w}} = \left(\frac{\partial J(\mathbf{w}, \mathbf{w}^*)}{\partial \mathbf{w}^*} \right)^* . \quad (4.16)$$

Therefore, for a real-valued cost function J , the following three conditions are equivalent [62]:

$$\nabla_{\mathbf{w}} J = \mathbf{0} \Leftrightarrow \frac{\partial J}{\partial \mathbf{w}} = \mathbf{0} \Leftrightarrow \frac{\partial J}{\partial \mathbf{w}^*} = \mathbf{0} \quad (4.17)$$

4.3.4 Iterative Minimization of a Real Valued Cost Function

For real valued cost functions, the differential change in the cost function (4.13) becomes

$$\begin{aligned} dJ(\mathbf{w}, \mathbf{w}^*) &= \frac{\partial J(\mathbf{w}, \mathbf{w}^*)}{\partial \mathbf{w}} d\mathbf{w} + \frac{\partial J(\mathbf{w}, \mathbf{w}^*)}{\partial \mathbf{w}^*} d\mathbf{w}^* \\ &= \frac{\partial J(\mathbf{w}, \mathbf{w}^*)}{\partial \mathbf{w}} d\mathbf{w} + \left(\frac{\partial J(\mathbf{w}, \mathbf{w}^*)}{\partial \mathbf{w}} \right)^* d\mathbf{w}^* \\ &= 2\Re \left\{ \frac{\partial J(\mathbf{w}, \mathbf{w}^*)}{\partial \mathbf{w}} d\mathbf{w} \right\} . \end{aligned} \quad (4.18)$$

²Here, J is a real valued non-holomorphic cost function.

4 Adaptive Interference Cancellation

In case of an iterative minimization of the cost function J , we seek for the greatest reduction $dJ(\mathbf{w}, \mathbf{w}^*)$ between consecutive iterations. The maximum real valued change $dJ(\mathbf{w}, \mathbf{w}^*)$ is given when the scalar product in the last line of (4.18) is maximized. This is achieved when $d\mathbf{w}$ is a scaled version of $\left[\frac{\partial J(\mathbf{w}, \mathbf{w}^*)}{\partial \mathbf{w}}\right]^*$ and therefore of $\frac{\partial J(\mathbf{w}, \mathbf{w}^*)}{\partial \mathbf{w}^*}$ [58, 63] having in mind that $J(\mathbf{w}, \mathbf{w}^*)$ is real valued. To get the highest sensitivity of changes in the cost function it is therefore favorable to move towards the \mathbb{R}^* – derivative (4.15) such that the coefficient update for the stochastic gradient algorithm using the Wirtinger Calculus becomes [24, 58, 64, 65]

$$\mathbf{w}[n] = \mathbf{w}[n-1] - 2\mu \left[\frac{\partial J(\mathbf{w}, \mathbf{w}^*)}{\partial \mathbf{w}^*} \right]^T. \quad (4.19)$$

4.4 The Least-Mean-Squares Algorithm

The traditional LMS algorithm may be derived from the Wiener solution [59, 61] by minimizing the mean-square-error (MSE) cost function

$$\begin{aligned} J(\mathbf{w}, \mathbf{w}^*) &= E \left\{ |e[n]|^2 \right\} \\ &= E \{ dd^* \} - E \{ d\mathbf{x}^H \} \mathbf{w}^* - E \{ d^* \mathbf{x}^T \} \mathbf{w} + \mathbf{w}^T E \{ \mathbf{x}\mathbf{x}^H \} \mathbf{w} \\ &= \sigma_d^2 - \mathbf{r}^T \mathbf{w}^* - \mathbf{r}^H \mathbf{w} + \mathbf{w}^T \mathbf{R}_{\mathbf{x}\mathbf{x}} \mathbf{w} \end{aligned} \quad (4.20)$$

where $d[n]$ is the desired signal, $\mathbf{x}[n] = [x[n], x[n-1], \dots, x[n-M+1]]^T$ the delay-line input signal vector, \mathbf{w} the length M coefficient vector, $e[n] = d[n] - \mathbf{x}^T[n]\mathbf{w}$ the error, $\mathbf{r} = E \{ d\mathbf{x}^* \}$ is the cross-correlation vector and $\mathbf{R}_{\mathbf{x}\mathbf{x}} = E \{ \mathbf{x}\mathbf{x}^H \}$ the autocorrelation matrix. The obtained cost function is dependent on \mathbf{w}^* and therefore not analytic. Using the Wirtinger derivative, we get

$$\left[\frac{\partial J}{\partial \mathbf{w}^*} \right]^T = -(\mathbf{r} - \mathbf{R}_{\mathbf{x}\mathbf{x}}^T \mathbf{w}), \quad (4.21)$$

and setting the derivative to zero results in the Wiener solution

$$\mathbf{w} = (\mathbf{R}_{\mathbf{x}\mathbf{x}}^T)^{-1} \mathbf{r}. \quad (4.22)$$

The optimal coefficient vector may also be obtained iteratively by the steepest descent method

$$\begin{aligned} \mathbf{w}[n] &= \mathbf{w}[n-1] - 2\mu \left[\frac{\partial J}{\partial \mathbf{w}^*} \right]^T \\ &= \mathbf{w}[n-1] + 2\mu (\mathbf{r} - \mathbf{R}_{\mathbf{x}\mathbf{x}}^T \mathbf{w}[n-1]). \end{aligned} \quad (4.23)$$

The LMS algorithm operates iteratively on a sample basis by approximating the cross-correlation vector and autocorrelation matrix by their instantaneous estimates. The approximations $\mathbf{r} \approx d[n]\mathbf{x}^*[n]$ and $\mathbf{R}_{\mathbf{x}\mathbf{x}}^T \approx \mathbf{x}^*[n]\mathbf{x}^T[n]$, lead to the LMS algorithm

$$\begin{aligned} \mathbf{w}[n] &= \mathbf{w}[n-1] - 2\mu (d[n] + \mathbf{x}^T[n]\mathbf{w}[n-1]) \mathbf{x}^*[n] \\ &= \mathbf{w}[n-1] + 2\mu e[n]\mathbf{x}^*[n] \end{aligned} \quad (4.24)$$

where $e[n] = d[n] - \hat{y}[n]$ is the error between the desired signal $d[n]$ and the estimated signal $\hat{y}[n] = \mathbf{x}^T[n]\mathbf{w}[n-1]$, and μ the step-size. The same result is obtained if the instantaneous cost function

$$\begin{aligned} J(\mathbf{w}, \mathbf{w}^*) &= |e[n]|^2 \\ &= d[n]d^*[n] - d[n]\mathbf{x}^H[n]\mathbf{w}^*[n-1] - d^*[n]\mathbf{x}^T[n]\mathbf{w}[n-1] + \mathbf{w}^T[n-1]\mathbf{x}[n]\mathbf{x}^H[n]\mathbf{w}^*[n-1] \end{aligned} \quad (4.25)$$

is minimized iteratively. Using the Wirtinger Calculus we get

$$\begin{aligned} \left[\frac{\partial J}{\partial \mathbf{w}^*[n-1]} \right]^T &= (-d[n]\mathbf{x}^H[n] + \mathbf{w}^T[n-1]\mathbf{x}[n]\mathbf{x}^H[n])^T \\ &= -e[n]\mathbf{x}^*[n], \end{aligned} \quad (4.26)$$

which leads to the LMS coefficient update

$$\begin{aligned} \mathbf{w}[n] &= \mathbf{w}[n-1] - 2\mu \left[\frac{\partial J}{\partial \mathbf{w}^*[n-1]} \right]^T \\ &= \mathbf{w}[n-1] + 2\mu e[n]\mathbf{x}^*[n]. \end{aligned} \quad (4.27)$$

The Normalized Least-Mean-Squares Algorithm

Normalization improves the convergence speed³ of adaptive learning algorithms and provides step-size bounds to maintain stability of the algorithm. In the following, two normalization methods for the LMS algorithm are demonstrated:

Lets assume that the desired response is generated by $d[n] = \mathbf{x}^T[n]\mathbf{w}_0 + q[n]$, where $q[n]$ is complex white Gaussian noise with zero mean and \mathbf{w}_0 the optimal coefficient vector. The coefficient error vector $\mathbf{v}[n] = \mathbf{w}[n] - \mathbf{w}_0$

$$\mathbf{v}[n] = \mathbf{v}[n-1] - 2\mu\mathbf{x}^*[n]\mathbf{x}[n]\mathbf{v}[n-1] + 2\mu q[n]\mathbf{x}^*[n] \quad (4.28)$$

can be derived by inserting $e[n] = d[n] - \mathbf{x}^T[n]\mathbf{w}[n-1]$ in (4.27) and subtracting \mathbf{w}_0 from both sides [58]. Applying the statistical expectation operator on both sides of (4.28) and assuming that $q[n]$ and $\mathbf{x}^*[n]$ are statistically independent we obtain

$$\begin{aligned} E\{\mathbf{v}[n]\} &= (\mathbf{I} - 2\mu E\{\mathbf{x}^*[n]\mathbf{x}[n]\}) E\{\mathbf{v}[n-1]\} \\ &= (\mathbf{I} - 2\mu\mathbf{R}_{\mathbf{xx}}^T) E\{\mathbf{v}[n-1]\} \end{aligned} \quad (4.29)$$

which leads to the step-size bounds [58]

$$0 < \mu < \frac{1}{\text{trace}(\mathbf{R}_{\mathbf{xx}})} = \frac{1}{ME\{|x[n]|^2\}} \leq \frac{1}{\lambda_{\max}}. \quad (4.30)$$

Here, λ_{\max} is the maximum eigenvalue of the autocorrelation matrix $\mathbf{R}_{\mathbf{xx}}$, M the length of the coefficient vector \mathbf{w} and $x[n]$ the input signal. Incorporating this result for the step-size bounds into the LMS algorithm (4.27), we obtain the normalized coefficient update

$$\mathbf{w}[n] = \mathbf{w}[n-1] + \frac{\mu_0 e[n]\mathbf{x}^*[n]}{ME\{|x[n]|^2\}} \quad (4.31)$$

³With convergence speed, the speed of error reduction in the mean square sense is meant.

4 Adaptive Interference Cancellation

with the step-size bounds $0 < \mu_0 < 2$.

The second normalization approach can be used for linear and nonlinear adaptive algorithms and is based on [66]. In LMS-based algorithms, the *a priori* error signal $e[n] = d[n] - \mathbf{x}^T[n]\mathbf{w}[n-1]$ is used to update the filter coefficients. Step-size bounds to maintain convergence of the LMS algorithm (4.27) may be derived by analyzing the relationship between the errors $e[n]$ and $e[n+1]$. For that we expand the instantaneous error by a first order Taylor series expansion. However, as in [66] we use only the expansion of the error with respect to the weight vector which is the driving term of the algorithm. The first order Taylor series expansion results in

$$e[n+1] \approx e[n] + \frac{\partial e[n]}{\partial \mathbf{w}[n-1]} \Delta \mathbf{w}[n], \quad (4.32)$$

where $\Delta \mathbf{w}[n] = 2\mu e[n]\mathbf{x}^*[n]$. It has to be pointed out that the term $e[n]$ is analytic (holomorphic) and therefore the standard complex derivative with respect to $\mathbf{w}[n-1]$ is used to derive the first-order derivative (see page 9 in [67]). The first-order Taylor series expansion therefore becomes⁴

$$e[n+1] \approx (1 - 2\mu \mathbf{x}^H[n]\mathbf{x}[n]) e[n]. \quad (4.33)$$

To maintain convergence [66] of the adaptive filter, the condition

$$|1 - 2\mu \mathbf{x}^H[n]\mathbf{x}[n]| < 1 \quad (4.34)$$

has to be fulfilled. To guarantee the condition (4.34), two cases have to be considered:

1. $1 - 2\mu \mathbf{x}^H[n]\mathbf{x}[n] < 1$

which leads to $\mu > 0$ and

2. $1 - 2\mu \mathbf{x}^H[n]\mathbf{x}[n] > -1$

which results in $\mu < \frac{1}{\mathbf{x}^H[n]\mathbf{x}[n]}$.

Combining both limits gives

$$0 < \mu < \frac{1}{\mathbf{x}^H[n]\mathbf{x}[n]} \quad (4.35)$$

which can be seen as a sample based approximation of (4.30). Including the factor 2 in (4.27) into the step-size limits, the final normalized least-mean-squares (ϵ -NLMS) algorithm [61] with the regularization parameter ϵ becomes Algorithm 1. The small positive-valued real regularization parameter ϵ is used to prevent possible instabilities when $|\mathbf{x}[n]|_2^2$ is very small and may be chosen as e.g. $\epsilon = 0.001$.

⁴Here, the identity $\mathbf{x}^T[n]\mathbf{x}^*[n] = \mathbf{x}^H[n]\mathbf{x}[n]$ is used.

Initialization:

```

0 < μ < 2
ε > 0
w[-1] = 0
for n = 0, 1, 2... do
    y-hat[n] = x^T[n]w[n-1]
    e[n] = d[n] - y-hat[n]
    w[n] = w[n-1] + (μ e[n] x*[n]) / (ε + x^H[n]x[n])
end

```

Algorithm 1: The complex valued ϵ -NLMS algorithm.

4.5 The Recursive Least-Squares Algorithm

In the following derivation of the RLS algorithm, the conjugate coefficient vector is used in the estimated output signal $\hat{y}[n] = \mathbf{x}^T[n]\mathbf{w}^*[n-1]$. Without this small modification, the estimated inverse autocorrelation matrix $\mathbf{P} = \mathbf{R}^{-1}$ would appear transposed in the final RLS algorithm. This is avoided to keep the analogy to the real valued RLS algorithm. The least-squares cost function up to the time index n using the forgetting factor $0 < \lambda \leq 1$ is

$$\begin{aligned}
 J_{\text{LS}}[n] &= \sum_{i=0}^n \lambda^{n-i} |d[i] - \mathbf{x}^T[i]\mathbf{w}^*[n]|^2 \\
 &= \sum_{i=0}^n \lambda^{n-i} [d[i]d^*[i] - d[i]\mathbf{x}^H[i]\mathbf{w}[n] - d^*[i]\mathbf{x}^T[i]\mathbf{w}^*[n] + \mathbf{x}^T[i]\mathbf{w}^*[n]\mathbf{x}^H[i]\mathbf{w}[n]].
 \end{aligned} \tag{4.36}$$

The \mathbb{R}^* Wirtinger derivative becomes⁵

$$\left[\frac{\partial J_{\text{LS}}[n]}{\partial \mathbf{w}^*[n]} \right]^T = \sum_{i=0}^n \lambda^{n-i} [-d^*[i]\mathbf{x}[i] + \mathbf{x}[i]\mathbf{x}^H[i]\mathbf{w}[n]], \tag{4.37}$$

and setting it to zero leads to

$$\begin{aligned}
 \sum_{i=0}^n \lambda^{n-i} [\mathbf{x}[i]\mathbf{x}^H[i]] \mathbf{w}[n] &= \sum_{i=0}^n \lambda^{n-i} [d^*[i]\mathbf{x}[i]] \\
 \mathbf{R}[n]\mathbf{w}[n] &= \mathbf{r}[n]
 \end{aligned} \tag{4.38}$$

using $\mathbf{R}[n] = \sum_{i=0}^n \lambda^{n-i} [\mathbf{x}[i]\mathbf{x}^H[i]]$ and $\mathbf{r}[n] = \sum_{i=0}^n \lambda^{n-i} [d^*[i]\mathbf{x}[i]]$. Note the difference between the matrix $\mathbf{R}[n]$ and $\mathbf{R}_{\mathbf{xx}} = E\{\mathbf{xx}^H\}$ which is used in the derivation of the Wiener solution. Reformulating the above equation gives

$$\mathbf{w}[n] = \mathbf{R}^{-1}[n]\mathbf{r}[n] = \mathbf{P}[n]\mathbf{r}[n] \tag{4.39}$$

which may be solved recursively. Expressing the vector $\mathbf{r}[n]$ by its previous estimate $\mathbf{r}[n-1]$, the recursive estimation

$$\mathbf{r}[n] = \lambda\mathbf{r}[n-1] + d^*[n]\mathbf{x}[n] \tag{4.40}$$

⁵Because we seek for the minimum of an LS cost function using n samples, both Wirtinger derivatives can be used here.

4 Adaptive Interference Cancellation

is obtained. Similarly, the matrix $\mathbf{R}[n]$ is updated recursively using

$$\begin{aligned}\mathbf{R}[n] &= \lambda \sum_{i=0}^{n-1} \lambda^{n-i-1} \mathbf{x}[i] \mathbf{x}^H[i] + \mathbf{x}[n] \mathbf{x}^H[n] \\ &= \lambda \mathbf{R}[n-1] + \mathbf{x}[n] \mathbf{x}^H[n].\end{aligned}\quad (4.41)$$

Using the matrix-inversion lemma [68]

$$(\mathbf{A} + \mathbf{BCD})^{-1} = \mathbf{A}^{-1} - \mathbf{A}^{-1} \mathbf{B} (\mathbf{C}^{-1} + \mathbf{DA}^{-1} \mathbf{B})^{-1} \mathbf{DA}^{-1} \quad (4.42)$$

the matrix $\mathbf{P}[n] = \mathbf{R}^{-1}[n]$ with $\mathbf{A} = \lambda \mathbf{R}[n-1]$, $\mathbf{B} = \mathbf{x}[n]$, $\mathbf{C} = 1$ and $\mathbf{D} = \mathbf{x}^H[n]$ becomes

$$\begin{aligned}\mathbf{P}[n] &= \frac{1}{\lambda} \mathbf{P}[n-1] - \frac{\frac{1}{\lambda} \mathbf{P}[n-1] \mathbf{x}[n]}{1 + \frac{1}{\lambda} \mathbf{x}^H[n] \mathbf{P}[n-1] \mathbf{x}[n]} \mathbf{x}^H[n] \frac{1}{\lambda} \mathbf{P}[n-1]} \\ &= \frac{1}{\lambda} (\mathbf{P}[n-1] - \mathbf{k}[n] \mathbf{x}^H[n] \mathbf{P}[n-1])\end{aligned}\quad (4.43)$$

where the gain vector is

$$\mathbf{k}[n] = \frac{\mathbf{P}[n-1] \mathbf{x}[n]}{\lambda + \mathbf{x}^H[n] \mathbf{P}[n-1] \mathbf{x}[n]}.\quad (4.44)$$

Reformulating (4.44) leads to

$$\mathbf{k}[n] = \mathbf{P}[n] \mathbf{x}[n].\quad (4.45)$$

The recursive update of the coefficient vector $\mathbf{w}[n]$ is obtained by inserting (4.40), (4.43) and (4.45) into (4.39). This leads to the coefficient update

$$\begin{aligned}\mathbf{w}[n] &= \mathbf{P}[n] \mathbf{r}[n] \\ &= \mathbf{P}[n] (\lambda \mathbf{r}[n-1] + d^*[n] \mathbf{x}[n]) \\ &= \lambda \mathbf{P}[n] \mathbf{r}[n-1] + d^*[n] \mathbf{P}[n] \mathbf{x}[n] \\ &= \lambda \left(\frac{1}{\lambda} \mathbf{P}[n-1] - \mathbf{k}[n] \mathbf{x}^H[n] \frac{1}{\lambda} \mathbf{P}[n-1] \right) \mathbf{r}[n-1] + d^*[n] \mathbf{k}[n] \\ &= \mathbf{w}[n-1] + \mathbf{k}[n] (d^*[n] - \mathbf{x}^H[n] \mathbf{w}[n-1]) \\ &= \mathbf{w}[n-1] + e^*[n] \mathbf{k}[n].\end{aligned}\quad (4.46)$$

The final RLS algorithm is summarized in Algorithm 2.

Initialization:
 $\mathbf{P}[-1] = \nu \mathbf{I}$ with $\nu > 0$
 $0 < \lambda \leq 1$
 $\mathbf{w}[-1] = \mathbf{0}$
for $n = 0, 1, 2 \dots$ **do**
 $\hat{y}[n] = \mathbf{x}^T[n] \mathbf{w}^*[n-1]$
 $e[n] = d[n] - \hat{y}[n]$
 $\mathbf{k}[n] = \frac{\mathbf{P}^{[n-1]}\mathbf{x}[n]}{\lambda + \mathbf{x}^H[n]\mathbf{P}^{[n-1]}\mathbf{x}[n]}$
 $\mathbf{P}[n] = \frac{1}{\lambda} (\mathbf{P}[n-1] - \mathbf{k}[n]\mathbf{x}^H[n]\mathbf{P}[n-1])$
 $\mathbf{w}[n] = \mathbf{w}[n-1] + e^*[n]\mathbf{k}[n]$
end

Algorithm 2: The complex valued RLS algorithm.

4.6 Modulated Spur Cancellation

In this section, the pure digital modulated spur interference cancellation using the derived complex valued ϵ -NLMS- and RLS algorithm is presented. As discussed in the previous chapters, the modulated spur interference may be either generated by LO-LO cross-talk in inter-band CA (Section 2.3.4), or the split-LNA configuration in intra-band CA (Section 2.5). In both cases a main and image modulated spur signal component may appear in the digital BB which disturbs the wanted Rx signal. Fig. 4.2 depicts the block diagram of an LTE-A FDD transceiver employing downlink CA with two receivers and one transmitter. The duplexer connects the Tx and Rx paths to one common antenna. Typically the Tx-to-Rx stop-band attenuation provided by the duplexer is around 50 dB [4]. However, the TDK band 5 duplexer [28] used in our investigations attenuates the Tx signal by about 63 dB at the transmit frequency $f_{\text{Tx}} = 831$ MHz before it leaks into the Rx path. The magnitude response of the duplexer obtained by a 4-pole S-parameter measurement is shown in Fig. 2.1. It can be observed that the Tx-to-Rx stop-band response is heavily frequency-selective. The Tx-to-Rx leakage channel is dependent on the antenna impedance mismatch and therefore time-variant. Because of this reason an adaptive interference cancellation technique is chosen. The content of this section without spur IQ-imbalance is published in [9].

In the following example configuration we assume a DL inter-band CA case with LTE band 5 and band 12 with the receiver frequencies at $f_{\text{Rx1}} = 876$ MHz, $f_{\text{Rx2}} = 738$ MHz, and the transmitter UL frequency at $f_{\text{Tx}} = 831$ MHz. In this example, we assume a spur generation law according to

$$f_{\text{sp}} = 6f_{\text{Rx1}} - 6f_{\text{Rx2}} = 6 \cdot 876 \text{ MHz} - 6 \cdot 738 \text{ MHz} = 828 \text{ MHz}. \quad (4.47)$$

This spur generation scenario was also used in the interference overview provided in Section 2.1 where it is illustrated in Fig. 2.2. The physical spur location is near the Rx1 mixer on the chip (see Fig. 4.2), where it is down-converting the TxL signal into the receiver BB. Thus, if the spur has an IQ-imbalance (see Section 2.3.3), the main and image modulated spur interference appears in the receiver BB where it severely deteriorates the received signal. The main and image modulated spur components appear in the BB with the frequency offset $f_{\Delta} = f_{\text{Tx}} - f_{\text{sp}} = 3$ MHz and $-f_{\Delta}$, respectively. The modulated spur interference part outside the LTE signal BW is attenuated by the

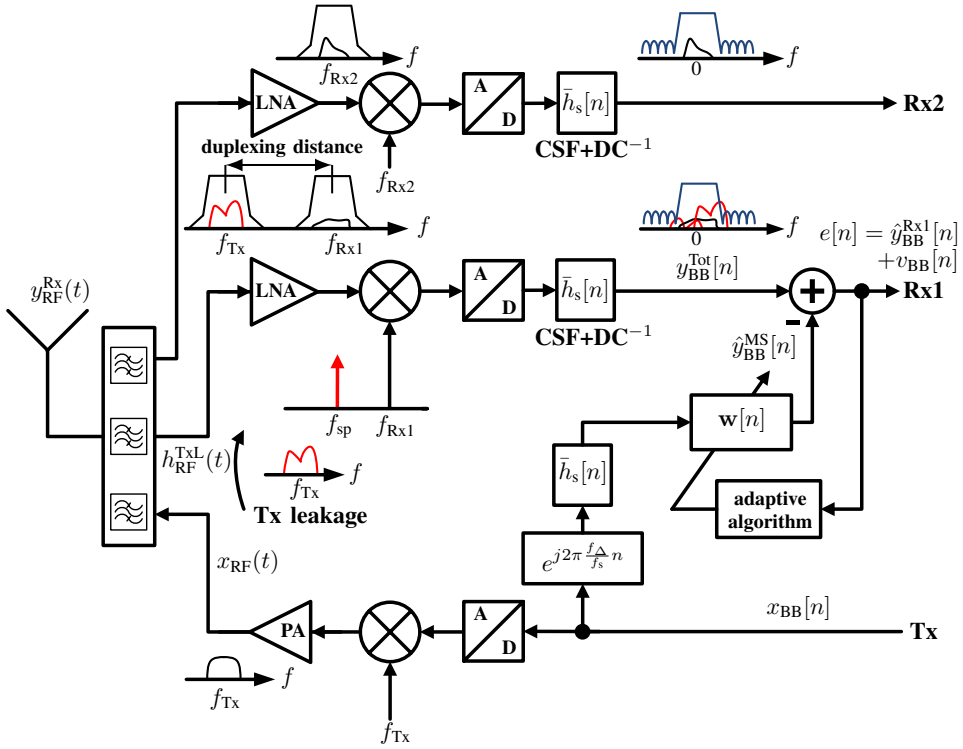


Figure 4.2: LTE-A FDD carrier aggregation transceiver employing downlink CA. Receive path Rx1 is affected by the modulated spur interference. The BB modulated spur interference is regenerated by an adaptive filter.

CSF. For a maximum output power of 23 dBm and a mean duplexer attenuation of 63 dB, the TxL signal level can be as strong as -40 dBm at the receiver input. The TxL signal is amplified by the LNA and down-converted by the spur. In our example, we assume a combined LNA and spur gain of 10 dB, and the spur IQ-imbalance is modeled using the gain and phase imbalance of $g = 3$ dB and $\phi = 5^\circ$, respectively. Thus, the resulting modulated spur power is -30 dBm (around -58 dBm/15 kHz). Fig. 4.3 depicts the spectra of the received LTE signals with 10 MHz bandwidth at receiver Rx1. The Tx power is 23 dBm, and the Rx SNR is 20 dB. The thermal noise power level at the input of the receiver is assumed at -104 dBm per 10 MHz (see Appendix A.3) and the assumed receiver noise figure (NF) is 5 dB. With the LNA gain of 20 dB, this results in a noise floor at -104 dBm + 5 dBm + 20 dB = -79 dBm at the LNA output. The total received BB signal $y_{\text{BB}}^{\text{Tot}}[n]$ contains the modulated spur interference (main + image), the desired Rx signal $y_{\text{BB}}^{\text{Rx}}[n]$ and the noise signal $v_{\text{BB}}[n]$.

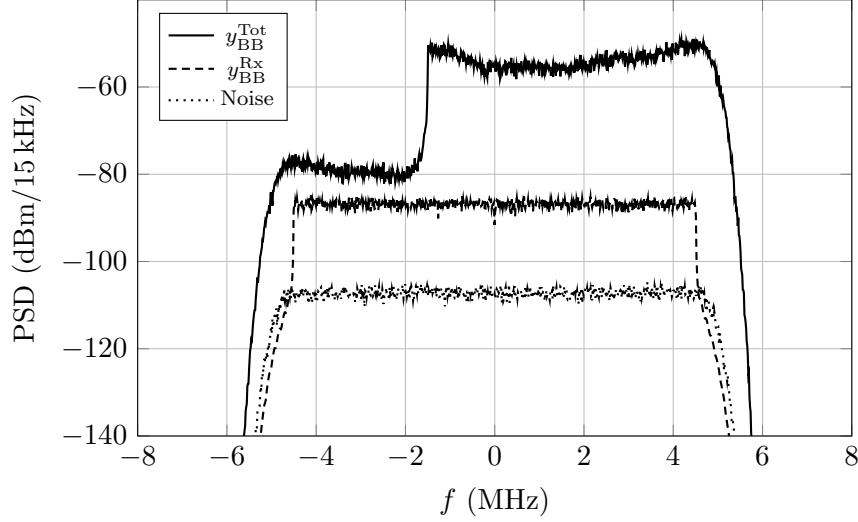


Figure 4.3: Baseband spectrum of the total received signal, wanted Rx signal (SNR = 20 dB) and the receiver noise floor at $-79 \text{ dBm} \hat{=} -106.8 \text{ dBm}/15 \text{ kHz}$ (at the output of the LNA). The total received signal contains the $f_{\Delta} = 3 \text{ MHz}$ shifted modulated spur with duplexer shaping. The transmit power is $P_{\text{Tx}} = 23 \text{ dBm}$.

4.6.1 Widely-Linear Modulated Spur Cancellation

To recover the Rx signal a widely-linear adaptive filter structure [58] for the cancellation of the modulated spur interference is developed. The advantage of the widely-linear cancellation structure is that it is able to cancel interferences which are correlated with the transmit signal and its conjugate. Using the modulated spur interference model

$$\begin{aligned}
 y_{\text{BB}}^{\text{Tot}}[n] &= \underbrace{x_{\text{BB}}^{\text{s}}[n] * h_{\text{BB},1}^{\text{Tot}}[n] + x_{\text{BB}}^{\text{s}*}[n] * h_{\text{BB},2}^{\text{Tot}}[n]}_{y_{\text{BB}}^{\text{MS}}[n]} \\
 &+ \frac{A_{\text{LNA}}}{2} y_{\text{BB}}^{\text{Rx}}[n] * \bar{h}_{\text{s}}[n] + \frac{A_{\text{LNA}}}{2} v_{\text{BB}}[n] * \bar{h}_{\text{s}}[n]
 \end{aligned} \tag{4.48}$$

which was derived in Section 2.3.4 it is obvious that the interference signal $y_{\text{BB}}^{\text{MS}}[n]$ is a function of the transmit samples and their conjugates. Consequently, using a widely-linear adaptive filter structure the modulated spur interference may be regenerated and subtracted from the received signal $y_{\text{BB}}^{\text{Tot}}[n]$. To generate a replica of the modulated spur interference, the total Tx-to-Rx leakage channels $h_{\text{BB},1}^{\text{Tot}}[n]$ and $h_{\text{BB},2}^{\text{Tot}}[n]$ (of the main and image interference) need to be estimated. Having in mind that for the estimation of $h_{\text{BB},1}^{\text{Tot}}[n]$ and $h_{\text{BB},2}^{\text{Tot}}[n]$ the wanted Rx signal acts as noise, the wanted Rx and the noise signal are combined to $v'_{\text{BB}}[n]$. Based on that, we are able to rewrite the model (4.48) to

$$y_{\text{BB}}^{\text{Tot}}[n] = \mathbf{x}_{\text{s}}^T[n] \mathbf{h}_1[n] + \mathbf{x}_{\text{s}}^{*T}[n] \mathbf{h}_2[n] + v'_{\text{BB}}[n] \tag{4.49}$$

where $\mathbf{h}_1[n] = [h_{1,0}, h_{1,1}, \dots, h_{1,M-1}]^T$ and $\mathbf{h}_2[n] = [h_{2,0}, h_{2,1}, \dots, h_{2,M-1}]^T$ are the length M finite impulse response (FIR) leakage channel approximations and

$$\mathbf{x}_{\text{s}}[n] = [x_{\text{BB}}^{\text{s}}[n], x_{\text{BB}}^{\text{s}}[n-1], \dots, x_{\text{BB}}^{\text{s}}[n-M+1]]^T \tag{4.50}$$

4 Adaptive Interference Cancellation

the delay-line input signal vector containing the frequency-shifted and channel-select filtered BB Tx samples

$$x_{\text{BB}}^{\text{s}}[n] = \left[x_{\text{BB}}[n] e^{j2\pi \frac{f_{\Delta}}{f_s} n} \right] * \bar{h}_s[n]. \quad (4.51)$$

Here, f_s denotes the sampling frequency. The modulated spur interference is regenerated by the widely-linear adaptive filter [58]

$$\hat{y}[n] = \mathbf{x}^T[n] \mathbf{w}[n-1] \quad (4.52)$$

where

$$\mathbf{w}[n] = \begin{bmatrix} \mathbf{w}_1[n] \\ \mathbf{w}_2[n] \end{bmatrix} \quad (4.53)$$

and

$$\mathbf{x}[n] = \begin{bmatrix} \mathbf{x}_s[n] \\ \mathbf{x}_s^*[n] \end{bmatrix} \quad (4.54)$$

is the augmented input signal vector containing the delay-line input signal vector $\mathbf{x}_s[n]$ and its conjugate.

The performance of four adaptive algorithms to perform a modulated spur interference cancellation is compared. For this, the number of adaptive filter taps is set to $M = 10$ which corresponds to the length of the used Tx-to-Rx FIR leakage channel (duplexer) model. This means, the augmented adaptive filter to estimate the main and image modulated spur interference has $2M = 20$ taps. The ϵ -NLMS algorithm (Algorithm 1), the variable step-size normalized LMS (ϵ -VSSNLMS) algorithm, the regularized affine-projection algorithm (ϵ -APA), and the RLS algorithm (Algorithm 2) are evaluated regarding convergence time and cancellation performance. The ϵ -NLMS-, and the RLS-algorithm are derived in Section 4.3, and a detailed description of the ϵ -APA algorithm may be found in [61]. The proposed ϵ -VSSNLMS algorithm is an ϵ -NLMS variant with the monotonically decreasing step-size

$$\mu[n] = \frac{\mu_0}{\alpha \cdot n + \beta} + \mu_{\min}. \quad (4.55)$$

In this step-size update, μ_0 sets the starting, and μ_{\min} the steady-state step-size value, respectively. With α and β the convergence rate can be adjusted, and stability is guaranteed for $0 < \mu[n] < 2$. The modulated spur replica signal⁶

$$\hat{y}[n] = \mathbf{x}^T[n] \mathbf{w}[n-1] \quad (4.56)$$

is subtracted from the total received signal to form the error

$$e[n] = y_{\text{BB}}^{\text{Tot}}[n] - \hat{y}[n] \quad (4.57)$$

which is used to employ an estimate of the leakage channel using the coefficient update

$$\mathbf{w}[n] = \mathbf{w}[n-1] + \frac{\mu[n] e[n] \mathbf{x}^*[n]}{\epsilon + \mathbf{x}^H[n] \mathbf{x}[n]}. \quad (4.58)$$

⁶The RLS algorithm uses $\hat{y}[n] = \mathbf{x}^T[n] \mathbf{w}^*[n-1]$.

To compare the convergence behaviour of the algorithms, the ensemble normalized mean-square-error (NMSE)

$$\text{NMSE}[n] = \frac{\text{E} \left[|y_{\text{BB}}^{\text{MS}}[n] - \hat{y}[n]|^2 \right]}{\text{E} \left[|y_{\text{BB}}^{\text{MS}}[n]|^2 \right]} \quad (4.59)$$

is used as performance measure [23]. The steady-state cancellation performance is evaluated with the SINR

$$\text{SINR} = \frac{\text{E} \left[|y_{\text{BB}}^{\text{Rx}}[n]|^2 \right]}{\text{E} \left[|y_{\text{BB}}^{\text{Tot}}[n] - y_{\text{BB}}^{\text{Rx}}[n] - \hat{y}[n]|^2 \right]}. \quad (4.60)$$

4.6.2 Simulation Results

The main goal is to select an adaptive algorithm which converges within the first OFDM symbol and restores the wanted Rx signal as good as possible. The measured duplexer frequency response is approximated with a 10 tap FIR filter within a bandwidth of 10 MHz centered at f_{Tx} [69]. Also the adaptive filter length is chosen as $M = 10$. For the RLS algorithm $\lambda = 0.9999$ (forgetting factor) and $\mathbf{P}[-1] = 10^6 \mathbf{I}$ are chosen, respectively. The parameter $K = 5$ defines the order of the ϵ -APA, and $\mu_{\epsilon\text{-APA}} = 0.005$ is the used step size. The choice for the ϵ -NLMS algorithm is $\mu_{\epsilon\text{-NLMS}} = 0.02$, and for the ϵ -VSSNLMS algorithm $\mu_0 = 1.5$, $\mu_{\text{min}} = 0.001$, $\alpha = 0.001$ and $\beta = 1$, respectively. The common regularization term is $\epsilon = 0.0001$. The parameters of the algorithms are selected to achieve convergence within the first OFDM symbol which has 1104 samples for a 10 MHz LTE signal with short cyclic-prefix [70]. The convergence behavior of the investigated algorithms for the Tx power of $P_{\text{Tx}} = 23$ dBm and the Rx SNR of 20 dB is depicted in Fig. 4.4. The algorithms converge after about 1 OFDM symbol.

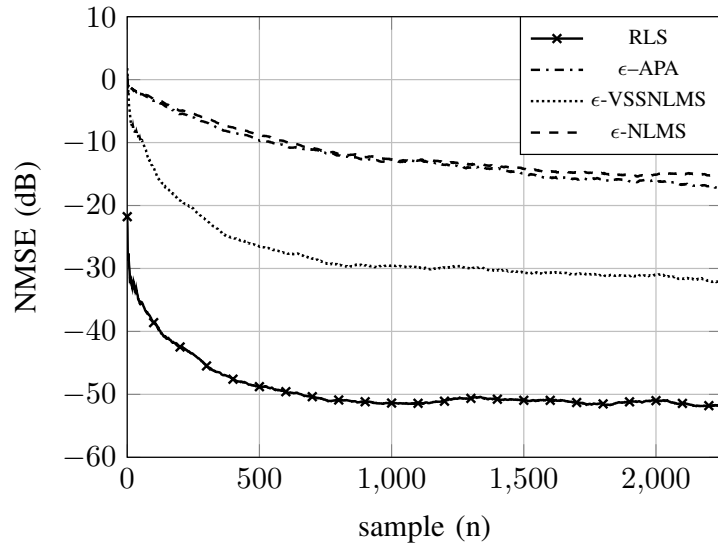


Figure 4.4: Convergence behavior of the different adaptive algorithms for $P_{\text{Tx}} = 23$ dBm.

4 Adaptive Interference Cancellation

The steady-state cancellation performance at different Tx power levels is evaluated at the three different Rx signal SNRs of 20 dB, 10 dB and 3 dB, and the results are visualized in Fig. 4.5, Fig. 4.6 and Fig. 4.7, respectively. As can be seen, the RLS algorithm is able to improve the Rx SINR up to the SNR value for all three scenarios. However, for the low SNR of 3 dB, the ϵ -VSSNLMS algorithm nearly achieves the steady state performance of the RLS algorithm (Fig. 4.7).

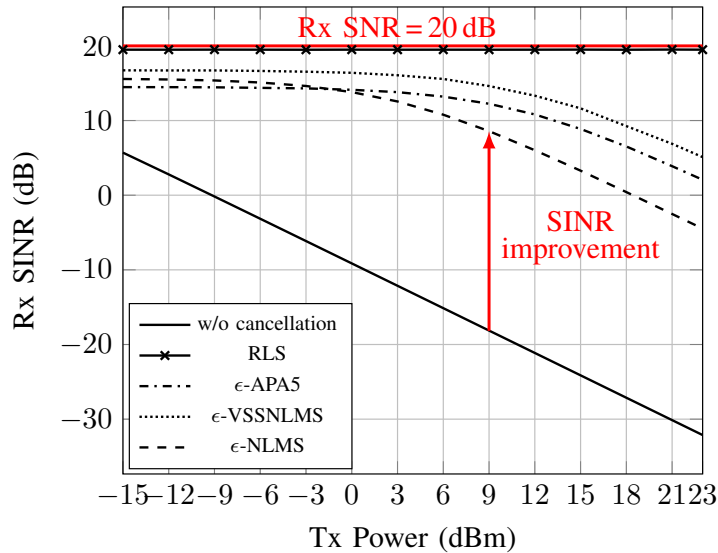


Figure 4.5: Improvement of the Rx SINR for an Rx SNR of 20 dB.

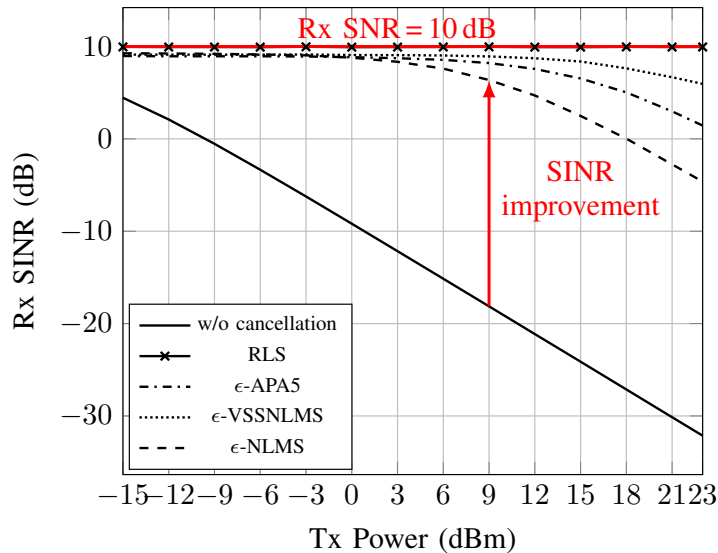


Figure 4.6: Improvement of the Rx SINR for an Rx SNR of 10 dB.

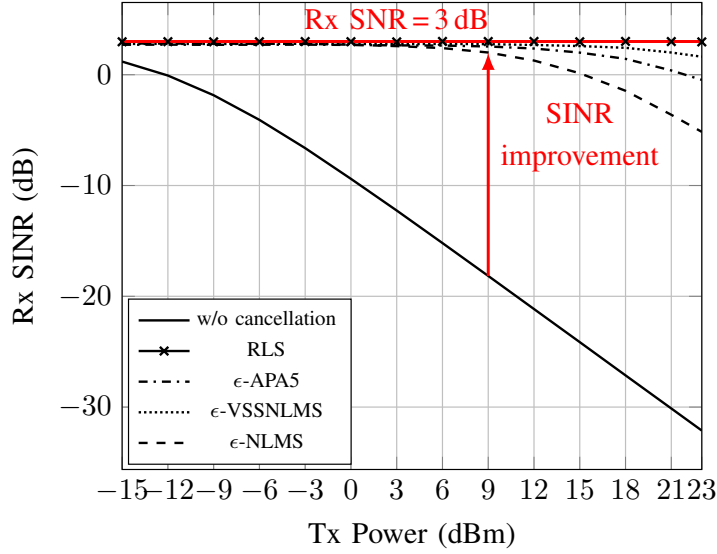


Figure 4.7: Improvement of the Rx SINR for an Rx SNR of 3 dB.

In the time-domain simulation 10 LTE slots⁷ are used and the steady-state SINR for each simulation is determined using the samples from the 5th to the 10th slot. The complexity of the widely-linear algorithms with $M = 10$ (the widely-linear filter has $2M = 20$ taps) and $K = 5$ according to [61], are listed in Table 4.1. Comparing their complexity shows,

Table 4.1: Computational cost per iteration for the widely-linear algorithms with $M=10$

Algorithm	Real mult.	Real add.	Real div.
RLS	1921	1839	1
ϵ -APA, K=5	3320	3350	-
ϵ -VSSNLMS	167	167	2
ϵ -NLMS	166	165	1

that the ϵ -VSSNLMS algorithm needs one order of magnitude less real multiplications than the RLS algorithm. Appendix A.4 provides some useful hints on how signals with a certain power level, SNR and SINR can be realized in Matlab.

4.6.3 Conclusion

Four adaptive algorithms are compared with respect to the modulated spur interference cancellation performance. Simulation results for LTE10 signals show that the proposed ϵ -VSSNLMS algorithm converges within the first OFDM symbol, and is able to improve the SINR significantly. For low SNR scenarios, the ϵ -VSSNLMS algorithm nearly achieves the steady-state performance of the RLS algorithm. Furthermore, the ϵ -VSSNLMS algorithm has only a slightly increased computational cost per iteration compared to the traditional ϵ -NLMS algorithm. The ϵ -VSSNLMS algorithm solves the dilemma of a low excess mean-square-error (EMSE) [61] or fast adaptation speed. The

⁷1 LTE slot contains 7 LTE symbols, and 1 LTE10 symbol consists of 1104 samples.

4 Adaptive Interference Cancellation

EMSE is connected to the MSE via

$$\text{MSE} = \text{EMSE} + E \left\{ |v'_{\text{BB}}[n]|^2 \right\}, \quad (4.61)$$

and for the ϵ -NLMS algorithm the EMSE may be approximated by [61]

$$\text{EMSE} = \frac{\mu E \left\{ |v'_{\text{BB}}[n]|^2 \right\}}{2 - \mu}. \quad (4.62)$$

Consequently, for small values of the step-size μ , the MSE approaches the variance of the noise term $v'_{\text{BB}}[n]$ which includes the Rx signal and the noise.

5

Adaptive IMD2 Cancellation

5.1 Introduction

This chapter is dedicated to the digital cancellation of the IMD2 interference by adaptive filtering. For this purpose, a novel Wiener model [25] based nonlinear LMS-type algorithm (IM2LMS), and a novel nonlinear RLS-type algorithm (IM2RLS) are derived to cancel the IMD2 interference in the digital BB. Simulation results demonstrate that the proposed IM2LMS algorithms outperforms traditional Hammerstein-, and Volterra model [25] based LMS algorithms in terms of convergence speed, steady-state performance and complexity. The proposed IM2LMS-, and IM2RLS algorithms are evaluated using measured IMD2 data which is obtained from two different measurement setups. The first setup includes a transceiver chip provided by the industrial partner, whereas the second setup uses discrete RF components. The derivation and the performance results of the IM2LMS-, and the IM2RLS algorithm have been presented in [7] and [27], respectively.

An interesting fact of the nonlinear IMD2 interference is, that one part of the generated second-order intermodulation products always falls around zero-frequency independent of the Tx-to-Rx frequency offset (duplexing distance). In case of direct-conversion receiver architectures, this leads to a BB interference which disturbs the wanted receive signal. The mathematical modeling in section 2.3.5 shows that the BB IMD2 interference contains the squared envelope of the BB equivalent TxL signal. The resulting BB IMD2 interference has twice the Tx signal bandwidth and contains a DC due to the envelope-squaring. The overall DC in the received signal is time-variant and may have many sources like e.g. LO-LO self mixing [8], and therefore must not be related explicitly to the DC which is generated by the IMD2 interference. Direct-conversion receivers employ a DC cancellation to suppress the DC in order to prevent the ADC from saturation. Consequently, the IMD2 interference related DC is removed from the received signal which complicates the IMD2 replica estimation. Furthermore, in the digital domain the signal is filtered by a CSF to reduce its bandwidth to the LTE signal bandwidth. Thereby, parts of the IMD2 interference are filtered away. Consequently, the adaptive filter needs to generate an IMD2 interference replica without DC and with reduced bandwidth. Both effects complicate the replica generation by the adaptive filter.

Section 5.2 gives an overview about the state-of-the-art IMD2 interference cancellation approaches. Section 5.3 describes how Hammerstein- and Volterra model based adaptive filters may be used to estimate the nonlinear IMD2 interference. In Section 5.4, the Wiener model IM2LMS-, and the IM2RLS algorithms are derived. The performance

of the algorithms is compared by simulations and measured data in Section 5.5 and Section 5.6, respectively.

5.2 State of the Art

In the existing literature, the authors of [21, 22, 71] discussed an IMD2 cancellation consisting of a Hammerstein model based LMS algorithm for frequency-flat duplexer stop-bands. In [23] a Volterra kernel based LS approach for frequency-selective Tx-to-Rx responses was proposed. The authors in [6] presented a two-step LS approach for the IMD2 cancellation and considered a static 3rd-order PA nonlinearity and IQ-imbalance in the transmit mixer. In [72] a Tx CA transceiver was considered where the transmit signal of two transmitters leaks through a diplexer into one of the CA receivers. The diplexer stop-band is modeled as a first-order FIR system which reflects a nearly frequency-flat response. The authors incorporated a fourth-order nonlinearity without memory into the estimation process, which results in an LS problem with four unknown coefficients. In the existing literature, the contributions [7, 23] considered the DC removal in the IMD2 interference replica, and in [6, 21, 22, 73] it is neglected. The IMD2 interference in the receiver may also be generated by external blocker signals received by the antenna. The author in [17, 18], extracts the blocker signal after the Rx mixer by a high-pass filter. The squared envelope of this signal is then used as a reference for the subsequent adaptive filter which cancels the generated IMD2 interference.

5.3 Polynomial Filters

State-of-the-art nonlinear adaptive filtering is performed by discrete-time polynomial filters [25] which are described with the input-output relationship

$$y[n] = \sum_{i=0}^P f_i(x[n], \dots, x[n-M+1], y[n-1], \dots, y[n-M+1]) \quad (5.1)$$

using the i^{th} -order polynomial functions $f_i(\cdot)$ and the polynomial order P . For the assumption of an underlying linear FIR system with the output relation

$$f_1[n] = \sum_{m=0}^{M-1} h_1[m]x[n-m], \quad (5.2)$$

the polynomial filter for $P = 2$ has the form [25]

$$\begin{aligned} y[n] = & h_0 + \sum_{m_1=0}^{M-1} h_1[m_1]x[n-m_1] \\ & + \sum_{m_1=0}^{M-1} \sum_{m_2=0}^{M-1} h_2[m_1, m_2]x[n-m_1]x[n-m_2]. \end{aligned} \quad (5.3)$$

Here, h_0 , $h_1[m_1]$ and $h_2[m_1, m_2]$ are the constant, the linear and the second-order system coefficients, respectively. Switching to complex valued signals and systems, the IMD2 interference may be described by a polynomial filter which has the order $i = 2$ with

$$f_2(\xi[n]) = \xi[n]\xi[n]^* = |\xi[n]|^2, \quad (5.4)$$

therefore reducing the polynomial filter to the truncated Volterra filter without constant and linear term. With $\xi[n] = x_{\text{BB}}[n] * h_{\text{BB}}^{\text{TxL}}[n]$ the IMD2 interference term

$$y_{\text{BB}}^{\text{IMD2}}[n] = \underbrace{\alpha_2 \frac{A_{\text{LNA}}^2 A_{\text{PA}}^2}{2}}_{\eta} |x_{\text{BB}}[n] * h_{\text{BB}}^{\text{TxL}}[n]|^2 * \bar{h}_s[n] \quad (5.5)$$

derived in (2.58) is expanded to

$$\begin{aligned} y_{\text{BB}}^{\text{IMD2}}[n] &= \eta \left[(x_{\text{BB}}[n] * h_{\text{BB}}^{\text{TxL}}[n]) \cdot (x_{\text{BB}}[n] * h_{\text{BB}}^{\text{TxL}}[n])^* \right] * \bar{h}_s[n] \\ &= \eta \left[\sum_{m_1=0}^{M-1} \sum_{m_2=0}^{M-1} h_{\text{BB}}^{\text{TxL}}[m_1] h_{\text{BB}}^{\text{TxL}*}[m_2] x_{\text{BB}}[n - m_1] x_{\text{BB}}^*[n - m_2] \right] * \bar{h}_s[n] \\ &= \eta \left[\sum_{m_1=0}^{M-1} \sum_{m_2=0}^{M-1} \tilde{h}_{\text{BB}}^{\text{TxL}}[m_1, m_2] x_{\text{BB}}[n - m_1] x_{\text{BB}}^*[n - m_2] \right] * \bar{h}_s[n] \end{aligned} \quad (5.6)$$

which shows the underlying truncated Volterra-kernel structure with the two dimensional impulse response $\tilde{h}_{\text{BB}}^{\text{TxL}}[m_1, m_2]$ of the IMD2 interference problem.

For the estimation of the IMD2 interference contained in (2.58), the wanted Rx signal acts as noise and is therefore combined with the noise signal to the noise term $v'_{\text{BB}}[n]$. Inserting (5.6) into the model of the total received signal (2.58) results in the truncated Volterra-kernel model

$$\tilde{y}_{\text{BB}}^{\text{Tot}}[n] = \eta \left[\sum_{m_1=0}^{M-1} \sum_{m_2=0}^{M-1} \tilde{h}_{\text{BB}}^{\text{TxL}}[m_1, m_2] x_{\text{BB}}[n - m_1] x_{\text{BB}}^*[n - m_2] \right] * \bar{h}_s[n] + v'_{\text{BB}}[n] \quad (5.7)$$

of the total received signal. The model (5.6) is the foundation for the Hammerstein-, and Volterra model based IMD2 interference cancellation which are presented in Section 5.3.1 and Section 5.3.2, respectively.

5.3.1 Hammerstein Model

The IMD2 model (5.6) incorporates M^2 coefficients to estimate one IMD2 interference sample. To lower the computational complexity of this Volterra model based cancellation approach, the authors in [73] derived a low-complexity cancellation structure. Setting the indexes $m_1 = m_2 = m$ in (5.6) means neglecting the cross terms of the two dimensional impulse response $\tilde{h}_{\text{BB}}^{\text{TxL}}[m_1, m_2]$. Therefore only the diagonal elements of $\tilde{h}_{\text{BB}}^{\text{TxL}}[m_1, m_2]$ are used. The resulting simplified model¹ with reduced complexity becomes

$$\begin{aligned} \bar{y}_{\text{BB}}^{\text{IMD2}}[n] &= \eta \left[\sum_{m=0}^{M-1} \tilde{h}_{\text{BB}}^{\text{TxL}}[m, m] |x_{\text{BB}}[n - m]|^2 \right] * \bar{h}_s[n] \\ &= \bar{\mathbf{h}}^T \bar{\mathbf{x}}[n] * \bar{h}_s[n], \end{aligned} \quad (5.8)$$

where

$$\bar{\mathbf{h}} = \eta [h_0 h_0^*, h_1 h_1^*, \dots, h_{M-1} h_{M-1}^*]^T \quad (5.9)$$

¹This low complexity model assumes a frequency-flat Tx-to-Rx response. This assumption is only valid for Tx signals with very narrow bandwidth.

5 Adaptive IMD2 Cancellation

and

$$\bar{\mathbf{x}}[n] = \left[|x_{\text{BB}}[n]|^2, |x_{\text{BB}}[n-1]|^2, \dots, |x_{\text{BB}}[n-M+1]|^2 \right]^T. \quad (5.10)$$

This Hammerstein model assumption is used in [22] to perform a digital IMD2 interference cancellation. The envelope-squaring nonlinearity is applied to the BB transmit samples before the signal is convoluted with the diagonal elements of the two-dimensional leakage path impulse response which is mainly determined by the duplexer. Another interesting case is given if the duplexer is perfectly frequency flat in the Tx signal frequency range which implies that all duplexer impulse response coefficients except one are zero [21]. Even for narrowband Tx signals used e.g. in UMTS this only holds approximately, but in general for wide-band LTE signals this is not valid. However, assuming a frequency flat duplexer with the signal delay δT_s where $\delta \geq 0$ is an integer number and T_s the sampling time, the model (5.6) is equivalent to

$$\hat{y}_{\text{BB}}^{\text{IMD2}}[n] = \left(h_\delta |x_{\text{BB}}[n-\delta]|^2 \right) * \bar{h}_s[n], \quad (5.11)$$

with $h_\delta = \eta \tilde{h}_{\text{BB}}^{\text{TxL}}[\delta, \delta]$. By allowing a fractional signal delay (e.g. $\delta = 2.4$), which can be approximated by an LMS adaptive filter [22], (5.11) changes to

$$\hat{y}_{\text{BB}}^{\text{IMD2}}[n] = (\mathbf{h}'^T \bar{\mathbf{x}}[n]) * \bar{h}_s[n]. \quad (5.12)$$

In this approximation, the vector \mathbf{h}' accounts for the fractional delay. Interestingly, the structure of (5.12) is the same as in (5.8), although the underlying assumptions are fundamentally different. The adaptive IMD2 interference regeneration may be performed with the ϵ -NLMS algorithm (Algorithm 1) where the interference replica generation

$$\hat{y}_{\text{AC}}[n] = (\bar{\mathbf{x}}^T[n] \mathbf{w}[n-1]) * \bar{h}_s[n] \quad (5.13)$$

contains the channel-select-, and DC filtering, and the length M coefficient vector $\mathbf{w}[n]$. Using $d_{\text{AC}}[n]$ as the channel-select- and DC filtered total received signal, the error signal

$$e_{\text{AC}}[n] = d_{\text{AC}}[n] - \hat{y}_{\text{AC}}[n] \quad (5.14)$$

is used for the adaptive coefficient update

$$\mathbf{w}[n] = \mathbf{w}[n-1] + \frac{\mu e_{\text{AC}}[n] \bar{\mathbf{x}}_s^*[n]}{\epsilon + \bar{\mathbf{x}}_s^H[n] \bar{\mathbf{x}}_s[n]} \quad (5.15)$$

to employ an estimate of the IMD2 interference. It has to be highlighted, that the convolution of the adaptive filter output signal with $\bar{h}_s[n]$ introduces a signal delay due to the group delay of the CSF. This signal delay has to be taken into account in the coefficient update equation (5.15) to achieve a time-alignment between the error signal e_{AC} and the input signal vector. This is achieved by filtering the input signal with the CSF

$$\bar{x}_s[n] = \left(|x_{\text{BB}}[n]|^2 - \sigma_x^2 \right) * h_s[n]. \quad (5.16)$$

The DC cancellation in the adaptive filter input signal (5.16) is achieved by subtracting the expectation value

$$\sigma_x^2 = E \left\{ |x_{\text{BB}}[n]|^2 \right\} \quad (5.17)$$

of the squared Tx signal envelope. In a real application this DC value has to be estimated. By using (5.16), the input signal vector

$$\bar{\mathbf{x}}_s[n] = [\bar{x}_s[n], \bar{x}_s[n-1], \dots, \bar{x}_s[n-M+1]]^T \quad (5.18)$$

can be formed which contains the DC canceled and channel-select filtered squared Tx signal envelope. Using this input signal vector, the IMD2 replica generation (5.13) may be reformulated as

$$\hat{y}_{AC}[n] = \bar{\mathbf{x}}_s^T[n] \mathbf{w}[n-1]. \quad (5.19)$$

The final Hammerstein model based LMS algorithm for the IMD2 interference cancel-

Initialization:

$$0 < \mu < 2$$

$$\epsilon > 0$$

$$\mathbf{w}[-1] = \mathbf{0}$$

$$\sigma_x^2 = E \{ |x_{BB}[n]|^2 \}$$

for $n = 0, 1, 2, \dots$ **do**

$$\bar{x}_s[n] = (|x_{BB}[n]|^2 - \sigma_x^2) * h_s[n]$$

$$\bar{\mathbf{x}}_s[n] = [\bar{x}_s[n], \bar{x}_s[n-1], \dots, \bar{x}_s[n-M+1]]^T$$

$$\hat{y}_{AC}[n] = \bar{\mathbf{x}}_s^T[n] \mathbf{w}[n-1]$$

$$e_{AC}[n] = d_{AC}[n] - \hat{y}_{AC}[n]$$

$$\mathbf{w}[n] = \mathbf{w}[n-1] + \frac{\mu e_{AC}[n] \bar{\mathbf{x}}_s[n]}{\epsilon + \bar{\mathbf{x}}_s^H[n] \bar{\mathbf{x}}_s[n]}$$

end

Algorithm 3: Hammerstein model based ϵ -NLMS algorithm to for the IMD2 interference cancellation. The algorithm is designed for frequency-flat Tx-to-Rx responses.

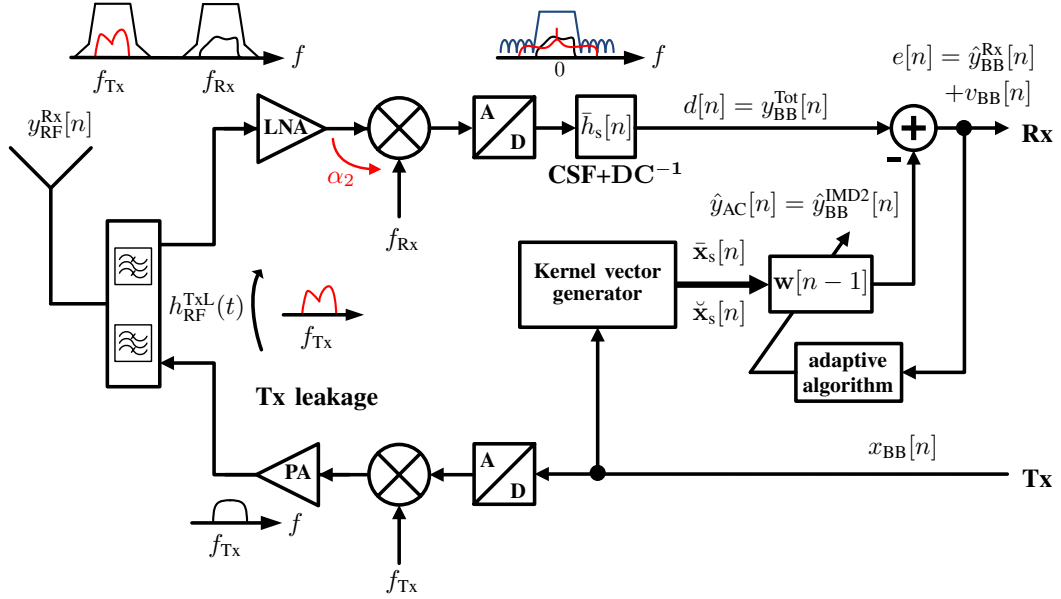


Figure 5.1: Block diagram of the polynomial adaptive filter.

lation is summarized in Algorithm 3. Fig. 5.1 shows the adaptive filter structure with the kernel generator to form the nonlinear input signal vector $\tilde{\mathbf{x}}_s[n]$.

5.3.2 Truncated Volterra Model

The IMD2 interference is a nonlinear interference including memory. This results from the fact that the Tx signal first leaks through the frequency-selective duplexer (which introduces a memory effect) and afterwards experiences the second-order nonlinearity of the mixer. By using the FIR Tx-to-Rx leakage channel approximation, the IMD2 interference model (5.5) may be reformulated into a linear estimation problem [23]. Approximating the duplexer by an FIR system of length M

$$h_{\text{BB}}^{\text{TxL}}[n] = [h_0, h_1, h_2, \dots, h_{M-1}]^T, \quad (5.20)$$

the model (5.6) may be rewritten to

$$\begin{aligned} y_{\text{BB}}^{\text{IMD2}}[n] &= \eta \left[\sum_{m_1=0}^{M-1} \sum_{m_2=0}^{M-1} \tilde{h}_{\text{BB}}^{\text{TxL}}[m_1, m_2] x_{\text{BB}}[n - m_1] x_{\text{BB}}^*[n - m_2] \right] * \bar{h}_s[n] \\ &= \left(\tilde{\mathbf{h}}^T[n] \tilde{\mathbf{x}}[n] \right) * \bar{h}_s[n] \end{aligned} \quad (5.21)$$

which leads for e.g. $M = 4$ to the coefficient vector

$$\begin{aligned} \tilde{\mathbf{h}}[n] &= \eta [h_0 h_0^*, h_1 h_1^*, h_2 h_2^*, h_3 h_3^*, \\ &h_0 h_1^*, h_0 h_2^*, h_0 h_3^*, h_1 h_2^*, h_1 h_3^*, h_2 h_3^*, \\ &h_1 h_0^*, h_2 h_0^*, h_3 h_0^*, h_2 h_1^*, h_3 h_1^*, h_3 h_2^*]^T \end{aligned} \quad (5.22)$$

and the corresponding Tx-kernel vector

$$\begin{aligned} \tilde{\mathbf{x}}[n] &= [x_{\text{BB}}[n] x_{\text{BB}}^*[n], x_{\text{BB}}[n-1] x_{\text{BB}}^*[n-1], x_{\text{BB}}[n-2] x_{\text{BB}}^*[n-2], \\ &x_{\text{BB}}[n-3] x_{\text{BB}}^*[n-3], x_{\text{BB}}[n] x_{\text{BB}}^*[n-1], x_{\text{BB}}[n] x_{\text{BB}}^*[n-2], \\ &x_{\text{BB}}[n] x_{\text{BB}}^*[n-3], x_{\text{BB}}[n-1] x_{\text{BB}}^*[n-2], x_{\text{BB}}[n-1] x_{\text{BB}}^*[n-3], \\ &x_{\text{BB}}[n-2] x_{\text{BB}}^*[n-3], x_{\text{BB}}[n-1] x_{\text{BB}}^*[n], x_{\text{BB}}[n-2] x_{\text{BB}}^*[n], \\ &x_{\text{BB}}[n-3] x_{\text{BB}}^*[n], x_{\text{BB}}[n-2] x_{\text{BB}}^*[n-1], x_{\text{BB}}[n-3] x_{\text{BB}}^*[n-1], \\ &x_{\text{BB}}[n-3] x_{\text{BB}}^*[n-2]]^T \end{aligned} \quad (5.23)$$

with dimension M^2 . Both vectors have M real valued and $M^2 - M$ complex entries. By using the identity

$$\begin{aligned} x_{\text{BB}}[n] x_{\text{BB}}^*[n-1] h_0 h_1^* + x_{\text{BB}}[n-1] x_{\text{BB}}^*[n] h_1 h_0^* &= \\ &= 2 \left(\Re \{ x_{\text{BB}}[n] x_{\text{BB}}^*[n-1] \} \Re \{ h_0 h_1^* \} \right. \\ &\quad \left. - \Im \{ x_{\text{BB}}[n] x_{\text{BB}}^*[n-1] \} \Im \{ h_0 h_1^* \} \right), \end{aligned} \quad (5.24)$$

the complex scalar-product in (5.21) may be rewritten as a scalar-product with the real valued vectors

$$\begin{aligned} \tilde{\mathbf{h}}'[n] &= \eta [h_0 h_0^*, h_1 h_1^*, h_2 h_2^*, h_3 h_3^*, \\ &2\Re \{ h_0 h_1^* \}, 2\Re \{ h_0 h_2^* \}, 2\Re \{ h_0 h_3^* \}, 2\Re \{ h_1 h_2^* \}, 2\Re \{ h_1 h_3^* \}, \\ &2\Re \{ h_2 h_3^* \}, 2\Im \{ h_1 h_0^* \}, 2\Im \{ h_2 h_0^* \}, 2\Im \{ h_3 h_0^* \}, \\ &2\Im \{ h_2 h_1^* \}, 2\Im \{ h_3 h_1^* \}, 2\Im \{ h_3 h_2^* \}]^T \end{aligned} \quad (5.25)$$

and

$$\begin{aligned}
 \tilde{\mathbf{x}}'[n] = & [x_{\text{BB}}[n]x_{\text{BB}}^*[n], x_{\text{BB}}[n-1]x_{\text{BB}}^*[n-1], x_{\text{BB}}[n-2]x_{\text{BB}}^*[n-2], \\
 & x_{\text{BB}}[n-3]x_{\text{BB}}^*[n-3], \Re\{x_{\text{BB}}[n]x_{\text{BB}}^*[n-1]\}, \Re\{x_{\text{BB}}[n]x_{\text{BB}}^*[n-2]\}, \\
 & \Re\{x_{\text{BB}}[n]x_{\text{BB}}^*[n-3]\}, \Re\{x_{\text{BB}}[n-1]x_{\text{BB}}^*[n-2]\}, \\
 & \Re\{x_{\text{BB}}[n-1]x_{\text{BB}}^*[n-3]\}, \Re\{x_{\text{BB}}[n-2]x_{\text{BB}}^*[n-3]\}, \\
 & \Im\{x_{\text{BB}}[n]x_{\text{BB}}^*[n-1]\}, \Im\{x_{\text{BB}}[n]x_{\text{BB}}^*[n-2]\}, \\
 & \Im\{x_{\text{BB}}[n]x_{\text{BB}}^*[n-3]\}, \Im\{x_{\text{BB}}[n-1]x_{\text{BB}}^*[n-2]\}, \\
 & \Im\{x_{\text{BB}}[n-1]x_{\text{BB}}^*[n-3]\}, \Im\{x_{\text{BB}}[n-2]x_{\text{BB}}^*[n-3]\}]^T
 \end{aligned} \tag{5.26}$$

where the minus sign of the imaginary part in (5.24) is included into the coefficients to be estimated. For the estimation of the IMD2 interference with the normalized LMS algorithm, the replica

$$\hat{y}_{\text{AC}}[n] = (\tilde{\mathbf{x}}'^T[n]\mathbf{w}[n-1]) * \bar{h}_s[n] \tag{5.27}$$

is used to generate the error signal

$$e_{\text{AC}}[n] = d_{\text{AC}}[n] - \hat{y}_{\text{AC}}[n] \tag{5.28}$$

which is needed for the coefficient update

$$\mathbf{w}[n] = \mathbf{w}[n-1] + \frac{\mu e_{\text{AC}}[n]\tilde{\mathbf{x}}_s'^*[n]}{\epsilon + \tilde{\mathbf{x}}_s'^H[n]\tilde{\mathbf{x}}_s'[n]}. \tag{5.29}$$

Also in the Volterra kernel based LMS update equation the signal delay introduced by the convolution with the filter $\bar{h}_s[n]$ in (5.27) has to be considered. This may be done by introducing the new input signal vector

$$\begin{aligned}
 \check{\mathbf{x}}_s[n] = & [|x[n]|^2 - \sigma_x^2, |x[n-1]|^2 - \sigma_x^2, |x[n-2]|^2 - \sigma_x^2, \\
 & |x[n-3]|^2 - \sigma_x^2, \Re\{x[n]x[n-1]^*\}, \Re\{x[n]x[n-2]^*\}, \\
 & \Re\{x[n]x[n-3]^*\}, \Re\{x[n-1]x[n-2]^*\}, \\
 & \Re\{x[n-1]x[n-3]^*\}, \Re\{x[n-2]x[n-3]^*\}, \\
 & \Im\{x[n]x[n-1]^*\}, \Im\{x[n]x[n-2]^*\}, \\
 & \Im\{x[n]x[n-3]^*\}, \Im\{x[n-1]x[n-2]^*\}, \\
 & \Im\{x[n-1]x[n-3]^*\}, \Im\{x[n-2]x[n-3]^*\}]^T * h_s[n]
 \end{aligned} \tag{5.30}$$

which includes an implicit DC cancellation and the channel-select filtering. Unfortunately, in the Volterra LMS case the input signal vector is not a delay-line vector. Consequently, each of the M^2 entries of the vector $\check{\mathbf{x}}_s[n]$ needs to be filtered by $h_s[n]$ separately. This significantly increases the computational complexity of the Volterra kernel LMS algorithm. By using the new introduced input signal vector $\check{\mathbf{x}}_s[n]$ which incorporates the DC cancellation and the channel-select filtering, the replica generation (5.27) may be rewritten to

$$\hat{y}_{\text{AC}}[n] = \check{\mathbf{x}}_s^T[n]\mathbf{w}[n-1]. \tag{5.31}$$

The final Volterra kernel LMS algorithm is summarized in Algorithm 4 and the adaptive filter structure is depicted in Fig. 5.1.

Initialization:

$$0 < \mu < 2$$

$$\epsilon > 0$$

$$\mathbf{w}[-1] = \mathbf{0}$$

for $n = 0, 1, 2, \dots$ **do**

$$\left| \begin{array}{l} \hat{y}_{AC}[n] = \check{\mathbf{x}}_s^T[n] \mathbf{w}[n-1] \\ e_{AC}[n] = d_{AC}[n] - \hat{y}_{AC}[n] \\ \mathbf{w}[n] = \mathbf{w}[n-1] + \frac{\mu e_{AC}[n] \check{\mathbf{x}}_s^*[n]}{\epsilon + \check{\mathbf{x}}_s^H[n] \check{\mathbf{x}}_s[n]} \end{array} \right.$$

end

Algorithm 4: Volterra kernel based ϵ -NLMS algorithm for the IMD2 interference cancellation with frequency-selective Tx-to-Rx responses.

5.4 Wiener Model Based Cancellation

In this section the nonlinear Wiener model is explored for the development of a nonlinear LMS/RLS type adaptive filter to estimate the IMD2 interference. The goal is to reduce the computational complexity of the Volterra kernel based adaptive filter described in Section 5.3.2. Especially for highly frequency-selective duplexer responses a large number of FIR coefficients is required to model the Tx-to-Rx response. The Wiener model uses a static nonlinearity at the output of the adaptive filter which has the advantage that less coefficients are necessary in the estimation process compared to a Volterra kernel based adaptive filter [25]. In case of the IMD2 interference, this static nonlinearity is the envelope-squaring operation and the Tx-to-Rx path is estimated by an underlying FIR model.

The following differences between the Wiener-, Hammerstein-, and Volterra models for the adaptive IMD2 interference cancellation may be identified.

- In LTE scenarios, the Tx-to-Rx leakage channel may be heavily frequency-selective because of the duplexer stop-band. Therefore, the Hammerstein model which assumes a frequency-flat leakage channel is not applicable. Consequently, the use of a Volterra-, or Wiener model based cancellation approach is necessary.
- With increasing frequency-selectivity in general more FIR filter coefficients are necessary to model the leakage channel. The computational complexity of the Wiener model adaptive filter increases with the order $\mathcal{O}(M)$, whereas the complexity of the Volterra model based cancellation increases by $\mathcal{O}(M^2)$.
- Due to the envelope-squaring at the output of the Wiener model, the IMD2 related DC is automatically regenerated in the interference replica signal. This DC needs to be removed afterwards because the main receiver employs a DC-cancellation.
- The output signal of the Wiener filter using the envelope-squaring nonlinearity at the output is always real valued. Reasoned by that, it is impossible to estimate the complex valued IMD2 interference in the I-, and Q-path simultaneously with one combined adaptive filter.

However, the interference replica model described below will show that the Q-path IMD2 interference is only a scaled version of the I-path interference. Therefore, once the I-path IMD2 interference is estimated by the Wiener model adaptive filter, the I-path replica signal may be used as a reference to estimate the Q-path IMD2 interference.

5.4.1 Interference Replica Model

For the adaptive filter development to cancel the IMD2 interference in the digital BB, the interference model (2.58) is rewritten to the form

$$\begin{aligned}
 y_{\text{BB}}^{\text{Tot}}[n] &= \underbrace{\frac{\alpha_2^{\text{I}}}{2} |A_{\text{LNA}} A_{\text{PA}} x_{\text{BB}}[n] * h_{\text{BB}}^{\text{TxL}}[n]|^2 * \bar{h}_{\text{s}}[n]}_{y_{\text{BB}}^{\text{IMD2,I}}[n]} \\
 &+ j \underbrace{\frac{\alpha_2^{\text{Q}}}{2} |A_{\text{LNA}} A_{\text{PA}} x_{\text{BB}}[n] * h_{\text{BB}}^{\text{TxL}}[n]|^2 * \bar{h}_{\text{s}}[n]}_{y_{\text{BB}}^{\text{IMD2,Q}}[n]} + v'_{\text{BB}}[n]
 \end{aligned} \tag{5.32}$$

5 Adaptive IMD2 Cancellation

where the complex valued wanted signal and the noise signal are combined in $v'_{\text{BB}}[n]$. Assuming $\alpha_2^{\text{I}} > 0$, and approximating the duplexer impulse response $h_{\text{BB}}^{\text{TxL}}[n]$ by the FIR impulse response vector $\mathbf{h}_{\text{BB}}^{\text{TxL}}$ of length M , we may express the I-path IMD2 interference as

$$y_{\text{BB}}^{\text{IMD2,I}}[n] = \left(|\mathbf{x}^T[n] \mathbf{h}_{\text{I}}|^2 \right) * \bar{h}_s[n] \quad (5.33)$$

where \mathbf{h}_{I} incorporates $\mathbf{h}_{\text{BB}}^{\text{TxL}}$ and all scalar scaling factors in the I-path. The used vector $\mathbf{x}[n]$ is the complex valued tapped delay-line input signal vector

$$\mathbf{x}[n] = [x_{\text{BB}}[n], x_{\text{BB}}[n-1], \dots, x_{\text{BB}}[n-M+1]]^T. \quad (5.34)$$

As can be seen from (5.32), the Q-path IMD2 interference is just a scaled version of the I-path IMD2 interference (with possible sign change). Therefore, the total received signal model (5.32) may be rewritten to

$$y_{\text{BB}}^{\text{Tot}}[n] = y_{\text{BB}}^{\text{IMD2,I}}[n] + j h_{\text{Q}} y_{\text{BB}}^{\text{IMD2,I}}[n] + v'_{\text{BB}}[n] \quad (5.35)$$

using the real valued scaling factor h_{Q} for the Q-path IMD2 interference. Motivated by the model (5.35), the I-path IMD2 interference replica model is

$$\hat{y}_{\text{AC,I}}[n] = \left(|\mathbf{x}^T[n] \mathbf{w}_{\text{I}}[n]|^2 \right) * \bar{h}_s[n], \quad (5.36)$$

using the adaptive filter coefficient vector $\mathbf{w}_{\text{I}}[n]$ and delay-line input signal vector $\mathbf{x}[n]$ of length M . The replica model comprises an adaptive Wiener model FIR filter where the output signal is DC-, and channel-select filtered. The Q-path IMD2 interference is generated by estimating the scaling parameter h_{Q} using a linear single-tap LMS or RLS algorithm which uses the estimated I-path IMD2 interference as reference input. The proposed adaptive filter structure to cancel the IMD2 interference in the digital BB is shown in Fig. 5.2. For the case $\alpha_2^{\text{I}} < 0$, the sign of the desired signal in the I-path $d_{\text{I}}[n]$ and the sign of the replica signal of the adaptive filter need to be changed. The sign of α_2^{I} may be estimated by evaluating the cross-correlation function

$$\hat{\phi}_{d_{\text{I}},s}[\tau] = \frac{1}{N} \sum_{k=0}^{N-1} d_{\text{I}}[k] s[k-\tau] \quad (5.37)$$

using N samples of the signals $d_{\text{I}}[n]$ and the sequence

$$s[n] = |x_{\text{BB}}[n]|^2 - E \left\{ |x_{\text{BB}}[n]|^2 \right\} = |x_{\text{BB}}[n]|^2 - \sigma_x^2. \quad (5.38)$$

The cross-correlation function may also be determined by using the recursive formulation [74]

$$\hat{\phi}_{d_{\text{I}},s}[\tau, k] = \hat{\phi}_{d_{\text{I}},s}[\tau, k-1] + \frac{1}{k+1} \left(d_{\text{I}}[k-\tau] s[k] - \hat{\phi}_{d_{\text{I}},s}[\tau, k-1] \right), \quad (5.39)$$

which is equivalent to (5.37) for $k \rightarrow N$. The sign of α_2^{I} is then extracted from the cross-correlation function. If the maximum peak value is positive, then $\alpha_2^{\text{I}} > 0$, and if it is negative then $\alpha_2^{\text{I}} < 0$. In the same manner the delay between the received signal $d_{\text{I}}[n]$

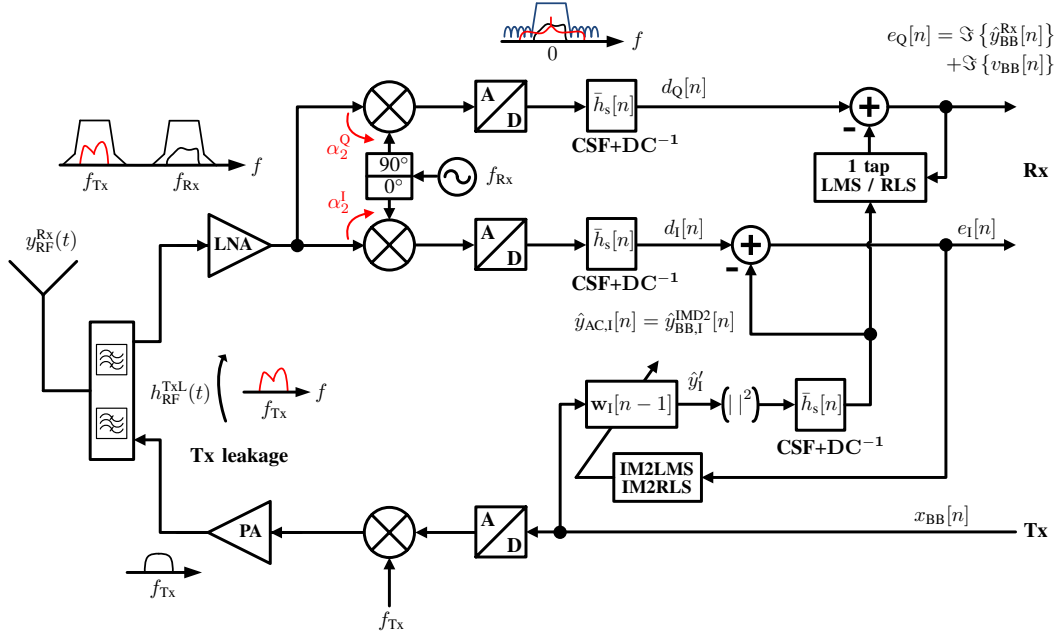


Figure 5.2: Block diagram depicting an RF transceiver operating in FDD mode which experiences a second-order intermodulation distortion in the receiver due to the transmitter leakage signal and the Rx mixer RF-to-LO terminal coupling. A nonlinear LMS/RLS-type adaptive filter is used to estimate the I-path IMD2 interference. The Q-path IMD2 interference is estimated with a linear 1-tap LMS/RLS adaptive filter which uses the estimated I-path IMD2 replica as reference input.

and the transmit signal $x_{\text{BB}}[n]$ is estimated. For this, the delay

$$\tau_{\text{comp}} = \arg \max_{\tau} \left| \hat{\phi}_{d_I, s}[\tau] \right| \quad (5.40)$$

has to be determined. The signals need to be aligned to compensate the time delay τ_{comp} before they are fed into the adaptive filter. Based on the I-path IMD2 interference model (5.36) nonlinear LMS-, and RLS type adaptive filters will be derived in the next sections.

5.4.2 The IMD2 Problem from an Optimization Point of View

Using the IMD2 interference model (5.35) and the I-path IMD2 replica signal (5.36), the IMD2 replica model may be formulated as

$$\begin{aligned} \hat{y}_{\text{AC}}[n] &= \hat{y}_{\text{AC}, \text{I}}[n] + j\hat{y}_{\text{AC}, \text{Q}}[n] \\ &= \hat{y}_{\text{AC}, \text{I}}[n] + jw_{\text{Q}} \hat{y}_{\text{AC}, \text{I}}[n] \\ &= \left(\mathbf{x}^T[n] \mathbf{w}_{\text{I}} \right)^2 * \bar{h}_{\text{s}}[n] + jw_{\text{Q}} \left(\mathbf{x}^T[n] \mathbf{w}_{\text{I}} \right)^2 * \bar{h}_{\text{s}}[n], \end{aligned} \quad (5.41)$$

where the coefficient vector \mathbf{w}_{I} represents the estimated impulse response \mathbf{h}_{I} . It can be observed, that the IMD2 interference replica generation includes the estimation of the

5 Adaptive IMD2 Cancellation

I-path coefficient vector \mathbf{w}_I and the estimation of the scalar Q-path scaling factor w_Q . Once the vector \mathbf{w}_I is successfully estimated, the scalar w_Q may be easily estimated using a linear estimator. The idea of the Wiener model based IMD2 interference estimation is to estimate the I-path coefficient vector \mathbf{w}_I by a nonlinear estimation algorithm and use the obtained I-path IMD2 replica signal to estimate the Q-path scaling factor w_Q . To get insight into the underlying optimization problem when the I-path IMD2 interference (and therefore the coefficient vector \mathbf{w}_I) is estimated, the I-path LS cost function w/o DC cancellation

$$J_{LS}[n] = \sum_{i=0}^n \left| d_I[i] - |\mathbf{x}^T[n]\mathbf{w}_I|^2 * h_s[n] \right|^2, \quad (5.42)$$

and w/ DC cancellation in the main receiver and replica path

$$J_{LS}[n] = \sum_{i=0}^n \left| d_{AC,I}[i] - |\mathbf{x}^T[n]\mathbf{w}_I|^2 * \bar{h}_s[n] \right|^2 \quad (5.43)$$

is inspected. Again, the index AC in $d_{AC,I}$ indicates that the DC is canceled from the total received signal. In Fig. 5.3, the cost function without DC cancellation, for an example impulse response $\mathbf{h}_I = [1, 0.5]^T$ is presented. Furthermore, the estimated coefficients $w_{I,0}$ and $w_{I,1}$ are constrained to be real valued. Two global minimum points and a local

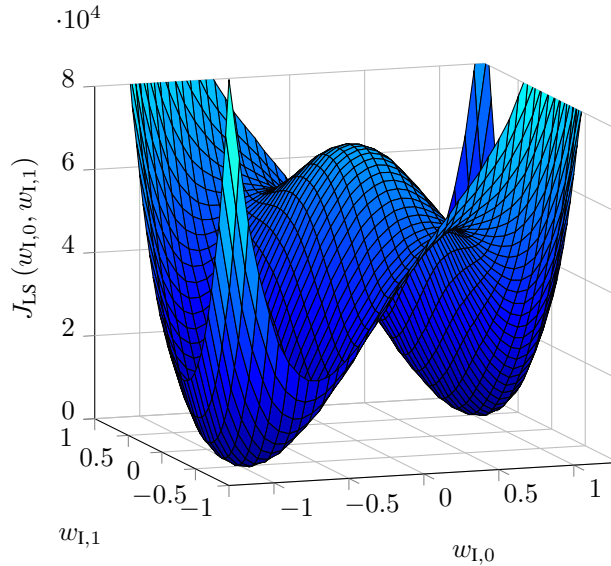


Figure 5.3: Surface of the LS cost function (5.42) w/o DC cancellation.

maximum at the origin $\mathbf{w}_I = \mathbf{0}$ can be observed. The two solutions $\mathbf{w}_{I,1} = [1, 0.5]^T$, and $\mathbf{w}_{I,2} = [-1, -0.5]^T$ minimize the cost function which can be explained with the absolute-squaring nature of the IMD2 interference. Both solutions lead to the same IMD2 replica signal.

Second-Order Condition

The complex Hessian [65, 62] of the cost function (5.42) w/o DC cancellation at the coefficient value $\mathbf{w}_I = \mathbf{0}$ becomes

$$\begin{aligned} H_I &= \frac{\partial}{\partial \mathbf{w}_I} \left[\frac{\partial J_{LS}}{\partial \mathbf{w}_I^*} \right]^T \Big|_{\mathbf{w}_I = \mathbf{0}} \\ &= \sum_{i=0}^n \lambda^{n-i} [-2 d_I[i] (\mathbf{x}^*[i] \mathbf{x}^T[i]) * h_s[i]]. \end{aligned} \quad (5.44)$$

If the desired signal $d_I[n]$ contains the DC (when the receiver has no DC filtering), then $E\{d_I[n]\} \geq 0$. The matrix $E\{\mathbf{x}^*[i] \mathbf{x}^T[i]\}$ is Hermitian and positive semi-definite [58]. Therefore, because of the minus sign the Hessian matrix becomes negative semi-definite as depicted with the local maximum in Fig. 5.3.

In case of DC filtering in the main receiver, $E\{d_I[n]\} = 0$, and the Hessian matrix (5.44) at $\mathbf{w}_I = \mathbf{0}$ is not negative semi-definite anymore. Then the local maximum becomes a saddle-point like depicted in Fig. 5.4.

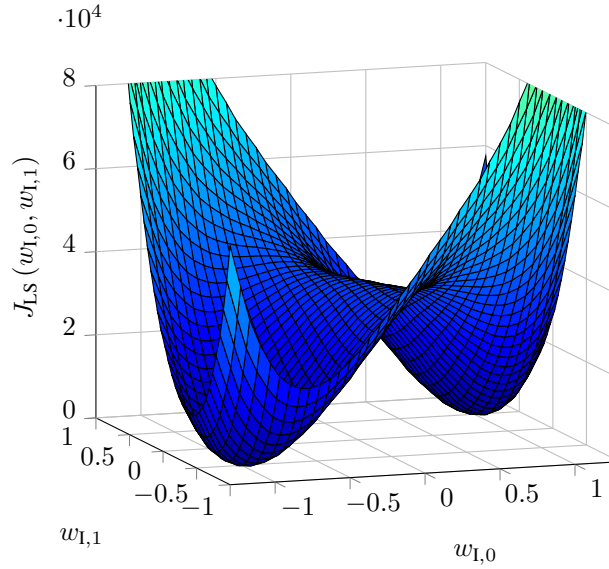


Figure 5.4: Surface of the LS cost function (5.43) w/ DC cancellation.

5.4.3 Multiple Solutions

In the cost functions depicted in Fig. 5.3 and Fig. 5.4, the estimated impulse response coefficients w_0 and w_1 (omitting the index I for the I-path) are constrained to be real valued. It can be observed that the two solutions $\mathbf{w}_0 = [1, 0.5]^T$, and $\mathbf{w}_1 = [-1, -0.5]^T$ minimize the cost function. The existence of multiple solutions can be explained by the absolute-squaring nature of the IMD2 interference. If the coefficients are allowed to be complex valued, all coefficient pairs $\{w_0, w_1\}$ converge to $|w_0^{\text{end}}| = |h_0|$ and $|w_1^{\text{end}}| = |h_1|$. This behavior is visualized in Fig. 5.5 where the convergence of the coefficients with the 10 different initializations $\mathbf{w}_i[-1] = [10^{-3}, 0]^T \exp(j2\pi/10i)$ for $i = 0 \dots 9$ is depicted. The coefficients are estimated with the nonlinear IM2RLS algorithm which will be developed in Section 5.4.7.

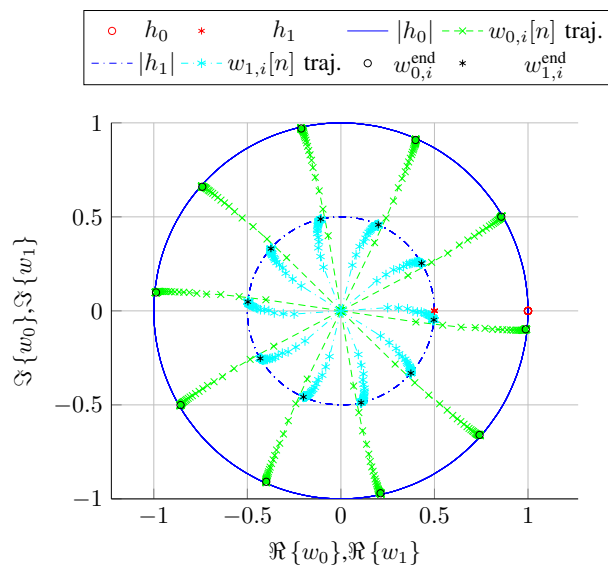


Figure 5.5: Multiple solutions of the coefficient vector for the IMD2 interference estimation.

5.4.4 Wiener-Model LMS Based IMD2 Cancellation (IM2LMS)

In this section, a nonlinear Wiener model based LMS type adaptive algorithm (IM2LMS) to cancel the IMD2 interference is presented. In LMS based adaptive filters, the current filter output value is obtained by using the coefficient vector estimate of the previous iteration. This *a-priori* estimate $\mathbf{w}_I[n-1]$ is incorporated into the interference replica model (5.36) to develop a nonlinear LMS type adaptive filter to cancel the I-path IMD2 interference in the digital baseband. Using an implicit DC cancellation, the DC value $E\left\{|\mathbf{x}^T[n]\mathbf{w}_I|^2\right\} = \mathbf{w}_I^T E\left\{\mathbf{x}[n]\mathbf{x}^H[n]\right\}\mathbf{w}_I^*$ which is generated by the envelope-squaring is implicitly subtracted within the adaptive filter. With this implicit DC cancellation approach, the DC-filtering at the output of the interference replica model (5.36) may be replaced. This leads to the I-path IMD2 replica generation

$$\begin{aligned}\hat{y}_{AC,I}[n] &= \left(|\mathbf{x}^T[n]\mathbf{w}_I[n-1]|^2\right) * \bar{h}_s[n] \\ &= \left[\left(|\mathbf{x}^T[n]\mathbf{w}_I[n-1]|^2 - \mathbf{w}_I^T[n-1]E\left\{\mathbf{x}[n]\mathbf{x}^H[n]\right\}\mathbf{w}_I^*[n-1]\right)\right] * h_s[n] \\ &= \left[\left(|\mathbf{x}^T[n]\mathbf{w}_I[n-1]|^2 - \mathbf{w}_I^T[n-1]\mathbf{R}_{\mathbf{xx}}\mathbf{w}_I^*[n-1]\right)\right] * h_s[n] \\ &= \left[\mathbf{w}_I^T[n-1]\left(\mathbf{x}[n]\mathbf{x}^H[n] - \mathbf{R}_{\mathbf{xx}}\right)\mathbf{w}_I^*[n-1]\right] * h_s[n]\end{aligned}\quad (5.45)$$

where the autocorrelation matrix $\mathbf{R}_{\mathbf{xx}} = E\left\{\mathbf{x}[n]\mathbf{x}^H[n]\right\}$ is used². Assuming real valued CSF impulse response coefficients $h_s[n]$, and observing that $d_{AC,I}[i]$ is the desired signal in the I-path, and therefore real valued, the instantaneous squared error cost function based on the error

$$e_{AC,I}[n] = d_{AC,I}[n] - \hat{y}_{AC,I}[n] \quad (5.46)$$

becomes

$$\begin{aligned}J &= |e_{AC,I}[n]|^2 \\ &= |d_{AC,I}[n] - [\mathbf{w}_I^T[n-1]\left(\mathbf{x}[n]\mathbf{x}^H[n] - \mathbf{R}_{\mathbf{xx}}\right)\mathbf{w}_I^*[n-1]] * h_s[n]|^2 \\ &= d_{AC,I}^2[n] - 2d_{AC,I}[n][\mathbf{w}_I^T[n-1]\left(\mathbf{x}[n]\mathbf{x}^H[n] - \mathbf{R}_{\mathbf{xx}}\right)\mathbf{w}_I^*[n-1]] * h_s[n] \\ &\quad + ([\mathbf{w}_I^T[n-1]\left(\mathbf{x}[n]\mathbf{x}^H[n] - \mathbf{R}_{\mathbf{xx}}\right)\mathbf{w}_I^*[n-1]] * h_s[n])^2.\end{aligned}\quad (5.47)$$

To develop a stochastic-gradient LMS type estimation algorithm, the \mathbb{R}^* -derivative (see Section 4.3) of the cost function (5.47) is evaluated which becomes

$$\begin{aligned}\left[\frac{\partial J}{\partial \mathbf{w}_I^*}\right]^T &= [-2d_{AC,I}[n][\mathbf{w}_I^T[n-1]\left(\mathbf{x}[n]\mathbf{x}^H[n] - \mathbf{R}_{\mathbf{xx}}\right)] * h_s[n] \\ &\quad + 2([\mathbf{w}_I^T[n-1]\left(\mathbf{x}[n]\mathbf{x}^H[n] - \mathbf{R}_{\mathbf{xx}}\right)\mathbf{w}_I^*[n-1]] * h_s[n]) \\ &\quad \cdot [\mathbf{w}_I^T[n-1]\left(\mathbf{x}[n]\mathbf{x}^H[n] - \mathbf{R}_{\mathbf{xx}}\right)] * h_s[n]^T.\end{aligned}\quad (5.48)$$

A detailed derivation of the derivative (5.48) incorporating the channel-select filter in the cost function (5.47) is presented in Appendix A.5. By using the IMD2 replica $\hat{y}_{AC,I}[n]$

²An autocorrelation matrix $\mathbf{R}_{\mathbf{xx}}$ is defined for wide-sense stationary signals. Each LTE symbol can be considered as a section of a wide-sense stationary signal. However, subsequent symbols are statistically independent. But it makes sense to introduce an $\mathbf{R}_{\mathbf{xx}}$ because the length of \mathbf{w} is much smaller than the symbol duration.

5 Adaptive IMD2 Cancellation

and the *a priori* FIR filter output $\hat{y}'[n] = \mathbf{x}^T[n]\mathbf{w}_I[n-1]$, the derivative is simplified to

$$\begin{aligned} \left[\frac{\partial J}{\partial \mathbf{w}_I^*} \right]^T &= -(2d_{AC,I}[n] - 2\hat{y}_{AC,I}[n]) \left[[\mathbf{w}_I^T[n-1] (\mathbf{x}[n]\mathbf{x}^H[n] - \mathbf{R}_{xx}) * h_s[n]]^T \right. \\ &= -2e_{AC,I}[n] \left[(\hat{y}'[n]\mathbf{x}^*[n] - \mathbf{R}_{xx}^T \mathbf{w}_I[n-1]) * h_s[n] \right] \end{aligned} \quad (5.49)$$

which leads to the stochastic gradient coefficient update

$$\begin{aligned} \mathbf{w}_I[n] &= \mathbf{w}_I[n-1] - 2\mu \left[\frac{\partial J}{\partial \mathbf{w}_I^*} \right]^T \\ &= \mathbf{w}_I[n-1] + 4\mu e_{AC,I}[n] \left[(\hat{y}'[n]\mathbf{x}^*[n] - \mathbf{R}_{xx}^T \mathbf{w}_I[n-1]) * h_s[n] \right] \end{aligned} \quad (5.50)$$

with the step-size μ .

Normalization of the IM2LMS algorithm

In the IMD2 LMS type adaptive filter, the *a priori* error signal

$$e_{AC,I}[n] = d_{AC,I}[n] - \left[\mathbf{x}^T[n]\mathbf{w}_I[n-1] \right]^2 - \mathbf{w}_I^T[n-1]\mathbf{R}_{xx}\mathbf{w}_I^*[n-1] * h_s[n] \quad (5.51)$$

is used to update the filter coefficients. To analyze the convergence of the LMS type algorithm (5.50) it is beneficial to analyze the relationship between the errors $e_{AC,I}[n]$ and $e_{AC,I}[n+1]$ [58, 66]. For this, a first order Taylor series expansion of the non-holomorphic term $e_{AC,I}[n]$ with respect to the coefficient vector is needed. As a reminder, in the derivation of the ϵ -NLMS (Algorithm 1), the term $e[n]$ was holomorphic and therefore the standard complex derivative was applied to derive the Taylor series expansion. For the nonlinear IM2LMS case, $e_{AC,I}[n]$ is real valued and a function of the complex vector $\mathbf{w}_I[n-1]$. In this case the first-order Taylor expansion becomes (see equation (85) in [67])

$$e_{AC,I}[n+1] \approx e_{AC,I}[n] + 2\Re \left\{ \frac{\partial e_{AC,I}[n]}{\partial \mathbf{w}_I[n-1]} \Delta \mathbf{w}_I[n] \right\} \quad (5.52)$$

and by using the IMD2-nonlinearity $\phi(\cdot) = |\cdot|^2$ and $\hat{y}'[n] = \mathbf{x}^T[n]\mathbf{w}_I[n-1]$ it follows that

$$\begin{aligned} \frac{\partial e_{AC,I}[n]}{\partial \mathbf{w}_I[n-1]} &= - \left(\frac{\partial \phi(\hat{y}')}{\partial \hat{y}'} \frac{\partial \hat{y}'}{\partial \mathbf{w}_I[n-1]} - \mathbf{w}_I^H[n-1]\mathbf{R}_{xx}^T \right) * h_s \\ &= - (\hat{y}'^*[n]\mathbf{x}^T[n] - \mathbf{w}_I^H[n-1]\mathbf{R}_{xx}^T) * h_s. \end{aligned} \quad (5.53)$$

With

$$\Delta \mathbf{w}_I[n] = 4\mu e_{AC,I}[n] \left[(\hat{y}'[n]\mathbf{x}^*[n] - \mathbf{R}_{xx}^T \mathbf{w}_I[n-1]) * h_s[n] \right], \quad (5.54)$$

the first-order Taylor series expansion (5.52) becomes

$$\begin{aligned} e_{AC,I}[n+1] &\approx e_{AC,I}[n] - 2\Re \left\{ \left[(\hat{y}'^*[n]\mathbf{x}^T[n] - \mathbf{w}_I^H[n-1]\mathbf{R}_{xx}^T) * h_s \right] \right. \\ &\quad \cdot 4\mu e_{AC,I}[n] \left[(\hat{y}'[n]\mathbf{x}^*[n] - \mathbf{R}_{xx}^T \mathbf{w}_I[n-1]) * h_s[n] \right] \left. \right\} \\ &\approx \left(1 - 8\mu \left[\left(|\hat{y}'[n]|^2 \mathbf{x}^H[n]\mathbf{x}[n] - 2\Re \{ \hat{y}'^*[n]\mathbf{x}^T[n]\mathbf{R}_{xx}^T \mathbf{w}_I[n-1] \} \right. \right. \right. \\ &\quad \left. \left. \left. + \mathbf{w}_I^H[n-1] (\mathbf{R}_{xx}^T)^2 \mathbf{w}_I[n-1] \right) * h_s[n] \right] \right) e_{AC,I}[n] \\ &\approx (1 - 8\mu\Psi[n]) e_{AC,I}[n], \end{aligned} \quad (5.55)$$

where

$$\begin{aligned} \Psi[n] = & \left(|\hat{y}'[n]|^2 \mathbf{x}^H[n] \mathbf{x}[n] - 2\Re \{ \hat{y}'^*[n] \mathbf{x}^T[n] \mathbf{R}_{\mathbf{xx}}^T \mathbf{w}_I[n-1] \} \right. \\ & \left. + \mathbf{w}_I^H[n-1] (\mathbf{R}_{\mathbf{xx}}^T)^2 \mathbf{w}_I[n-1] \right) * h_s[n]. \end{aligned} \quad (5.56)$$

To maintain convergence [66] of the adaptive filter, the condition

$$|1 - 8\mu\Psi[n]| < 1 \quad (5.57)$$

has to be fulfilled. To guarantee the condition (5.57), two cases have to be considered:

1. $1 - 8\mu\Psi[n] < 1$

which leads to $\mu > 0$ and

2. $1 - 8\mu\Psi[n] > -1$

which results in $\mu < \frac{1}{4\Psi[n]}$.

Combining both limits gives

$$0 < \mu < \frac{1}{4\Psi[n]}. \quad (5.58)$$

Incorporating the factor 4 in (5.50) into the step-size limit, the final normalized IM2LMS algorithm with the regularization parameter ϵ is obtained with Algorithm 5.

Initialization:

$$0 < \mu < \mu_{\tau_g} < \mu_{\max} = 1$$

$$\epsilon > 0$$

$$\mathbf{w}_I[-1] \neq \mathbf{0}$$

$$\mathbf{R}_{\mathbf{xx}} = E \{ \mathbf{xx}^H \}$$

for $n = 0, 1, 2, \dots$ **do**

$$\hat{y}'[n] = \mathbf{x}^T[n] \mathbf{w}_I[n-1]$$

$$\hat{y}_{AC,I}[n] = \left[|\hat{y}'[n]|^2 - \mathbf{w}_I^T[n-1] \mathbf{R}_{\mathbf{xx}} \mathbf{w}_I^*[n-1] \right] * h_s[n]$$

$$e_{AC,I}[n] = d_{AC,I}[n] - \hat{y}_{AC,I}[n]$$

$$\mathbf{w}_I[n] = \mathbf{w}_I[n-1] + \frac{\mu e_{AC,I}[n] \left[(\hat{y}'[n] \mathbf{x}^*[n] - \mathbf{R}_{\mathbf{xx}}^T \mathbf{w}_I[n-1]) * h_s[n] \right]}{\epsilon + \Psi[n]}$$

end

Algorithm 5: Normalized and regularized IM2LMS algorithm (ϵ -IM2LMS) with implicit DC cancellation and regularization.

In the above consideration the influence of the CSF group delay on the maximum allowed step-size is neglected. The group delay τ_g of the CSF delays the adaptive filter output signal which leads to a further reduction of the maximum allowed step size μ_{\max} . The CSF delay has the effect, that changes in the replica signal due to an update of the coefficient vector appear delayed at the output of the adaptive filter. This is similar to a dead-time in control systems where the loop gain needs to be reduced to maintain stability. In [75], the influence of a signal delay in the ϵ -NLMS algorithm as it occurs in the ϵ -IM2LMS algorithm is investigated. The authors derived a delay dependent maximum step size for the ϵ -NLMS algorithm. Using the results from [75] which are

5 Adaptive IMD2 Cancellation

also applicable for the ϵ -IM2LMS algorithm, the final CSF delay dependent maximum step-size becomes

$$\mu_{\tau_g} = \mu_{\max} \sin \left(\frac{\pi}{2(2\tau_g + 1)} \right), \quad (5.59)$$

where the delay τ_g in samples is used. Simulations confirmed that by choosing the maximum step-size according to (5.59), Algorithm 5 remains stable for arbitrary delays τ_g .

The usual choice of the zero-vector as initialization of $\mathbf{w}_I[-1]$ results in a vanishing derivative (5.49) for all n . This is due to the nature of the cost function (5.42) depicted in Fig. 5.3 having a local maximum at $\mathbf{w}_I = \mathbf{0}$ and therefore a vanishing derivative. If the DC is canceled, the cost function (5.43) has a saddle point at $\mathbf{w}_I = \mathbf{0}$ which causes a vanishing derivative, too. Consequently, the Wiener model based algorithm needs to be initialized with $\mathbf{w}_I[-1] \neq \mathbf{0}$. If no prior knowledge about the Tx-to-Rx leakage channel is available, an initialization close to the zero vector, e.g., $\mathbf{w}_I[-1] = [w_{I,0}, 0, 0, \dots, 0]^T$ where $w_{I,0}$ is a small real valued positive number is a reasonable choice.

The derived nonlinear Wiener model based LMS type algorithm uses the autocorrelation matrix to perform an implicit DC cancellation. The implied vector-matrix multiplication increases the computational complexity of the LMS type algorithm and lowers therefore its applicability in real applications. Furthermore, each entry of the coefficient update vector needs to be channel-select filtered which results in further computational load. To overcome these two limitations, reduced complexity variants of Algorithm 5 are developed in the next section.

5.4.5 Reduced Complexity IM2LMS Algorithm

The complexity of the digital IMD2 cancellation is significantly reduced by using the Wiener model instead of the Volterra model. However, the channel-select filtering of the coefficient update vector in the IM2LMS algorithm and the DC cancellation contribute to a much higher complexity compared to the traditional linear LMS. Furthermore, for interference cancellation in RF transceivers the adaptive filter input signal is an SC-FDMA modulated transmit signal. These signals are not wide-sense stationary since subsequent symbols are statistically independent, and therefore the autocorrelation matrix $\mathbf{R}_{\mathbf{xx}}$ is not defined. It still makes sense to introduce an $\mathbf{R}_{\mathbf{xx}}$ because the length of \mathbf{w} is much smaller than the symbol duration, and each LTE symbol can be considered as a section of a wide-sense stationary signal. However, it turned out that the usage of $\sigma_x^2 \mathbf{I}$ instead of $\mathbf{R}_{\mathbf{xx}}$ leads to good cancellation results, which can be used to reduce the complexity of the algorithm. The next sections will address possible complexity reductions for the IM2LMS algorithm.

Reducing the Complexity of the Implicit DC Cancellation

The implicit DC cancellation using the expression $\mathbf{w}_I^T[n-1] \mathbf{R}_{\mathbf{xx}} \mathbf{w}_I^*[n-1]$ increases the complexity to the order $\mathcal{O}(M^2)$. In order to simplify the implicit DC cancellation the expression $\sigma_x^2 \mathbf{I}$ is used instead of $\mathbf{R}_{\mathbf{xx}}$. By using this approximation, the DC value in

steady-state (where $\mathbf{w}_I[n] \approx \mathbf{w}_I[n-1]$ holds) becomes

$$\begin{aligned}
 E \left\{ |y'_I[n]|^2 \right\} &= E \left\{ \mathbf{w}_I^T[n-1] \mathbf{x}[n] \mathbf{x}^H[n] \mathbf{w}_I^*[n-1] \right\} \\
 &= \mathbf{w}_I^T[n-1] E \left\{ \mathbf{x}[n] \mathbf{x}^H[n] \right\} \mathbf{w}_I^*[n-1] \\
 &\approx \mathbf{w}_I^T[n-1] \left[\sigma_x^2 \mathbf{I} \right] \mathbf{w}_I^*[n-1] \\
 &\approx \sigma_x^2 \mathbf{w}_I^H[n-1] \mathbf{w}_I[n-1].
 \end{aligned} \tag{5.60}$$

Therefore, a simplified albeit approximate DC cancellation with lowered complexity is achieved. The computational effort for the DC cancellation may be reduced even further by skipping the implicit DC cancellation of the algorithm and replacing it by the DC-notch filter

$$\hat{y}_{AC,I}[n] = a \hat{y}_{AC,I}[n-1] + \hat{y}_I[n] - \hat{y}_I[n-1] \tag{5.61}$$

at the adaptive filter output to suppress the IMD2 related DC. The parameter $a = 0.998$ of the DC-notch filter is chosen for a good compromise between sharpness of the DC-notch and settling time of the adaptive filter. The resulting algorithm is summarized in Algorithm 6.

Initialization:

$$0 < \mu < \mu_{\tau_g}$$

$$\epsilon > 0$$

$$a = 0.998$$

$$\mathbf{w}_I[-1] \neq \mathbf{0}$$

$$\hat{y}_{AC,I}[-1] = \hat{y}_I[-1] = 0$$

for $n = 0, 1, 2, \dots$ **do**

$$\hat{y}'[n] = \mathbf{x}^T[n] \mathbf{w}_I[n-1]$$

$$\hat{y}_I[n] = |\hat{y}'[n]|^2 * h_s[n]$$

$$\hat{y}_{AC,I}[n] = a \hat{y}_{AC,I}[n-1] + \hat{y}_I[n] - \hat{y}_I[n-1]$$

$$e_{AC,I}[n] = d_{AC,I}[n] - \hat{y}_{AC,I}[n]$$

$$\mathbf{w}_I[n] = \mathbf{w}_I[n-1] + \frac{\mu e_{AC,I}[n] (\hat{y}'[n] \mathbf{x}^*[n]) * h_s[n]}{\epsilon + (|\hat{y}'[n]|^2 \mathbf{x}^H[n] \mathbf{x}[n]) * h_s[n]}$$

end

Algorithm 6: ϵ -IM2LMS algorithm with DC-notch filter and regularization.

Reducing the Channel-Select Filtering Complexity

The convolution with the CSF impulse response in the derivative (5.49) has two important roles: First, the error signal $e_{AC,I}[n]$ in the derivative (5.49) contains the signal delay of the CSF in the main receiver. This implies that also the term $\hat{y}'[n] \mathbf{x}^*[n] - \mathbf{R}_{\mathbf{xx}}^T \mathbf{w}_I[n-1]$ in the coefficient update needs to be aligned to this delay. To avoid the channel-select filtering of each element in the coefficient update, which is mainly necessary to align the signals due to the CSF group delay, the signals

$$x_f[n] = x[n] * h_s[n] \tag{5.62}$$

and

$$\hat{y}'_f[n] = (\mathbf{x}^T[n] \mathbf{w}_I[n-1]) * h_s[n] \tag{5.63}$$

5 Adaptive IMD2 Cancellation

may be introduced to simplify the coefficient update. Using the delay line vector

$$\mathbf{x}_f[n] = [x_f[n], x_f[n-1], \dots, x_f[n-M+1]]^T, \quad (5.64)$$

the coefficient update in Algorithm 6 may be simplified to

$$\mathbf{w}_I[n] = \mathbf{w}_I[n-1] + \frac{\mu e_{AC,I}[n] \hat{y}'_f[n] \mathbf{x}_f^*[n]}{\epsilon + |y'_f[n]|^2 \mathbf{x}_f^H[n] \mathbf{x}_f[n]}. \quad (5.65)$$

With this formulation, a fractional and non-constant group delay of the CSF may be incorporated although only the two scalar signals (5.62) and (5.63) need to be channel-select filtered instead of each element of the gradient vector. The second important aspect is the band-limiting operation of the CSF which limits the expanded bandwidth of the term $\hat{y}'[n] \mathbf{x}^*[n] - \mathbf{R}_{\mathbf{xx}}^T \mathbf{w}_I[n-1]$ in the coefficient update to the LTE signal bandwidth. By ignoring the band-limiting effect³ of h_s , and assuming a symmetric CSF impulse response with a group delay which is an integer multiple of the sampling time T_s (e.g. axisymmetric FIR filters with odd number of coefficients), the CSF may be approximated by a simple delay of τ_g . It turns out that ignoring the band-limiting effect has only a minor performance influence on the algorithm. Combined with the complexity reduction method of the DC cancellation this results in the very low complexity ϵ -IM2LMS algorithm summarized in Algorithm 7. The used delay-line input

Initialization:

$$0 < \mu < \mu_{\tau_g}$$

$$\epsilon > 0$$

$$a = 0.998$$

$$\mathbf{w}_I[-1] \neq \mathbf{0}$$

$$\hat{y}_{AC,I}[-1] = \hat{y}_I[-1] = 0$$

for $n = 0, 1, 2, \dots$ **do**

$$\hat{y}'[n] = \mathbf{x}^T[n] \mathbf{w}_I[n-1]$$

$$\hat{y}_I[n] = |\hat{y}'[n]|^2 * h_s[n]$$

$$\hat{y}_{AC,I}[n] = a \hat{y}_{AC,I}[n-1] + \hat{y}_I[n] - \hat{y}_I[n-1]$$

$$e_{AC,I}[n] = d_{AC,I}[n] - \hat{y}_{AC,I}[n]$$

$$\mathbf{w}_I[n] = \mathbf{w}_I[n-1] + \frac{\mu e_{AC,I}[n] \hat{y}'[n-\tau_g] \mathbf{x}^*[n-\tau_g]}{\epsilon + |y'[n-\tau_g]|^2 \mathbf{x}^H[n-\tau_g] \mathbf{x}[n-\tau_g]}$$

end

Algorithm 7: Patented ϵ -IM2LMS algorithm with DC-notch filter and CSF delay approximation.

signal vector

$$\mathbf{x}[n - \tau_g] = [x_{BB}[n - \tau_g], x_{BB}[n - \tau_g - 1], \dots, x_{BB}[n - \tau_g - M + 1]]^T \quad (5.66)$$

contains the delayed BB transmit samples. The replica generation in Algorithm 7 still contains the CSF to obtain an IMD2 replica which has the LTE signal BW. Algorithm 7 got filed as a patent in June 2017 by the industrial partner DMCE GmbH & Co KG which is part of Intel [76].

³The algorithm operates with twice the native LTE signal sampling rate because the envelope-squaring operation in the replica generation doubles the signal bandwidth.

The performance of the proposed low-complexity ϵ -IM2LMS algorithm (Algorithm 7) is compared to Algorithm 3, Algorithm 4 and Algorithm 6 in [7]. Algorithm 3 is an improved version of the normalized LMS algorithm published in [22] (added DC cancellation and channel-select filtering). Algorithm 4 is the normalized adaptive LMS version of the Volterra kernel based LS approach used in [23] and [6]. The proposed ϵ -IM2LMS algorithm shows an improved performance compared to [22], a lower complexity compared to [23], and is suitable for highly frequency-selective Tx-to-Rx duplexer stop-band responses. The lowered computational complexity of $\mathcal{O}(M)$ is achieved by the use of the nonlinear Wiener model and the DC-notch filter which replaces the implicit DC cancellation. On the contrary, the truncated Volterra kernel approach used in [23] results in a high dimensional linear estimation problem with complexity of $\mathcal{O}(M^2)$. The performance comparison of the different IMD2 cancellation algorithms may also be found in Section 5.5.1.

A good compromise between performance and complexity gives Algorithm 8 which incorporates the simplified implicit DC cancellation and the delay approximation in the coefficient update. The performance of this algorithm is evaluated with measured IMD2 data which are obtained from a real RF transceiver of the industrial partner. The used transceiver test device incorporates a duplexer which has a limited Tx-to-Rx isolation resulting in an TxL signal which generates an IMD2 interference in the receiver BB. The cancellation performance evaluation may be found in Section 5.6.

Initialization:

$$\begin{aligned}
 &0 < \mu < \mu_{\tau_g} \\
 &\epsilon > 0 \\
 &\mathbf{w}_I[-1] \neq \mathbf{0} \\
 &\sigma_x^2 = E \left\{ |x_{\text{BB}}[n]|^2 \right\} \\
 \text{for } n = 0, 1, 2, \dots \text{ do} \\
 &\left| \begin{aligned}
 \hat{y}'[n] &= \mathbf{x}^T[n] \mathbf{w}_I[n-1] \\
 \hat{y}_{\text{AC,I}}[n] &= \left[|\hat{y}'[n]|^2 - \sigma_x^2 \mathbf{w}_I^H[n-1] \mathbf{w}_I[n-1] \right] * h_s[n] \\
 e_{\text{AC,I}}[n] &= d_{\text{AC,I}}[n] - \hat{y}_{\text{AC,I}}[n] \\
 \mathbf{w}_I[n] &= \mathbf{w}_I[n-1] + \frac{\mu e_{\text{AC,I}}[n] (\hat{y}'[n-\tau_g] \mathbf{x}^*[n-\tau_g] - \sigma_x^2 \mathbf{w}_I[n-1])}{\epsilon + |\hat{y}'[n-\tau_g]|^2 (\mathbf{x}^H[n-\tau_g] \mathbf{x}[n-\tau_g] - 2\sigma_x^2) + \sigma_x^4 \mathbf{w}_I^H[n-1] \mathbf{w}_I[n-1]}
 \end{aligned} \right. \\
 \text{end}
 \end{aligned}$$

Algorithm 8: ϵ -IM2LMS algorithm with simplified implicit DC cancellation and CSF delay approximation.

5.4.6 Simplified Derivation of the IM2LMS Algorithm

The IM2LMS algorithm with implicit DC cancellation may be derived much more efficiently by introducing the new input signal vector $\mathbf{z}^T[n] = \mathbf{w}_I^T[n-1] (\mathbf{x}[n] \mathbf{x}^H[n] - \mathbf{R}_{\text{xx}})$ into the replica equation (5.45). Thereby the new replica model

$$\begin{aligned}
 \hat{y}_{\text{AC,I}}[n] &= [\mathbf{w}_I^T[n-1] (\mathbf{x}[n] \mathbf{x}^H[n] - \mathbf{R}_{\text{xx}}) \mathbf{w}_I^*[n-1]] * h_s[n] \\
 &= \mathbf{z}^T[n] \mathbf{w}_I^*[n-1] * h_s[n]
 \end{aligned} \tag{5.67}$$

5 Adaptive IMD2 Cancellation

is obtained. The cost function of the LMS type algorithm using the new input vector $\mathbf{z}[n]$ becomes

$$\begin{aligned}
J &= |e_{AC,I}[n]|^2 \\
&= |d_{AC,I}[n] - \mathbf{z}^T[n] \mathbf{w}_I^*[n-1] * h_s[n]|^2 \\
&= d_{AC,I}^2[n] - d_{AC,I}[n] (\mathbf{z}^H[n] \mathbf{w}_I[n-1] * h_s[n]) - d_{AC,I}[n] (\mathbf{z}^T[n] \mathbf{w}_I^*[n-1] * h_s[n]) \\
&\quad + (\mathbf{z}^H[n] \mathbf{w}_I[n-1] * h_s[n]) (\mathbf{z}^T[n] \mathbf{w}_I^*[n-1] * h_s[n]).
\end{aligned} \tag{5.68}$$

Having in mind that $\mathbf{z}^H[n] \mathbf{w}_I[n-1] = \mathbf{z}^T[n] \mathbf{w}_I^*[n-1]$, the cost function is obtained by

$$J = d_{AC,I}^2[n] - 2 d_{AC,I}[n] (\mathbf{z}^H[n] \mathbf{w}_I[n-1] * h_s[n]) + (\mathbf{z}^T[n] \mathbf{w}_I^*[n-1] * h_s[n])^2, \tag{5.69}$$

and the gradient using the Wirtinger Calculus results in

$$\begin{aligned}
\left[\frac{\partial J}{\partial \mathbf{w}_I^*} \right]^T &= \left[-2 d_{AC,I}[n] (\mathbf{z}^T[n] * h_s[n]) + 2 \underbrace{(\mathbf{z}^H[n] \mathbf{w}_I[n-1] * h_s[n])}_{\hat{y}_{AC,I}[n]} (\mathbf{z}^T[n] * h_s[n]) \right]^T \\
&= -2 e_{AC,I}[n] (\mathbf{z}[n] * h_s[n]) \\
&= -2 e_{AC,I}[n] \mathbf{z}_f[n].
\end{aligned} \tag{5.70}$$

Finally, the stochastic gradient coefficient update using $\mathbf{z}_f[n] = \mathbf{z}[n] * h_s[n]$ becomes

$$\begin{aligned}
\mathbf{w}_I[n] &= \mathbf{w}_I[n-1] - 2 \mu \left[\frac{\partial J}{\partial \mathbf{w}_I^*} \right]^T \\
&= \mathbf{w}_I[n-1] + 4 \mu e_{AC,I}[n] \mathbf{z}_f[n]
\end{aligned} \tag{5.71}$$

which is exactly the same as derived in (5.50). Now, the normalization is done in the same way as for the traditional normalized LMS algorithm (Algorithm 1) which gives

$$\mathbf{w}_I[n] = \mathbf{w}_I[n-1] + \frac{\mu e_{AC,I}[n] \mathbf{z}_f[n]}{\epsilon + \mathbf{z}_f^H[n] \mathbf{z}_f[n]} \tag{5.72}$$

with the regularization parameter ϵ . The factor 4 in (5.71) is canceled by the normalization in the same way as in Algorithm 5. The normalization term is slightly different compared to (5.55) where the two channel-select filtered terms $\mathbf{z}_f^H[n] \mathbf{z}_f[n]$ are combined. If we back substitute $\mathbf{z}[n]$ into the coefficient update this can be seen more clearly. By using

$$\mathbf{z}_f^T[n] = [\mathbf{w}_I^T[n-1] (\mathbf{x}[n] \mathbf{x}^H[n] - \mathbf{R}_{xx}) * h_s[n] \tag{5.73}$$

and setting $\mathbf{R}_{xx} = \mathbf{0}$ (as in the DC cancellation with DC-notch filter) the coefficient update results in

$$\mathbf{w}_I[n] = \mathbf{w}_I[n-1] + \frac{\mu e_{AC,I}[n] [(y'[n] \mathbf{x}^*[n]) * h_s[n]]}{\epsilon + [(y'^*[n] \mathbf{x}^T[n]) * h_s[n]] [(y'[n] \mathbf{x}^H[n]) * h_s[n]]}. \tag{5.74}$$

Combining the two channel-select filtered terms in the denominator gives

$$\mathbf{w}_I[n] = \mathbf{w}_I[n-1] + \frac{\mu e_{AC,I}[n] [(y'[n] \mathbf{x}^*[n]) * h_s[n]]}{\epsilon + (|y'[n]|^2 \mathbf{x}^H[n] \mathbf{x}[n]) * h_s[n]} \tag{5.75}$$

which is the same result as obtained in Algorithm 6.

5.4.7 Wiener-Model RLS Based IMD2 Cancellation (IM2RLS)

In this section, a nonlinear Wiener model based RLS type adaptive algorithm (IM2RLS) with exponential forgetting factor is derived. It is suitable for highly frequency selective duplexer stop-band frequency responses like indicated in Fig. 2.12 and targets the digital IMD2 cancellation for high performance cellular base stations and mobile phones. The derived IM2RLS algorithm is further extended by a regularization (R-IM2RLS) which makes the algorithm applicable for highly correlated BB transmit signals where the autocorrelation matrix can be close to singular. A high correlation in the transmit signal can be due to oversampling which happens e.g. in the case of multi-cluster transmissions (introduced in 3GPP LTE-A Release 11) where only a part of the available resource blocks (RBs) are allocated. The presented IM2RLS algorithm is an extension to the ϵ -IM2LMS algorithm which is derived in section 5.4.4 and published in [7]. The IM2RLS algorithm offers an improved steady-state cancellation and faster adaptation. Using the replica model (5.36) with implicit DC cancellation

$$\begin{aligned}\hat{y}_{AC,I}[n] &= |\mathbf{x}^T[n] \mathbf{w}_I[n]|^2 * \bar{h}_s[n] \\ &= [\mathbf{w}_I^T[n] (\mathbf{x}[n] \mathbf{x}^H[n] - \mathbf{R}_{\mathbf{xx}}) \mathbf{w}_I^*[n]] * h_s[n],\end{aligned}\quad (5.76)$$

the LS cost function up to the time index n with the exponential forgetting factor $0 \ll \lambda \leq 1$ becomes

$$J_{LS}[n] = \sum_{i=0}^n \lambda^{n-i} |d_{AC,I}[i] - [\mathbf{w}_I^T[n] (\mathbf{x}[i] \mathbf{x}^H[i] - \mathbf{R}_{\mathbf{xx}}) \mathbf{w}_I^*[n]] * h_s[i]|^2. \quad (5.77)$$

Assuming real valued CSF impulse response coefficients $h_s[n]$, and observing that $d_{AC,I}[i]$ is the desired signal in the I-path, and therefore real valued, the Wirtinger derivative of the cost function (5.77) may be derived. The \mathbb{R}^* Wirtinger derivative (see Section 4.3) becomes

$$\begin{aligned}\left[\frac{\partial J_{LS}[n]}{\partial \mathbf{w}_I^*[n]} \right]^T &= \sum_{i=0}^n \lambda^{n-i} \{ -2 d_{AC,I}[i] [(\mathbf{x}^*[i] \mathbf{x}^T[i] - \mathbf{R}_{\mathbf{xx}}^T) \mathbf{w}_I[n] * h_s[i]] \\ &\quad + 2 [(\mathbf{x}^*[i] \mathbf{x}^T[i] - \mathbf{R}_{\mathbf{xx}}^T) \mathbf{w}_I[n] * h_s[i]] \\ &\quad \cdot [\mathbf{w}_I^H[n] (\mathbf{x}^*[i] \mathbf{x}^T[i] - \mathbf{R}_{\mathbf{xx}}^*) * h_s[i]] \mathbf{w}_I[n] \}.\end{aligned}\quad (5.78)$$

The detailed derivation of the derivative (5.78) can be found in Appendix A.5. By setting the derivative to zero, an equation similar to the Wiener-Hopf equation is obtained:

$$\tilde{\mathbf{R}}(\mathbf{w}_I[n]) \mathbf{w}_I[n] = \tilde{\mathbf{r}}(\mathbf{w}_I[n]) \quad (5.79)$$

However, it can be observed that the matrix

$$\begin{aligned}\tilde{\mathbf{R}} &= \sum_{i=0}^n \lambda^{n-i} \{ [(\mathbf{x}^*[i] \mathbf{x}^T[i] - \mathbf{R}_{\mathbf{xx}}^T) \mathbf{w}_I[n] * h_s[i]] \\ &\quad \cdot [\mathbf{w}_I^H[n] (\mathbf{x}^*[i] \mathbf{x}^T[i] - \mathbf{R}_{\mathbf{xx}}^*) * h_s[i]] \mathbf{w}_I[n] \}\end{aligned}\quad (5.80)$$

and the vector

$$\tilde{\mathbf{r}} = \sum_{i=0}^n \lambda^{n-i} \{ d_{AC,I}[i] [(\mathbf{x}^*[i] \mathbf{x}^T[i] - \mathbf{R}_{\mathbf{xx}}^T) \mathbf{w}_I[n] * h_s[i]] \} \quad (5.81)$$

5 Adaptive IMD2 Cancellation

are functions of the unknown coefficient vector $\mathbf{w}_I[n]$. In a slowly varying or nearly stationary system environment it may be assumed that $\mathbf{x}^T[i]\mathbf{w}[n] \approx \mathbf{x}^T[i]\mathbf{w}[i-1]$ when the index i is close to n [77, 78]. If the index $i \ll n$, the approximation introduces an error which is however attenuated by the forgetting factor. Defining the new cost function

$$J'_{\text{LS}}[n] = \sum_{i=0}^n \lambda^{n-i} |d_{\text{AC,I}}[i] - [\mathbf{w}_I^T[i-1] (\mathbf{x}[i]\mathbf{x}^H[i] - \mathbf{R}_{\text{xx}}) \mathbf{w}_I^*[n]] * h_s[i]|^2 \quad (5.82)$$

where $\mathbf{w}_I^T[i-1]$ is used instead of $\mathbf{w}_I^T[n]$ we can overcome this limitation. As a next step, the same input vector $\mathbf{z}^T[i] = \mathbf{w}_I^T[i-1] (\mathbf{x}[i]\mathbf{x}^H[i] - \mathbf{R}_{\text{xx}})$ as it was used in the simplified derivation of the ϵ -IM2LMS algorithm is introduced, such that the new cost function becomes

$$\begin{aligned} J'_{\text{LS}}[n] &= \sum_{i=0}^n \lambda^{n-i} |d_{\text{AC,I}}[i] - \mathbf{z}^T[i]\mathbf{w}_I^*[n] * h_s[i]|^2 \\ &= \sum_{i=0}^n \lambda^{n-i} |e_{\text{AC,I}}[i]|^2. \end{aligned} \quad (5.83)$$

Following the traditional RLS derivation provided in Section 4.5, the IM2RLS algorithm to estimate the I-path IMD2 interference in the digital BB is summarized in Algorithm 9. Here, the channel-select filtered vector $\mathbf{z}_f^T[n] = \mathbf{z}^T[n] * h_s[n]$ is used to align the signals according to the delay introduced by the CSF. Because the error signal $e_{\text{AC,I}}[n]$ is real valued, its conjugation in the coefficient update equation is omitted. The usual choice of the zero-vector as initialization of $\mathbf{w}_I[-1]$ results in a zero-gain vector $\mathbf{k}[n]$ for all n . This is reasoned in the cost function (5.77) depicted in Fig. 5.4 which has a saddle point at $\mathbf{w}_I = \mathbf{0}$ and therefore a vanishing derivative. Consequently, the algorithm is initialized with $\mathbf{w}_I[-1] \neq \mathbf{0}$, and with the parameters $0 \ll \lambda \leq 1$, and $\mathbf{P}[-1] = \nu \mathbf{I}$ with $\nu > 0$. However, as for the ϵ -IM2LMS algorithm, an initialization close to the zero vector, e.g., $\mathbf{w}_I[-1] = [w_{\text{I},0}, 0, 0, \dots, 0]^T$ where $w_{\text{I},0}$ is a small real valued positive number can be used.

Reducing the Complexity of the Implicit DC Cancellation

In the ϵ -IM2LMS algorithm, the usage of $\sigma_x^2 \mathbf{I}$ instead of \mathbf{R}_{xx} leads to good cancellation results. This simplification can also be used to reduce the complexity of the IM2RLS algorithm. A further complexity reduction may be achieved by using the DC-notch filter (5.61) for the DC cancellation which has the advantage that the knowledge of the Tx signal statistics is not necessary. The parameter a determines the sharpness of the DC-notch. If the parameter a is chosen close to unity, the filter has a very sharp notch at DC but needs longer to settle which may influence the convergence time of the adaptive filter.

Reducing the Channel-Select Filtering Complexity

To avoid the channel-select filtering of the M elements in the vector $\mathbf{z}_f[n] = \mathbf{z}[n] * h_s[n]$, which is mainly necessary to align the signals due to the CSF group delay, the signals

Initialization:

$$\mathbf{P}[-1] = \nu \mathbf{I} \text{ with } \nu > 0$$

$$0 \ll \lambda \leq 1$$

$$\mathbf{w}_I[-1] \neq \mathbf{0}$$

$$\mathbf{R}_{\mathbf{x}\mathbf{x}} = E \{ \mathbf{x}\mathbf{x}^H \}$$

for $n = 0, 1, 2, \dots$ **do**

$$\mathbf{z}^T[n] = \mathbf{w}_I^T[n-1] (\mathbf{x}[n]\mathbf{x}^H[n] - \mathbf{R}_{\mathbf{x}\mathbf{x}})$$

$$\mathbf{z}_f[n] = \mathbf{z}[n] * h_s[n]$$

$$\hat{y}_{AC,I}[n] = \mathbf{z}^T[n] \mathbf{w}_I^*[n-1] * h_s[n]$$

$$e_{AC,I}[n] = d_{AC,I}[n] - \hat{y}_{AC,I}[n]$$

$$\mathbf{k}[n] = \frac{\mathbf{P}^{[n-1]}\mathbf{z}_f[n]}{\lambda + \mathbf{z}_f^H[n]\mathbf{P}^{[n-1]}\mathbf{z}_f[n]}$$

$$\mathbf{P}[n] = \frac{1}{\lambda} [\mathbf{P}[n-1] - \mathbf{k}[n]\mathbf{z}_f^H[n]\mathbf{P}[n-1]]$$

$$\mathbf{w}_I[n] = \mathbf{w}_I[n-1] + e_{AC,I}[n]\mathbf{k}[n]$$

end

Algorithm 9: IM2RLS algorithm with implicit DC cancellation using the autocorrelation matrix $\mathbf{R}_{\mathbf{x}\mathbf{x}}$.

$x_f[n] = x[n] * h_s[n]$ and $\hat{y}'_f[n] = \mathbf{x}^T[n]\mathbf{w}_I[n-1] * h_s[n]$ may be introduced. Using the delay line vector

$$\mathbf{x}_f[n] = [x_f[n], x_f[n-1], \dots, x_f[n-M+1]]^T, \quad (5.84)$$

the vector $\mathbf{z}_f[n]$ may be approximated by

$$\mathbf{z}_f[n] \approx \hat{y}'_f[n]\mathbf{x}_f^*[n]. \quad (5.85)$$

By using this formulation in Algorithm 9 only two scalar signals need to be filtered with the CSF impulse response. A big advantage of this simplification is, that also a fractional and non-constant group delay of the CSF may be incorporated. However, in this approximation the band-limiting effect of the CSF on $\mathbf{z}_f[n]$ is ignored. This may be tolerated due to the oversampling factor (OSF) of 2 which is anyhow necessary because of the envelope-squaring in the replica generation.

Channel-Select Filter Delay-Approximation

If the group delay τ_g of the CSF is constant and an integer multiple of the sampling time (e.g. axisymmetric FIR filters with odd number of coefficients), the CSF may be approximated by a simple signal delay given by

$$\mathbf{z}_f[n] \approx \mathbf{z}[n - \tau_g]. \quad (5.86)$$

Also in this approximation the band-limiting effect of the CSF on $\mathbf{z}[n]$ is ignored but may be tolerated because of the OSF of 2. The resulting IM2RLS algorithm with DC-notch filter and CSF delay-approximation is summarized in Algorithm 10. The performance of Algorithm 10 is presented in [27] where it shows an excellent IMD2 self-interference cancellation for a full allocated LTE10 transmit signal. However, to improve numerical stability for small bandwidth allocations like, e.g., used in multi-cluster transmissions, the regularized IM2RLS (R-IM2RLS) is derived in the next section.

Initialization:

$$\mathbf{P}[-1] = \nu \mathbf{I} \text{ with } \nu > 0$$

$$0 \ll \lambda \leq 1$$

$$\mathbf{w}_I[-1] \neq \mathbf{0}$$

$$a = 0.998$$

$$\hat{y}_{AC,I}[-1] = \hat{y}_I[-1] = 0$$

for $n = 0, 1, 2, \dots$ **do**

$$\mathbf{z}^T[n] = \mathbf{w}_I^T[n-1] \mathbf{x}[n] \mathbf{x}^H[n]$$

$$\mathbf{z}_f[n] = \mathbf{z}[n - \tau_g]$$

$$\hat{y}_I[n] = \mathbf{z}^T[n] \mathbf{w}_I^*[n-1] * h_s[n]$$

$$\hat{y}_{AC,I}[n] = a \hat{y}_{AC,I}[n-1] + \hat{y}_I[n] - \hat{y}_I[n-1]$$

$$e_{AC,I}[n] = d_{AC,I}[n] - \hat{y}_{AC,I}[n]$$

$$\mathbf{k}[n] = \frac{\mathbf{P}[n-1] \mathbf{z}_f[n]}{\lambda + \mathbf{z}_f^H[n] \mathbf{P}[n-1] \mathbf{z}_f[n]}$$

$$\mathbf{P}[n] = \frac{1}{\lambda} [\mathbf{P}[n-1] - \mathbf{k}[n] \mathbf{z}_f^H[n] \mathbf{P}[n-1]]$$

$$\mathbf{w}_I[n] = \mathbf{w}_I[n-1] + e_{AC,I}[n] \mathbf{k}[n]$$

end

Algorithm 10: IM2RLS algorithm with DC cancellation using a DC-notch filter and CSF delay approximation.

Tikhonov Regularization of the nonlinear IM2RLS

To reduce the spectral OOB emission of the LTE signals, not all available subcarriers are allocated. A portion of the subcarriers at the band-edges (guard-band) are forced to zero which introduces correlation in the transmit BB samples. E.g. in a 10 MHz LTE signal a maximum of 600 out of 1024 subcarriers may be occupied by data [79]. This correlation in the Tx BB signal $x_{BB}[n]$ leads to a badly-conditioned autocorrelation matrix⁴ $\mathbf{R} = E \{ \mathbf{x}_{BB}[n] \mathbf{x}_{BB}^H[n] \}$ and respectively $\tilde{\mathbf{R}} = E \{ \mathbf{z}_f[n] \mathbf{z}_f^H[n] \}$. Algorithms which need the estimation of the autocorrelation matrix or its inverse $\mathbf{P} = \mathbf{R}^{-1}$ are sensitive to the condition number of \mathbf{R} and may suffer from numerical instability if \mathbf{R} is badly-conditioned. Therefore, a regularized version of the IM2RLS algorithm (R-IM2RLS) is derived in this section.

A common method to overcome the problem of badly-conditioned autocorrelation matrices is regularization [61]. Adding a positive definite matrix to the estimated autocorrelation matrix in each iteration of the RLS algorithm guarantees that the regularized autocorrelation matrix $\tilde{\mathbf{R}}'$ stays positive definite and therefore maintains the necessary condition for convergence and existence of $\mathbf{P} = \tilde{\mathbf{R}}'^{-1}$ [80].

This method is commonly known as Tikhonov-regularization where a matrix \mathbf{L} is used for the regularization [81]. By including a regularization term in the cost function (5.83),

⁴The LTE transmit signal is not wide-sense stationary. However, each LTE symbol can be considered as a section of a wide-sense stationary signal. Therefore, because the length of \mathbf{w} is much smaller than the symbol duration it makes sense to introduce the matrix $\tilde{\mathbf{R}} = E \{ \mathbf{z}_f[n] \mathbf{z}_f^H[n] \}$.

the new cost function

$$\begin{aligned} J'_R[n] &= \sum_{i=0}^n \lambda^{n-i} \left[|e_{AC,I}[i]|^2 + \sigma \|\mathbf{L}\mathbf{w}_I[n]\|_2^2 \right] \\ &= \sum_{i=0}^n \lambda^{n-i} \left[|e_{AC,I}[i]|^2 + \sigma \mathbf{w}_I^T[n] \mathbf{L}^T \mathbf{L} \mathbf{w}_I^*[n] \right] \end{aligned} \quad (5.87)$$

is defined where $e_{AC,I}[i] = d_{AC,I}[i] - (\mathbf{z}^T[i] \mathbf{w}_I^*[n]) * h_s[i]$. The regularization parameter $\sigma \geq 0$ is used to adjust the amount of regularization and the real valued matrix \mathbf{L} is typically chosen as $\mathbf{L} = \mathbf{I}$ (standard Tikhonov regularization),

$$\mathbf{L} = \begin{bmatrix} -1 & 1 & & & & \\ & -1 & 1 & & & \\ & & -1 & 1 & & \\ & & & \ddots & \ddots & \\ & & & & -1 & 1 \end{bmatrix} \quad (5.88)$$

(first order derivative), or

$$\mathbf{L} = \begin{bmatrix} 1 & -2 & 1 & & & \\ & 1 & -2 & 1 & & \\ & & 1 & -2 & 1 & \\ & & & \ddots & \ddots & \ddots \\ & & & & 1 & -2 & -1 \end{bmatrix} \quad (5.89)$$

(second order derivative) [81]. Using the \mathbb{R}^* Wirtinger derivative (see Section 4.3) of the cost function (5.87), and setting it to zero results in

$$\underbrace{\left[\sum_{i=0}^n \lambda^{n-i} (\mathbf{z}_f[i] \mathbf{z}_f^H[i] + \sigma \mathbf{L}^T \mathbf{L}) \right]}_{\tilde{\mathbf{R}}'[n]} \mathbf{w}_I[n] = \underbrace{\sum_{i=0}^n \lambda^{n-i} d_{AC,I}[i] \mathbf{z}_f[i]}_{\tilde{\mathbf{r}}[n]}. \quad (5.90)$$

Reformulating the above equation leads to $\mathbf{w}_I[n] = \tilde{\mathbf{R}}'^{-1}[n] \tilde{\mathbf{r}}[n] = \mathbf{P}[n] \tilde{\mathbf{r}}[n]$ which is solved recursively using the RLS algorithm. By expressing the cross-correlation vector $\tilde{\mathbf{r}}[n]$ by its previous estimate $\tilde{\mathbf{r}}[n-1]$, a recursive estimation of the form

$$\tilde{\mathbf{r}}[n] = \lambda \tilde{\mathbf{r}}[n-1] + d_{AC,I}[n] \mathbf{z}_f[n] \quad (5.91)$$

may be formulated. Similarly, a recursive estimation of the regularized autocorrelation matrix is obtained by

$$\begin{aligned} \tilde{\mathbf{R}}'[n] &= \lambda \sum_{i=0}^{n-1} \lambda^{n-i-1} (\mathbf{z}_f[i] \mathbf{z}_f^H[i] + \sigma \mathbf{L}^T \mathbf{L}) + \mathbf{z}_f[n] \mathbf{z}_f^H[n] + \sigma \mathbf{L}^T \mathbf{L} \\ &= \lambda \tilde{\mathbf{R}}'[n-1] + \sigma \mathbf{L}^T \mathbf{L} + \mathbf{z}_f[n] \mathbf{z}_f^H[n]. \end{aligned} \quad (5.92)$$

Substituting $\mathbf{\Omega}[n]^{-1} = \lambda \tilde{\mathbf{R}}'[n-1] + \sigma \mathbf{L}^T \mathbf{L}$ into (5.92), the matrix $\mathbf{P}[n] = \tilde{\mathbf{R}}'^{-1}[n]$ becomes

$$\mathbf{P}[n] = [\mathbf{\Omega}[n]^{-1} + \mathbf{z}_f[n] \mathbf{z}_f^H[n]]^{-1}. \quad (5.93)$$

5 Adaptive IMD2 Cancellation

After applying the matrix inversion lemma [68]

$$(\mathbf{A} + \mathbf{BCD})^{-1} = \mathbf{A}^{-1} - \mathbf{A}^{-1}\mathbf{B}(\mathbf{C}^{-1} + \mathbf{DA}^{-1}\mathbf{B})^{-1}\mathbf{DA}^{-1} \quad (5.94)$$

to avoid the matrix inversion, (5.93) may be formulated as

$$\mathbf{P}[n] = \mathbf{\Omega}[n] - \mathbf{k}[n]\mathbf{z}_f^H[n]\mathbf{\Omega}[n], \quad (5.95)$$

where the gain vector

$$\mathbf{k}[n] = \frac{\mathbf{\Omega}[n]\mathbf{z}_f[n]}{1 + \mathbf{z}_f^H[n]\mathbf{\Omega}[n]\mathbf{z}_f[n]} \quad (5.96)$$

is introduced. For the inversion

$$\mathbf{\Omega}[n] = [\lambda\mathbf{P}^{-1}[n-1] + \sigma\mathbf{L}^T\mathbf{L}]^{-1}, \quad (5.97)$$

again the matrix inversion lemma is applied which yields

$$\mathbf{\Omega}[n] = \frac{1}{\lambda}(\mathbf{P}[n-1] - \mathbf{\Sigma}[n]\mathbf{L}\mathbf{P}[n-1]), \quad (5.98)$$

where the substitution

$$\mathbf{\Sigma}[n] = \sigma\mathbf{P}[n-1]\mathbf{L}^T[\lambda\mathbf{I} + \sigma\mathbf{L}\mathbf{P}[n-1]\mathbf{L}^T]^{-1} \quad (5.99)$$

is used. After rearranging (5.99), the expression

$$\begin{aligned} \mathbf{\Sigma}[n] &= \frac{\sigma}{\lambda}(\mathbf{P}[n-1] - \mathbf{\Sigma}[n]\mathbf{L}\mathbf{P}[n-1])\mathbf{L}^T \\ &= \sigma\mathbf{\Omega}[n]\mathbf{L}^T \end{aligned} \quad (5.100)$$

is obtained. Unfortunately, the calculation of $\mathbf{\Sigma}[n]$ in (5.99) and therefore $\mathbf{\Omega}[n]$ includes a matrix inversion even after applying the matrix inversion lemma. However, by decomposing the matrix $\mathbf{L}^T\mathbf{L}$ in (5.97) into a sum of V dyads [82]

$$\mathbf{\Omega}[n] = \left[\lambda\mathbf{P}^{-1}[n-1] + \sigma \sum_{k=1}^V \mathbf{p}_{k,1}\mathbf{p}_{k,2}^T \right]^{-1}, \quad (5.101)$$

applying the matrix inversion lemma results in the recursive calculation of (5.101) via

$$\mathbf{\Omega}_k[n] = \mathbf{\Omega}_{k-1}[n] - \frac{\mathbf{\Omega}_{k-1}[n]\mathbf{p}_{k,1}}{\frac{1}{\sigma} + \mathbf{p}_{k,2}^T\mathbf{\Omega}_{k-1}[n]\mathbf{p}_{k,1}}\mathbf{p}_{k,2}^T\mathbf{\Omega}_{k-1}[n] \quad (5.102)$$

for $k = 1 \dots V$ in each iteration n , and $\mathbf{\Omega}_0[n] = \frac{1}{\lambda}\mathbf{P}[n-1]$. Reformulating (5.96) yields

$$\mathbf{k}[n] = \mathbf{P}[n]\mathbf{z}_f[n]. \quad (5.103)$$

The recursive update of the coefficient vector $\mathbf{w}_1[n]$ is obtained by inserting (5.95), (5.91), (5.103), (5.98) and (5.100) into $\mathbf{w}_1[n] = \mathbf{P}[n]\hat{\mathbf{r}}[n]$. The final nonlinear R-IM2RLS algorithm to estimate the I-path IMD2 interference is summarized in Algorithm 11. Using the CSF delay-approximation and the DC-notch filter instead of the implicit DC cancellation results in Algorithm 12. The performance of Algorithm 12 has been evaluated by

Initialization:

$$\mathbf{P}[-1] = \nu \mathbf{I} \text{ with } \nu > 0$$

$$0 \ll \lambda \leq 1$$

$$\mathbf{w}_I[-1] \neq \mathbf{0}$$

$$\mathbf{R}_{\mathbf{xx}} = E \{ \mathbf{xx}^H \}$$

$$\sigma \geq 0$$

$$\mathbf{p}_{k,1} \text{ and } \mathbf{p}_{k,2} \text{ such that } \mathbf{L}^T \mathbf{L} = \sum_{k=1}^V \mathbf{p}_{k,1} \mathbf{p}_{k,2}^T$$

for $n = 0, 1, 2, \dots$ **do**

$$\mathbf{z}^T[n] = \mathbf{w}_I^T[n-1] (\mathbf{x}[n] \mathbf{x}^H[n] - \mathbf{R}_{\mathbf{xx}})$$

$$\mathbf{z}_f[n] = \mathbf{z}[n] * h_s[n]$$

$$\hat{y}_{AC,I}[n] = \mathbf{z}^T[n] \mathbf{w}_I^*[n-1] * h_s[n]$$

$$e_{AC,I}[n] = d_{AC,I}[n] - \hat{y}_{AC,I}[n]$$

$$\mathbf{\Omega}_0[n] = \frac{1}{\lambda} \mathbf{P}[n-1]$$

for $k = 1 \dots V$ **do**

$$\left| \mathbf{\Omega}_k[n] = \mathbf{\Omega}_{k-1}[n] - \frac{\mathbf{\Omega}_{k-1}[n] \mathbf{p}_{k,1}}{\frac{1}{\sigma} + \mathbf{p}_{k,2}^T \mathbf{\Omega}_{k-1}[n] \mathbf{p}_{k,1}} \mathbf{p}_{k,2}^T \mathbf{\Omega}_{k-1}[n] \right.$$

end

$$\mathbf{k}[n] = \frac{\mathbf{\Omega}_V[n] \mathbf{z}_f[n]}{1 + \mathbf{z}_f^H[n] \mathbf{\Omega}_V[n] \mathbf{z}_f[n]}$$

$$\mathbf{P}[n] = \mathbf{\Omega}_V[n] - \mathbf{k}[n] \mathbf{z}_f^H[n] \mathbf{\Omega}_V[n]$$

$$\mathbf{\Sigma}[n] = \sigma \mathbf{\Omega}_V[n] \mathbf{L}^T$$

$$\mathbf{w}_I[n] = [\mathbf{I} - (\mathbf{I} - \mathbf{k}[n] \mathbf{z}_f^H[n]) \mathbf{\Sigma}[n] \mathbf{L}] \mathbf{w}_I[n-1] + \mathbf{k}[n] e_{AC,I}[n]$$

end

Algorithm 11: Regularized IM2RLS algorithm with implicit DC cancellation using $\mathbf{R}_{\mathbf{xx}}$.

Initialization:

$$\mathbf{P}[-1] = \nu \mathbf{I} \text{ with } \nu > 0$$

$$0 \ll \lambda \leq 1$$

$$\mathbf{w}_I[-1] \neq \mathbf{0}$$

$$a = 0.998$$

$$\hat{y}_{AC,I}[-1] = \hat{y}_I[-1] = 0$$

$$\sigma \geq 0$$

$$\mathbf{p}_{k,1} \text{ and } \mathbf{p}_{k,2} \text{ such that } \mathbf{L}^T \mathbf{L} = \sum_{k=1}^V \mathbf{p}_{k,1} \mathbf{p}_{k,2}^T$$

for $n = 0, 1, 2, \dots$ **do**

$$\mathbf{z}^T[n] = \mathbf{w}_I^T[n-1] (\mathbf{x}[n] \mathbf{x}^H[n])$$

$$\mathbf{z}_f[n] = \mathbf{z}[n - \tau_g]$$

$$\hat{y}_I[n] = \mathbf{z}^T[n] \mathbf{w}_I^*[n-1] * h_s[n]$$

$$\hat{y}_{AC,I}[n] = a \hat{y}_{AC,I}[n-1] + \hat{y}_I[n] - \hat{y}_I[n-1]$$

$$e_{AC,I}[n] = d_{AC,I}[n] - \hat{y}_{AC,I}[n]$$

$$\mathbf{\Omega}_0[n] = \frac{1}{\lambda} \mathbf{P}[n-1]$$

for $k = 1 \dots V$ **do**

$$\left| \mathbf{\Omega}_k[n] = \mathbf{\Omega}_{k-1}[n] - \frac{\mathbf{\Omega}_{k-1}[n] \mathbf{p}_{k,1}}{\frac{1}{\sigma} + \mathbf{p}_{k,2}^T \mathbf{\Omega}_{k-1}[n] \mathbf{p}_{k,1}} \mathbf{p}_{k,2}^T \mathbf{\Omega}_{k-1}[n] \right.$$

end

$$\mathbf{k}[n] = \frac{\mathbf{\Omega}_V[n] \mathbf{z}_f[n]}{1 + \mathbf{z}_f^H[n] \mathbf{\Omega}_V[n] \mathbf{z}_f[n]}$$

$$\mathbf{P}[n] = \mathbf{\Omega}_V[n] - \mathbf{k}[n] \mathbf{z}_f^H[n] \mathbf{\Omega}_V[n]$$

$$\mathbf{\Sigma}[n] = \sigma \mathbf{\Omega}_V[n] \mathbf{L}^T$$

$$\mathbf{w}_I[n] = [\mathbf{I} - (\mathbf{I} - \mathbf{k}[n] \mathbf{z}_f^H[n]) \mathbf{\Sigma}[n] \mathbf{L}] \mathbf{w}_I[n-1] + \mathbf{k}[n] e_{AC,I}[n]$$

end

Algorithm 12: Regularized IM2RLS algorithm with CSF delay-approximation and DC-notch filter.

numerical simulations and measured data and the results are published in [27]. In the simulation results provided in Section 5.5.2, a clustered Tx signal is used which results in a high condition number of the autocorrelation matrix. The measurement setup which is used to generate the measurement data includes discrete RF components, and the cancellation results are presented in Section 5.6.2.

The CSF which is used in the replica generation introduces a time delay in the filter output signal. In case of the IM2LMS algorithm this led to a reduction of the maximally allowed step-size. For the IM2RLS algorithm this requires a reduction of the parameter ν which is used in the initialization of the matrix $\mathbf{P}[-1]$. Unfortunately, no analytical maximum value of ν depending on τ_g could be derived and also in the existing literature no reference could be found. In the provided simulation results in Section 5.5.2, and in the cancellations using measured data (Section 5.6.2) the value $\nu = 100$ was used.

5.4.8 Incorporating the Estimation of the Q-Path IMD2 Interference

Due to the fact, that the I-, and Q-path IMD2 interference differ only by a real valued scaling factor h_Q , the estimated I-path IMD2 replica signal may be used as a reference to estimate the Q-path IMD2 interference. This may be done by using a linear 1-tap LMS-, or RLS algorithm which estimates h_Q (the adaptive filter coefficient is w_Q) thereby enabling the estimation of a possible sign difference between the I-, and Q-path IMD2 interference signal. The proposed structure of the cancellation approach is visualized in Fig. 5.2. The 1-tap LMS-, and RLS algorithm to estimate the Q-path IMD2 interference is summarized in Algorithm 13 and Algorithm 14, respectively.

Initialization:

$$0 < \mu < 2$$

$$\epsilon > 0$$

$$w_Q[-1] = 0$$

for $n = 0, 1, 2, \dots$ **do**

$$\left| \begin{array}{l} \hat{y}_{AC,Q}[n] = w_Q[n-1] \hat{y}_{AC,I}[n] \\ e_{AC,Q}[n] = d_{AC,Q}[n] - \hat{y}_{AC,Q}[n] \\ w_Q[n] = w_Q[n-1] + \frac{\mu e_{AC,Q}[n] \hat{y}_{AC,I}[n]}{\epsilon + \hat{y}_{AC,I}^2[n]} \end{array} \right.$$

end

Algorithm 13: Linear 1-tap ϵ -NLMS to estimate the Q-path IMD2 interference using the I-path IMD2 replica as reference signal.

5.4.9 Complexity Comparison

The computational complexity per iteration of the different IMD2 cancellation algorithms in terms of required real valued multiplications, additions and divisions is summarized in Table. 5.1. It is assumed that all algorithms operate at twice the sampling rate due to the OSF of 2. The Hammerstein-, and Volterra based algorithms require a kernel generator to generate the input signal vector. This kernel generator involves the envelope-squaring operation which requires an OSF of 2. The ϵ -IM2LMS- and the IM2RLS algorithm are using the envelope-squaring in the replica generation which also

5 Adaptive IMD2 Cancellation

Initialization:

$$p[-1] = \nu_Q \text{ with } \nu_Q > 0$$

$$0 < \lambda_Q \leq 1$$

$$w_Q[-1] = 0$$

for $n = 0, 1, 2, \dots$ **do**

$$\hat{y}_{AC,Q}[n] = w_Q[n-1]\hat{y}_{AC,I}[n]$$

$$e_{AC,Q}[n] = d_{AC,Q}[n] - \hat{y}_{AC,Q}[n]$$

$$k[n] = \frac{p[n-1]\hat{y}_{AC,I}[n]}{\lambda_Q + \hat{y}_{AC,I}[n]p[n-1]\hat{y}_{AC,I}[n]}$$

$$p[n] = \frac{1}{\lambda_Q} (p[n-1] - k[n]\hat{y}_{AC,I}[n]p[n-1])$$

$$w_Q[n] = w_Q[n-1] + e_{AC,Q}[n]k[n]$$

end

Algorithm 14: Linear 1-tap RLS to estimate the Q-path IMD2 interference using the I-path IMD2 replica as reference signal.

requires an OSF of 2. It is assumed that the BB equivalent Tx-to-Rx leakage channel is modeled by a length M FIR channel at an OSF of 2. With this assumption, the complexity of all algorithms can be compared on the same basis, namely estimate an IMD2 interference which is caused by the Tx signal which leaked through the length M leakage channel model.

Furthermore, the complexity is compared for the estimation of the complex valued IMD2 interference thereby estimating the I-, and Q-path IMD2 interference. The Wiener model based ϵ -IM2LMS-, and IM2RLS algorithms use a 1-tap LMS- and 1-tap RLS algorithm for the estimation of the Q-path IMD2 interference, respectively. The complexity of the channel-select filtering may not be neglected and is therefore included in the comparison. It is assumed that the CSF difference equation consists of N real valued coefficients.

Table 5.1: Complexity per iteration of the IMD2 cancellation algorithms

Algorithm	real mult.	real add.	real div.	Cancellation
Hammerstein (Algorithm 3)	$5M + N + 5$	$5M + N$	2	low
Volterra (Algorithm 4)	$M^2N + 7M^2 - 2M + 6$	$(M^2 - 1)N + 6M^2 - M + 3$	2	medium
ϵ -IM2LMS (Algorithm 5)	$4M^3 + 8M^2 + 24M + 2MN + N + 9$	$4M^3 + 6M^2 + 16M + 2MN + N - 1$	1	medium
ϵ -IM2LMS (Algorithm 6)	$2MN + 12M + N + 6$	$2MN + 8M + N - 1$	1	high
ϵ -IM2LMS (Algorithm 7)	$12M + N + 5$	$10M + N + 1$	1	high
ϵ -IM2LMS (Algorithm 8)	$16M + N + 6$	$12M + N$	1	high
IM2RLS (Algorithm 9)	$14M^2 + 2MN + 14M + N$	$12M^2 + 2MN + 10M + N - 5$	2M	very high
IM2RLS (Algorithm 10)	$10M^2 + 18M + N + 1$	$8M^2 + 14M + N - 3$	2M	very high
R-IM2RLS (Algorithm 12) with $\mathbf{L} = \mathbf{I}$	$8M^3 + 26M^2 + 18M + N + 1$	$8M^3 + 16M^2 + 17M + N - 3$	2M	very high
Additionally 1-tap ϵ -NLMS to each ϵ -IM2LMS variant	4	3	1	-
Additionally 1-tap RLS to each IM2RLS variant	6	4	1	-

5.5 Simulation Results

5.5.1 LMS Based IMD2 Cancellation

In this section, the performance of the ϵ -IM2LMS algorithm with the CSF delay-approximation and the DC-notch filter (Algorithm 7) is evaluated. For this, an FDD scenario with LTE-A signals of 10 MHz bandwidth, QPSK modulation, short cyclic prefix, and an OSF of 2 is applied. The frequency-selective duplexer is approximated by a 15 tap FIR system (at the sampling rate of 15.36 MHz) which has an average of 50 dB suppression near the transmit frequency [4]. The two-tone Rx mixer IIP2 is set to +40 dBm as in [6], and the LNA gain to 20 dB. The LNA amplifies the wanted receive signal, the TxL signal and the noise. Assuming a thermal noise floor at the antenna of -104.5 dBm per 10 MHz and a receiver NF of 4.5 dB, the noise floor of the receiver is at -100 dBm. The Rx signal power at the antenna is -90 dBm which corresponds to an Rx SNR of 10 dB. The resulting Rx and noise power level at the mixer input are -70 dBm and -80 dBm (-108.2 dBm/15 kHz), respectively.

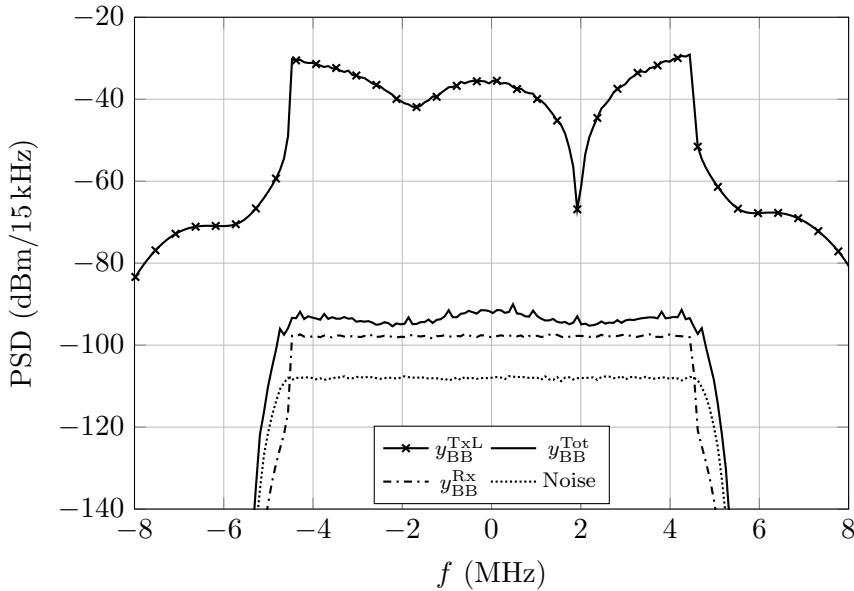


Figure 5.6: Spectrum of the signals at the transmit power of $P_{Tx} = 23$ dBm.

Fig. 5.6 shows the spectrum of the signals for an IIP2 of 40 dBm. The baseband equivalent leaked Tx signal y_{BB}^{TxL} is shaped by the frequency selective duplexer stop-band frequency response and amplified by the LNA. The total received signal y_{BB}^{Tot} contains the wanted Rx signal y_{BB}^{Rx} , the noise signal v_{BB} , and the IMD2 interference signal after channel-select-, and DC-filtering. The proposed ϵ -IM2LMS type algorithm is compared to the normalized Hammerstein model based LMS algorithm (Algorithm 3), and to the normalized Volterra kernel based LMS algorithm (Algorithm 4). To evaluate the influence of the CSF delay-approximation two versions of the IM2LMS algorithm (Algorithm 6 and Algorithm 7) are included in the comparison. Algorithm 3 uses 15 taps, and the truncated Volterra kernel based normalized LMS filter has $15^2 = 225$ taps. The

ϵ -IM2LMS uses 15 taps, the initial coefficient vector⁵ $\mathbf{w}[-1] = [10^{-3}, 0, 0, \dots, 0]^T$, and the parameter $a = 0.998$ for the DC-notch filter. The other algorithms are initialized with the zero-vector. All algorithms run on the sampling rate of 30.72 MHz (OSF=2) which means that the adaptive filters are not able to estimate the full leakage path (which has 15 FIR filter taps at 15.36 MHz). With this scenario, additionally the behavior of the algorithms for under-modeling of the leakage channel is evaluated. The Hammerstein-, and Volterra based algorithms directly estimate the complex valued IMD2 interference in the I-, and Q-path. The ϵ -IM2LMS algorithm is used to estimate the I-path IMD2 interference whereas the Q-path IMD2 interference is estimated by the 1-tap NLMS algorithm (Algorithm 13) which uses the I-path IMD2 replica as reference input. The step-size of the ϵ -IM2LMS algorithm is chosen as $\mu_0 = 1/500$, for the Hammerstein model based LMS $\mu = 1/1500$, and for the truncated Volterra kernel based LMS the step-size is set to $\mu = 1/300$. The 1-tap NLMS algorithm uses a step-size of $1/100$, and the initial coefficient is set to $w_Q[-1] = 0$. The common regularization term is chosen as $\epsilon = 0.001$. The step-sizes are chosen to give the best possible compromise between convergence time and steady-state cancellation for each algorithm. To compare the convergence behavior of the algorithms, the ensemble NMSE (5.104), and the SINR in steady-state (5.105) [9, 23] are used as performance measure:

$$\text{NMSE}_{\text{dB}}[n] = 10 \log_{10} \left(\frac{\text{E} \left[|y_{\text{BB}}^{\text{IMD2}}[n] - \hat{y}_{\text{AC}}[n]|^2 \right]}{\text{E} \left[|y_{\text{BB}}^{\text{IMD2}}[n]|^2 \right]} \right) \quad (5.104)$$

$$\text{SINR}_{\text{dB}} = 10 \log_{10} \left(\frac{\text{E} \left[|y_{\text{BB}}^{\text{Rx}}[n]|^2 \right]}{\text{E} \left[|y_{\text{BB}}^{\text{Tot}}[n] - y_{\text{BB}}^{\text{Rx}}[n] - \hat{y}_{\text{AC}}[n]|^2 \right]} \right) \quad (5.105)$$

The convergence behavior of the compared algorithms at a transmit power of 23 dBm is depicted in Fig. 5.7. The proposed ϵ -IM2LMS type algorithms reach -10 dB NMSE after three LTE slots (46080 samples with OSF=2) which is four times faster than the Volterra kernel based LMS. Note, that one LTE10 slot corresponds to 7 LTE10 symbols. Decreasing the step-size in the Hammerstein model based algorithm does not lead to a reduction of the NMSE because the algorithm is not suitable for strongly frequency-selective Tx-to-Rx responses. The truncated Volterra kernel based adaptive LMS uses a high number of taps which increases the EMSE [61]. The Rx SINR improvements at different transmit power levels for an Rx SNR of 10 dB, and 3 dB are depicted in Fig. 5.8 and Fig. 5.9, respectively. The proposed nonlinear ϵ -IM2LMS significantly improves the Rx SINR nearly up to the Rx SNR.

⁵For a practical implementation it is suggested to initialize the first entry of $\mathbf{w}[-1]$ with the smallest representable positive number.

5 Adaptive IMD2 Cancellation

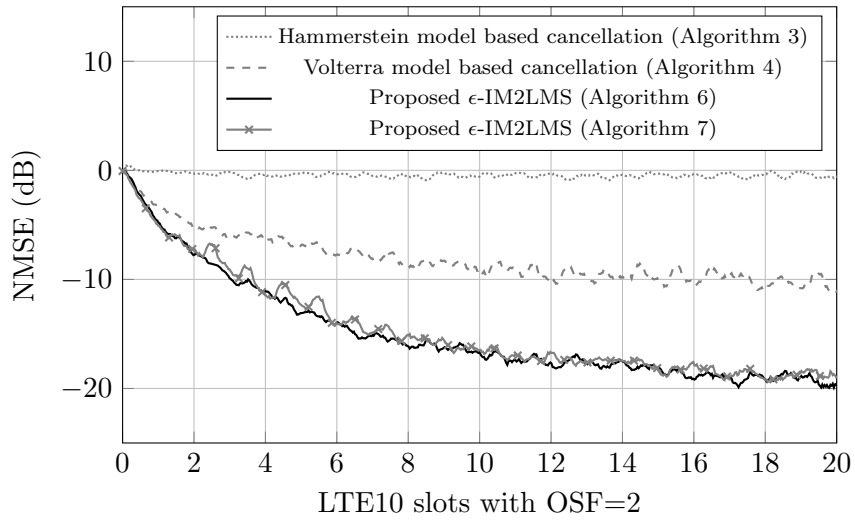


Figure 5.7: Convergence behavior of the different adaptive algorithms.

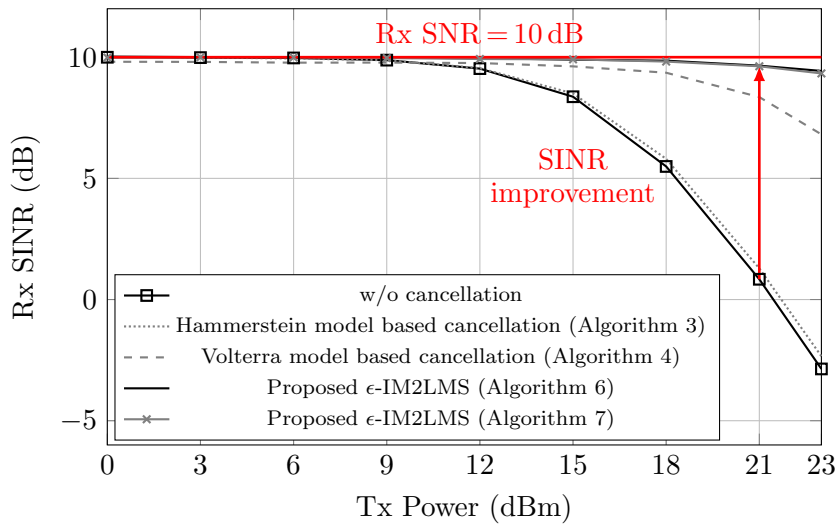


Figure 5.8: Improvement of the Rx SINR by the different adaptive IMD2 cancellation algorithms at different transmitter power levels and the Rx SNR of 10 dB.

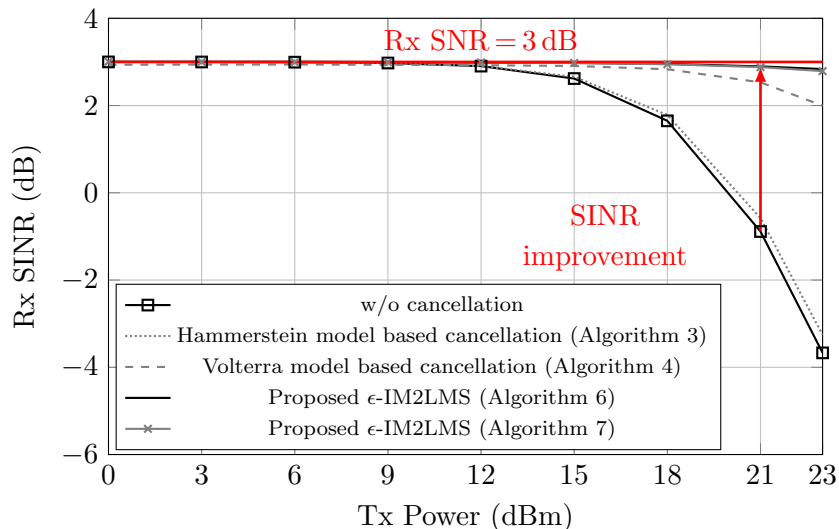


Figure 5.9: Improvement of the Rx SINR by the different adaptive IMD2 cancellation algorithms at different transmitter power levels and the Rx SNR of 3 dB.

5.5.2 RLS Based IMD2 Cancellation

The performance of the R-IM2RLS algorithm using the CSF delay-approximation and the DC-notch filter (Algorithm 12) is evaluated using an FDD scenario with an LTE10 multi-cluster intra-band Tx signal which has a native sampling frequency of 15.36 MHz, QPSK modulation and short cyclic prefix. The I-path IMD2 interference is estimated by the R-IM2RLS, while the Q-path IMD2 interference is estimated by the linear 1-tap RLS algorithm (Algorithm 14) which uses the I-path IMD2 replica signal as reference input. The resulting multi-cluster TxL signal has a strong frequency-selectivity as indicated by Fig. 5.10. The R-IM2RLS in the I-path has 15 taps and runs on the sampling rate of 30.72 MHz due to the OSF of 2. This means, the adaptive filter is not able to estimate the full leakage path (which has 15 FIR filter taps at 15.36 MHz). With this scenario, additionally the behavior of the algorithm for under-modeling of the leakage channel is evaluated. The linear 1-tap Q-path RLS runs on the sampling rate of 30.72 MHz, too.

The received signal $d[n]$ is DC filtered and the proposed algorithm is using the DC-notch filter to suppress the DC of the IMD2 replica signal. The thermal noise floor of the receiver is assumed at -104.5 dBm per 10 MHz and the receiver NF is 4.5 dB. The resulting receiver noise floor with 20 dB LNA gain is at -80 dBm $\hat{=}$ -108.2 dBm/15 kHz and the Rx power is -77 dBm assuming an Rx SNR of 3 dB. To have a more challenging scenario for the IM2RLS algorithm as for the ϵ -IM2LMS algorithm, the assumed Rx mixer IIP2 is increased from 40 dBm to 60 dBm. This corresponds to an Rx SNR decrease of 1 dB for the specific intra-band multi-cluster transmit signal at 23 dBm power level. The spectrum of the signals for $P_{Tx} = 23$ dBm is depicted in Fig. 5.10. It can be observed, that the resulting IMD2 interference y_{BB}^{IMD2} is below the receiver noise floor but still leads to an SNR degradation of 1 dB. The depicted estimated interference replica \hat{y}_{AC} is estimated by the R-IM2RLS in the I-path and the 1-tap RLS in the Q-path. The multi-cluster LTE10 Tx signal uses 21/50 RBs (252 subcarriers from 1024), which

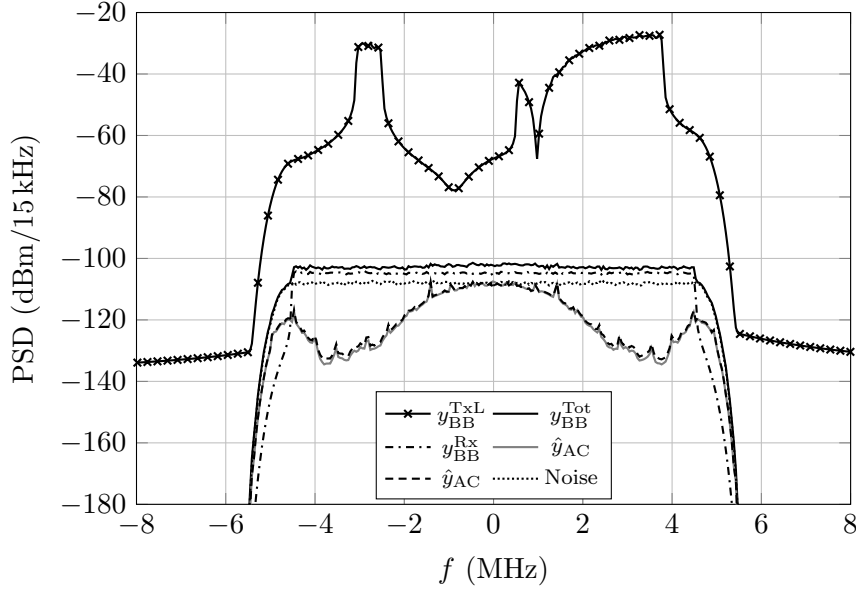


Figure 5.10: Spectrum of the signals for the multi-cluster Tx scenario with the transmit power $P_{\text{Tx}} = 23$ dBm and the mixer IIP2 of +60 dBm.

means that 3.78 MHz of the available 9.015 MHz are allocated. With an OSF of 2 this corresponds to an allocated bandwidth-to-sampling-rate ratio of $3.78/30.72 = 0.12$ which introduces a high correlation in the transmit BB samples. The resulting condition number $\text{cond}(\tilde{\mathbf{R}})$ of the 15×15 dimensional autocorrelation matrix $\tilde{\mathbf{R}} = E \{ \mathbf{z}_f \mathbf{z}_f^H \}$ is on the order of 10^7 which may lead to numerical problems. The regularization of the R-IM2RLS improves the numerical properties of the estimated matrix $\mathbf{P}[n]$. The forgetting factor of the R-IM2RLS is chosen as $\lambda = 0.9999$, $\mathbf{P}[-1] = 100\mathbf{I}$, and the regularization constant $\sigma = 1 \times 10^{-6}$. The 1-tap RLS in the Q-path uses the same forgetting factor but the initial value $p[-1] = 1 \times 10^3$. The coefficient vector of the R-IM2RLS is initialized with $\mathbf{w}_I[-1] = [10^{-3}, 0, 0, \dots, 0]^T$ for the I-path, and the 1-tap Q-path RLS is initialized with zero. The performance is evaluated for the different regularization matrices $\mathbf{L} = \mathbf{I}$ (Tikhonov regularization), \mathbf{L} as described by (5.88) (first order derivative smoothing matrix), and \mathbf{L} as described by (5.89) (second order derivative smoothing matrix). The IM2RLS without regularization is not included in the comparison due to numerical instability reasoned by the extremely high condition number of $\tilde{\mathbf{R}}$ which is on the order of 10^7 . The performance of the R-IM2RLS is compared with the ϵ -IM2LMS algorithm (Algorithm 7) [7]. The ϵ -IM2LMS algorithm uses the step-size $\mu = 0.005$, the regularization parameter $\gamma = 0.001$, and the initial coefficient vector $\mathbf{w}_I[-1] = [10^{-3}, 0, 0, \dots, 0]^T$. The Q-path IMD2 replica is estimated by a linear normalized 1-tap LMS (Algorithm 13) which uses the I-path IMD2 replica estimated by the ϵ -IM2LMS as reference input signal. The normalized 1-tap LMS uses a step-size of $1/100$, the regularization parameter is set to 0.001 and the initial coefficient is set to zero. The value of the step-size is set to the best compromise between steady-state cancellation and convergence time.

The convergence of the algorithms is compared using the ensemble NMSE, and the steady-state cancellation by the SINR. The convergence behavior of the algorithms is depicted in Fig. 5.11. The R-IM2RLS shows a faster initial convergence than the

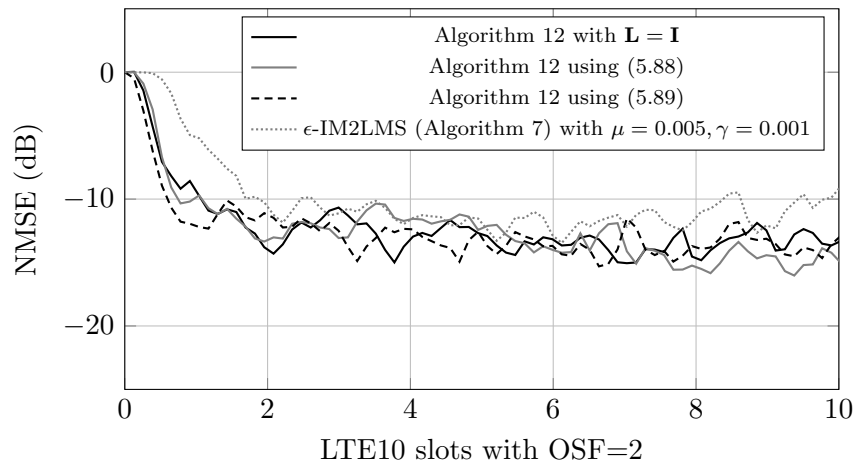


Figure 5.11: Convergence of the R-IM2RLS variants and the ϵ -IM2LMS algorithm at the transmit power level of $P_{Tx} = 23$ dBm.

ϵ -IM2LMS algorithm (including the 1-tap NLMS/RLS in the Q-path) which takes about twice as long to reach an NMSE of -10 dB. The SINR improvement of the Rx signal for the different algorithms and regularizations is depicted in Fig. 5.12. All three regularization matrices lead to nearly the same SINR improvement. The steady-state SINR improvement of the ϵ -IM2LMS algorithm is slightly below the IM2RLS algorithm. The evolution of the condition number of $\tilde{\mathbf{R}}'[n] = \mathbf{P}[n]^{-1}$ is illustrated in Fig. 5.13. The condition number of $\tilde{\mathbf{R}}$ estimated by the IM2RLS without regularization drastically increases up to values between 10^7 and 10^8 . In contrast to that, the condition number of $\tilde{\mathbf{R}}'$ estimated by the R-IM2RLS with different regularization matrices \mathbf{L} stays below 400

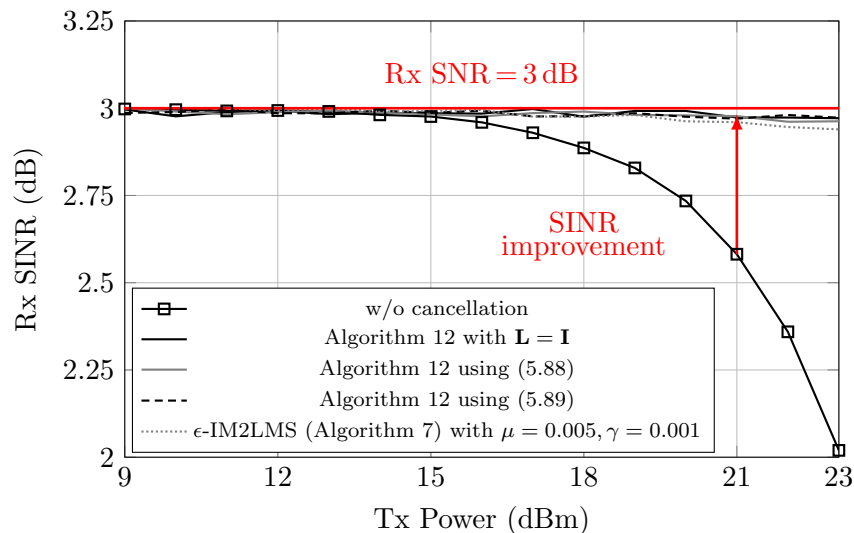


Figure 5.12: Improvement of the Rx SINR at different transmitter power levels and an Rx mixer IIP2 of +60 dBm. The algorithms are using the DC-filtered receive signal, and the R-IM2RLS/IM2LMS algorithms are using the DC-notch filter to remove the DC.

5 Adaptive IMD2 Cancellation

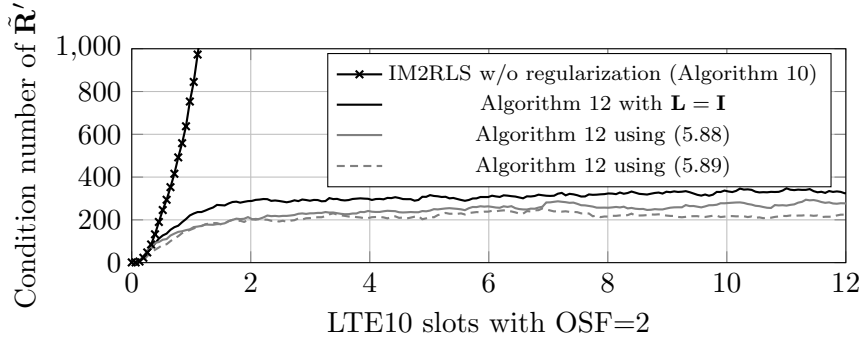


Figure 5.13: Evolution of the condition number of $\tilde{\mathbf{R}}'[n] = \mathbf{P}^{-1}[n]$ for a clustered allocation like depicted in Fig. 5.10 and 23 dBm transmit power. The condition number of $\tilde{\mathbf{R}} = E\{\mathbf{z}\mathbf{z}^H\}$ without regularization is on the order of 10^7 .

for the specific clustered Tx example. The IIP2 improvement after the digital IMD2 cancellation is summarized in Table 5.2 and may be calculated by reformulating (2.84) to:

$$\begin{aligned}
 \text{IIP2}_{\text{after canc.}} &= 2P_{\text{RF}}^{\text{TxL}} - P_{\text{IM2, after canc.}}^{\text{CSF,LTE}} - \text{CF} \\
 &= 2 \cdot (23 \text{ dBm} - 50 \text{ dB} + 20 \text{ dB}) \\
 &\quad + 102.05 \text{ dBm} - 10.85 \text{ dB} = 77.2 \text{ dBm} \quad (5.106)
 \end{aligned}$$

The correction factor of 10.85 dB, which is obtained by simulations, corrects the IMD2 power calculated with the 2-tone formula (2.64) to the channel-select, and DC-filtered in-band IMD2 power for the specific clustered LTE10 Tx signal case. For the calculation of the IIP2 improvement, the IMD2 power without DC is used. The R-IM2RLS-, and the ϵ -IM2LMS algorithm are improving the IIP2 from 60 dBm to about 77 dBm and 73 dBm, respectively.

Table 5.2: IIP2 improvement by digital cancellation for the clustered Tx signal

Algorithm	IIP2 after canc.
R-IM2RLS (Algorithm 12) with $\mathbf{L} = \mathbf{I}$	77.2 dBm
R-IM2RLS (Algorithm 12) using (5.88)	76.5 dBm
R-IM2RLS (Algorithm 12) using (5.89)	76.4 dBm
ϵ -IM2LMS (Algorithm 7)	73 dBm

5.6 Verification with Measured Data

The developed Wiener model based IMD2 cancellation algorithms are also tested with measurement data. Two measurement scenarios are investigated. The first measurement setup is based on a real RF transceiver chip provided by the industrial partner. Here, the TxL signal caused IMD2 self-interference is measured by the integrated IQ-receiver which includes 25% duty-cycle mixers. The following algorithms were evaluated with the obtained measurement data:

- Algorithm 6: ϵ -IM2LMS algorithm with DC-notch filter and CSF in the coefficient update.
- Algorithm 7: Patented ϵ -IM2LMS algorithm with DC-notch filter and CSF delay approximation.
- Algorithm 8: ϵ -IM2LMS algorithm with simplified implicit DC cancellation and CSF delay approximation.
- Algorithm 10: IM2RLS algorithm with DC-notch filter and CSF delay approximation.

In this comparison, the performance of different versions of the ϵ -IM2LMS algorithm is evaluated in a real measurement scenario. It turns out, that all variants have nearly the same IMD2 cancellation performance. Furthermore, their performance is compared to the IM2RLS algorithm.

In the second scenario, a measurement setup consisting of discrete RF components (PA, LNA, mixer, duplexer) compared to the integrated RF chip in the first scenario is used to generate the TxL signal caused IMD2 interference. In this scenario the following algorithms are evaluated:

- Algorithm 7: Patented ϵ -IM2LMS algorithm with DC-notch filter and CSF delay approximation.
- Algorithm 12: R-IM2RLS algorithm with DC-notch filter and CSF delay approximation.

In this scenario the performance of the R-IM2RLS algorithm is evaluated with measured data and its performance is compared to the ϵ -IM2LMS algorithm. However, no multi-cluster Tx signal is used and therefore also the IM2RLS algorithm without regularization is applicable in this scenario.

5.6.1 Measurements from the Transceiver Chip

The functionality of the derived ϵ -IM2LMS- and IM2RLS algorithm is demonstrated using measured IQ data streams from a real transceiver chip which contain the IMD2 interference. The mixers in the receiver are implemented as 25% duty-cycle current-driven passive mixers (see Section 2.2 for details). The transmitter within the transceiver operated at $f_{\text{Tx}} = 1856$ MHz, and the receiver LO was set to $f_{\text{Rx}} = 1936$ MHz which corresponds to LTE band 2. The transceiver chip is mounted on an engine-board

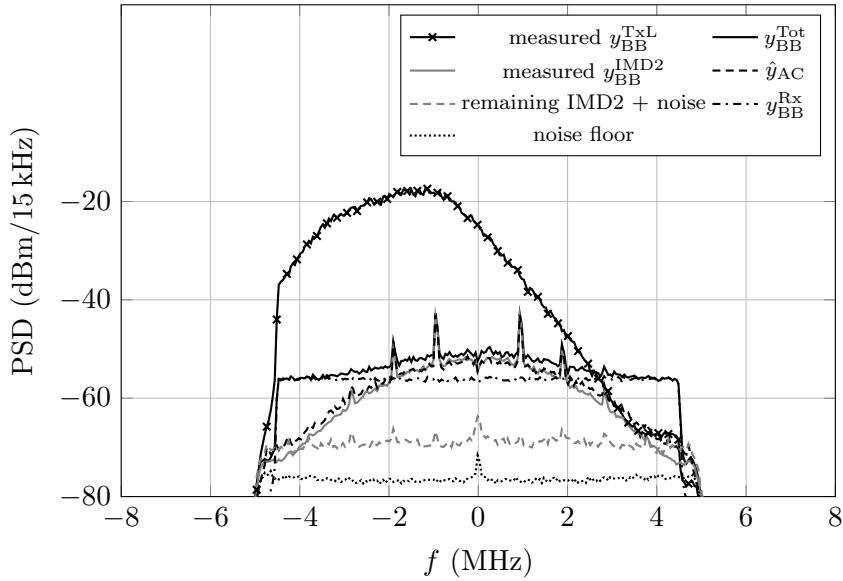


Figure 5.14: IMD2 interference cancellation with the ϵ -IM2LMS using the simplified implicit DC cancellation and the CSF delay approximation (Algorithm 8). The measured data was obtained from a real integrated RF transceiver.

which includes the band 2 duplexer. The measured IQ data streams were used for the digital post-cancellation in Matlab. The used cancellation architecture is depicted in Fig. 5.2. The I-path IMD2 interference was estimated using the ϵ -IM2LMS/IM2RLS algorithm, whereas the Q-path IMD2 interference was estimated by the 1-tap NLMS/RLS algorithm (Algorithm 13/Algorithm 14) which used the estimated I-path IMD2 replica signal as reference input. The transmit signal was an LTE10 signal with full allocation, short cyclic prefix and QPSK modulation. The resulting transmitter leakage signal $y_{\text{BB}}^{\text{TxL}}$ which is depicted in Fig. 5.14 indicates a highly frequency-selective duplexer stop-band frequency response. The TxL signal caused BB IMD2 interference $y_{\text{BB}}^{\text{IMD2}}$ was measured by the receiver in the chip. The total received signal $y_{\text{BB}}^{\text{Tot}}$ was obtained in Matlab by adding a simulated Rx signal with full allocation to the measured IMD2 interference signal stream $y_{\text{BB}}^{\text{IMD2}}$. With this approach any desired Rx SINR may be created. The spectrum of the total received signal $y_{\text{BB}}^{\text{Tot}}$ including the wanted Rx signal and the IMD2 interference is depicted in Fig. 5.14. Furthermore, the spectra of the estimated IMD2 interference $\hat{y}_{\text{AC}} = \hat{y}_{\text{AC,I}} + j\hat{y}_{\text{AC,Q}}$ (after convergence of the adaptive filters), the remaining IMD2 interference, the Rx signal and the noise floor are visualized. It can be observed, that a very good estimation of the IMD2 interference signal $y_{\text{BB}}^{\text{IMD2}}$ is obtained by the replica signal \hat{y}_{AC} . The Rx SINR before the digital cancellation was chosen to be -1 dB which increases to about 12.5 dB and 15.2 dB after the digital cancellation using the ϵ -IM2LMS- and the IM2RLS algorithm, respectively.

The step-size of the ϵ -IM2LMS algorithm is set to $\mu = 1/150$, the regularization parameter $\epsilon = 0.001$, the DC-notch parameter $a = 0.998$ and the coefficient vector was initialized with $\mathbf{w}_1[-1] = [10^{-3}, 0, 0, \dots, 0]^T$. The simulation showed that $M = 20$ coefficients were needed to cancel the IMD2 interference which was generated by the heavily frequency-selective TxL signal $y_{\text{BB}}^{\text{TxL}}$ (see Fig. 5.14). The 1-tap NLMS algorithm for the

Q-path uses the step-size $\mu = 1/100$, the regularization parameter $\epsilon = 0.001$, and the initial coefficient vector $w_Q[-1] = 0$. The IM2RLS algorithm uses the forgetting-factor $\lambda = 0.9999$ and $\mathbf{P}[-1] = 100\mathbf{I}$. The 1-tap RLS in the Q-path uses the same forgetting factor and the initial parameter $p[-1] = 1 \times 10^3$. The coefficient vector of the I-path IM2RLS algorithm was initialized with $\mathbf{w}_I[-1] = [10^{-3}, 0, 0, \dots, 0]^T$, and the 1-tap RLS with zero.

The convergence behavior of the ϵ -IM2LMS algorithm (Algorithm 8), and the 1-tap NLMS algorithm is depicted in Fig. 5.15. The ϵ -IM2LMS algorithm uses 20 complex valued coefficients ($w_{I,0} \dots w_{I,19}$) and the 1-tap NLMS the single real valued coefficient w_Q . The coefficients reach the steady-state after about 11 LTE10 symbols which corresponds to a convergence time of $785\mu\text{s}$. The real-, and imaginary parts of the 20 I-path coefficients in steady-state are depicted in Fig. 5.16. The coefficient w_Q which scales the I-path IMD2 estimate to the Q-path IMD2 interference is about 0.9 which proves that the I-, and Q-path IMD2 interference are not equal. The IM2RLS algorithm and different versions of the ϵ -IM2LMS algorithm are evaluated with respect to the Rx SINR improvement and convergence time. The Rx SINR improvement after the digital IMD2 cancellation from an initial SINR value of -1 dB and the required convergence time is summarized in Table 5.3.

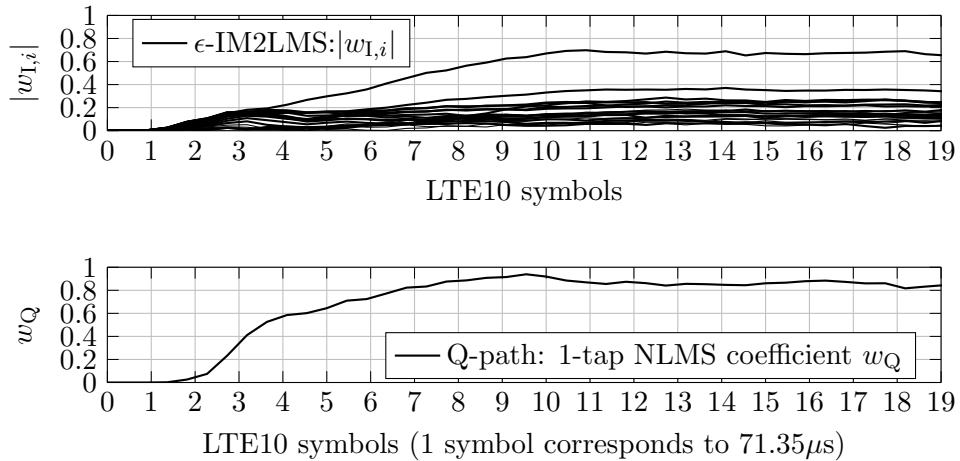


Figure 5.15: Convergence of the 20 I-path ϵ -IM2LMS coefficients (top) and the single Q-path coefficient (bottom).

5 Adaptive IMD2 Cancellation

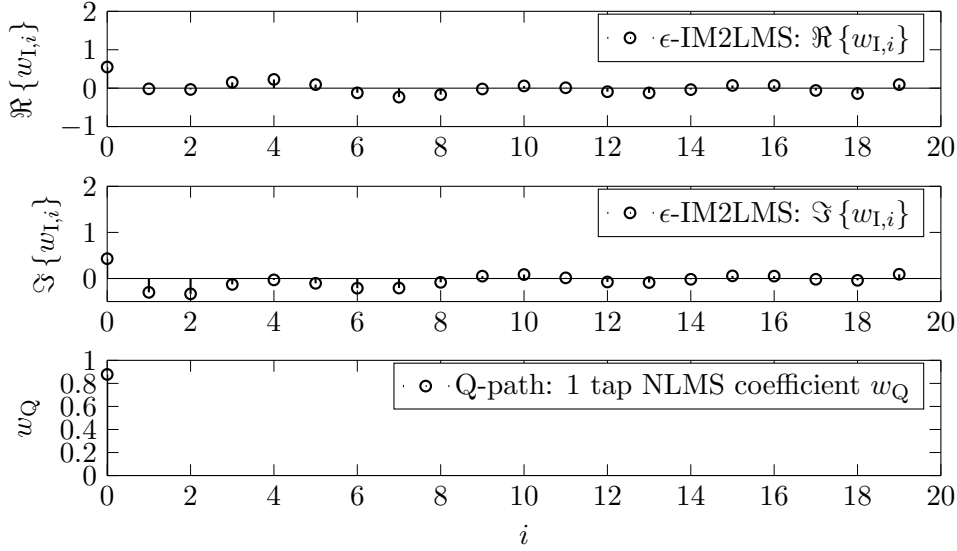


Figure 5.16: Real part of the estimated ϵ -IM2LMS coefficients (top), imaginary part of the estimated ϵ -IM2LMS coefficients (middle), and single real valued Q-path coefficient (bottom).

Table 5.3: Summary of the SINR improvement and the convergence time

Algorithm	SINR after canc.	Convergence time
ϵ -IM2LMS (Algorithm 6)	12.5 dB	10.5 LTE10 symbols
ϵ -IM2LMS (Algorithm 7)	12.5 dB	11 LTE10 symbols
ϵ -IM2LMS (Algorithm 8)	12.4 dB	11 LTE10 symbols
IM2RLS (Algorithm 10)	15.2 dB	6 LTE10 symbols

5.6.2 Measurement Setup with Discrete RF Components

The proposed R-IM2RLS algorithm (Algorithm 12) with the 1-tap RLS algorithm (Algorithm 14) in the Q-path was evaluated with measurement data from a setup with discrete RF components and Matlab post-processing. For this evaluation the adaptive filter structure shown in Fig. 5.2 was used. The measurement setup (A) depicted in Fig. 5.17 included the PA ZVA-183G+ which has a gain of 38 dB, a 1 dB compression point of $P_{1\text{dB}} = 25$ dBm and an IP3 of 36 dBm. The output of the PA was connected to the commercial LTE band 2 duplexer model B8663 from TDK. The antenna port of the duplexer was terminated with a $50\ \Omega$ impedance, and the Rx port of the duplexer was connected to the LNA ZX60-83LN12+ which has 22 dB gain, a NF of 1.4 dB, and an IP3 of 35.2 dBm (at 2 GHz). For the down-conversion, the ZAM-42 Level 7 mixer was used which has 25 dB LO-to-RF terminal isolation. No additional filters were used in the transmitter and receiver chain. The measurement was carried out for the I-path mixer and a fully allocated LTE-A transmit signal with 10 MHz bandwidth, QPSK modulation and short cyclic prefix. The transmit frequency was set to $f_{\text{Tx}} = 1.855$ GHz and the mixer LO frequency was $f_{\text{Rx}} = 1.935$ GHz (80 MHz duplexing distance). The LTE trans-

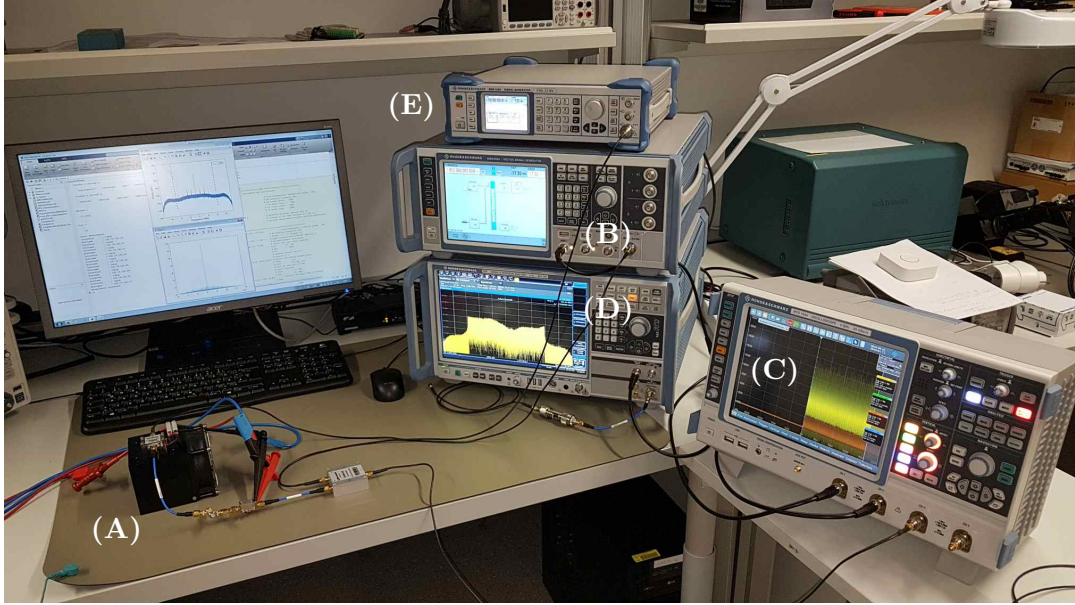


Figure 5.17: Measurement setup including the DUT (A) with the PA ZVA-183G+, the LNA ZX60-83LN12+, the mixer ZAM-42 from Mini Circuits and the LTE band 2 duplexer B8663. The signal generator R&S SMW 200A (B) generates the LTE transmit signal which is amplified by the PA. The R&S real-time oscilloscope RTO 1044 (C) is used to measure the BB signal at the output of the mixer. The R&S FSW26 spectrum analyzer (D) is used to measure the TxL signal, and the signal generator R&S SMB 100A (E) generates the mixer LO signal.

mit signal was generated by the R&S SMW 200A signal generator (B) and amplified by the PA. The transmit signal leaked through the duplexer stop-band into the receiver with 80 MHz frequency offset to the LO signal and was amplified by the LNA. This amplified TxL signal generated the BB IMD2 interference at the output of the mixer which was measured with the real-time oscilloscope RTO 1044 (C) using the BB I/Q-interface (RTO-K11 option). This option allows to set the oscilloscope sampling frequency to the native LTE sampling frequency (a sampling rate of 15.36 MHz for 10 MHz LTE signals was used) and includes also a channel-select filtering. The TxL signal at the output of the LNA was measured by the R&S FSW26 spectrum analyzer (D), and the LO signal with 7 dBm for the ZAM-42 mixer was generated by the R&S SMB 100A signal generator (E). The measurement of the TxL signal, and the BB IMD2 interference were performed separately such that the circuit load was always kept constant with $50\ \Omega$ impedance. The transmit power at the output of the PA was set to $P_{\text{RF}}^{\text{Tx}} = 24\ \text{dBm}$, which in combination with the duplexer attenuation of 66.6 dB (at $f_{\text{Tx}} = 1.855\ \text{GHz}$) and the LNA gain of 22 dB led to the TxL signal power of $P_{\text{RF}}^{\text{TxL}} = 24\ \text{dBm} - 66.6\ \text{dB} + 22\ \text{dB} = -20.6\ \text{dBm}$. The measured I-path mixer BB output data stream and the complex valued BB transmit samples are up-sampled by the factor of 2 (because the proposed algorithm includes the envelope-squaring which doubles the signal bandwidth) and used for the Matlab post-processing. The spectrum of the signals before and after the digital cancellation with the R-IM2RLS (Algorithm 12) using a Tikhonov regularization and the param-

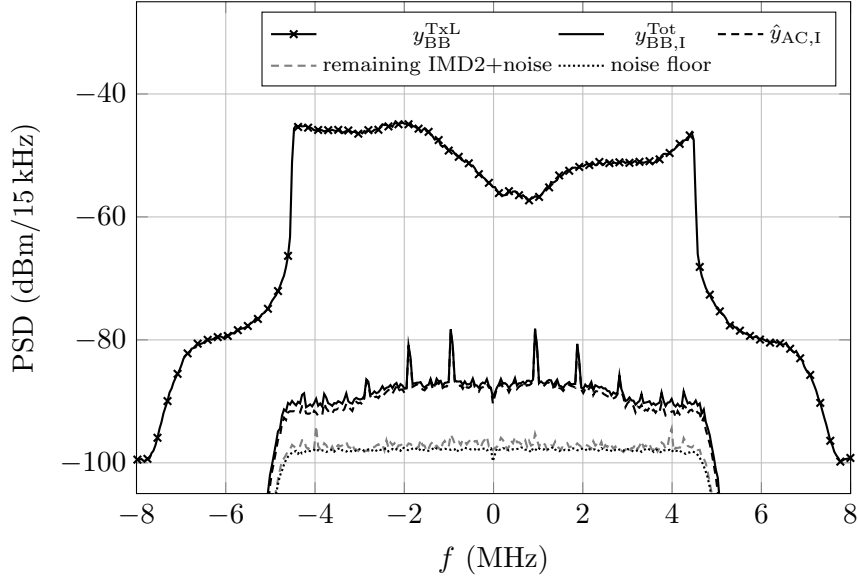


Figure 5.18: Spectrum of the measured BB equivalent TxL signal $y_{\text{BB}}^{\text{TxL}}$ and the receive signal $y_{\text{BB},\text{I}}^{\text{Tot}}$ including noise and the IMD2 interference. The BB equivalent TxL signal shows a strong frequency selectivity. Also shown are the spectra of the estimated IMD2 replica $\hat{y}_{\text{AC},\text{I}}$ and the remaining IMD2 interference plus noise after the cancellation.

eters $\mathbf{P}[-1] = 100\mathbf{I}$, $\lambda = 0.9999$, $\sigma = 10^{-6}$ and $\mathbf{L} = \mathbf{I}$ are depicted in Fig. 5.18. The Matlab post-cancellation revealed that 15 taps were sufficient to reduce the IMD2 interference nearly down to the noise floor. The coefficient vector was initialized with $\mathbf{w}_{\text{I}}[-1] = [10^{-3}, 0, 0, \dots, 0]^T$, and the convergence behavior of the 15 coefficients is shown in Fig. 5.19 which indicates that the algorithm converged after about 5 LTE symbols. To determine the IIP2 improvement achieved by the digital cancellation, the true BB IMD2 interference signal needs to be known. In the measurement, the true IMD2 interference is embedded in noise and cannot be measured explicitly. Additionally, the correction factor CF used in (5.106) is not known because it is duplexer dependent. However, the true IMD2 signal may be approximately reconstructed by computing the envelope of the measured TxL signal

$$\hat{y}_{\text{BB},\text{I}}^{\text{IMD2,TxL}}[n] = \alpha_2^{\text{TxL,I}} |y_{\text{BB}}^{\text{TxL}}[n]|^2 * \bar{h}_{\text{s}}[n] \quad (5.107)$$

with subsequent channel-select filtering and removal of the DC component. Finally, the factor $\alpha_2^{\text{TxL,I}}$ is adjusted until the reconstructed IMD2 interference $\hat{y}_{\text{BB},\text{I}}^{\text{IMD2,TxL}}$ gives the best spectral match with the measured signal $y_{\text{BB},\text{I}}^{\text{Tot}}$. The resulting spectrum of the reconstructed IMD2 interference using (5.107) is depicted in Fig. 5.20 where a good match with the total received signal $y_{\text{BB},\text{I}}^{\text{Tot}}$ is achieved. Also the error signal between the reconstructed IMD2 interference $\hat{y}_{\text{BB},\text{I}}^{\text{IMD2,TxL}}$ and the IMD2 replica signal $\hat{y}_{\text{AC},\text{I}}$ is visualized. Finally, the obtained IMD2 cancellation is estimated by using the NMSE in

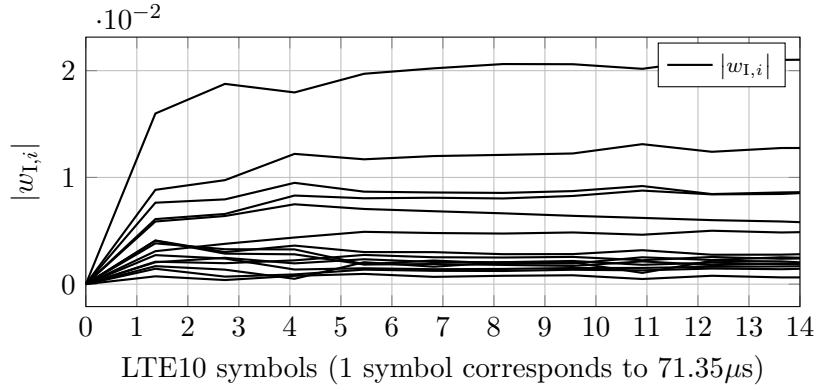


Figure 5.19: Evolution of the 15 coefficients $|w_{1,i}|$ for $i = 0 \dots 14$ which are estimated by the R-IM2RLS algorithm. Plotted are the absolute values of the complex valued coefficients. Convergence is achieved after around 5 LTE symbols (1 LTE symbol has the duration of $71.35 \mu s$).

steady-state [9]

$$\begin{aligned} \text{NMSE}_{\text{dB}} &= 10 \log_{10} \left(\frac{\text{E} \left[\left| \hat{y}_{\text{BB},\text{I}}^{\text{IMD2,TxL}}[n] - \hat{y}_{\text{AC},\text{I}}[n] \right|^2 \right]}{\text{E} \left[\left| \hat{y}_{\text{BB},\text{I}}^{\text{IMD2,TxL}}[n] \right|^2 \right]} \right) \\ &= -16 \text{ dB} \end{aligned} \quad (5.108)$$

which indicates an IMD2 interference cancellation of 16 dB. This corresponds to an increase of the IIP2 of the same amount. In Table 5.4, the performance of the R-IM2RLS algorithm is compared to the ϵ -IM2LMS algorithm. In this scenario no Rx signal is used, therefore the IIP2 improvement is used as performance measure instead of the SINR. The parameters for the ϵ -IM2LMS algorithm are chosen to give a good compromise between convergence time and steady-state performance. The step-size is chosen as $\mu = 1/150$, the regularization term $\epsilon = 0.001$ and the parameter of the DC-notch filter is $a = 0.998$. It can be observed, that the ϵ -IM2LMS algorithm needs a long time to converge. In contrast to that, the R-IM2RLS algorithm shows a better IIP2 improvement and converges within 5 LTE10 symbols which corresponds to $357 \mu s$.

Table 5.4: Improvement of the effective IIP2

Algorithm	IIP2 improvement	Convergence time
ϵ -IM2LMS (Algorithm 7)	12.8 dB	37 LTE10 symbols
R-IM2RLS, $\mathbf{L} = \mathbf{I}$ (Algorithm 12)	16 dB	5 LTE10 symbols

5.7 Conclusion

Different variants of the nonlinear ϵ -IM2LMS-, and the IM2RLS algorithm were evaluated in simulations and with measured IMD2 data. Simulations using the ϵ -IM2LMS algorithm validated that the CSF delay approximation has a minor performance influence. The performance of the R-IM2RLS algorithm was assessed in an intra-band

5 Adaptive IMD2 Cancellation

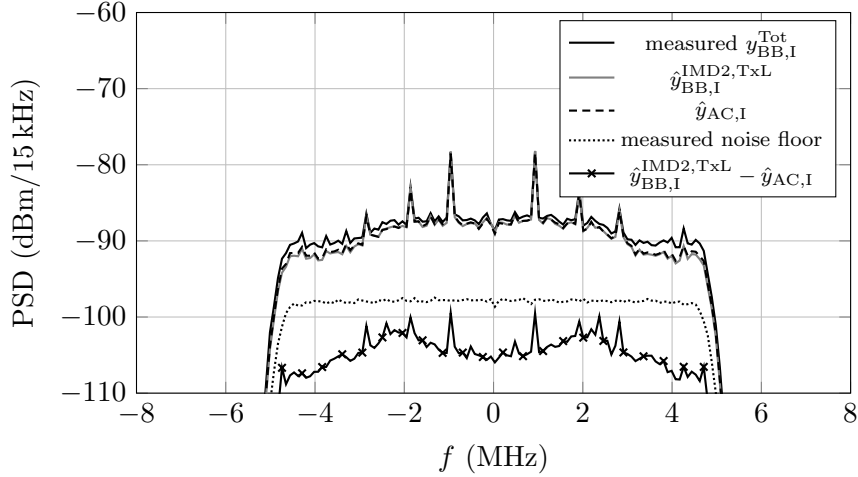


Figure 5.20: Spectrum of the reconstructed IMD2 signal $\hat{y}_{BB,I}^{\text{IMD2,TxL}}$ using the measured TxL signal. The IMD2 signal which is estimated by the R-IM2RLS algorithm using the total received signal $y_{BB,I}^{\text{Tot}}$ and the ideal transmit IQ-samples closely matches the reconstructed IMD2 signal. The remaining IMD2 signal spectrum lies below the noise floor.

multi-cluster transmission scenario where regularization was needed to provide stability of the algorithm. The R-IM2RLS algorithm showed an improved performance compared to the ϵ -IM2LMS algorithm in terms of convergence speed and steady-state cancellation. However, in a real implementation the ϵ -IM2LMS algorithm might be preferred due to its lowered computational complexity. The algorithms were also evaluated with measured IMD2 data. In the first setup the measurement data was obtained from a real RF transceiver chip. An SINR improvement of 13.5 dB and 16.2 dB could be achieved by using the ϵ -IM2LMS-, and the IM2RLS algorithm, respectively. In the second scenario, the measurement data was obtained by a setup with discrete RF components. Here, an IIP2 improvement of 12.8 dB, and 16 dB could be achieved by using the ϵ -IM2LMS-, and the IM2RLS algorithm, respectively.

6

Conclusion and Outlook

In this thesis, two main receiver desensitization effects have been addressed. The first effect occurs in FDD transceivers, where a part of the transmit signal leaks into the receiver and causes a receiver self-interference. The second effect is the harmonic down-conversion of blocker signals due to the harmonic response of the receive mixers which are implemented as square-wave mixers. To be able to find countermeasures for both types of receiver interferences, a detailed modeling of the TxL signal caused receiver self-interferences and also the used 25% duty-cycle current-driven passive mixers is provided in this thesis.

In this work, the receiver self-interference which is caused by the TxL signal is mitigated by adaptive filtering in the digital BB. For this purpose, the mathematical models of several linear and nonlinear receiver interferences have been derived. The adaptive filtering sections in this thesis focus on the digital cancellation of the modulated spur-, and the IMD2 interference. The modulated spur interference may be generated by LO-LO cross-talk in inter-band CA or also in intra-band CA scenarios where a split-LNA is used. For both cases the modulated spur interference may consist of a main and an image interference part. The derived widely-linear adaptive filter structure to cancel the main and the image modulated spur interference can be used in both cases. In this work the cancellation of the modulated spur interference was demonstrated by simulations, and the results were published in [9]. The performance of four different adaptive algorithms was compared and it turns out that the ϵ -VSSNLMS algorithm represents the best compromise regarding performance and computational complexity.

The main focus of this thesis is the pure digital cancellation of the IMD2 interference which is generated by the second-order nonlinearity of the Rx mixer. Traditional Volterra kernel based approaches to cancel the IMD2 interference suffer from a high computational complexity of order $\mathcal{O}(M^2)$ for LMS based algorithms and $\mathcal{O}(M^4)$ for RLS based algorithms, respectively. This thesis presented novel nonlinear Wiener model LMS-, and RLS based algorithms to cancel the IMD2 interference in the digital BB. The computational complexity of the proposed algorithms is $\mathcal{O}(M)$ and $\mathcal{O}(M^2)$ for the LMS-, and the RLS algorithm based cancellation, respectively. The Wiener model uses a static nonlinearity at the output of the adaptive filter which has the advantage that less coefficients are necessary in the estimation process compared to a Volterra kernel based adaptive filter. The proposed ϵ -IM2LMS algorithm is a nonlinear normalized and regularized LMS based algorithm. For the IM2RLS algorithm also a regularized version was derived (R-IM2RLS) which is applicable for highly correlated transmit signals like used in LTE multi-cluster transmissions. Both algorithms are able to estimate the IMD2 interference in case of a highly frequency-selective Tx-to-Rx frequency responses. The

6 Conclusion and Outlook

performance of the algorithms was demonstrated by simulations with different Rx SNR scenarios, and both algorithms outperformed the traditional Volterra kernel LMS based approach in terms of adaptation speed and cancellation performance.

The performance of the Wiener model based algorithms was also demonstrated using measurement data. In the first setup the measurement data was obtained from a real integrated RF transceiver chip which is developed and manufactured by the industrial partner. The proposed ϵ -IM2LMS algorithm and the R-IM2RLS algorithm were able to improve the Rx SINR from -1 dB up to 12.5 dB and 15.2 dB, respectively. The coefficients of the ϵ -IM2LMS algorithm converged after 11 LTE10 symbols whereas the R-IM2RLS algorithm needed only 6 LTE10 symbols. The second measurement setup included discrete RF components. Here, the mixer IIP2 could be increased by 12.8 dB and 16 dB with the ϵ -IM2LMS-, and the R-IM2RLS algorithm, respectively. The presented ϵ -IM2LMS algorithm was patented by the industrial partner and resulted in the U.S. patent US 2018/015417 which was filed in June 2017. The derivation and the performance evaluation of the ϵ -IM2LMS-, and the R-IM2RLS algorithm were published in [7], and [27], respectively.

The square-wave mixer implementation in the receiver causes harmonics in the transistor control signals. This leads to a harmonic response of the mixer which down-converts unwanted spectral components to the BB. Consequently, the reception of the wanted Rx signal is degraded. In this thesis, a harmonic rejection concept to reject specific harmonics in the control signal of the 25% duty-cycle current driven passive mixer was presented. The proposed control scheme was implemented in a Cadence circuit simulation using the Virtuoso platform and a 28 nm technology package. The proposed harmonic rejection approach showed a superior suppression of the harmonic mixer response. The developed HR mixer concept for 25% duty-cycle mixers was patented by the industrial partner and resulted in the U.S. patent US 9,935,722 B2 which was filed in June 2016 and granted in March 2018. The generation of the HR control signals using digital-to-time converters (DTCs) was also patented by the industrial partner and resulted in the U.S. patent US 9,755,872 B1, which was filed in August 2016 and granted in September 2017.

Future investigations may contain the digital cancellation of Tx harmonics and of higher even-order intermodulation distortions as the IMD4-, and the IMD6 interference. Furthermore, in this thesis it is assumed that only one interference desensitizes the receiver at a certain time. Another obvious aspect to be addressed is therefore the investigation of optimum digital cancellation strategies for co-existing receiver interferences.

A

Appendix

A.1 Power Spectral Density Plots

The PSDs in this thesis are plotted with respect to the signal power within a specific bandwidth e.g. dBm/15kHz. If the signal has a frequency-flat spectrum (which is approximately true for LTE signals), then the magnitude value of one frequency bin with the bin spacing $\Delta f = 15$ kHz may be calculated as

$$P_{bin} = \frac{P_{Rx}}{B} \Delta f \left[\frac{W}{15 \text{ kHz}} \right]. \quad (\text{A.1})$$

Here P_{Rx} is the signal power, B the signal bandwidth (e.g. 9.015 MHz for LTE10) and $\Delta f = f_s/N_{FFT}$ where f_s is the sampling frequency and N_{FFT} the number of FFT bins. The bin power in dBm/15 kHz is then

$$P_{bin} = 10 \log_{10} \left(\frac{P_{bin}}{1 \text{ mW}} \right) \left[\frac{\text{dBm}}{15 \text{ kHz}} \right]. \quad (\text{A.2})$$

A.2 Spur Generation in 25% Duty-Cycle Mixers with the Split-LNA Configuration

The Fourier coefficients of the I+ control signal in the 25% duty-cycle mixer with the pulse width jitter 2δ , and the LO phase offset φ_{LO} are

$$\begin{aligned} c_k &= \frac{1}{T_{LO}} \int_0^{T_{LO}} p_{I+}(t) e^{-jk(2\pi f_{LO}t + \varphi_{LO})} dt \\ &= \frac{1}{T_{LO}} \int_{-\delta}^{T_{LO}/4 + \delta} A e^{-jk(2\pi f_{LO}t + \varphi_{LO})} dt \\ &= \frac{-A}{jk2\pi} \left[e^{-jk(2\pi f_{LO}t + \varphi_{LO})} \right] \Bigg|_{-\delta}^{\frac{T_{LO}}{4} + \delta} \\ &= \frac{-A}{jk2\pi} \left[e^{-jk\left(2\pi f_{LO}\left(\frac{T_{LO}}{4} + \delta\right) + \varphi_{LO}\right)} - e^{jk(2\pi f_{LO}\delta - \varphi_{LO})} \right] \\ &= \frac{A}{k\pi} e^{-jk\left(\frac{\pi}{4} + \varphi_{LO}\right)} \frac{1}{2j} \left[e^{jk\left(\frac{\pi}{4} + 2\pi f_{LO}\delta\right)} - e^{-jk\left(\frac{\pi}{4} + 2\pi f_{LO}\delta\right)} \right] \\ &= \frac{A}{k\pi} e^{-jk\left(\frac{\pi}{4} + \varphi_{LO}\right)} \sin \left(k \frac{\pi}{4} + k2\pi \frac{\delta}{T_{LO}} \right) \\ &= A \left[\frac{1}{4} + 2 \frac{\delta}{T_{LO}} \right] e^{-jk\frac{\pi}{4}} \text{sinc} \left(k \frac{\pi}{4} + k2\pi \frac{\delta}{T_{LO}} \right) e^{-jk\varphi_{LO}}, \end{aligned} \quad (\text{A.3})$$

A Appendix

and allowing slow variations of δ and φ compared to f_{LO} , the Fourier coefficients including amplitude- and phase-noise may be expressed as

$$c_k(t) = A \left[\frac{1}{4} + 2 \frac{\delta(t)}{T_{\text{LO}}} \right] e^{-jk\frac{\pi}{4}} \text{sinc} \left(k \frac{\pi}{4} + k 2\pi \frac{\delta(t)}{T_{\text{LO}}} \right) e^{-jk\varphi_{\text{LO}}(t)}. \quad (\text{A.4})$$

By using $c'_k(t) = A \left[\frac{1}{4} + 2 \frac{\delta(t)}{T_{\text{LO}}} \right] \text{sinc} \left(k \frac{\pi}{4} + k 2\pi \frac{\delta(t)}{T_{\text{LO}}} \right)$, the coefficients $c_k(t)$ may be rewritten as $c_k(t) = c'_k(t) e^{-jk\frac{\pi}{4}} e^{-jk\varphi_{\text{LO}}(t)}$. The resulting model for the four mixer phases I+, I-, Q+ and Q- of the first 25% duty-cycle IQ-mixer (aggressor) including amplitude-, and phase-noise becomes [29]

$$p_{\text{LO}_1, \text{I}+}(t) = \sum_{m_1=-\infty}^{\infty} a_{m_1}(t) e^{jm_1 2\pi f_{\text{LO}_1} t} \quad (\text{A.5})$$

$$p_{\text{LO}_1, \text{I}-}(t) = \sum_{m_1=-\infty}^{\infty} (-1)^{m_1} a_{m_1}(t) e^{jm_1 2\pi f_{\text{LO}_1} t} \quad (\text{A.6})$$

$$p_{\text{LO}_1, \text{Q}+}(t) = \sum_{m_1=-\infty}^{\infty} e^{-jm_1 \frac{\pi}{2}} a_{m_1}(t) e^{jm_1 2\pi f_{\text{LO}_1} t} \quad (\text{A.7})$$

$$p_{\text{LO}_1, \text{Q}-}(t) = \sum_{m_1=-\infty}^{\infty} e^{jm_1 \frac{\pi}{2}} a_{m_1}(t) e^{jm_1 2\pi f_{\text{LO}_1} t}. \quad (\text{A.8})$$

The control signals of the second mixer (victim) are

$$p_{\text{LO}_2, \text{I}+}(t) = \sum_{m_2=-\infty}^{\infty} b_{m_2}(t) e^{jm_2 2\pi f_{\text{LO}_2} t} \quad (\text{A.9})$$

$$p_{\text{LO}_2, \text{I}-}(t) = \sum_{m_2=-\infty}^{\infty} (-1)^{m_2} b_{m_2}(t) e^{jm_2 2\pi f_{\text{LO}_2} t} \quad (\text{A.10})$$

$$p_{\text{LO}_2, \text{Q}+}(t) = \sum_{m_2=-\infty}^{\infty} e^{-jm_2 \frac{\pi}{2}} b_{m_2}(t) e^{jm_2 2\pi f_{\text{LO}_2} t} \quad (\text{A.11})$$

$$p_{\text{LO}_2, \text{Q}-}(t) = \sum_{m_2=-\infty}^{\infty} e^{jm_2 \frac{\pi}{2}} b_{m_2}(t) e^{jm_2 2\pi f_{\text{LO}_2} t}, \quad (\text{A.12})$$

where a_{m_1} and b_{m_2} are the Fourier coefficients (A.4) of the first (LO_1) and second (LO_2) mixer, respectively. In the following spur model it is assumed, that each of the four mixer control signals of LO_1 (aggressor) couples to each of the four phases of LO_2 (victim). This corresponds to 16 coupling paths as depicted in Fig. 2.13. The resulting spur current in the victim mixer LO_2 generated by a coupling between the second harmonic of LO_1 ($m_1 = \pm 2$), and the fundamental of LO_2 ($m_2 = \pm 1$) becomes

$$\begin{aligned} i_{\text{RF}, \text{I}+}^{\text{LO}_2}(t) &= i_{\text{RF}}^{\text{TxL}}(t) [\gamma_{\text{I}+\text{I}+} p_{\text{LO}_1, \text{I}+}(t) + \gamma_{\text{I}-\text{I}+} p_{\text{LO}_1, \text{I}-}(t) + \gamma_{\text{Q}+\text{I}+} p_{\text{LO}_1, \text{Q}+}(t) \\ &\quad + \gamma_{\text{Q}-\text{I}+} p_{\text{LO}_1, \text{Q}-}(t)] p_{\text{LO}_2, \text{I}+}(t) \\ &= i_{\text{RF}}^{\text{TxL}}(t) [\gamma_{\text{I}+\text{I}+} (a_2(t) e^{j2\omega_1 t} + a_2^*(t) e^{-j2\omega_1 t}) + \gamma_{\text{I}-\text{I}+} (a_2(t) e^{j2\omega_1 t} + a_2^*(t) e^{-j2\omega_1 t}) \\ &\quad + \gamma_{\text{Q}+\text{I}+} (a_2(t) e^{-j\pi} e^{j2\omega_1 t} + a_2^*(t) e^{j\pi} e^{-j2\omega_1 t}) \\ &\quad + \gamma_{\text{Q}-\text{I}+} (a_2(t) e^{j\pi} e^{j2\omega_1 t} + a_2^*(t) e^{-j\pi} e^{-j2\omega_1 t})] \cdot (b_1(t) e^{j\omega_2 t} + b_1^*(t) e^{-j\omega_2 t}), \end{aligned} \quad (\text{A.13})$$

A.2 Spur Generation in 25% Duty-Cycle Mixers with the Split-LNA Configuration

where $\omega_{\text{LO}_1} = 2\pi f_{\text{LO}_1}$, $\omega_{\text{LO}_2} = 2\pi f_{\text{LO}_2}$ and γ is the coupling coefficient between the mixer branches. E.g. $\gamma_{\text{I-I+}}$ is the coupling coefficient from the I- phase of LO_1 to the I+ phase of LO_2 . By defining $\omega_{\text{sp}} = 2\omega_{\text{LO}_1} - \omega_{\text{LO}_2}$, the current in the I+ branch of LO_2 becomes

$$\begin{aligned} i_{\text{RF,I+}}^{\text{LO}_2}(t) &= i_{\text{RF}}^{\text{TxL}}(t) [\gamma_{\text{I+I+}} + \gamma_{\text{I-I+}} - \gamma_{\text{Q+I+}} - \gamma_{\text{Q-I+}}] (a_2(t)b_1^*(t)e^{j\omega_{\text{sp}}t} + a_2^*(t)b_1(t)e^{-j2\omega_{\text{sp}}t}) \\ &= 2i_{\text{RF}}^{\text{TxL}}(t) [\gamma_{\text{I+I+}} + \gamma_{\text{I-I+}} - \gamma_{\text{Q+I+}} - \gamma_{\text{Q-I+}}] \\ &\quad \cdot a_2'(t)b_1'(t)\cos\left(\omega_{\text{sp}}t - 2\varphi_{\text{LO}_1}(t) + \varphi_{\text{LO}_2}(t) - \frac{\pi}{4}\right). \end{aligned} \quad (\text{A.14})$$

The I- branch current becomes

$$\begin{aligned} i_{\text{RF,I-}}^{\text{LO}_2}(t) &= i_{\text{RF}}^{\text{TxL}}(t) [\gamma_{\text{I+I-}p\text{LO}_1,\text{I+}}(t) + \gamma_{\text{I-I}p\text{LO}_1,\text{I-}}(t) + \gamma_{\text{Q+I-}p\text{LO}_1,\text{Q+}}(t) \\ &\quad + \gamma_{\text{Q-I}p\text{LO}_1,\text{Q-}}(t)] p_{\text{LO}_2,\text{I-}}(t) \\ &= -2i_{\text{RF}}^{\text{TxL}}(t) [\gamma_{\text{I+I-}} + \gamma_{\text{I-I-}} - \gamma_{\text{Q+I-}} - \gamma_{\text{Q-I-}}] \\ &\quad \cdot a_2'(t)b_1'(t)\cos\left(\omega_{\text{sp}}t - 2\varphi_{\text{LO}_1}(t) + \varphi_{\text{LO}_2}(t) - \frac{\pi}{4}\right), \end{aligned} \quad (\text{A.15})$$

and the resulting differential spur current in the I-phase results in

$$\begin{aligned} i_{\text{RF,I}}^{\text{LO}_2}(t) &= i_{\text{RF,I+}}^{\text{LO}_2}(t) - i_{\text{RF,I-}}^{\text{LO}_2}(t) \\ &= 2i_{\text{RF}}^{\text{TxL}}(t) \left[\underbrace{\gamma_{\text{I+I+}} + \gamma_{\text{I-I+}} - \gamma_{\text{Q+I+}} - \gamma_{\text{Q-I+}} + \gamma_{\text{I+I-}} + \gamma_{\text{I-I-}} - \gamma_{\text{Q+I-}} - \gamma_{\text{Q-I-}}}_{\gamma} \right] \\ &\quad \cdot a_2'(t)b_1'(t)\cos\left(\omega_{\text{sp}}t - 2\varphi_{\text{LO}_1}(t) + \varphi_{\text{LO}_2}(t) - \frac{\pi}{4}\right). \end{aligned} \quad (\text{A.16})$$

Similarly, the currents in the Q-branch are

$$\begin{aligned} i_{\text{RF,Q+}}^{\text{LO}_2}(t) &= i_{\text{RF}}^{\text{TxL}}(t) [\gamma_{\text{I+Q+}p\text{LO}_1,\text{I+}}(t) + \gamma_{\text{I-Q+}p\text{LO}_1,\text{I-}}(t) + \gamma_{\text{Q+Q+}p\text{LO}_1,\text{Q+}}(t) \\ &\quad + \gamma_{\text{Q-Q+}p\text{LO}_1,\text{Q-}}(t)] p_{\text{LO}_2,\text{Q+}}(t) \\ &= -2i_{\text{RF}}^{\text{TxL}}(t) [\gamma_{\text{I+Q+}} + \gamma_{\text{I-Q+}} - \gamma_{\text{Q+Q+}} - \gamma_{\text{Q-Q+}}] \\ &\quad \cdot a_2'(t)b_1'(t)\sin\left(\omega_{\text{sp}}t - 2\varphi_{\text{LO}_1}(t) + \varphi_{\text{LO}_2}(t) - \frac{\pi}{4}\right), \end{aligned} \quad (\text{A.17})$$

and

$$\begin{aligned} i_{\text{RF,Q-}}^{\text{LO}_2}(t) &= i_{\text{RF}}^{\text{TxL}}(t) [\gamma_{\text{I+Q-}p\text{LO}_1,\text{I+}}(t) + \gamma_{\text{I-Q-}p\text{LO}_1,\text{I-}}(t) + \gamma_{\text{Q+Q-}p\text{LO}_1,\text{Q+}}(t) \\ &\quad + \gamma_{\text{Q-Q-}p\text{LO}_1,\text{Q-}}(t)] p_{\text{LO}_2,\text{Q-}}(t) \\ &= -2i_{\text{RF}}^{\text{TxL}}(t) [\gamma_{\text{I+Q-}} + \gamma_{\text{I-Q-}} - \gamma_{\text{Q+Q-}} - \gamma_{\text{Q-Q-}}] \\ &\quad \cdot a_2'(t)b_1'(t)\sin\left(\omega_{\text{sp}}t - 2\varphi_{\text{LO}_1}(t) + \varphi_{\text{LO}_2}(t) - \frac{\pi}{4}\right), \end{aligned} \quad (\text{A.18})$$

which leads to the differential spur current in the Q-path

$$\begin{aligned} i_{\text{RF,Q}}^{\text{LO}_2}(t) &= -(i_{\text{RF,Q+}}(t) - i_{\text{RF,Q-}}(t)) \\ &= -2i_{\text{RF}}^{\text{TxL}}(t)\gamma_{\text{Q}}a_2'(t)b_1'(t)\sin\left(\omega_{\text{sp}}t - 2\varphi_{\text{LO}_1}(t) + \varphi_{\text{LO}_2}(t) - \frac{\pi}{4}\right), \end{aligned} \quad (\text{A.19})$$

A Appendix

where $\gamma_Q = -\gamma_{I+Q+} - \gamma_{I-Q-} + \gamma_{Q+Q+} + \gamma_{Q-Q+} + \gamma_{I+Q-} + \gamma_{I-Q-} - \gamma_{Q+Q-} - \gamma_{Q-Q-}$. The transmitter leakage signal creates the LNA output current $i_{\text{RF}}^{\text{TxL}}(t)$ which is first mixed by the aggressor LO_1 and subsequently mixed by the victim LO_2 . Combining these mixing processes with the I-, and Q-component of the complex valued spur, the complex RF current in the victim LO_2 results in

$$\begin{aligned} i_{\text{RF}}^{\text{LO}_2}(t) &= i_{\text{RF,I}}^{\text{LO}_2}(t) + j i_{\text{RF,Q}}^{\text{LO}_2}(t) \\ &= 2 i_{\text{RF}}^{\text{TxL}}(t) a_2'(t) b_1'(t) \left[\gamma_I \cos \left(\omega_{\text{sp}} t - 2\varphi_{\text{LO}_1}(t) + \varphi_{\text{LO}_2}(t) - \frac{\pi}{4} \right) \right. \\ &\quad \left. - j \gamma_Q \sin \left(\omega_{\text{sp}} t - 2\varphi_{\text{LO}_1}(t) + \varphi_{\text{LO}_2}(t) - \frac{\pi}{4} \right) \right], \end{aligned} \quad (\text{A.20})$$

and with the identities, $\cos(\varphi) = \frac{1}{2} (e^{j\varphi} + e^{-j\varphi})$ and $\sin(\varphi) = \frac{1}{2j} (e^{j\varphi} - e^{-j\varphi})$ the current becomes

$$\begin{aligned} i_{\text{RF}}^{\text{LO}_2}(t) &= 2 i_{\text{RF}}^{\text{TxL}}(t) a_2'(t) b_1'(t) \\ &\cdot \left[\underbrace{\frac{\gamma_I + \gamma_Q}{2}}_{K_1} e^{-j(\omega_{\text{sp}} t - 2\varphi_{\text{LO}_1}(t) + \varphi_{\text{LO}_2}(t) - \frac{\pi}{4})} + \underbrace{\frac{\gamma_I - \gamma_Q}{2}}_{K_2} e^{j(\omega_{\text{sp}} t - 2\varphi_{\text{LO}_1}(t) + \varphi_{\text{LO}_2}(t) - \frac{\pi}{4})} \right] \\ &= 2 i_{\text{RF}}^{\text{TxL}}(t) \left[K_1 a_2^*(t) b_1(t) e^{-j\omega_{\text{sp}} t} + K_2 a_2(t) b_1^*(t) e^{j\omega_{\text{sp}} t} \right] \\ &= 2 \Re \left\{ i_{\text{BB}}^{\text{TxL}}(t) e^{j\omega_{\text{Tx}} t} \right\} \left[K_1 a_2^*(t) b_1(t) e^{-j\omega_{\text{sp}} t} + K_2 a_2(t) b_1^*(t) e^{j\omega_{\text{sp}} t} \right] \\ &= \left[i_{\text{BB}}^{\text{TxL}}(t) e^{j\omega_{\text{Tx}} t} + i_{\text{BB}}^{\text{TxL}*}(t) e^{-j\omega_{\text{Tx}} t} \right] \\ &\quad \cdot \underbrace{\left[K_1 a_2^*(t) b_1(t) e^{-j\omega_{\text{sp}} t} + K_2 a_2(t) b_1^*(t) e^{j\omega_{\text{sp}} t} \right]}_{p_{\text{sp}}(t)}. \end{aligned} \quad (\text{A.21})$$

It can be observed, that the spur has a gain imbalance if $\gamma_I \neq \gamma_Q$ which results in a main and image signal component. The BB spur voltage with $f_{\Delta} = f_{\text{Tx}} - f_{\text{sp}}$ after low-pass filtering with the BB impedance $z_{\text{BB}}(t)$ becomes

$$\begin{aligned} u_{\text{BB}}^{\text{LO}_2}(t) &= i_{\text{RF}}^{\text{LO}_2}(t) * z_{\text{BB}} \\ &= \left[K_1 a_2^*(t) b_1(t) i_{\text{BB}}^{\text{TxL}}(t) e^{j2\pi f_{\Delta} t} + K_2 a_2(t) b_1^*(t) i_{\text{BB}}^{\text{TxL}*}(t) e^{-j2\pi f_{\Delta} t} \right] Z_{\text{BB}}. \end{aligned} \quad (\text{A.22})$$

which shows that the modulated spur interference has a main and image component.

A.3 Receiver Noise Floor

The thermal in-band noise floor within the CSF pass-band bandwidth for LTE10 signals with 9.015 MHz bandwidth may be calculated by

$$\begin{aligned} P_{th,\text{dBm}} &= 10 \log_{10} \frac{kTB}{1\text{mW}} \\ &= 10 \log_{10} \frac{1.38 \cdot 10^{-23} \text{m}^2 \text{kg s}^{-2} \text{K}^{-1} \cdot 323\text{K} \cdot 9.015 \text{MHz}}{1\text{mW}} = -104 \text{dBm}, \end{aligned} \quad (\text{A.23})$$

where $k = 1.3810^{-23} \text{m}^2 \text{kg s}^{-2} \text{K}^{-1}$ is the Boltzmann constant, $T = 323\text{K}$ the temperature in Kelvin (50°C), and B the bandwidth. To the thermal noise floor, the receiver

A.4 Scaling of Complex Baseband Signals for a Desired Power Level, SNR and SINR

NF which is the noise contribution of the front-end circuit components (e.g. LNA) is added. A typical value for the NF is 5 dB which results in the receiver noise floor

$$P_{n,\text{dBm}} = P_{th,\text{dBm}} + \text{NF} = -104 \text{ dBm} + 5 \text{ dBm} = -99 \text{ dBm}. \quad (\text{A.24})$$

A.4 Scaling of Complex Baseband Signals for a Desired Power Level, SNR and SINR

A.4.1 Complex White Gaussian Noise

To generate a zero mean complex white Gaussian noise (CWGN) sequence

$$z[n] = x[n] + jy[n], n = 1 \dots N$$

with the desired power P_n at the network impedance Z_0 , it is necessary to derive the variance

$$\begin{aligned} \sigma_z^2 &= E \{ (z[n] - \mu_z)(z[n] - \mu_z)^* \} = E \{ x^2[n] + y^2[n] \} \\ &= E \{ x^2[n] \} + E \{ y^2[n] \}, \text{ for } \mu_z = 0 \end{aligned} \quad (\text{A.25})$$

of the complex valued sequence. The real and the imaginary part of $z[n]$ have the same power, therefore

$$E \{ x^2[n] \} = E \{ y^2[n] \}$$

holds, and the power becomes

$$P_n = \frac{E \{ (z[n] - \mu_z)(z[n] - \mu_z)^* \}}{Z_0} = \frac{2E \{ x^2[n] \}}{Z_0} = \frac{2\sigma_x^2}{Z_0}.$$

Consequently, the standard deviation of the random variables x and y are given with

$$\sigma_x = \sigma_y = \sqrt{\frac{P_n Z_0}{2}}$$

```
% Matlab code to generate a zero mean complex Gaussian distributed random ...
vector with power Pn at the impedance Z0
z = sqrt(Pn/Z0/2)*(randn(1,N)+j*randn(1,N));
```

A.4.2 Generation of an Rx Signal with Desired Power Level

It is assumed that a complex valued zero-mean discrete-time Rx signal $y_{\text{BB}}^{\text{Rx}}[n]$ is already generated in Matlab which shall be scaled for the desired power level $P_{\text{Rx,dBm}}^{\text{des}}$. The actual power level of the signal is

$$P_{\text{Rx}} = \frac{E \{ |y_{\text{BB}}^{\text{Rx}}[n]|^2 \}}{Z_0} \quad (\text{A.26})$$

assuming the network impedance of Z_0 . The desired power in linear scaling is

$$P_{\text{Rx}}^{\text{des}} = 1 \text{ mW} \cdot 10^{\frac{P_{\text{Rx,dBm}}^{\text{des}}}{10}} \quad (\text{A.27})$$

A Appendix

and by solving the equation

$$P_{\text{Rx}}^{\text{des}} \stackrel{!}{=} \frac{1}{Z_0} \frac{1}{N} \sum_n |k \cdot y_{\text{BB}}^{\text{Rx}}[n]|^2 \quad (\text{A.28})$$

the scaling factor

$$k = \sqrt{\frac{P_{\text{Rx}}^{\text{des}}}{P_{\text{Rx}}}} \quad (\text{A.29})$$

is obtained. The resulting Rx signal with the desired power becomes

$$y_{\text{BB}}^{\text{Rx,des}}[n] = k \cdot y_{\text{BB}}^{\text{Rx}}[n]. \quad (\text{A.30})$$

A.4.3 Generation of an Rx Signal with Desired SNR

The complex valued and zero-mean Rx signal which has the desired power P_{Rx} shall be degraded by a band-limited noise signal resulting in the desired SNR_{dB} . The SNR in decibel is

$$\text{SNR}_{\text{dB}} = 10 \log_{10} \frac{P_{\text{Rx}}}{P_n^{\text{des}}}, \quad (\text{A.31})$$

and therefore the desired noise power is

$$P_n^{\text{des}} = \frac{P_{\text{Rx}}}{10^{\text{SNR}_{\text{dB}}/10}}. \quad (\text{A.32})$$

A complex valued AWGN signal $v'[n]$ is generated and filtered by the CSF with impulse response $h_s[n]$ to generate the band-limited noise $v_{\text{BB}}[n] = v'[n] * h_s[n]$ with the actual power P_n . This band-limited noise signal has to be scaled correctly with the factor k to obtain the desired Rx SNR by solving

$$P_n^{\text{des}} \stackrel{!}{=} \frac{1}{Z_0} \frac{1}{N} \sum_n |k \cdot v_{\text{BB}}[n]|^2 \quad (\text{A.33})$$

which results in

$$k = \sqrt{\frac{P_n^{\text{des}}}{P_n}}. \quad (\text{A.34})$$

The noise signal with the desired power is finally obtained with the scaling

$$v_{\text{BB}}^{\text{des}}[n] = k \cdot v_{\text{BB}}[n]. \quad (\text{A.35})$$

A.4.4 Generation of an Rx Signal with Desired SINR

The scaling of the zero mean complex valued interference signal may be of interest when the interference is generated through systems with different frequency responses (e.g. duplexer impulse responses with varying attenuation). To evaluate the performance of the adaptive filter the interference power is normalized to the desired SINR to get comparable results. The SINR in decibel with the interference power P_{int} of the discrete time interference signal $i_{\text{BB}}[n]$ is calculated by

$$\text{SINR}_{\text{dB}} = 10 \log_{10} \left(\frac{P_{\text{Rx}}}{P_n + P_{\text{int}}} \right), \quad (\text{A.36})$$

where

$$P_{\text{int}} = \frac{E \left\{ |i_{\text{BB}}|^2 \right\}}{Z_0}. \quad (\text{A.37})$$

When the noise power P_n is chosen for a desired Rx SNR, then the interference power for a desired SINR may be derived by

$$P_{\text{int}}^{\text{des}} = P_{\text{Rx}} \cdot 10^{-\frac{\text{SINR}_{\text{dB}}}{10}} - P_n. \quad (\text{A.38})$$

The scaling factor becomes

$$k = \sqrt{\frac{P_{\text{int}}^{\text{des}}}{P_{\text{int}}}}, \quad (\text{A.39})$$

and the scaled interference signal to obtain a desired SINR is

$$i_{\text{BB}}^{\text{des}}[n] = k \cdot i_{\text{BB}}[n]. \quad (\text{A.40})$$

A.5 Derivative of a Channel-Select Filtered Signal

In the derivation of the IM2LMS algorithm in Section 5.4.4, the derivative of the non-holomorphic expression $s[n] = [\mathbf{w}^T (\mathbf{x}[n]\mathbf{x}^H[n] - \mathbf{R}_{\mathbf{xx}}) \mathbf{w}^*] * h_s[n]$ with respect to the coefficient vector \mathbf{w}^* including the channel-select filtering appears in the cost function. In this derivation using the Wirtinger Calculus the CSF $h_s[n]$ is assumed as an FIR filter, and the unknown coefficient vector \mathbf{w} which minimizes the cost function is assumed to be deterministic and is therefore not time varying. Rewriting $s[n]$ to

$$\begin{aligned} s[n] &= \left[\underbrace{\mathbf{w}^T (\mathbf{x}[n]\mathbf{x}^H[n] - \mathbf{R}_{\mathbf{xx}}) \mathbf{w}^*}_{=\mathbf{z}^T[n]} \right] * h_s[n] \\ &= h_{s,0}\mathbf{z}^T[n]\mathbf{w}^* + h_{s,1}\mathbf{z}^T[n-1]\mathbf{w}^* + \dots + h_{s,K-1}\mathbf{z}^T[n-K+1]\mathbf{w}^* \\ &= [h_{s,0} \quad h_{s,1} \quad \dots \quad h_{s,K-1}] \begin{bmatrix} \mathbf{z}^T[n] \\ \mathbf{z}^T[n-1] \\ \vdots \\ \mathbf{z}^T[n-K+1] \end{bmatrix} \mathbf{w}^* \\ &= [h_{s,0}, h_{s,1}, \dots, h_{s,K-1}] \begin{bmatrix} z_0[n] & z_1[n] & \dots & z_{M-1}[n] \\ z_0[n-1] & z_1[n-1] & \dots & z_{M-1}[n-1] \\ \vdots & \vdots & & \vdots \\ z_0[n-K+1] & z_1[n-K+1] & \dots & z_{M-1}[n-K+1] \end{bmatrix} \mathbf{w}^* \end{aligned} \quad (\text{A.41})$$

A Appendix

where K is the length of the finite CSF impulse response, the derivative of $s[n]$ using the Wirtinger Calculus becomes

$$\begin{aligned}
\left[\frac{\partial s}{\partial \mathbf{w}^*} \right]^T &= \begin{bmatrix} z_0[n] & z_0[n-1] & \cdots & z_0[n-K+1] \\ z_1[n] & z_1[n-1] & \cdots & z_1[n-K+1] \\ \vdots & \vdots & & \vdots \\ z_{M-1}[n] & z_{M-1}[n-1] & \cdots & z_{M-1}[n-K+1] \end{bmatrix} \begin{bmatrix} h_{s,0} \\ h_{s,1} \\ \vdots \\ h_{s,K-1} \end{bmatrix} \\
&= \begin{bmatrix} z_0[n] * h_s[n] \\ z_1[n] * h_s[n] \\ \vdots \\ z_{M-1}[n] * h_s[n] \end{bmatrix} \\
&= \mathbf{z}[n] * h_s[n] \\
&= \mathbf{z}_f[n] \\
&= (y'[n] \mathbf{x}^*[n] - \mathbf{R}_{\mathbf{xx}}^T \mathbf{w}) * h_s[n]
\end{aligned} \tag{A.42}$$

where the scalar FIR filter output $y'[n] = \mathbf{x}^T[n] \mathbf{w}$ is used. Additionally in the derivation of the IM2RLS algorithm the reformulation

$$\begin{aligned}
s[n] &= (\mathbf{z}^T[n] \mathbf{w}^*) * h_s[n] \\
&= (\mathbf{z}^H[n] \mathbf{w}) * h_s[n] \\
&= h_{s,0} \mathbf{z}^H[n] \mathbf{w} + h_{s,1} \mathbf{z}^H[n-1] \mathbf{w} + h_{s,K-1} \mathbf{z}^H[n-K+1] \mathbf{w} \\
&= [h_{s,0} \quad h_{s,1} \quad \cdots \quad h_{s,K-1}] \begin{bmatrix} \mathbf{z}^H[n] \\ \mathbf{z}^H[n-1] \\ \vdots \\ \mathbf{z}^H[n-K+1] \end{bmatrix} \mathbf{w}
\end{aligned} \tag{A.43}$$

$$\begin{aligned}
s^T[n] &= \mathbf{w}^T [\mathbf{z}^*[n] \quad \mathbf{z}^*[n-1] \quad \cdots \quad \mathbf{z}^*[n-K+1]] \begin{bmatrix} h_{s,0} \\ h_{s,1} \\ \vdots \\ h_{s,K-1} \end{bmatrix} \\
&= \mathbf{w}^T \begin{bmatrix} z_0^*[n] & z_0^*[n-1] & \cdots & z_0^*[n-K+1] \\ z_1^*[n] & z_1^*[n-1] & \cdots & z_1^*[n-K+1] \\ \vdots & \vdots & & \vdots \\ z_{M-1}^*[n] & z_{M-1}^*[n-1] & \cdots & z_{M-1}^*[n-K+1] \end{bmatrix} \begin{bmatrix} h_{s,0} \\ h_{s,1} \\ \vdots \\ h_{s,K-1} \end{bmatrix} \\
&= \mathbf{w}^T \begin{bmatrix} z_0^*[n] * h_s[n] \\ z_1^*[n] * h_s[n] \\ \vdots \\ z_{M-1}^*[n] * h_s[n] \end{bmatrix} \\
&= \mathbf{w}^T \begin{bmatrix} z_0^*[n] \\ z_1^*[n] \\ \vdots \\ z_{M-1}^*[n] \end{bmatrix} * h_s[n] \\
&= \mathbf{w}^T \mathbf{z}^*[n] * h_s[n]
\end{aligned} \tag{A.44}$$

which leads to

$$s[n] = (\mathbf{z}^H[n] * h_s[n]) \mathbf{w} \quad (\text{A.45})$$

is used.

List of Abbreviations

AAF	anti-aliasing-filter
ADC	analog-to-digital converter
BB	baseband
BW	bandwidth
CA	carrier aggregation
CC	component carriers
CSF	channel-select filter
CW	continuous wave
CWGN	complex white Gaussian noise
DAC	digital-to-analog converter
DC	direct-current
DCO	digitally controlled oscillator
DFE	digital front-end
DL	downlink
DTC	digital-to-time converter
EMSE	excess mean-square-error
FDD	frequency division duplex
FIR	finite impulse response
GPS	Global Positioning System
GSM	Global System for Mobile Communications
HR	harmonic rejection
I	in-phase
IF	intermediate frequency
IIP2	second-order input intercept point
IIP3	third-order input intercept point
IM2	second-order intermodulation product
IMD2	second-order intermodulation distortion
IMD3	third-order intermodulation distortion
IM3	third-order intermodulation product
LMS	least-mean-squares
LNA	low noise amplifier
LO	local oscillator
LS	least-squares

List of Abbreviations

LTE	Long Term Evolution
LTE-A	Long Term Evolution-Advanced
MSE	mean-square-error
NF	noise figure
NFC	near field communication
ϵ-NLMS	normalized least-mean-squares
NMSE	normalized mean-square-error
ϵ-VSSNLMS	variable step-size normalized LMS
OFDM	orthogonal frequency-division multiplexing
OOB	out-of-band
OR	output-referred
OSF	oversampling factor
PA	power amplifier
PCC	primary component carrier
PN	phase noise
PSD	power spectral density
Q	quadrature-phase
RB	resource block
RF	radio frequency
RLS	recursive-least-squares
Rx	receive
ϵ-APA	regularized affine-projection algorithm
SC-FDMA	single-carrier frequency-division multiple access
SCC	secondary component carrier
SINR	signal-to-interference-plus-noise ratio
SNR	signal-to-noise ratio
TDD	time-division duplex
Tx	transmit
TxL	transmitter leakage
UMTS	Universal Mobile Telecommunication System
UE	user equipment
UL	uplink
VSWR	voltage-standing-wave-ratio
2t	two-tone
3GPP	3rd Generation Partnership Project

Bibliography

- [1] 3GPP, “3rd Generation Partnership Project; Technical Specification Group Radio Access Network; Evolved Universal Terrestrial Radio Access (E-UTRA); User Equipment (UE) radio transmission and reception (Release 10),” 3GPP, Tech. Rep., May 2015. [Online]. Available: http://www.3gpp.org/ftp/Specs/latest_prior-to-2018-03/Rel-10/36_series/36807-a00.zip
- [2] A. A. Abidi, “Direct-conversion radio transceivers for digital communications,” In *IEEE Journal of Solid-State Circuits*, Vol. 30, No. 12, pp. 1399–1410, Dec 1995.
- [3] 3GPP, “Evolved Universal Terrestrial Radio Access (E-UTRA); User Equipment (UE) radio transmission and reception,” 3GPP, Tech. Rep., May 2015. [Online]. Available: http://www.3gpp.org/ftp/specs/archive/36_series/36.101/36101-bg0.zip
- [4] Ericsson and ST-Ericsson, “R4-126964, REFSSENS with one UL carrier for NC intra-band CA,” Ericsson, Tech. Rep., November 2012. [Online]. Available: http://www.3gpp.org/ftp/tsg_ran/WG4_Radio/TSGR4.65/docs/R4-126964.zip
- [5] R. Vazny, W. Schelmbauer, H. Pretl, S. Herzinger, and R. Weigel, “An interstage filter-free mobile radio receiver with integrated TX leakage filtering,” In Proceedings of the *IEEE Radio Frequency Integrated Circuits Symposium*, May 2010, pp. 21–24.
- [6] A. Kiayani, L. Anttila, and M. Valkama, “Modeling and dynamic cancellation of TX-RX leakage in FDD transceivers,” In Proceedings of the *56th International Midwest Symposium on Circuits and Systems (MWSCAS)*, Aug 2013, pp. 1089–1094.
- [7] A. Gebhard, C. Motz, R. S. Kanumalli, H. Pretl, and M. Huemer, “Nonlinear least-mean-squares type algorithm for second-order interference cancellation in LTE-A RF transceivers,” In Proceedings of the *51st Asilomar Conference on Signals, Systems, and Computers*, Oct 2017, pp. 802–807.
- [8] B. Razavi, “Design considerations for direct-conversion receivers,” In *IEEE Transactions on Circuits and Systems II: Analog and Digital Signal Processing*, Vol. 44, No. 6, pp. 428–435, Jun 1997.
- [9] A. Gebhard, R. S. Kanumalli, B. Neurauter, and M. Huemer, “Adaptive self-interference cancelation in LTE-A carrier aggregation FDD direct-conversion transceivers,” In Proceedings of the *9th IEEE Sensor Array and Multichannel Signal Processing Workshop (SAM 2016)*, July 2016, pp. 1–5.
- [10] R. S. Kanumalli, A. Gebhard, A. Elmaghraby, A. Mayer, D. Schwartz, and M. Huemer, “Active Digital Cancellation of Transmitter Induced Modulated Spur Interference in 4G LTE Carrier Aggregation Transceivers,” In Proceedings of the *83rd IEEE Vehicular Technology Conference (VTC Spring)*, May 2016, pp. 1–5.
- [11] A. Kiayani, M. Abdelaziz, L. Anttila, V. Lehtinen, and M. Valkama, “Digital Mitigation of Transmitter-Induced Receiver Desensitization in Carrier Aggregation FDD

Bibliography

- Transceivers,” In *IEEE Transactions on Microwave Theory and Techniques*, Vol. 63, No. 11, pp. 3608–3623, Nov 2015.
- [12] A. Kiayani, M. Z. Waheed, L. Anttila, M. Abdelaziz, D. Korpi, V. Syrjälä, M. Kosunen, K. Stadius, J. Ryyänen, and M. Valkama, “Adaptive Nonlinear RF Cancellation for Improved Isolation in Simultaneous Transmit–Receive Systems,” In *IEEE Transactions on Microwave Theory and Techniques*, Vol. 66, No. 5, pp. 2299–2312, May 2018.
- [13] A. Elmaghraby, “Transmitter Leakage Cancellation in Cellular Handset Receivers,” Dissertation, University of Erlangen-Nuremberg, July 2016.
- [14] H. Khatri, P. S. Gudem, and L. E. Larson, “An Active Transmitter Leakage Suppression Technique for CMOS SAW-Less CDMA Receivers,” In *IEEE Journal of Solid-State Circuits*, Vol. 45, No. 8, pp. 1590–1601, Aug 2010.
- [15] A. Elmaghraby, R. S. Kanumalli, W. Schelmbauer, A. Mayer, S. Herzinger, D. Schwartz, M. Huemer, and R. Weigel, “A Mixed-Signal Technique for TX-Induced Modulated Spur Cancellation in LTE-CA Receivers,” In *IEEE Transactions on Circuits and Systems I: Regular Papers*, Vol. 65, No. 9, pp. 3060–3073, Sep. 2018.
- [16] S. Sadjina, R. S. Kanumalli, A. Gebhard, K. Dufrêne, M. Huemer, and H. Pretl, “A Mixed-Signal Circuit Technique for Cancellation of Interferers Modulated by LO Phase-Noise in 4G/5G CA Transceivers,” In *IEEE Transactions on Circuits and Systems I: Regular Papers*, Vol. 65, No. 11, pp. 3745–3755, Nov 2018.
- [17] M. Faulkner, “DC offset and IM2 removal in direct conversion receivers,” In *IEE Proceedings - Communications*, Vol. 149, No. 3, pp. 179–184, Jun 2002.
- [18] M. Faulkner, “IM2 removal in direct conversion receivers,” In *Proceedings of the 53rd Vehicular Technology Conference*, Vol. 3, May 2001, pp. 1897–1901.
- [19] A. Kiayani, L. Anttila, M. Kosunen, K. Stadius, J. Ryyänen, and M. Valkama, “Modeling and Joint Mitigation of TX and RX Nonlinearity-Induced Receiver Desensitization,” In *IEEE Transactions on Microwave Theory and Techniques*, Vol. 65, No. 7, pp. 2427–2442, July 2017.
- [20] A. Kiayani, L. Anttila, and M. Valkama, “Digital Suppression of Power Amplifier Spurious Emissions at Receiver Band in FDD Transceivers,” In *IEEE Signal Processing Letters*, Vol. 21, No. 1, pp. 69–73, Jan 2014.
- [21] A. Frotzcher and G. Fettweis, “A Stochastic Gradient LMS Algorithm for Digital Compensation of Tx Leakage in Zero-IF-Receivers,” In *Proceedings of the Vehicular Technology Conference (VTC Spring 2008)*, May 2008, pp. 1067–1071.
- [22] C. Lederer and M. Huemer, “LMS Based Digital Cancellation of Second-Order TX Intermodulation Products in Homodyne Receivers,” In *Proceedings of the Radio and Wireless Symposium (RWS)*, Jan 2011, pp. 207–210.

- [23] A. Frotzsch and G. Fettweis, “Least Squares Estimation for the Digital Compensation of Tx Leakage in zero-IF Receivers,” In Proceedings of the *Global Telecommunications Conference (GLOBECOM 2009)*, Nov 2009, pp. 1–6.
- [24] D. H. Brandwood, “A complex gradient operator and its application in adaptive array theory,” In *IEE Proceedings F - Communications, Radar and Signal Processing*, Vol. 130, No. 1, pp. 11–16, February 1983.
- [25] V. J. Mathews and G. L. Sicuranza, *Polynomial signal processing*. Wiley-Interscience, 2000.
- [26] T. Ogunfunmi, *Adaptive nonlinear system identification: the Volterra and Wiener model approaches*. Springer Science & Business Media, 2007.
- [27] A. Gebhard, O. Lang, M. Lunglmayr, C. Motz, R. S. Kanumalli, C. Auer, T. Paireder, M. Wagner, H. Pretl, and M. Huemer, “A Robust Nonlinear RLS Type Adaptive Filter for Second-Order-Intermodulation Distortion Cancellation in FDD LTE and 5G Direct Conversion Transceivers,” In *IEEE Transactions on Microwave Theory and Techniques*, 16 pages, Early Access, January 2019.
- [28] TDK, “SAW Duplexer B8576,” TDK, Tech. Rep., February 2015. [Online]. Available: <https://en.rf360jv.com/inf/40/ds/mc/B8576.pdf>
- [29] A. Mirzaei, H. Darabi, J. Leete, and Y. Chang, “Analysis and Optimization of Direct-Conversion Receivers With 25% Duty-Cycle Current-Driven Passive Mixers,” In *Circuits and Systems I: Regular Papers, IEEE Transactions on*, Vol. 57, No. 9, pp. 2353–2366, Sept 2010.
- [30] A. Kiayani, V. Lehtinen, L. Anttila, T. Lahteensuo, and M. Valkama, “Linearity Challenges of LTE-Advanced Mobile Transmitters: Requirements and Potential Solutions,” In *IEEE Communications Magazine*, Vol. 55, No. 6, pp. 170–179, 2017.
- [31] M. Mikhemar, D. Murphy, A. Mirzaei, and H. Darabi, “A Cancellation Technique for Reciprocal-Mixing Caused by Phase Noise and Spurs,” In *IEEE Journal of Solid-State Circuits*, Vol. 48, No. 12, pp. 3080–3089, Dec 2013.
- [32] H. T. Dabag, H. Gheidi, P. Gudem, and P. M. Asbeck, “All-digital cancellation technique to mitigate self-jamming in uplink carrier aggregation in cellular handsets,” In *2013 IEEE MTT-S International Microwave Symposium Digest (MTT)*, June 2013, pp. 1–3.
- [33] W. Rhee and K. Iniewski, *Wireless Transceiver Circuits*. CRC Press, 2015.
- [34] R. Tzschoppe and J. B. Huber, “Causal discrete-time system approximation of non-bandlimited continuous-time systems by means of discrete prolate spheroidal wave functions,” In *European Transactions on Telecommunications*, Vol. 20, No. 6, pp. 604–616, Aug 2008.
- [35] A. V. Oppenheim, R. W. Schaffer, and J. R. Buck, *Discrete-time signal processing*. Prentice Hall, 1999.

Bibliography

- [36] M. Valkama, M. Renfors, and V. Koivunen, “Advanced Methods for I/Q Imbalance Compensation in Communication Receivers,” In *IEEE Transactions on Signal Processing*, Vol. 49, No. 10, pp. 2335–2344, Oct 2001.
- [37] M. Valkama, A. Springer, and G. Hueber, “Digital signal processing for reducing the effects of RF imperfections in radio devices - An overview,” In Proceedings of the *IEEE International Symposium on Circuits and Systems*, May 2010, pp. 813–816.
- [38] H. Darabi, *Radio Frequency Integrated Circuits and Systems*. Cambridge University Press, 2015.
- [39] A. Walid, “Effective IM2 products estimation for two-tone and W-CDMA modulated blockers in 3GPP direct-conversion receivers,” Maxim Integrated, Tech. Rep., 2004.
- [40] J. Héctor, C. Sturm, and J. Ponte, *Radio Systems Engineering: A Tutorial Approach*. Springer, 2014.
- [41] I. Reed, “On a moment theorem for complex Gaussian processes,” In *IRE Transactions on Information Theory*, Vol. 8, No. 3, pp. 194–195, April 1962.
- [42] M. Ahsanullah, B. G. Kibria, and M. Shakil, *Normal and student’s t distributions and their applications*. Springer, 2014.
- [43] D. Stuetzle, “Understanding IP2 and IP3 Issues in Direct Conversion Receivers for WCDMA Wide Area Basestations,” In *High Frequency Electronics*, Vol. 7, No. 6, 2008.
- [44] E. S. Atalla, A. Bellaouar, and P. T. Balsara, “IIP2 requirements in 4G LTE handset receivers,” In Proceedings of the *56th International Midwest Symposium on Circuits and Systems (MWSCAS)*, Aug 2013, pp. 1132–1135.
- [45] C. W. Liu and M. Dangaard, “IP2 and IP3 nonlinearity specifications for 3G/WCDMA receivers,” In *High Frequency Electronics*, pp. 16–29, 2009.
- [46] I. Madadi, M. Tohidian, K. Cornelissens, P. Vandenameele, and R. B. Staszewski, “A High IIP2 SAW-Less Superheterodyne Receiver With Multistage Harmonic Rejection,” In *IEEE Journal of Solid-State Circuits*, Vol. 51, No. 2, pp. 332–347, Feb 2016.
- [47] K. Dufrene, Z. Boos, and R. Weigel, “Digital Adaptive IIP2 Calibration Scheme for CMOS Downconversion Mixers,” In *IEEE Journal of Solid-State Circuits*, Vol. 43, No. 11, pp. 2434–2445, Nov 2008.
- [48] A. Mirzaei, H. Darabi, J. C. Leete, X. Chen, K. Juan, and A. Yazdi, “Analysis and Optimization of Current-Driven Passive Mixers in Narrowband Direct-Conversion Receivers,” In *IEEE Journal of Solid-State Circuits*, Vol. 44, No. 10, pp. 2678–2688, Oct 2009.
- [49] J. Weldon, R. Narayanaswami, J. Rudell, L. Lin, M. Otsuka, S. Dedieu, L. Tee, K.-C. Tsai, C.-W. Lee, and P. Gray, “A 1.75-GHz highly integrated narrow-band CMOS transmitter with harmonic-rejection mixers,” In *IEEE Journal of Solid-State Circuits*, Vol. 36, No. 12, pp. 2003–2015, Dec 2001.

- [50] T. Forbes, W.-G. Ho, and R. Gharpurey, “Design and Analysis of Harmonic Rejection Mixers With Programmable LO Frequency,” In *IEEE Journal of Solid-State Circuits*, Vol. 48, No. 10, pp. 2363–2374, Oct 2013.
- [51] H. Zhang, T. B. Gao, S. Tan, and O. Shana’A, “A harmonic-rejection mixer with improved design algorithm for broadband TV tuners,” In Proceedings of the *IEEE Radio Frequency Integrated Circuits Symposium (RFIC)*, June 2012, pp. 163–166.
- [52] Y. H. Chen, N. Fong, B. Xu, and C. Wang, “An LTE SAW-less transmitter using 33% duty-cycle LO signals for harmonic suppression,” In *2015 IEEE International Solid-State Circuits Conference - (ISSCC) Digest of Technical Papers*, Feb 2015, pp. 1–3.
- [53] R. Bagheri, A. Mirzaei, S. Chehrazi, M. E. Heidari, M. Lee, M. Mikhemar, W. Tang, and A. A. Abidi, “An 800-MHz ndash;6-GHz Software-Defined Wireless Receiver in 90-nm CMOS,” In *IEEE Journal of Solid-State Circuits*, Vol. 41, No. 12, pp. 2860–2876, Dec 2006.
- [54] F. Gatta, R. Gomez, Y. Shin, T. Hayashi, H. Zou, J. Y. C. Chang, L. Dauphinee, J. Xiao, D. S. H. Chang, T. H. Chih, M. Brandolini, D. Koh, B. J. J. Hung, T. Wu, M. Introini, G. Cusmai, L. Tan, B. Currivan, L. He, P. Cangiane, and P. Vorenkamp, “An embedded 65nm CMOS low-IF 48MHz-to-1GHz dual tuner for DOCSIS 3.0,” In *2009 IEEE International Solid-State Circuits Conference - Digest of Technical Papers*, Feb 2009, pp. 122–123,123a.
- [55] K. Kibaroglu and G. M. Rebeiz, “A 0.05 –6 GHz voltage-mode harmonic rejection mixer with up to 30 dBm in-band IIP3 and 35 dBc HRR in 32 nm SOI CMOS,” In *2017 IEEE Radio Frequency Integrated Circuits Symposium (RFIC)*, June 2017, pp. 304–307.
- [56] D. Murphy, H. Darabi, and H. Xu, “A Noise-Cancelling Receiver Resilient to Large Harmonic Blockers,” In *IEEE Journal of Solid-State Circuits*, Vol. 50, No. 6, pp. 1336–1350, June 2015.
- [57] A. Gebhard, S. Sadjina, K. Dufrene, and S. Tertinek, “Harmonic Suppressing Local Oscillator Signal Generation,” US Patent 9,935,722 B2, granted March 2018.
- [58] D. P. Mandic and V. S. L. Goh, *Complex valued nonlinear adaptive filters: noncircularity, widely linear and neural models*. John Wiley & Sons, 2009, Vol. 59.
- [59] P. S. Diniz, *Adaptive Filtering, Algorithms and Practical Implementation*. Springer, 2013.
- [60] H. G. Myung, “Introduction to single carrier FDMA,” In Proceedings of the *15th European Signal Processing Conference (EUSIPCO)*, Sept 2007, pp. 2144–2148.
- [61] A. H. Sayed, *Fundamentals of adaptive filtering*. John Wiley & Sons, 2003.
- [62] P. Schreier and L. L. Scharf, *Statistical Signal Processing of Complex-Valued Data: The Theory of Improper and Noncircular Signals*. Cambridge University Press, 2010.

Bibliography

- [63] R. Hunger, “An introduction to complex differentials and complex differentiability,” Technische Universität München. TUM-LNS-TR-07-06, October 2007., Tech. Rep., 2007.
- [64] R. F. H. Fischer, *Appendix A: Wirtinger Calculus*. Wiley-Blackwell, 2005, pp. 405–413. [Online]. Available: <https://onlinelibrary.wiley.com/doi/abs/10.1002/0471439002.app1>
- [65] A. van den Bos, “Complex gradient and Hessian,” In *IEE Proceedings - Vision, Image and Signal Processing*, Vol. 141, No. 6, pp. 380–383, Dec 1994.
- [66] A. I. Hanna and D. P. Mandic, “A fully adaptive normalized nonlinear gradient descent algorithm for complex-valued nonlinear adaptive filters,” In *IEEE Transactions on Signal Processing*, Vol. 51, No. 10, pp. 2540–2549, Oct 2003.
- [67] K. Kreutz-Delgado, “The Complex Gradient Operator and the CR-Calculus,” Electrical and Computer Engineering, Jacobs School of Engineering, University of California, San Diego, Tech. Rep., 2009. [Online]. Available: <https://arxiv.org/pdf/0906.4835.pdf>
- [68] M. A. Woodbury, “Inverting Modified Matrices,” Statistical Research Group Memorandum Reports. Princeton, NJ: Princeton University, 1950, No. 42., Tech. Rep., 1950.
- [69] E. C. Levy, “Complex-curve fitting,” In *IRE Transactions on Automatic Control*, Vol. AC-4, No. 1, pp. 37–43, May 1959.
- [70] J. Zyren and W. McCoy, “Overview of the 3GPP long term evolution physical layer,” Freescale Semiconductor, Inc., Tech. Rep., 2007. [Online]. Available: https://www.nxp.com/files/wireless_comm/doc/white_paper/3GPPEVOLUTIONWP.pdf
- [71] M. Kahrizi, J. Komaili, J. E. Vasa, and D. Agahi, “Adaptive filtering using LMS for digital TX IM2 cancellation in WCDMA receiver,” In *Proceedings of the IEEE Radio and Wireless Symposium*, Jan 2008, pp. 519–522.
- [72] H. Gheidi, H. T. Dabag, Y. Liu, P. M. Asbeck, and P. Gudem, “Digital cancellation technique to mitigate receiver desensitization in cellular handsets operating in carrier aggregation mode with multiple uplinks and multiple downlinks,” In *Proceedings of the IEEE Radio and Wireless Symposium (RWS)*, Jan 2015, pp. 221–224.
- [73] C. Lederer and M. Huemer, “Simplified complex LMS algorithm for the cancellation of second-order TX intermodulation distortions in homodyne receivers,” In *Proceedings of the Forty Fifth Asilomar Conference on Signals, Systems and Computers (ACSSC)*, Nov 2011, pp. 533–537.
- [74] R. Isermann, *Identifikation dynamischer Systeme 1*. Springer-Verlag, 1991.
- [75] M. Rupp and R. Frenzel, “Analysis of LMS and NLMS algorithms with delayed coefficient update under the presence of spherically invariant processes,” In *IEEE Transactions on Signal Processing*, Vol. 42, No. 3, pp. 668–672, March 1994.

- [76] A. Gebhard, “Second Order Intermodulation Cancellation for RF Transceivers,” US Patent 2018/015 417, filed June 2017.
- [77] Y. Chen, T. Le-Ngoc, B. Champagne, and C. Xu, “Recursive least squares constant modulus algorithm for blind adaptive array,” In *IEEE Transactions on Signal Processing*, Vol. 52, No. 5, pp. 1452–1456, May 2004.
- [78] Y. X. Chen, Z. Y. He, T. S. Ng, and P. C. K. Kwok, “RLS adaptive blind beamforming algorithm for cyclostationary signals,” In *Electronics Letters*, Vol. 35, No. 14, pp. 1136–1138, July 1999.
- [79] R. Ferrús and O. Sallent, *Mobile Broadband Communications for Public Safety: The Road Ahead Through LTE Technology*. Wiley, 2015.
- [80] S. Gunnarsson, “Combining tracking and regularization in recursive least squares identification,” In *Proceedings of 35th IEEE Conference on Decision and Control*, Dec 1996, pp. 2551–2552.
- [81] T. Huckle and M. Sedlacek, “Data Based Regularization Matrices for the Tikhonov-Phillips Regularization,” In *Proceedings of the Applied Mathematics and Mechanics (PAMM)*. Wiley Online Library, 2012, pp. 643–644.
- [82] J. Dokoupil and V. Burlak, “Variable Regularized Square Root Recursive Least Square Method,” In *Proceedings of the 11th IFAC IEEE International Conference on Programmable Devices and Embedded Systems*, 2012, pp. 78–82.

Curriculum Vitae

Personal Information

Andreas Gebhard
Parkstraße 8/9
4230 Pregarten, Austria
+43 (0)680 1411494
andreas.gebhard@jku.at

Education

- 2014 – 2018 **PhD in Technical Sciences, *Johannes Kepler University Linz***
- PhD thesis: "Self-Interference Cancellation and Rejection in FDD RF-Transceivers" conducted at the *Institute of Signal Processing (ISP)*, and in cooperation with DMCE/Intel Austria.
- 2009 – 2011 **MSc (Dipl.-Ing.) in Electrical Engineering, *Graz University of Technology, with distinction***
- Major in *Control and Automation*.
 - Master thesis: Construction and Control of the Laboratory Model "Car on a Rotatable Beam" conducted at the *Institute for Control and Automation (IRT)*.
- 2006 – 2009 **BSc in Electrical Engineering, *Graz University of Technology***
- Bachelor Thesis: "Modeling, Control and Simulation of Switched Mode Power Supplies" conducted at the *Institute for Control and Automation (IRT)*.
- 1996 – 2001 **Technical College (Telecommunications), *HTL Rankweil***
- Degree project: "Class-D Switched Mode Audio Power Amplifier".

Experience

- Since
12/2014 **PhD in Technical Sciences, *Johannes Kepler University Linz*
in cooperation with DMCE/Intel, Linz, full time**
- Mentor of three PhD students
 - Co-supervisor of one master thesis
 - Reviewer for several journal and conference papers
 - Various PR activities in form of talks, seminars, and exhibitions
- 03/2013 –
11/2014 **Development of Mechatronic Systems, *Linz Center of
Mechatronics, Linz, full time***
- Condition monitoring concepts for gas valves and injection molding machines
 - Control design for an electronic shaft of a manned transport system
 - Acoustic localization of miners around the digging machine using time-of-flight measurements
- 04/2012 –
02/2013 **Implementation of Control Algorithms in PLC Control
Units, *Schelling Anlagenbau, Schwarzach, full time***
- Control of fully automated and time optimized wood and steel saws
 - Implementation of digital filters
 - Commissioning of saws in Germany and Spain
- 11/2011 –
02/2012 **Trip to New Zealand and Australia**
- 08/2010 –
09/2010 **Internship, *ATB Motors, Lustenau, full time***
- Control of a brush-less DC motor with back-EMF detection
- 07/2008 –
08/2008 **Internship, *Tridonic.ATCO, Dornbirn, full time***
- Patent-department: Analysis of competitive products for patent violations
- 05/2002 –
07/2006 **Design of electronic control gears for fluorescent lamps,
*Tridonic.ATCO, Dornbirn, full time***
- Dimensioning of the electrical components (L,C) required for the resonance circuitry
 - Testing of the electronic gears for standardization requirements (ENEC, EN, ISO)
 - Accompaniment of the products till the null-series and series maturity

07/1999 – **Internship, Siemens, Bregenz, full time**

08/1999

- Testing of fireboxes
- Construction of electric cabinets

07/1998 – **Internship, Fawai & Co, Bregenz, full time**

08/1998

- Repairing of televisions and radios
- Commissioning televisions at customers

Language Skills

- German (mother tongue)
- English

Patents / Patent Applications

- A. Gebhard, S. Sadjina, K. Dufrene and S. Tertinek, "Harmonic Suppressing Local Oscillator Signal Generation," U.S. Patent US 9,935,722 B2, filed June 2016, granted April 2018.
- S. Tertinek, A. Gebhard, S. Sadjina and K. Dufrene, "Pulse Generation Using Digital-to-Time Converter," U.S. Patent US 9,755,872 B1, filed August 2016, granted September 2017.
- K. Dufrene, Ram S. Kanumalli, S. Sadjina and A. Gebhard, "Multiple Modulated Spur Cancellation Apparatus," U.S. Patent Application US 2017/0359136 A1, filed June 2016, published December 2017.
- A. Gebhard, "Second Order Intermodulation Cancellation for RF Transceivers," U.S. Patent US 10,172,143 B2, filed June 2017, granted January 2019.
- K. Dufrene, S. Sadjina, A. Gebhard and Ram S. Kanumalli, "Interference Detection Device, Interference Detection Apparatus, Interference Detection Method, Computer Program, Receiver, Mobile Terminal and Base Station," U.S. Patent US 10,097,220 B2, filed May 2017, granted October 2018.

Journal Publications

- A. Gebhard, O. Lang, M. Lunglmayr, C. Motz, R. S. Kanumalli, C. Auer, T. Paireder, M. Wagner, H. Pretl and M. Huemer, "A Robust Nonlinear RLS Type Adaptive Filter for Second-Order-Intermodulation Distortion Cancellation in FDD LTE and 5G Direct Conversion Transceivers," In *IEEE Transactions on Microwave Theory and Techniques*, 16 pages, Early Access, January 2019.
- S. Sadjina, R. S. Kanumalli, A. Gebhard, K. Dufrene, M. Huemer and H. Pretl, "A Mixed-Signal Circuit Technique for Cancellation of Interferers Modulated by LO Phase-Noise in 4G/5G CA Transceivers," In *IEEE Transactions on Circuits and Systems – I Regular Papers*, Vol. 65, No. 11, pp. 3745-3755, Nov 2018.
- R. S. Kanumalli, T. Buckel, C. Preissl, P. Preyler, A. Gebhard, C. Motz, J. Markovic, D. Hamidovic, E. Hager, H. Pretl, A. Springer and M. Huemer, "Digitally-intensive Transceivers for Future Mobile Communications - Emerging Trends and Challenges," In *e&i Elektrotechnik und Informationstechnik*, Vol. 135, No. 1, pp. 30-39, January 2018.

Conference Publications

- A. Gebhard and C. Motz and R. S. Kanumalli and H. Pretl and M. Huemer, "Non-linear Least-Mean-Squares Type Algorithm for Second-Order Interference Cancellation in LTE-A RF Transceivers," In *Proceedings of the 51st IEEE Asilomar Conference on Signals, Systems, and Computers (ACSSC)*, Oct 2017, pp. 802-807.
- A. Gebhard, M. Lunglmayr and M. Huemer, "Investigations on Sparse System Identification with l_0 -LMS, Zero-Attracting LMS and Linearized Bregman Iterations," In *Proceedings of the 16th International Conference on Computer Aided System Theory - EUROCAST*, February 2018.
- A. Gebhard and R. S. Kanumalli and B. Neurauder and M. Huemer, "Adaptive Self-Interference Cancellation in LTE-A Carrier Aggregation FDD Direct-Conversion Transceivers," In *Proceedings of the IEEE Sensor Array and Multichannel Signal Processing Workshop (SAM 2016)*, July 2016, pp. 1-5.
- R. S. Kanumalli, A. Gebhard, A. Elmaghraby, A. Mayer, D. Schwartz and M. Huemer, "Active Digital Cancellation of Transmitter Induced Modulated Spur Interference in 4G LTE Carrier Aggregation Transceivers," In *Proceedings of the 83rd IEEE Vehicular Technology Conference (VTC Spring)*, May 2016, pp. 1-5.